



HAL
open science

Terre de Feu : Interactions entre tectonique et climat à la terminaison sud de l'Amérique

Sandrine Roy

► **To cite this version:**

Sandrine Roy. Terre de Feu: Interactions entre tectonique et climat à la terminaison sud de l'Amérique. Géomorphologie. Université Savoie Mont Blanc, 2020. Français. NNT: 2020CHAMA057 . tel-03919584

HAL Id: tel-03919584

<https://theses.hal.science/tel-03919584>

Submitted on 3 Jan 2023

HAL is a multi-disciplinary open access archive for the deposit and dissemination of scientific research documents, whether they are published or not. The documents may come from teaching and research institutions in France or abroad, or from public or private research centers.

L'archive ouverte pluridisciplinaire **HAL**, est destinée au dépôt et à la diffusion de documents scientifiques de niveau recherche, publiés ou non, émanant des établissements d'enseignement et de recherche français ou étrangers, des laboratoires publics ou privés.



Institut des Sciences de la Terre



THESIS

for the Degree of

DOCTOR OF PHILOSOPHY IN GEOLOGY

UNIVERSITY SAVOIE MONT BLANC

Speciality:

Sciences of the Earth, the Universe and the Environment.

Arrêté ministériel : 25 Mai 2016

Author

Sandrine ROY

Supervisors **Riccardo VASSALLO** and **Joseph MARTINOD**

Prepared in the **Institute of Earth Sciences ISTerre**
Doctoral school Earth, Universe and Environment

Tierra del Fuego: Interaction between tectonics and climate in the southern end of America

Defended at Bourget du Lac, France,

18th December 2020

in front of advisory committee:

Stéphane MAZZOTTI

Professeur, Université Montpellier 2, France - reporter

Edwin NISSEN

Associate Professor, University of Victoria, British Columbia - reporter

Sébastien CASTELLTORT

Associate Professor, Université de Genève – examiner

Magali RIZZA

Maître de conférences, Université Aix-Marseille – examiner

Daniel MELNICK

Professor, Universidad Austral de Chile, Valdivia – examiner

Jean-Louis MUGNIER

Directeur de recherche CNRS, Université Savoie Mont Blanc – examiner

Joseph MARTINOD

Professeur, Université Savoie Mont Blanc – supervisor

Riccardo VASSALLO

Maître de conférences, Université Savoie Mont Blanc – supervisor

Corrected version of 28. December 2020, after the Ph.D Defense and in agreement with precious comments and suggestions of the advisory committee.

Sandrine Roy, Tierra del Fuego: Interaction between tectonics and climate in the southern end of America, Université Savoie Mont Blanc, 2020.



Institut des Sciences de la Terre



THÈSE

Pour obtenir le grade de

DOCTORESSE DE L'UNIVERSITÉ SAVOIE MONT BLANC

Spécialité : **Sciences de la Terre, de l'Univers et de l'Environnement**

Arrêté ministériel : 25 Mai 2016

Présenté par

Sandrine ROY

Thèse dirigée par **Riccardo VASSALLO** et **Joseph MARTINOD**

Préparée au sein de l'**Institut des Sciences de la Terre**
Dans l'école doctorale **Terre Univers Environnement**

Terre de Feu : Interaction entre tectonique et climat à la terminaison Sud de l'Amérique

Thèse soutenue publiquement au Bourget du Lac,
18 Décembre 2020,
Devant le jury composé de :

Stéphane MAZZOTTI

Professeur, Université Montpellier 2, France - reporter

Edwin NISSEN

Associate Professor, University of Victoria, British Columbia - reporter

Sébastien CASTELLTORT

Associate Professor, Université de Genève – examiner

Magali RIZZA

Maître de conférences, Université Aix-Marseille – examiner

Daniel MELNICK

Professor, Universidad Austral de Chile, Valdivia – examiner

Jean-Louis MUGNIER

Directeur de recherche CNRS, Université Savoie Mont Blanc – examiner

Joseph MARTINOD

Professeur, Université Savoie Mont Blanc – supervisor

Riccardo VASSALLO

Maître de conférences, Université Savoie Mont Blanc – supervisor

Version corrigée du 28 décembre 2020, après soutenance et sur les recommandations et suggestions du Jury.

Sandrine Roy, Terre de Feu : Interaction entre tectonique et climat à la terminaison Sud de l'Amérique, Université Savoie Mont Blanc, 2020.

Remerciements, Acknowledgments

Ça y est ? Ce sont les remerciements ? Serait-ce la ligne d'arrivée ? Après ce marathon doctoral, et ce long sprint final, j'ai l'impression que mes jambes courent toutes seules, sans plus personne aux commandes. Il y a trois ans, je ne me doutais pas que l'un de mes futurs directeurs écrivait dans son mémoire une décennie plus tôt : « il faut être complètement fou pour décider volontairement de faire une thèse ». A la lecture de ces mots (il y a peu – fort heureusement), d'une part je me suis rappelée du sérieux de mes deux directeurs lors de mon entretien, puis des éclats de rires lors de nos terrains. D'autre part cela m'a rassuré, je ne suis donc pas la seule à être dans cet état, on ferait tous partie du même navire !

Cette thèse, c'est le fruit de trois années de travail, qui furent une incroyable aventure scientifique et humaine, et qui n'aurait pu voir le jour sans un certain (grand) nombre de personnes.

Tout d'abord, il me semble que je n'aurais peut-être pas rencontré Joseph et Riccardo, mes directeurs, sans l'aide précieuse de Jean-Louis. J'en profite également pour le remercier de sa confiance, et de son amitié en haute-montagne comme au laboratoire.

Bien-sûr, d'immenses remerciements s'adressent spécialement à mes deux directeurs Riccardo et Joseph. Chacun dans un style qui lui est propre, m'a offert une grande liberté de travailler de manière autonome, m'a permis d'explorer mes idées tout en me maintenant les pieds sur terres (essayant) et mon esprit dans la bonne direction. Je suis très reconnaissante pour leur confiance à travers ces trois ans épatants de recherche sur la Patagonie Australe. Leur porte était toujours ouverte, et leur accueil chaleureux, je savais donc pertinemment que je pouvais les questionner, discuter, et plaisanter à la première occasion. Je mesure la chance que j'ai eue d'avoir été encadrée par des chercheurs d'excellence, mais qui ont en outre de grandes qualités humaines.

Je pense également à Christian Sue, qui nous a aidé pour chacun des terrains dans ces environnements hostiles en Terre de Feu et dans le Détroit de Magellan. Un grand merci pour son enthousiasme débordant et ses conseils stratégiques d'organisation. Egalement, je le remercie de m'avoir permis de travailler dans le massif du Fitz Roy. Malgré les grands vents de cette région, soulevant nos tentes et nous y compris, ce fut un privilège en tant que grimpeuse de découvrir ce massif.

A huge thanks to Matias Ghiglione. I was particularly lucky to work alongside Matias for the first years of my Ph.D., whose knowledge of the remote Tierra del Fuego Atlantic coast and of the South America geodynamic, meant I never needed to look far for help. He greatly facilitated my investigations in the Argentinian lands, patiently introduced me to the local communities, and generously provided historical documents and hospitality during my stays in Buenos Aires.

Un grand merci à Laurent Astrade, pour l'énergie et les shots d'enthousiasme au pied des glaciers des Cordillères Darwin et Paciencia. C'était passionnant d'apprendre à ses côtés ce que racontent les arbres, un art étonnant qui débute dans la peau d'un bucheron et finit entre les mains d'orfèvres. Merci pour notre collaboration et ces dernières semaines d'échanges !

También me gustaría agradecer a Pablo Morales Vasquez, quien ciertamente pensó que estábamos locos cavando trincheras en medio de la nada. Siempre fue el primero en echar una mano y siempre con un ojo atento a la geología local. Muchas gracias Pablo.

Tous ses collègues ci-dessus, ont accepté (subi) vaillamment de me suivre dans mes terrains, de temps en temps en mer (déchainée), quelques fois dans les grands vents Patagoniens, parfois dans le froid, souvent sous la pluie et toujours dans la tourbe ! Je leur tire mon chapeau, d'avoir fait confiance à mes points GPS sur photo sat détrempée, d'avoir marché de longues heures, à s'enfoncer dans cette tourbe, trébucher, se relever et toujours garder le sourire. Un grandissime merci !

Tengo una inmensa gratitud por todas las personas sensibles e increíbles que me han ayudado, acogido y apoyado en el campo en Tierra del Fuego (Argentina y Chile) : Cristian Maure y Marina Bauduco | Mónica P. Escayola y Daniel A. Fernández (UNTDF, CONICET) | Nativo Expediciones : Fredy Moreno Azua, Camilo Uribe Padilla y Andrés Fabián Huenchucho | Annemie Eyer | Ivette Martínez | Cesar | German Genskowski and Maricela Díaz |



*Tanu, Espíritu Feminino Selk'nam, Diosa del Inframundo, Pintura de propiedad intelectual, perteneciente a la artista visual Elby Huerta – Santiago, Chile. Uso exclusiva para esta tesis, derechos reservados de la autora **Copyright © Elby Huerta***

Muchas gracias a mi amiga, la artista Elby Huerta (Santiago, Chile) con quien compartimos la misma pasión y curiosidad por la cultura de las primeras mujeres y hombres que vivieron en armonía con la naturaleza sublime del último confín de la Tierra del Fuego. Gracias por compartir tus increíbles pinturas.

Le Labo ISTerre, entre Chambéry et Grenoble, m'a offert une ambiance relax, studieuse et souvent pleine d'humour pour réaliser cette thèse. Je voudrais remercier sincèrement Fabien Massot non seulement pour avoir assuré comme un chef du côté administratif durant toute ma thèse, mais aussi pour sa bonne humeur permanente ! Egalement, je tiens à remercier Olivier Romeyer et Jean-Noël Bouvier qui ont toujours été rapides pour dénouer les problèmes informatiques ! Je remercie grandement Julien Carcaillet pour son encadrement précieux, indispensable et joyeux pour les datations Béryllium, malgré ma maladresse matinale. Un grand merci à Pascal Lacroix et Pascal Allemand pour leur savoir-faire tristérophotogrammétrique !

Pour m'avoir aiguillée lors des comités de suivi de thèse, je tiens à remercier Laurent Husson, Sébastien Carretier et Jean Chéry. Je remercie également Jean pour avoir partagé son expérience d'Adeli.

For kindly accepting to review my work I thank the examination committee: Stéphane Mazzoti, Edwin Nissen, Sébastien Castellort, Magali Rizza, Daniel Melnick et Jean-Louis Mugnier.

Merci également à Tarik Belhamiti, pour son aide précieuse et ses conseils de dernières minutes pour la mise en page de ce manuscrit. Merci également à Alexandra Asanovna Elbakyan pour rendre la science plus libre.

Hors cadre des travaux de thèse, je suis reconnaissante pour les nombreuses discussions et petites actions écologistes et féministes menées au sein du labo avec l'atelier Eco-responsabilité et le groupe Parité. Vraiment génial de pouvoir faire bouger un peu les lignes avec vous ! Je remercie donc toutes et tous mes collègues engagé.es de près ou de loin, qui montrent l'exemple à suivre : Géraldine Sarret | Phillip Lesage | Catherine Annen | Anne Replumaz | Sophie Giffard-Roisin | Alejandro Fernandez-Martinez | Julie Gattelet | Fabienne Giraud | Helle Pedersen | Eric Lewin | Anne Socquet | Laurent Husson.

Je n'oublie pas de remercier également, Mathieu Schuster, Patrick Wassmer, Carine Heitz qui ont cru en moi dans mes années d'études à l'EOST à Strasbourg mais également à l'Université de Canterbury en Nouvelle-Zélande. I kindly thank Heather Purdie, who always encouraged me to continue my career in sciences and supported my applications for a Ph.D. position.

On en vient à terminer une thèse aussi parce qu'on a été soutenu à des moments particuliers par ses co-bureau, ses collocs', ses amis, ses copains de promo. Alors je tiens à remercier chaleureusement :

Timothé Tartrat | Delphine Smittarello | Antoine Coperey | Séverine Furst | Huber A. Riviera Rosado | Cédric Lachaud | Judith Marinière | Mathilde Banjan | Thibault Roattino | Rodrigo Javier Suarez | Alice Prudhomme | Francisco Muñoz | Calypso Bardot | Julien Coutouly | Michel Tomasino | Yvain Mahe | Alexia Valdez | Landry Moreau | Fabien Blondel | Maël Riu | Clémence Loiselet | Jose Gabriel Egas Ortuño | Gabriella Schalemburger | Coralie & Morgan Scully | Lucie Pellequier | Emma Cassou | Maira Raimondi | Shna Galindas | Louis Schwartz | Tom Rose | Nils Martin | Yann Plard | Joseph Vallone | Patrick Simões Pereira | Marc Melichar | David Fries | Hugo Nguyen | Camille Pattalochi | Alexandre Schohn | Vincent Fauchoux | Jérémy Brossier | Milena Lemarquis | Marie-Eva Epin | Marine Treffot | Valentin Basch | Matthias Jauvin | Carlotta Ferrando | Fanny Verrier | Hugo Jeagler | Charlotte Raulin | Jeanne Vidal | Rodolphe Jean Lescoutre | Pierre-Antoine Bergeret | Jérôme Gagneur |

Je dois dire un immense merci à Steve Durville, pour l'inconditionnel soutien pendant les deux dernières années de ce doctorat, sa présence, ses encouragements, sa bonne humeur et sa philosophie de vie étonnamment simple et efficace. Merci aussi à sa famille, qui a toujours eu un mot attentionné et encourageant à mon égard.

Milles merci à ma sœur Jessica, qui m'a toujours accompagnée dans les décisions les plus difficiles de la thèse et de la vie, sans jugement, et toujours avec une empathie et une compassion infinies. Je suis fière que l'on se soit serré les coudes à travers les épreuves de ces derniers mois.

Et enfin un grand merci à mes parents Patrick et Marie-Christine, pour le soutien dans les coups durs, de n'avoir pas été trop préoccupés de mon engagement dans des études longues et d'avoir toujours écouté mes histoires de « tectonique-machin-chouette de faille du fin fond de la Patagonie ».

Merci à toutes et à tous !

Muchísimas Gracias !

Big Thanks !

Abstract

This thesis focuses on the present and past deformation along the active strike-slip Magallanes-Fagnano Fault (MFF), accommodating the relative motion between South-American and Scotia plates in Tierra del Fuego. At the southern edge of South America, the long-lasting left-lateral deformation and the successive massive glaciations sculpted sharp disrupted morphologies and vast straits and fjords, whose imprints are tightly intertwined. I take advantage of this unique setting to explore tectonic and climate interaction and improve our understanding of the fault activity over several time-scales: the historical period, Holocene, and Late Pleistocene. Detailed mapping and dendroseismological investigation of the 1879 and 1949 shocks demonstrate their magnitude exceed $M_w \geq 7.5$, with a minimal rupture length of 200 km, suggesting the modern largest seismicity is directly triggered by the South American – Scotia plates relative movement. I describe scarps, ridges, pop-ups, flower structures, and Riedel fractures both in Chile and Argentina, which reveal that most of the post-glacial strike-slip activity concentrated along the master fault. Based on paleoseismic trench investigations, I present a newly-developed paleo-earthquake catalog with at least seven major events of $M_w \geq \sim 7$ during the Holocene. Back-slip restorations of cumulated sinistral offset combined with ^{10}Be dating gives the first quantification of Quaternary slip-rate in Argentina. Our results yield a geomorphic slip-rate of $6.4 \pm 0.9 \text{ mm.yr}^{-1}$ since $18 \pm 2 \text{ ka}$, which is lined-up with geodetic velocity models, indicating stable behavior for the last twenty thousand years. Our results indicate irregular time of intervals between the Holocene major earthquakes in the eastern Magallanes-Fagnano Fault. Two recurrence times of ~ 1000 years and ~ 70 years suggests we may not expect a predictable interval between major earthquake in Tierra del Fuego. In Chile, at the Cordillera Darwin foothill, new glacial polish ^{10}Be datings, paleoseismic trenching, and back-slip restoration of river channels evidence an exceptionally rapid post-LGM slip-rate of $19.5 \pm 4.2 \text{ mm.yr}^{-1}$. These results suggest a pronounced E-W velocity gradient. This substantial velocity discrepancy coincides geometrically with the unequal distribution of the Pleistocene ice-sheet, voluminous and extensive in the west, and limited in the east. Thus, I propose to evaluate how the ice masses acted as a surface load producing a long-lasting viscoelastic deformation of the Earth's crust and interfered with the regional tectonic field. Using an analytical approach and then a 3D-finite element numerical modeling, I show how material rheologies, load history, and icecap orientation control the fault response. Both approaches model a decrease fault velocity at loading and a post-glacial seismic burst. However, the predicted post-glacial slip-rate increment remains insufficient, and explain no more than $\sim 4\text{-}15 \%$ of the velocity discrepancy along the Magallanes-Fagnano Fault. It notably stresses the importance to better constrain the glacial isostasy adjustment contribution from the neotectonic uplift process along the southernmost Fuegian Andes.

Résumé

Cette thèse est dédiée à l'étude de la faille active décrochante Magellan-Fagnano (MFF), accommodant le déplacement relatif des plaques Sud-Américaine et Scotia. L'extrême sud du continent américain a été sculpté par les activités conjointes du décrochement sénestre et des grandes glaciations patagoniennes, incisant de proéminents escarpements de faille et façonnant d'immenses détroits et fjords, lesquelles sont étroitement entrecroisés. Dans ces travaux, nous appuyons sur la configuration exceptionnelle de la Terre de Feu, pour étudier l'interaction entre tectonique et climat, ainsi que pour quantifier le comportement de la faille MFF sur plusieurs échelles de temps : sur la période historique d'une part (au cours des deux derniers siècles), et depuis la fin de la dernière glaciation d'autre part (depuis 20 000 ans). Au Chili et en Argentine, l'étude de tranchées paléosismologiques, la cartographie des escarpements, et l'analyse dendroseismologique ont permis pour la première fois de cartographier les surfaces de rupture des séismes de 1879 et 1949 et de mesurer les déplacements cosismique associés. Nos données suggèrent des longueurs de rupture minimales ≥ 200 km et une magnitude en 1879 de $M_w \geq 7.5$ pour chacun de séismes. Les déformations postglaciaires (rides allongées, dépressions fermées, pop-ups, structures en fleur, failles en échelon) témoignent d'une activité Quaternaire particulièrement localisée sur la section principale du système de failles. L'interprétation paléosismologique de tranchée réalisée dans le secteur argentin permet, en particulier grâce à la datation ^{14}C de niveaux stratigraphiques, d'établir un premier catalogue de séismes majeurs anciens, incluant un minimum de sept événements survenus au cours de l'Holocène. En outre, la datation par cosmonucléide ^{10}Be d'un marqueur postglaciaire fossile décalé par la faille et sa retrodéformation, indiquent un taux de glissement moyen en Argentine à 6.4 ± 0.9 mm/a depuis 18 ± 2 ka BP. Ces vitesses correspondent aux vitesses actuelles déduites des mesures GPS, et indiquent un comportement stable du secteur argentin depuis les derniers vingt-mille ans. Par ailleurs, les écarts temporels variables entre les séismes majeurs depuis l'Holocène, révèlent deux périodes de récurrences moyennes de 1000 et 70 ans, montrant ainsi que la faille de Magellan-Fagnano a un comportement irrégulier dans le temps. Au Chili, sur le versant nord de la Cordillère Darwin, nous mesurons le décalage horizontal cumulé d'un réseau hydrographique dont la mise en place date de la dernière déglaciation. Ce décalage met en évidence un taux de glissement exceptionnellement rapide de 19.5 ± 4.2 mm/an. Ces résultats indiquent une forte différence de vitesse entre le secteur Ouest de la Terre de Feu, autrefois recouvert par une calotte glaciaire épaisse, et le secteur oriental où la couverture glaciaire a été limitée, voire absente. C'est pourquoi nous explorons comment ces variations de chargement glaciaire interfèrent avec les contraintes tectoniques régionales et peuvent affecter le glissement sur la faille. Nous adoptons une première approche analytique simplifiée, puis une modélisation 3D par éléments finis, afin d'étudier comment la rhéologie de la lithosphère, l'évolution de la charge glaciaire, et son orientation par rapport à celle de la faille, influencent l'activité de la faille. Dans la configuration de la faille de Magellan-Fagnano, les deux approches montrent un ralentissement de l'activité de la faille lors d'une glaciation, suivie d'une augmentation lors de la déglaciation. Néanmoins, l'augmentation du taux de glissement lors du déchargement glaciaire reste faible, et ne peut expliquer seulement 4 à 15% du gradient de vitesse observé. Cela souligne notamment

l'importance de mieux contraindre la contribution relative de l'ajustement glaciaire isostatique de celle d'un processus néotectonique de soulèvement le long de la Cordillère des Andes Fuégiennes.

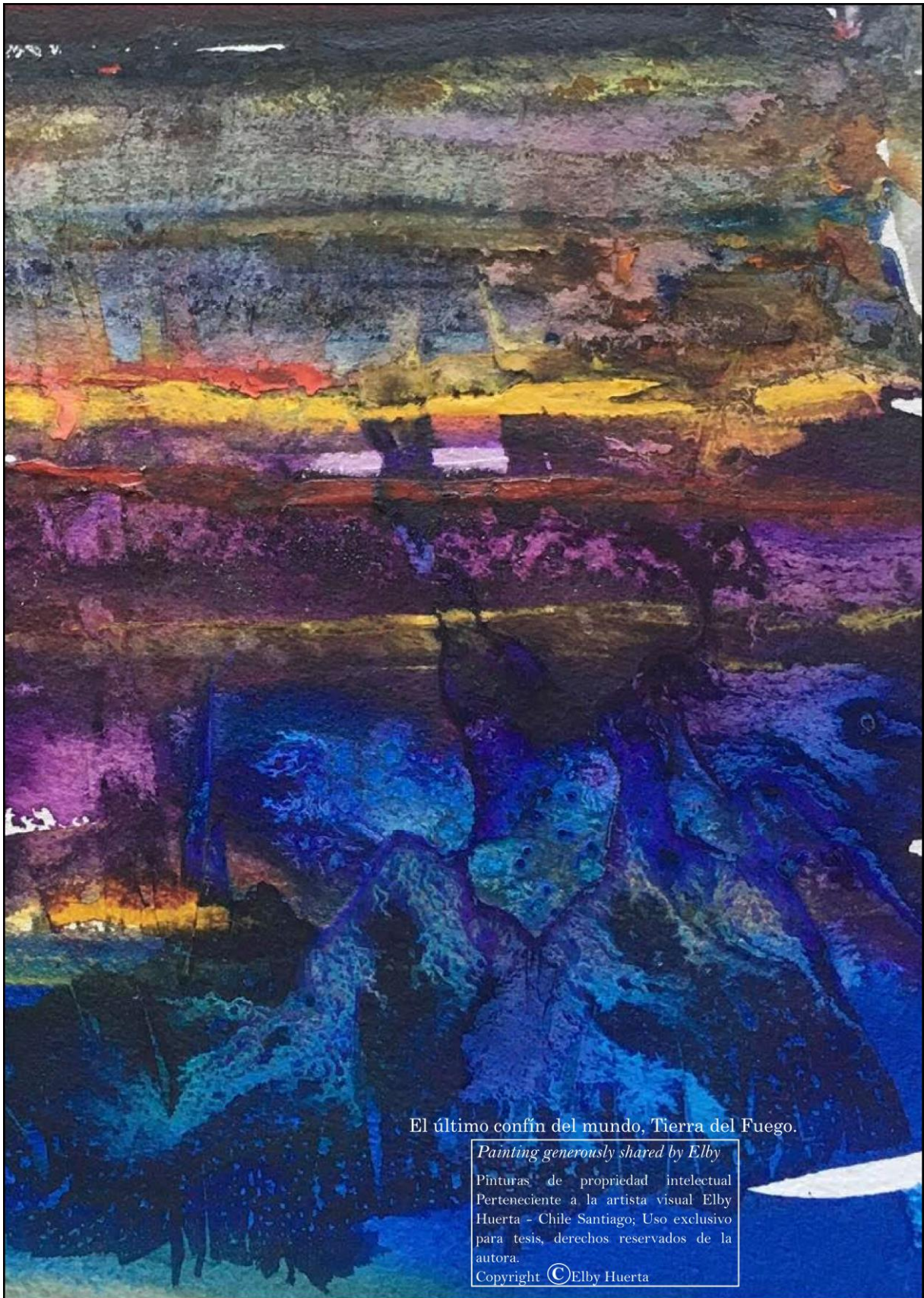
LIST OF ABBREVIATIONS

AD: Anno Domini	GPG: Great Patagonian Glaciations
Be: Beryllium	ILGM: local Last Glacial Maximum
cal. ka BP: calibrated thousands of years before present	LGM: Last Glacial Maximum
DEM: Digital Elevation Model	Ma: 10 ⁶ years, million years
DSM: Digital Surface Model	m asl: meters above sea level
FSM: fault stability margin	m bsl: meters below sea level
FTB: Fold and Thrust Belt	MFF : Magallanes-Fagnano Fault
GIA: glacial isostatic adjustment	MIS : Marine Isotope Stage
GIE: glacially induced earthquake which include syn-post and late glacial earthquake	MM : Mercalli intensity scale
GIF: glacially induced fault which include syn-post and late glacial fault grow.	Mw : moment magnitude
gLGM: global Last Glacial Maximum	PIS : Patagonian Ice Sheet
ka: thousands of years	PGF : post-glacial fault
GPS: Global Positioning System	TDF : Isla Grande de Tierra Del Fuego
	SPI: Southern Patagonian Ice Sheet
	SfM: Structure from Motion

Contents

REMERCIEMENTS, ACKNOWLEDGMENTS.....	1
ABSTRACT	5
RESUME.....	7
LIST OF ABBREVIATIONS	9
CONTENTS	1
CHAPTER I: GENERAL INTRODUCTION.....	4
I.1 OBJECTIVES AND SCIENTIFIC QUESTIONING	4
I.2 TECTONIC SETTING OF THE SOUTHERNMOST ANDES.....	11
I.3 GLACIERS AND GLACIATIONS IN THE FUEGIAN ANDES	25
I.4 TWELVE THOUSAND YEARS OF FIRE IN THE FUEGIAN ANDES	33
CHAPTER II: CO-SEISMIC DEFORMATION AND POST-GLACIAL SLIP RATE ALONG THE MAGALLANES- FAGNANO FAULT, TIERRA DEL FUEGO, ARGENTINA	43
II.1 INTRODUCTION	45
II.2 EASTERN MAGALLANES-FAGNANO FAULT GEOMETRY.....	49
II.3 THE 1949 CO-SEISMIC RUPTURE.....	50
II.4 POST-GLACIAL SLIP RATE	53
II.5 DISCUSSION AND CONCLUSIONS.....	56
CHAPTER III: NEW INSIGHTS INTO PALEOSEISMIC RECORDS OF THE MAGALLANES FAGNANO STRIKE-SLIP FAULT, ARGENTINA	61
III.1 INTRODUCTION	63
III.2 HISTORICAL LARGE EARTHQUAKES	65
III.3 STUDY SITE.....	66
III.4 PALEOSEISMIC INVESTIGATIONS	71
III.5 DISCUSSION	80
CHAPTER IV: PALEOSEISMOLOGY AND DENDROSEISMOLOGY APPLIED ON THE ACTIVE WESTERN MAGALLANES-FAGNANO FAULT, CHILE.....	89
IV.1 INTRODUCTION	91
IV.2 WESTERN MAGALLANES-FAGNANO FAULT GEOMETRY	95
IV.3 FAULT RUPTURE OVER THE PAST TWO CENTURIES	110
IV.4 QUATERNARY ACTIVITY ALONG PENINSULA AINSWORTH	119
IV.5 DISCUSSION AND CONCLUSION.....	132

CHAPTER V: NUMERICAL MODELING OF STRIKE-SLIP FAULT DURING ICECAP GROWTH AND MELTING	137
V.1 STATE-OF-THE-ART	138
V.2 ANALYTICAL EVALUATION OF THE GLACIAL LOADING EFFECT ON STRIKE-SLIP FAULT	161
V.3 SETUP OF THE 3D-FINITE ELEMENT MODEL	175
V.4 MODEL RESULTS	193
V.5 DISCUSSIONS AND CONCLUSION	215
CHAPTER VI: CONCLUSIONS AND PERSPECTIVES	219
REFERENCES	225
ANNEXE A - CHAPTER II	261
ANNEXE B - CHAPTER II - COORDINATES AND PHOTOGRAPHS OF THE TWO TRENCHES ; PHOTOGRAPHS OF TRENCHES SAMPLES	272
ANNEXE C - CHAPTER III - MORPHOTECTONICS: LA BLANCA SEGMENT	276
ANNEXE D – CHAPTER III - 3D ANALYSIS OF RIEDEL IN TRENCH SITE LA BLANCA	280
ANNEXE E - CHAPTER III - MULTIPLE DEVIATED RIVERS IN THE SIERRA IRIGOYEN	282
ANNEXE F – CHAPTER IV, TRENCH CHILE EASTERN WALL	284
ANNEXE G – CHAPTER IV, BE10 SAMPLE SITES CORDILLERA PACIENCIA AND PUERTO TOTO.	285
ANNEXE H – CHAPTER IV – MODERN LANDSLIDES IN ALMIRANTAZGO SOUND	289
ANNEXE I – CHAPTER III – TRENCH WALLS LA BLANCA	1



El último confín del mundo, Tierra del Fuego.

Painting generously shared by Elby

Pinturas de propiedad intelectual
Pertenece a la artista visual Elby
Huerta - Chile Santiago; Uso exclusivo
para tesis, derechos reservados de la
autora.

Copyright © Elby Huerta

← *The Chilean artist **Elby Huerta** does us the honor of sketching small touches of art within this doctoral thesis. Elby explores sensitively the overwhelming landscapes of Tierra del Fuego and the myths carried by its native peoples. Her works are on watercolors jointly with azurite mineral pigment.*

L'artiste Chilienne Elby Huerta, nous fait l'honneur d'esquisser de petites touches d'art au sein de cette thèse. Ses travaux à l'aquarelle et au pigment minéral d'azurite, représentent de manière sensible les paysages bouleversant de la Terre de Feu et les mythes portés par ses peuples natifs

CHAPTER I: General Introduction

I.1 Objectives and scientific questioning

I.1.1 Objectives and General problematic

Earth's landscape can be thought to be the result of the natural competition among the tectonic endogenic Earth's processes and exogenic climatic processes. At the southern edge of South America, the struggle is fierce between a highly active plate boundary against the extreme climatic conditions. The connection between the South American and the Scotia plates defines the narrow Magallanes-Fagnano Fault system, accommodating their relative left-lateral sliding. This strike-slip fault is capable of producing major earthquakes, as illustrated by the last seismic events that occurred the 17 December 1949 with two successive shocks of Mw7.75. In addition to tremendous seismicity, this austral region underwent colossal glaciations since the Americas detached from the Antarctic Peninsula. In the Magallanes region and in Tierra del Fuego, these processes sculpted sharp faulting morphologies and vast glacial straits and fjords. The strike-slip deformation and the glacial erosion left tightly intertwined imprints as anywhere else in the world. Thereby, the Austral Patagonia offers an extraordinary territory to explore tectonic and climate interactions. In this thesis, the leading objective is to improve our understanding of the Quaternary faulting and its interactions with climate-driven changes.

The general objectives of the thesis are the following:

- To characterise the Magallanes-Fagnano Fault's activity in the last centuries;
- To identify ancient ruptures in paleoseismological trenches and establish a paleoseismic calendar as large as possible;
- To quantify deformation velocities over several seismic cycles by measuring and dating interpreted glacial and post-glacial Quaternary landforms shifted by the fault;
- To assess the roles of the Eastern and the Western sections in greatest Holocene earthquake genesis;
- To model the effect of climate-driven ice-mass changes above strike-slip fault, and evaluate the extent to which Patagonian's glaciers and glaciations might have affected the fault behavior.

I.1.2 Thesis development

The thesis is presented in six chapters. Chapter I describes the regional geological setting, presents a state-of-the-art of the Patagonian glaciations, and introduces our research based on the glacial and tectonic interactions. To close this introductory chapter, we offer a short digression about the Fuegian Natives, for those interested by the southernmost humanity history.

Chapter II and Chapter III are dedicated to the results obtained in the Argentinian part of Magallanes-Fagnano Fault. Despite the remarkably prominent scarps from the two 1949 earthquakes of magnitude 7.8 and 7.5, the quantification of this rupture remained limited and poorly documented. Besides, the Quaternary cover was strikingly disrupted along a unique spectacular E-W scarp. We take advantages of this particular setting to answer the following questions:

- What is the rupture length associated with the 1949's event? (Chapter II)
- Are there consistent patterns of co-seismic offset along fault, and how to define the eastern end of the 1949's ruptures? (Chapter II)

- Do the Quaternary drainage incisions have recorded the deformation, and could we use them as reliable tectonic markers? (Chapter II)
- Is the geomorphic slip rate of the eastern MFF in agreement with the present-day geodetic motion between South America and Scotia plates? (Chapter II)
- What is the characteristic recurrence interval of major earthquakes ($M > 7$)? (Chapter II and III).
- What is the paleoearthquake chronology, and does it agree with the recurrence interval? (Chapter III)

Chapter IV is devoted to our results in Chile, where the fault follows the same sea-passages that the last-glaciations have carved. Little is known about the kinematics of the western part of the MFF strike-slip system, and only seldom inshore sites expose the Magallanes Faults. After a complete review of the Chilean fault geometry, we present new insights into the problematic:

- Did the Chilean sections rupture in 1949?
- What is the paleo-earthquake chronology?
- In this formerly glaciated region, how the strike-slip morphologies and glaciation's landforms are intertwined, and which information can we extract from this interaction?
- What is the Western Holocene slip-rate? Is the long-term deformation temporally and spatially variable along the Magallanes-Fagnano Fault?

The penultimate chapter V proposes to investigate the impact of the glaciations on the temporal and spatial variation of the slip rates along the fault. We first establish the scientific context surrounding the actual questioning about glacial (un)loading and faults interactions. We present a worldwide overview of past and present open-questions about Fennoscandia and Laurentide fault-(re)activation potential. Conversely to the well-documented effects on normal and reverse faults, there is no investigation on strike-slip configuration. Through this chapter, we tackle the problem, first with basic analytical approach, and then with a more sophisticated finite element numerical modeling of strike-slip fault's response to glacial loading. We propose preliminary findings to these questions:

- How strike-slip and ice stress fields interact?
- What are the primary parameters governing the fault's response?
- Is the icecap effect significant enough to explain part of the observed Holocene slip-rate discrepancy between the Western MFF and the Eastern section?

Chapter VI concludes the thesis with a discussion of the role played by both climatic change and by tectonic factors on the strike-slip fault system of Magallanes-Fagnano. The main conclusions are presented and directions for further research suggested.

At the time of thesis completion, one paper is published (Chapter II – Terra Nova), and two are in preparation (Chapter III, and IV).

I.1.3 Methods

To study the MFF's behavior at variable timescales, from the Late-Pleistocene Quaternary (11 700 – 50 000) to the modern activity (10 - 200 yrs), we combine the following approaches: tectonic geomorphology, paleoseismology, dendroseismology, and numerical modeling.

Tectonic geomorphology investigates the past and modern landsystem evolutions by characterizing the interaction between tectonic (faulting, crust uplift, subsidence or folding) and Earth's surface processes (glacial erosion, denudation, incision, transportation, deposition). Since the pioneer's works applied on active faulting (Solonenko, 1973; Wallace, 1977; Matsuda *et al.*, 1978; Philip and Meghraoui, 1983), the morphometry and the dating methods have radically improved, refining the spatial and temporal resolution of the results.

I.1.3.1 Morphometry: tristereogrammetry and ultrafine-mapping

I detect and measure the MFF's fault trace using Pleiades optical images to generate High Resolution digital surface models (DSM). The Pleiades images are suitable for tristereogrammetry and geometric evaluation of terrestrial morphologies (Berthier *et al.*, 2014; Stumpf *et al.*, 2014; Poli *et al.*, 2015; Lacroix *et al.*, 2020). The images acquired in December 2017 and March 2018 cover the Magallanes Fagnano Fault from the Atlantic coast to the Almirantazgo Sound with a 20-km imaging-swath. I process the photos with the NASA's open-source

Automated Stereogrammetry Software Ames Stereo Pipeline (ASP 2.6.0) and the MicMac photogrammetric suite developed by the IGN (French National Geographic Institute) and ENSG (French national school for geographic sciences). I auto-correlate triplets and build DSM with a horizontal and vertical resolution of 5 and 10 meters/pixel, respectively (Appendix AMS quick start) (Shean *et al.*, 2016). Locally, and where the region was uncovered by trees, which is seldom the case in Tierra del Fuego, we collect overlapping aerial photographs from unmanned aerial vehicle. I build the digital elevation models (DEM) using topographic point correlation (Structure from Motion) with Agisoft PhotoScan software. Combining Pleiades-DSM, local SfM-DEM, Bing Satellite maps, historical aerial photographs (1/10 000 – 1 / 50 000), and extensive field surveys (1/1 – 1 / 100), I identify and measure subtle rupturing surfaces, terraces, colluvial and alluvial fans, subglacial morphologies, and past and existing hydrological networks.

I.1.3.2 Paleoseismology and cosmogenic dating

Based on this ultra-fine mapping, we target suitable sites for paleoseismological work. Ideal configuration requires: exposing rupture-record associated with several seismic cycles and unambiguous and datable offset onset timing (Sieh, 1981; Wallace, 1981; McCalpin, 1996). Only then, it allows quantifying the active tectonic of a fault across a longer timescale than is possible from the short instrumental record.

We carry out two complementary investigations: long-term offset measurements and trenching. We focus on post-glacial fluvial incisions that developed normal to fault strike and recorded the horizontally offset by repeated surface-rupturing earthquakes. The cosmogenic ^{10}Be dating method allows determining the exposure age of the fossil surface youngest sediments on a timescale from 0 to 100 ka (Lal, 1988; Nishiizumi *et al.*, 1989). The in situ ^{10}Be analysis is performed along depth profiles or at surface on quartz samples, which are reasonably present in Tierra del Fuego alluvial terraces and glacial polishes. The ^{10}Be concentration represents the exposure time to cosmic rays depending on latitude, altitude and depth (Lal, 1991; Gosse and Phillips, 2001). I prepared most of the samples at ISTERRE GeoThermoChronology platform, supervised by J. Carcaillet. The preparation steps include the quartz extraction, quartz decontamination, atmospheric ^{10}Be removal, spiking ^9Be , sample dissolution (hydrofluoric acid), blank preparation, evaporations/dry-downs (perchloric & hydrochloric acids), exchange columns

with dowex resins (anion exchanges for separation of Be from Iron & Manganese; cations exchanges for separation of Be from Boron), precipitations/washes, pH8 rinses and transfer samples to quartz crucibles. Measurements of $\frac{9\text{Be}}{10\text{Be}}$ were completed at the accelerator mass spectrometry facility ASTER (Aix-en-Provence, France).

In fluvial setting, this method estimates the age of the marker abandonment, and determines the onset of the subsequent tectonic deformation (Bierman *et al.*, 1995; Ritz *et al.*, 1995). Knowing the amount of offset, it provides the rates of slip averaged over the Quaternary (Scholz, 2002). Time and spatial fault behavior variations are identified when comparing the Quaternary rate to additional regional and time-scale velocities (Geodetic velocity, Late-Holocene slip-rate). Since the first studies applied this principle to active deformation, this technique has become a fundamental tool to characterize the long-term motion of hundreds of worldwide active faults (Vassallo *et al.*, 2005; Ritz *et al.*, 2006; Nissen *et al.*, 2009; Chevalier *et al.*, 2016).

The cross-fault excavation completes this approach and refines the rupture history (Swan *et al.*, 1980; Schwartz and Coppersmith, 1984). We favor sites that are likely to present a continuous sedimentary archive. We maximize the chance to find the complete record of the last seismic events by selecting sites on the principal scarp in which most of the past deformation is localised. Using radiocarbon dating on peat and charcoals (Libby, 1955; Stuiver, 1970), stratigraphy and structural markers interpretations (McCalpin, 2009), and trench retrodeformation analysis, this method can document the successive deformations back to several ten of thousand years.

I.1.3.3 Modern earthquake markers, instrumental records and dendroseismology

To improve knowledge of the 1949 (M7.8) ruptures in Tierra Del Fuego, we combine extensive mapping of the coseismic markers and tree-ring analyses. Giant earthquakes (M>7.5) can devastate a region and cause widespread damages that, even decades after the shock, remain visible in the landscape and the tree stems (Figure 1.1).

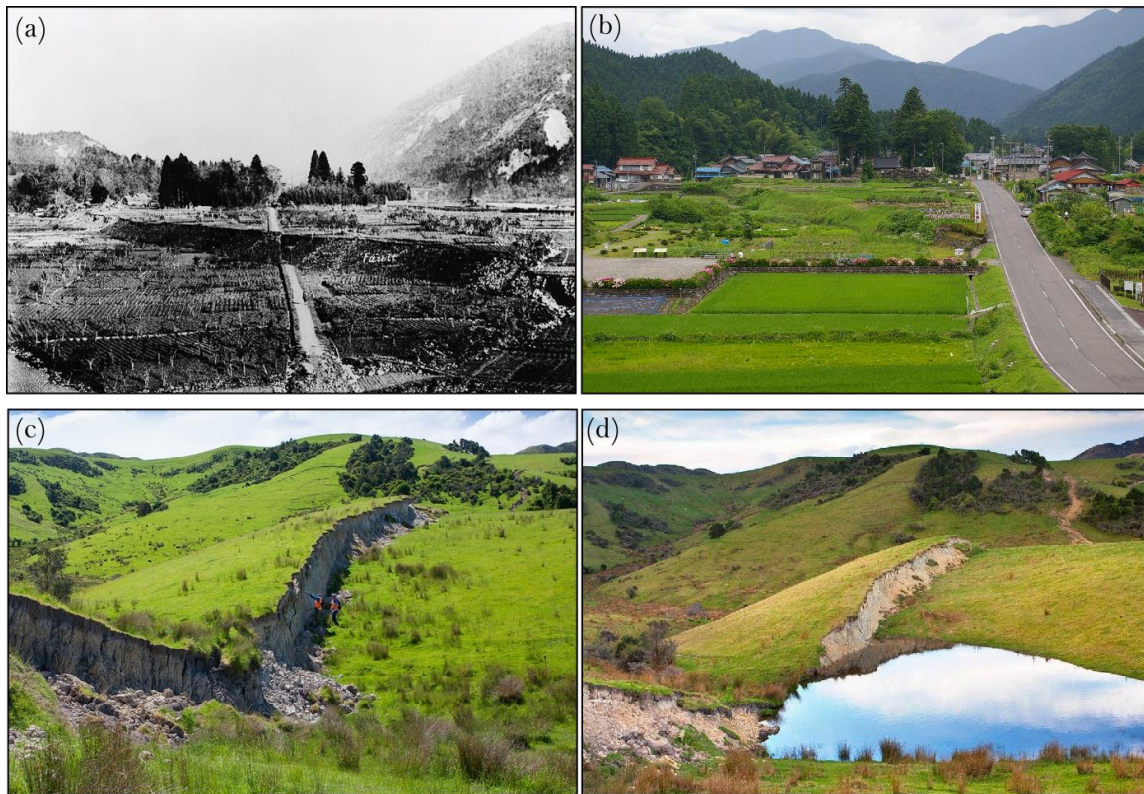


Figure 1.1: (a) Neodani Fault in 1891, Japan. The Mino–Owari earthquake struck in 1891, M 8.0. Photo from (Koto, 1893), with left-lateral offset up to 8 m, and vertical slip in the range of 2–5 m. (b) Neodani Fault in 2007. Notice the vegetation that colonized and protected the scarp from rainfall erosion during a century. (c) The “Woodchester wall” scarps from the Waiiau fault (Leader Fault) in 2016, New Zealand, after the Kaikōura earthquake of M7.8. (d) Waiiau fault in 2017 (photos Kate Pedley, Canterbury University). Note the rapid colluvial wedge and pond formations along the scarp in less than 1 year since the rupture.

The dendrochronology relies in the analysis of the radial tree growth (narrow or wide annual rings), the cell anomalies (reaction wood, modification of cell structure), and the tree-ring morphology (scarps, tilting) (Astrade *et al.*, 2012). The application of these principles to injured or tilted trees, following coseismic topographic disturbance, is widely used since the '80-'90s, and defined the dendroseismology (Jacoby and Ulan, 1983; Jacoby *et al.*, 1988; Yamaguchi and Hoblitt, 1995; Yamaguchi *et al.*, 1997; McCalpin, 2009). Here, we combine instrumental record with the tree-ring analysis to extend the modern earthquake chronology back to 1850.

I.1.3.4 Numerical modeling

To study the strike-slip fault's response to ice-mass changes, we use the 3D finite element software ADELI. We choose this approach as it enables various Earth's material configurations (crust, lithospheric mantle, asthenosphere) in which we can set a strike-slip fault geometry, and model its behavior under different glaciation scenarios (load temporal evolution and spatial distribution). The ADELI code (Hassani *et al.*, 1997) considers the temporal evolution of boundary conditions (pressure, velocity) applied on the external borders of the modeled earth's material. The output consists of a single file (grid of displacements and velocities) that can be visualized at different time steps (Paraview, GMT), and in various cross-sections. We use SPYDER, the scientific Python Development Environment within the ANACONDA open-source console, to perform graphical outputs.

I.2 Tectonic setting of the Southernmost Andes

I.2.1 Geodynamic evolution

At the continental scale, the most distinctive feature of Southern Patagonia is the southernmost curvature of its mountainous spinal column: The Andes. In this region, the Austral Andes bend of about 90° from a N-S trend in the Santa Cruz Province (50°S) to an E-W orientation in Tierra del Fuego (55°S) (Figure 1.2). This section of the Cordillera is also named the Fuegian Andes, relating to the indigenous people "Tierra del Los Fueguinos". In this section, we

present a simplified literature synthesis, reviewing the main debates about the Patagonian bend and the onset of the Magallanes-Fagnano Fault.

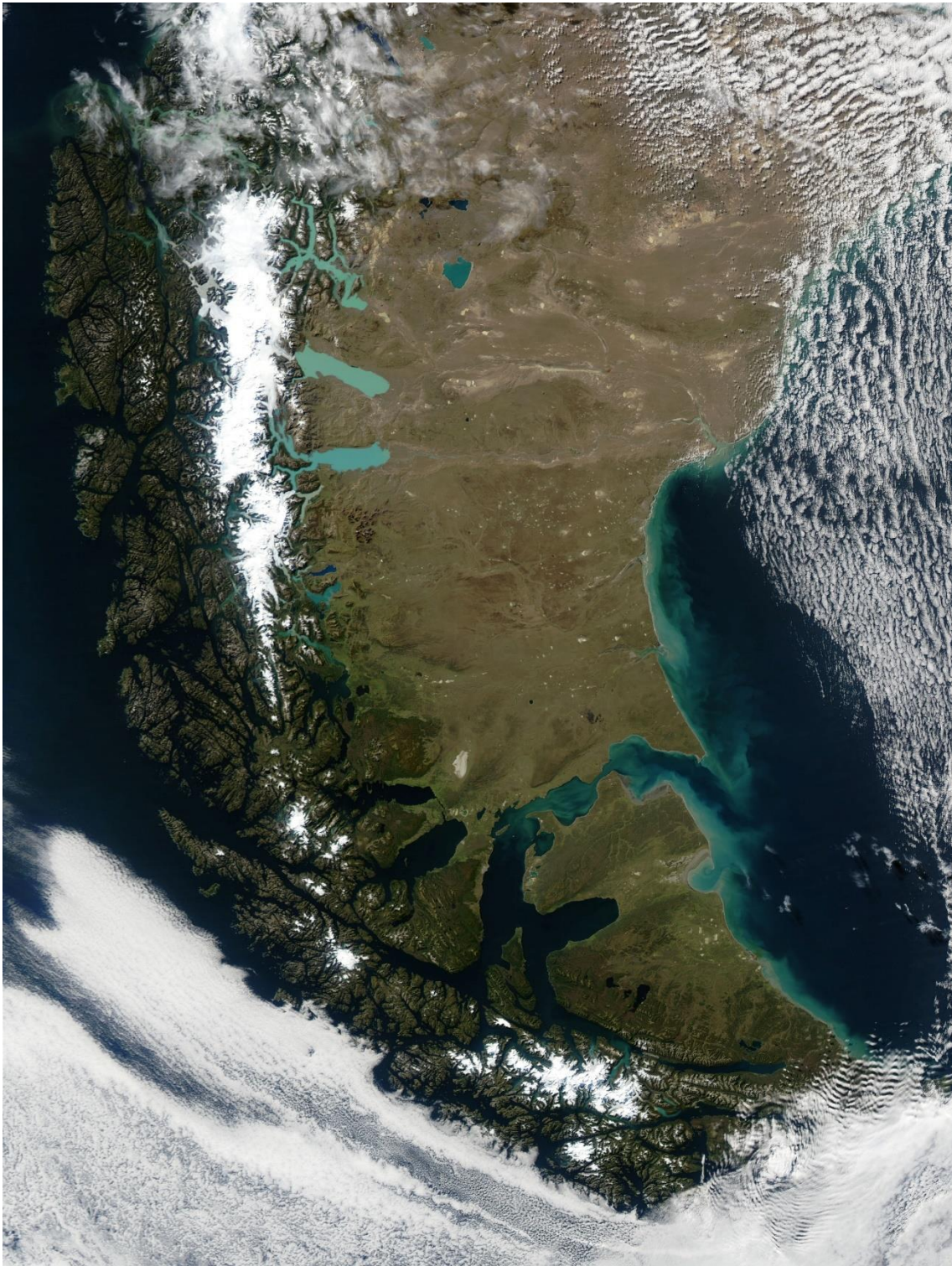


Figure 1.2: Southernmost America on March 28, 2003 (image from the Terra-MODIS Moderate Resolution Imaging Spectroradiometer, NASA, GSFC, Image courtesy Jeffrey Schmaltz).

In "The Origin of Continents and Oceans," 1929, Alfred Wegner proposed this arc-shape was linked to South America's relative western motion. A century later, its origin remains contested between an oroclinal bend (orogenesis, i.e., rotation during the mountain creation) (Carey, 1958) or an inherited feature (Ghiglione and Cristallini, 2007).

The debate involves data from a margin basin, the Rocas Verdes (Figure 1.3). The Rocas Verdes (Verdes for the green color of its ophiolites complex) is a back-arc basin that opened (Figure 1.4a,b) and filled up in the Middle to Late Jurassic time (Pankhurst, 2000). It constitutes the main geological feature of the region (Figure 1.3). It was associated to the oceanic subduction under the west American active margin. Authors show the basin opening was coeval to regional crustal extension which occurred before the Gondwana breakup (Dalziel and Cortés, 1972; Suárez, 1979; Dalziel, 1981). Besides, the Basin appeared to result also from the slimming of the continental plate before the south Atlantic Ocean irreversibly divided the America from the Africa. In Tierra del Fuego, Dalziel (1981) concluded that the basin was at least 100 km-wide. In our study area, the Late Jurassic syn-rift rocks outcrop in the Sierra Dientes del Dragón and correspond to marine mudstones and volcanoclastic rocks (Rojas and Mpodozis, 2006).

The paleomagnetic data from the Rocas Verdes basin are interpreted in two ways. Some authors analyze the Patagonia Bend related to the basin closure and subsequent uplift (Dalziel et al., 1973; Burns et al., 1980; Cunningham et al., 1991). In contrast, researchers suggest with analog sandbox models and tectonic analysis, that the structural pattern could be anterior to the orogeny. Their model meets the present-day curve with analog oceanic plate subducting beneath a pristine continental corner in L-shape (Diraison et al., 2000; Ghiglione and Cristallini, 2007).

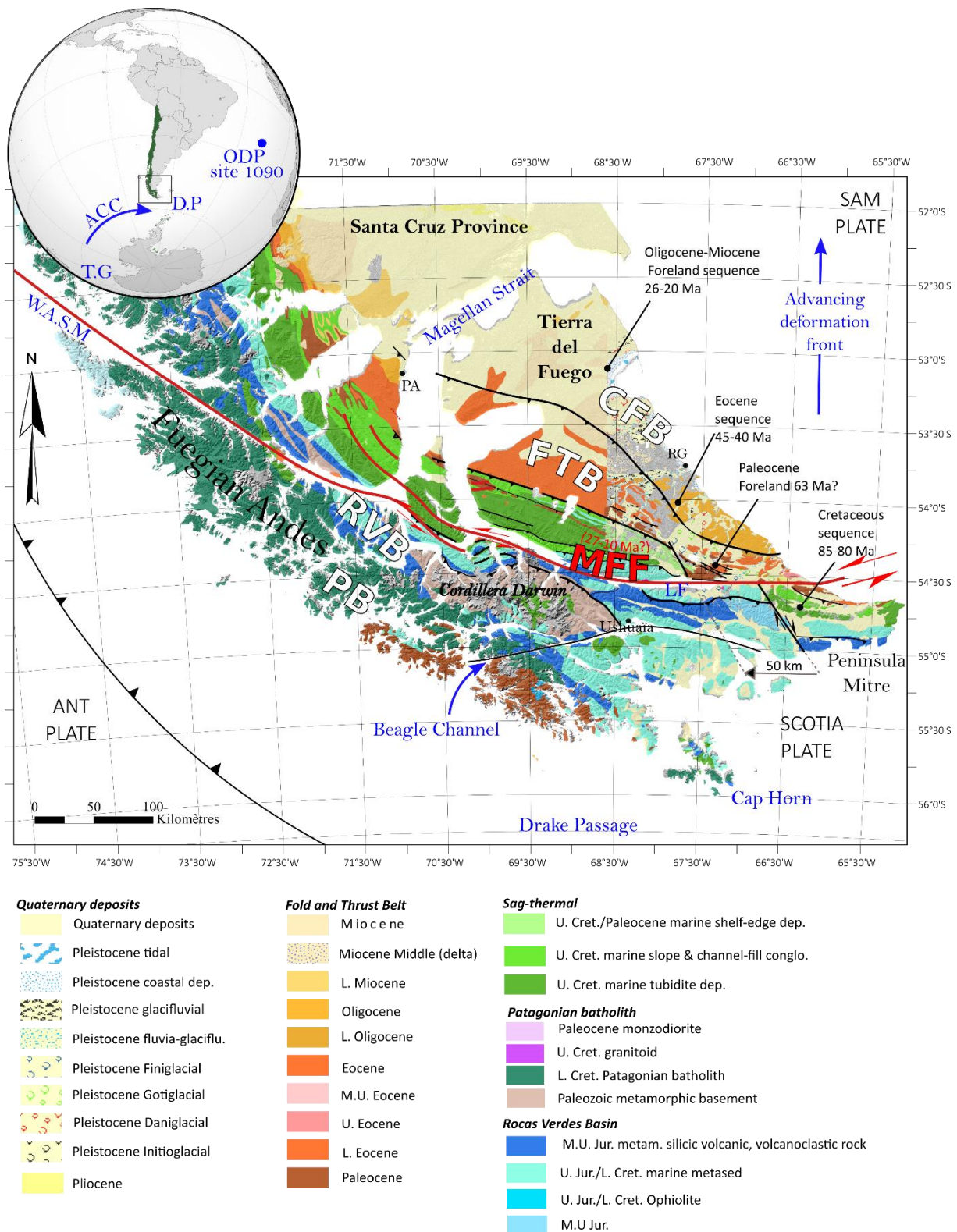


Figure 1.3: Simplified regional geologic map of Tierra del Fuego and Patagonian Andes. Geologic layers from (Hervé et al., 1984; Suárez et al., 1985; SERNAGEOMIN, 2003; Olivero and Malumián, 2008; Klepeis, 2010). Deformation phases from (Rojas and Mpodozis, 2006; Fosdick et al., 2011;

Mpodozis et al., 2011; Ghiglione, 2016). Abbreviations: ACC: Antarctic Circumpolar Current; ANT: Antarctic plate; CFB: Cenozoic Foreland Basin; D.P: Drake Passage; FTB: Fold and Thrust Belt; L: Lower (i.e., Early); LF: Lake Fagnano; MFF: Magallanes-Fagnano Fault; PB: Patagonian Batholith; RVB: Rocas Verdes Basin; SAM: South American Plate; TG: Tasmanian Gateway; U: Upper (i.e., Late); W.A.S.M: Western Arm Strait of Magellan.

In the end of Early Cretaceous (<100 Ma), the south Atlantic Ocean spreading accelerated (Figure 1.4b), increasing the subduction rate along the Pacific margin, initiating the westward motion of South America, and causing the Patagonian extension phase to wane ([Rabinowitz and LaBrecque, 1979](#); [Dalziel, 1986](#); [Ramos, 1989](#)). These two processes are thought to initiate the transition from extension to compression phase and close the Rocas Verdes ([Bruhn and Dalziel, 1977](#); [Hervé et al., 2007](#)). The Rocas Verdes Basin began to close during Late-Cretaceous and was lately associated with magmatism that build up the Patagonian Batholith ([Hervé et al., 1984](#)). Batholith rocks now exposed along the southern Cordillera Darwin, experienced metamorphism in Late Cretaceous (amphibolite facies), and constitute today the Darwin metamorphic complex ([Hervé et al., 1984](#)). New paleomagnetic data ([Poblete et al., 2016](#); [Poblete et al., 2014](#)) show a counterclockwise rotation of the Southern Patagonia during the obduction of the Rocas Verdes basin. However, it would have trigger no more than ~30-50° of the curve shape ([Poblete et al., 2016](#)). Therefore, part of the arch-shape was acquired before, and the authors concluded that it is mainly an inherited shape ([Poblete et al., 2014](#)).

Shortening is proposed to have continued in the Paleocene, coeval to the exhumation of the Darwin Cordillera (crystalline massif), and the NE advance of the compressional front into the foreland basin ([Alvarez-Marron et al., 1993](#); [Klepeis, 1993](#)). This compression was associated with a flexural loading, folding, and thrusting belt (FTB) which migrated northward ([Fildani and Hessler, 2005](#); [Fosdick et al., 2011](#)) and resulted in the formation of the early Cenozoic foreland basin (CFB) ([Alvarez-Marron et al., 1993](#); [Mpodozis et al., 2011](#)) (Figure 1.3). The overall NE-SW shortening is > 100 km and continued in Tierra del Fuego with successive thrust episodes until the Oligo-Miocene ([Alvarez-Marron et al., 1993](#); [Torres-Carbonell et al., 2008](#); [Rojas and Mpodozis, 2006](#); [Torres Carbonell et al., 2014](#); [Ghiglione et al., 2014](#)).

To precise the geodynamic context, it is generally accepted this period is divided in four steps: 72-47 Ma, 47-24 Ma, 24-18 Ma and 18–0 Ma. In the first step (72-47 Ma), the Farallón plate in the north and the Aluk plate (either called Phoenix) in Tierra del Fuego, subducted along the Peru/Chile trench (South American Plate SAM). The associated junction Farallón/Aluk migrated southward (Cande and Leslie, 1986) (Figure 1.4c, d). In the second step (47-24 Ma), Farallón plunged roughly in a NNW direction beneath SAM plate and broke by ~24 Ma in the two plates Cocos and Nazca. In the third step (24-18 Ma), the Nazca plunged in an eastward direction beneath SAM Plate (Somoza and Ghidella de Hurtis, 2005) (Figure 1.4e). At 18 Ma (4th step), the triple junction of Nazca/Aluk/Antarctic started to plunged under the South American ocean ridge, creating a unique setting of quadruple junction until 16 Ma (Breitsprecher and Thorkelson, 2009), initiating the subduction of the Antarctic plate (Figure 1.4f). Finally, the contractional phase end is marked by the deposition of fluvial pebbles (Santa Cruz Formation) capping the foreland after 18 Ma (Malumián and Caramés, 1997; Malumián, 1999; Malumián et al., 2000; Blisniuk et al., 2005; Guillaume et al., 2009; Fosdick et al., 2011)

The subduction direction change of Farallón/Nazca plate from NNW to E (24 Ma) is coeval to observed strike-slip fabrics in Punta Gruesa (Península Mitre) (Ghiglione and Cristallini, 2007). This Miocene clastic dikes of Punta Gruesa, are interpreted linked to strike-slip phase between 26 to 14 Ma, and intruded the FTB sequence (Ghiglione and Ramos, 2005). Therefore the authors distinguish the strike-slip initiation separated from the thrust event, and conclude the sinistral deformation overprinted the thrust fabrics since the Oligocene $\leq \approx 30$ Ma (Klepeis, 1994; Klepeis and Austin, 1997; Lodolo et al., 2003; Ghiglione and Ramos, 2005). Recently, authors proposed a younger age of 7-11 Ma for the strike-slip inception (Torres Carbonell et al., 2014) based on a left-lateral offset of ~50 km in the foreland FTB (Torres-Carbonell et al., 2008). The authors constrained the measured offset with the present-day geodetic velocity ~4.4 to 6.6 mm/ yr (Smalley et al., 2003; Mendoza et al., 2011).

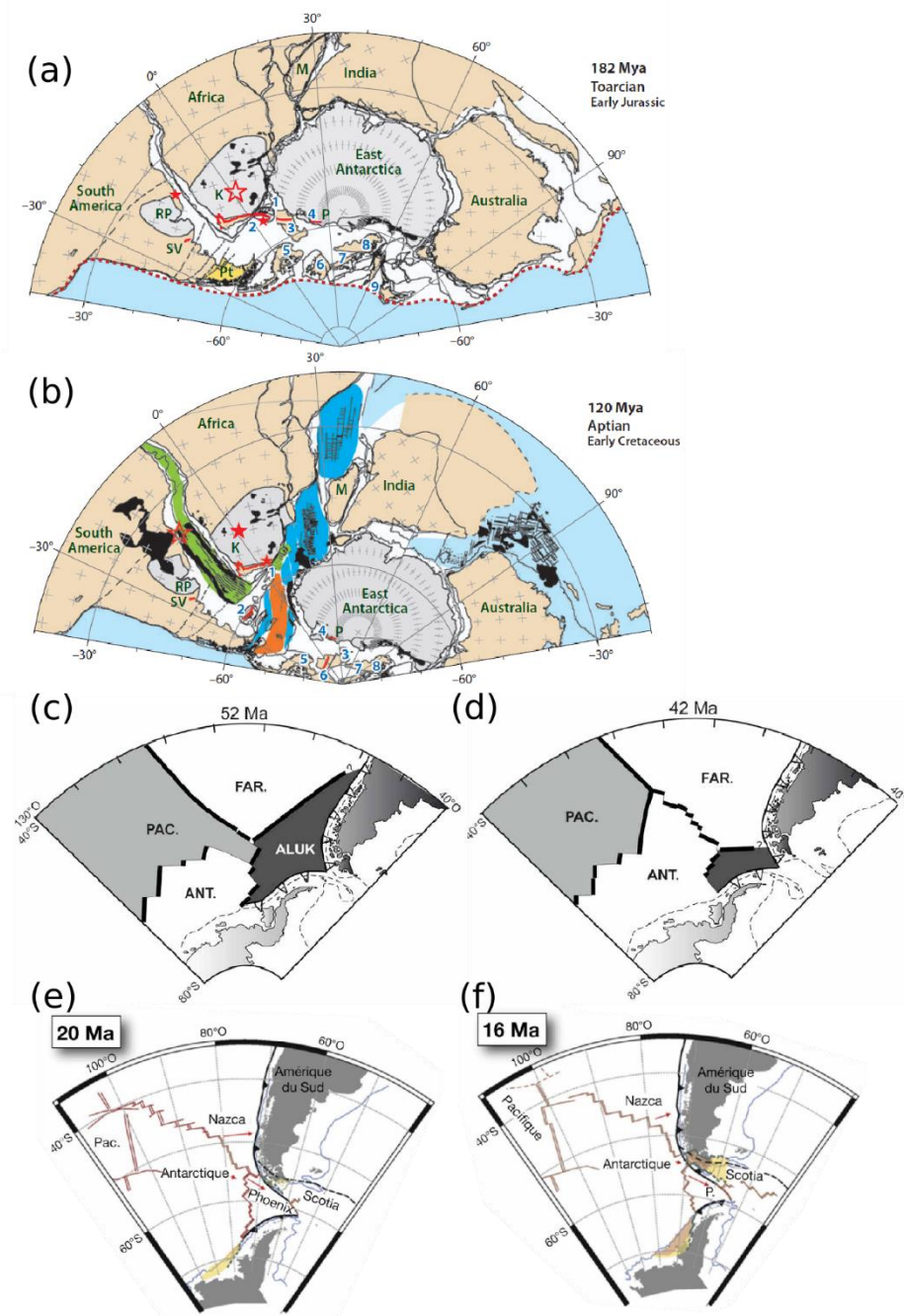


Figure 1.4: Tectonic reconstruction from (Cande and Leslie, 1986; Guillaume, 2008; Dalziel et al., 2013). (a) 182 Ma. The Gondwana supercontinent in a paleomagnetic reference frame (Van der Voo 1993). Patagonia is shown in yellow. Abbreviations: K, Kalahari craton; M, Madagascar; P, Pensacola Mountains; Pt, Patagonia; RP, Rio de la Plata craton; SV, Sierra de la Ventana. Numbering is (1) Maurice Ewing Bank, (2) Falkland/Malvinas microplate, (3) Ellsworth-Whitmore block, (4) Berkner Island, (5) Antarctic Peninsula, (6) Thurston Island–Eights block, (7) Eastern Marie Byrd Land block, (8) Western Marie Byrd Land block, and (9) Zealandia; (b) 135–120 Ma:

Two-plate separation of East and West Gondwana. The blue region south of Patagonia is the opening of the Rocas Verdes basin. The orange regions are contemporaneous opening of Weddell Sea floor and Central Scotia Sea floor. The green region is the opening of the South Atlantic Ocean. (c and d) 52 Ma to 42 Ma Southward migration of junction Aluk/Farallon. (e and f) 20 Ma to 16 Ma. The triple junction of Nazca/Aluk/Antarctic plunged under the South American ocean ridge, initiating the subduction of the Antarctic plate. Abbreviations are : ANT : Antarctica plate ; FAR : Farallon ; K : Kalahari craton ; Pt : Patagonia ; Rp : Rio de la Plata craton ; Sv : Sierra Ventana.

In term of paleoclimate, this period is fundamental as the subduction direction change is coeval to the Drake Passage opening, whose formation resulted from the continuous Scotia plate spreading since ~50 Ma. The opening of this strait separating Antarctica from Tierra del Fuego, and the opening of the Tasmanian Gateway around 35 Ma (subsidence of Tasmanian land bridge separating Antarctic from Tasmania) were synchronic with an abrupt global climate cooling (Eagles, 2004; Livermore et al., 2005; Livermore et al., 2007). These sea passages initiated the free transfer of oceanic water masses, establishing the Antarctic Circumpolar Current (ACC), and cutting Antarctica off warm currents flowing from the tropics (Lagabrielle et al., 2009). Using neodymium isotopes in fossil fish teeth from central Atlantic Ocean core (ODP site 1090, Figure 1.3 inset), authors suggested an influx of shallow Pacific seawater approximately ~41 Ma in the Atlantic (Scher and Martin, 2006).

To conclude, the exact timings of MFF strike-slip onset remain controversial. However, the MFF may have gained its predominant strike slip function around 7 Ma, by accommodating the relative motion between Scotia and South America Plate (Lodolo et al., 2003). With a very simplistic view of the southern tip of South America, the region can be divided in a four units: The Patagonian batholith (PB), the Rocas Verdes basin (RVB), the Magallanes Fold and Thrust Belt (FTB), and the Cenozoic Magallanes foreland basin (CFB).

1.2.2 Present-day configuration

The Magallanes Fagnano Fault system (MFF) is the inland transform boundary between South American (SAM) and Scotia plates (SCO). Its eastern continuation is the North-Scotia ridge (Figure 1.5). In Tierra del Fuego, the GPS network is scarce, and even more in the Chilean territory, with none GPS campaigns, and a single IGS permanent station in Punta Arenas. The remote

Southern Chilean territories is less monitored, primarily due to the limited access (by sea or off-road), and the lack of suitable station anchor (recovered by thick unconsolidated peat deposit). The current geodetic motion is therefore poorly constrained in the Chilean Tierra del Fuego while, in Argentina, a few GPS-campaigns enable to estimate the present-day geodetic relative motion between SAM and SCO at 5.9 ± 0.2 mm/yr (Smalley *et al.*, 2003; Mendoza *et al.*, 2015).

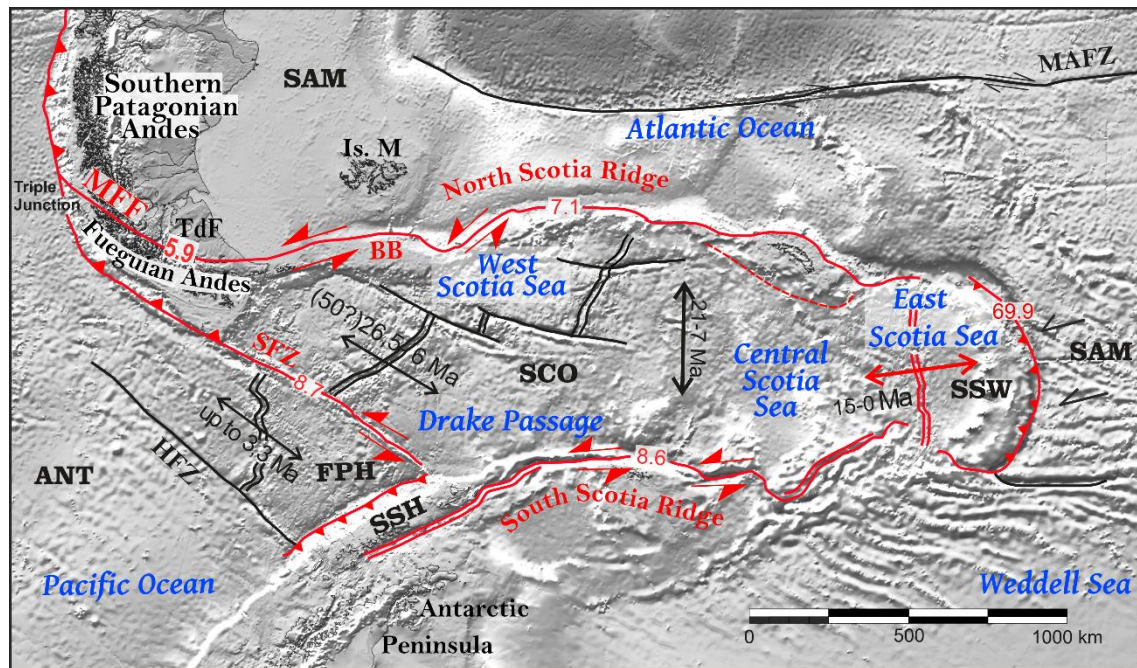


*Figure 1.5: Tectonic setting of southernmost Andes with plate boundary velocities ($\text{mm}\cdot\text{yr}^{-1}$) (from (Barker, 2001; Thomas *et al.*, 2003; Ghiglione *et al.*, 2010; Dalziel *et al.*, 2013), superimposed on greyscale topography and bathymetry (Sandwell and Smith, 1997). Relative strike-slip motion of MFF from (Mendoza *et al.*, 2015). Red lines are active structures; black lines are extinct tectonic features. ANT: Antarctic plate; BB: Burdwood Bank; FPH: Former Phoenix plate; HFZ: Hero Fracture Zone; Is. M: Islas Malvinas; MFF: Magallanes-Fagnano Fault; MAFZ: Malvinas-Agulhas Fracture Zone; SAM: South America plate; SCO: Scotia plate; SFZ: Shackleton Fracture Zone; SSH: South Shetland plate; SSW: South Sandwich plate; TdF: Isla Grande de Tierra del Fuego.*

As illustrated with the global plate models Nuvel 1A and Morvel 2010 (Figure 1.6), the Scotia plate motion relative to a fixed SAM plate remains poorly constrained (DeMets *et al.*, 1990; DeMets *et al.*, 1994; DeMets *et al.*, 2010). These models suggest contrastive velocities from 5.24 to 9.85 mm/yr, and compute different rotation pole locations distanced from each other, and far from Tierra del Fuego (Pelayo and Wiens, 1989; DeMets *et al.*, 1994; Thomas *et al.*, 2003;

UNAVCO). Necessarily, it implies the relative motion of SCO and SAM is accommodated by transtensional /transpressional regions, and/or internal deformation in the plates' inner part. At a larger scale, the global plate models indicate 15-18 mm/yr of SAM's relative sinistral motion with respect to Antarctica plate (DeMets *et al.*, 1990). Therefore, the global movement is partitioned between transform faults along the MFF, North Scotia Ridge, the Shackleton Fracture Zone, and the South Scotia Ridge (Smalley *et al.*, 2003).

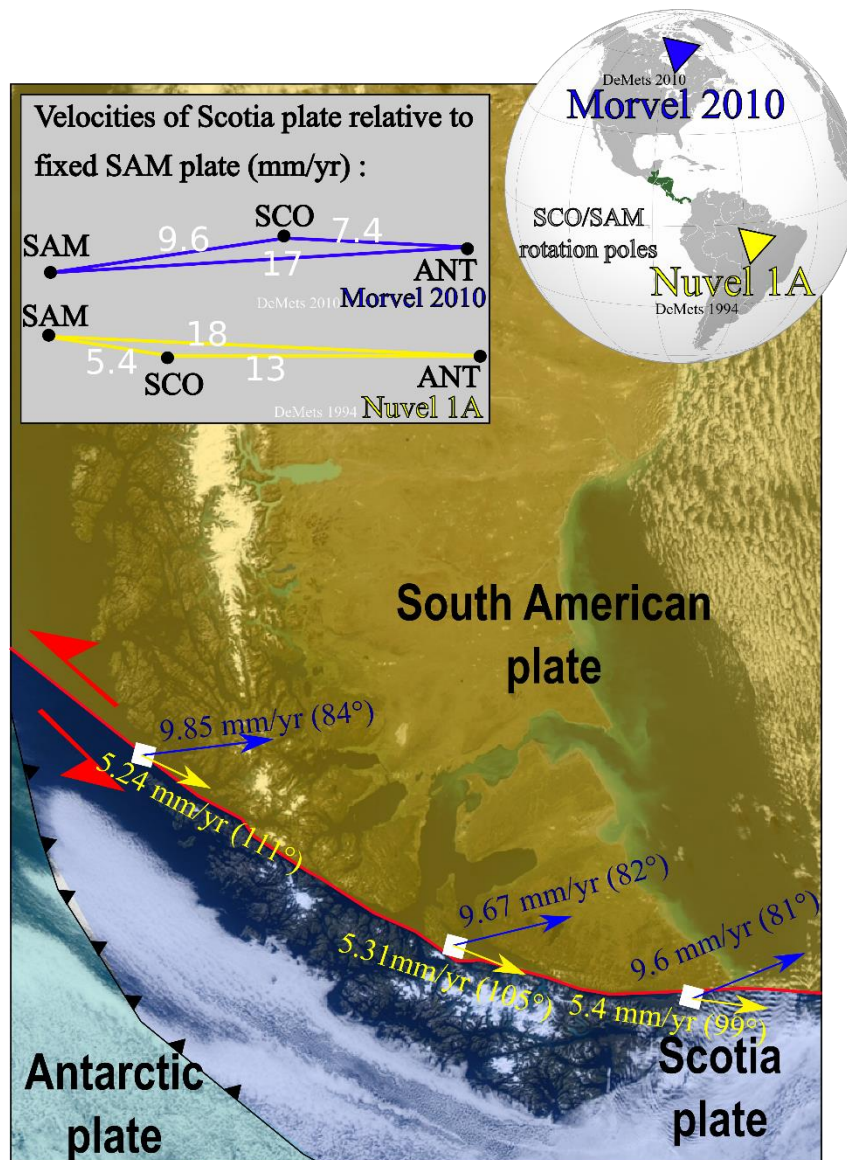


Figure 1.6: Global plate models Morvel 2010 (DeMets *et al.*, 2010) and Nuvel 1A (DeMets *et al.*, 1994) showing the relative velocities of Scotia (SCO) plates to a fixed South American plates (SAM).

Blue and yellow triangles are the rotation poles of Morvel 2010 and Nuvel 1A, respectively. Red line indicates MFF fault. ANT: Antarctic plate.

The MFF extends from the Chile Triple Junction to the Atlantic coast, running in a WNW-ESE trend in the Strait of Magellan's western arm, and in E–W direction in Tierra del Fuego (Figure 1.3). The MFF divides the Tierra del Fuego into two blocks with geomorphological expression in a series of lineaments (scarp, ridge, shutter ridge, truncated vegetation) and depressions (lake, pull-apart, sea passages) (Figure 1.7).



Figure 1.7: Southern Isla Grande de Tierra del Fuego from the International Space Station (ISS) NASA taken the 14 February 2014. Available: NASA's Earth Observatory web site Photo ID: ISS038-E-47389.

The Magallanes Fagnano Fault can produce major earthquakes up to magnitude 7 to 8. The historical record of past earthquakes is particularly short in Tierra del Fuego, and the location and the extent of the penultimate earthquakes are poorly characterized (Figure 1.8). Most of significant modern seismicity $M > 7$ (events 1879, 1949, 1970) are directly triggered by the South American – Scotia plates relative motion, predominantly accommodated along the Magallanes-Fagnano Fault. Furthermore, recently localised crustal earthquakes (from $1.9 < ML < 5.3$) show a

good correlation with the presence of the Magallanes- Fagnano Fault (Ammirati et al., 2020). However, shallow seismic events distributed under the Cordillera Darwin would be mostly associated with isostatic rebound following the retreat of the Patagonian Ice sheet (Ammirati et al., 2020). The Tierra del Fuego is a sparsely instrumented region as the permanent seismological stations were installed only after 2011 (Barrientos, 2018; Ammirati et al., 2020), which implies a large epicentral uncertainty on smaller magnitude pre-2011 events.

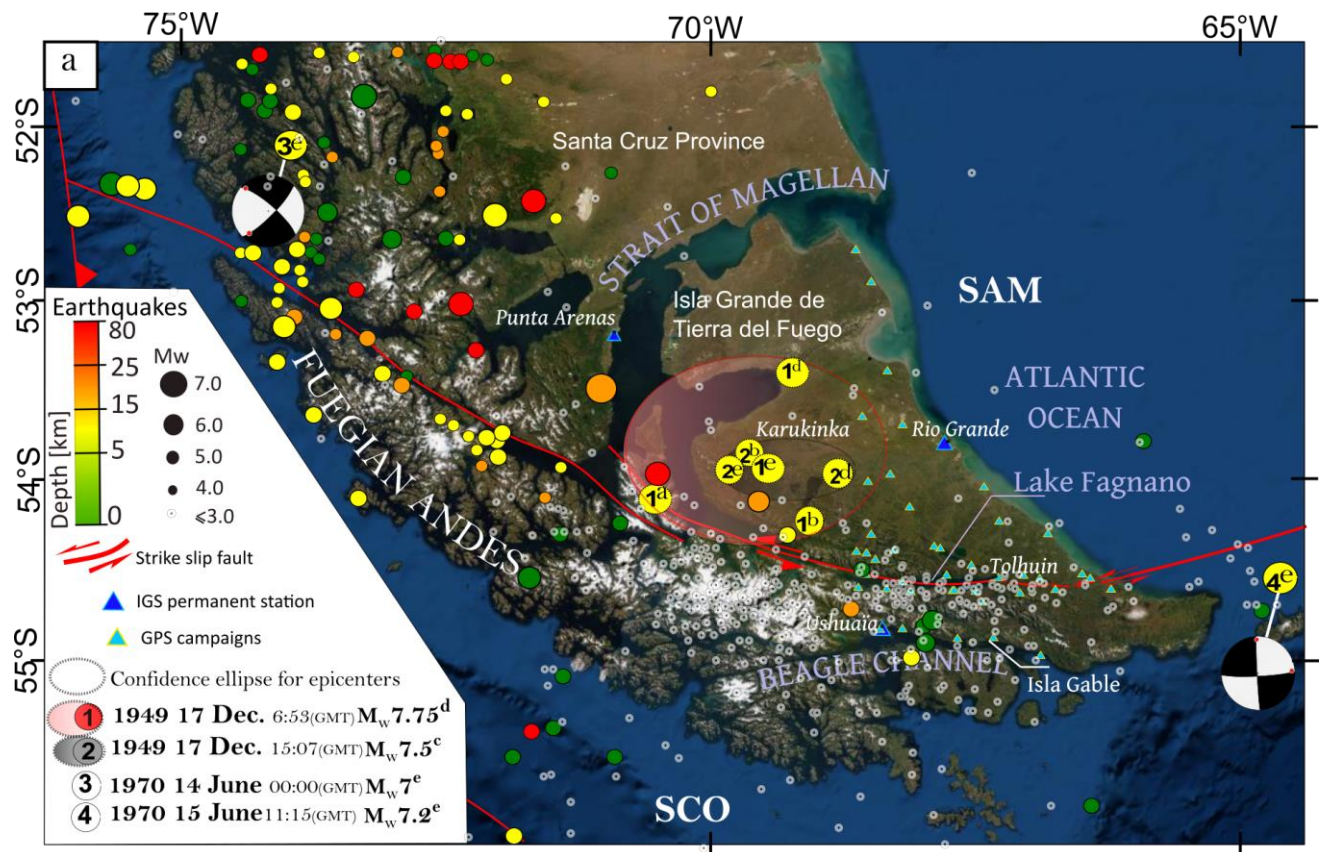


Figure 1.8: Tectonic setting and instrumental records of earthquakes superimposed on World map ESRI. We reported historical 1949 earthquakes epicentre locations proposed by (a) Castano (1977); (b) Jaschek et al., (1982); (c) Lomnitz (1970); (d) Pelayo and Wiens (1989); (e) U.S Geological Survey (2017); Red and grey shaded ellipses refer to the most consistent region for epicentre location of the two main 1949 shocks. Focal mechanisms of the 1970 earthquakes are from (Forsyth, 1975). Catalog of earthquakes are from (Pelayo and Wiens, 1989; Febrer et al., 2000; Buffoni et al., 2009; Flores Véliz, 2017). GPS-station locations from (Mendoza et al., 2015). SAM: South American plate; SCO: Scotia Plate.

The analysis of GPS data predicts a fault dipping $66^\circ \pm 4^\circ$ southward in Eastern Tierra del Fuego, and a locking depth of 11 ± 5 km (Mendoza *et al.*, 2015) in Eastern Tierra del Fuego. Geodetic data evidence the MFF is a narrow deformation belt of ~30-km-wide (Figure 1.9). Global earth model and analysis of gravity data predicted a Moho depth of 26 ± 5 km (Bassin, 2000; Reguzzoni *et al.*, 2013). Also, 1–2 mm/year of relative plate motion may be diffusely distributed from 50° to 56° . It might be accommodated through secondary sub-parallel faults, such as in the Beagle channel, the Carbajal valley, and the Deseado catchment (Smalley *et al.*, 2003; Menichetti *et al.*, 2008).

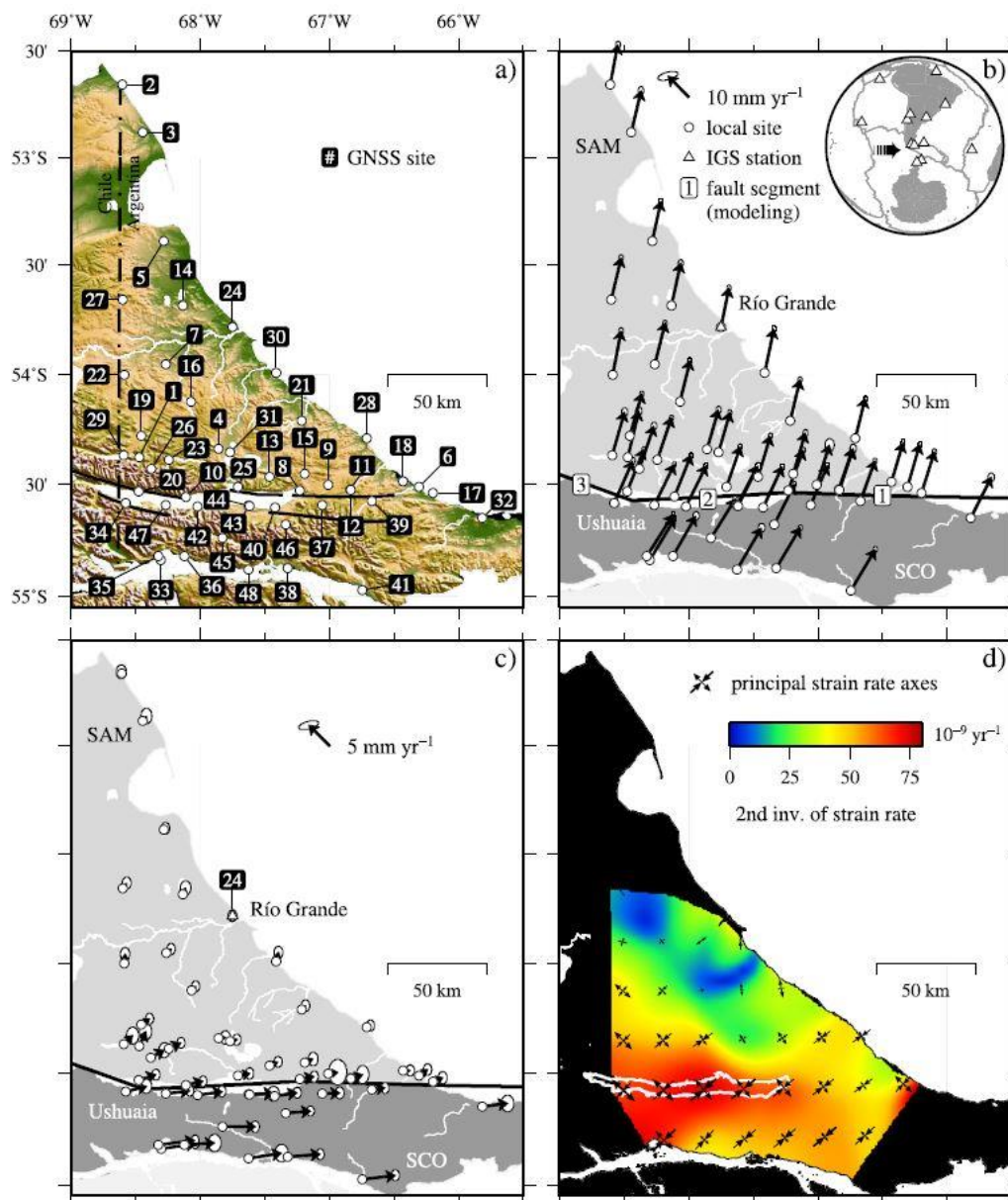


Figure 1.9: GPS results from Mendoza et al. 2015. (a) Regional GNSS network. (b) Observed interseismic velocities in GNSS sites, referred to the terrestrial reference frame IGS08. (c) Same observed velocities referred to the IGS tracking station Rio Grande (RIOG). (d) Near-fault surface deformation was obtained by inverting observed interseismic velocity. Color code is the magnitude of the second invariant of the strain rate.

I.3 Glaciers and glaciations in the Fuegian Andes

The Patagonian glaciations have greatly contributed to carve the present-day Southernmost American shape. From the previous chapter, we know that the tectonic evolution can drastically impact the climate, as illustrated by the Drake passage opening and the concomitant global climate cooling. The other way around, climate can trigger tectonic modifications that remain visible in the landscape. In some cases, changes are perceptible in the crustal motion. For instance, geodetic studies in the Southern Patagonian reveal high uplift rates, which are inherited from the large ice-losses since the Late-Holocene (Dietrich *et al.*, 2010; Lange *et al.*, 2014; Richter *et al.*, 2016; Richter *et al.*, 2019). Therefore, in this intensely formerly glaciated region, the understanding of glaciers and glaciations is fundamental to study the tectonic strike-slip evolution.

In Southernmost Patagonia, the fjords often correspond to weaker geological structures that have been widened during successive glaciations (Glasser and Ghiglione, 2009). The paleoglaciers have deepened the pre-existing structures such as the geological contacts, the over folded terranes, and the plate boundaries (Figure 1.10). The MFF has been activated since the Miocene-Oligocene times and is responsible for the presence of faulting structures lined up in the same orientation than the glacial lineations. Because of the great extent of Late Cenozoic to Quaternary glacial processes in South America, the study of Magallanes-Fagnano strike-slip cannot be separated from the glacial evolution.

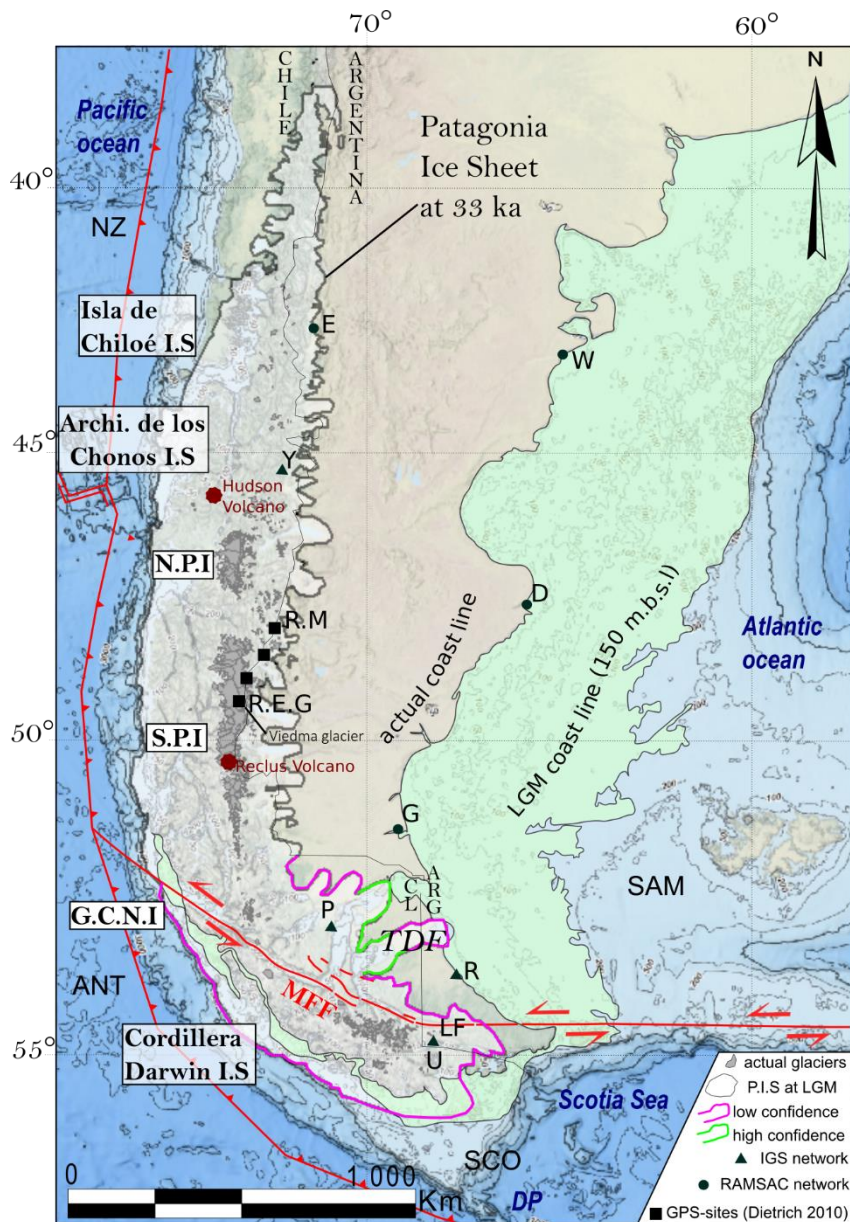


Figure 1.10: Patagonian Ice-sheet (PIS) at 35 ka corresponding to the global Last Glacial Maximum (gLGM) (Davies et al., 2020) above the simplified Magallanes-Fagnano Fault system (MFF, red lines). Abbreviations as follow: AR: Argentina; CL: Chile; D: Puerto Deseado; DP: Drake Passage; E: Esquel; G: Rio Gallegos; G.C.N.I: Gran Campo Navedo Ice-sheet; LF: Lago Fagnano; NPI: Northern Patagonian Ice-sheet; P: Punta Arenas; NZ: Nazca plate; R: Rio Grande; RAMSAC: Argentine Network for Continuous Satellite Monitoring; R.M: Rio Mayer; R.E.G: Refugio Eduardo Garcia; SAM: South American plate; SCO: Scotia plate; SPI: Southern Patagonian Ice-sheet; U: Ushuaia; Y: Coyhaique; W: Rawson. The base map is general bathymetric chart of the oceans (SHOA Chilean Navy, 1998 and

GEBCO 2014; National Centers for Environmental Information NCEI, NOAA). with 100 meters interval below sea level).

1.3.1 Late-Miocene – Early Pliocene glaciations

Patagonian's oldest glacial archive was recorded at 47°S in a 30-m till deposits interbedded with basalt lava-flows, and dated between ~7 and ~5 Ma (Ton-That *et al.*, 1999). Between 7 Ma up to 2 Ma, ice-caps extended 30 km east of the mountain front (Thomson, 2002).

1.3.2 Late Pliocene-Early Pleistocene glaciations

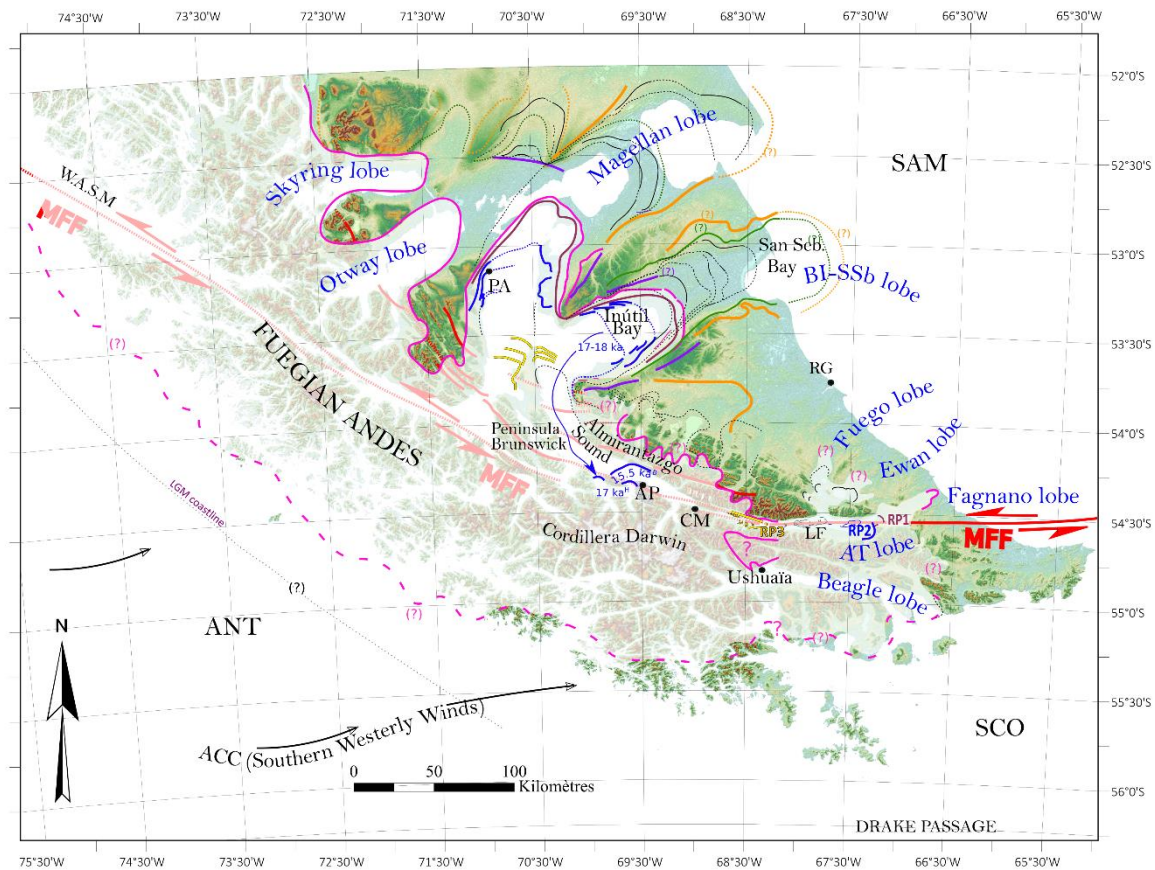
Studies, based on lava flow dating above and below paleoglacigenic deposits, evidence glaciation between 3.0-2.25 Ma and 2.13-1.43 Ma (Mercer, 1983, Wenzens 2000). A minimum of seven glaciations have been recognized, which would have taken place between 3-1.43 Ma (Ton-That, 1997; Ton-That *et al.*, 1999).

1.3.3 Late Pleistocene – the Great Patagonian Glaciation

The most extensive glaciation occurred during the lower Pleistocene at ~ 1.1 Ma (K/Ar dating, Mercer, 1983). This event is either named Llanquihue glaciation (Coronato *et al.*, 2002a), Greatest Patagonian Glaciation (GPG) (Mercer, 1983), or 'Initioglacial' (Caldenius, 1932). This pre-Quaternary glaciation extended farther than the Last Glacial Maximum (LGM) and most likely, included more than one glacial advance (Rabassa *et al.*, 2000). During the GPG, the ice tongues would have rimmed the Atlantic coast north of the Magellan Straits. However, the exact easternmost ice position remains unclear, and some authors propose the ice front was located about 200 km east of the present coast. Massive ice-lobes, such as the Magellan and the Bahia Inutil-San Sebastian lobes, would have carved the main fjords during successive advances (Meglioli, 1993).

1.3.4 Post-GPG glaciation

The most important 'fjord-carving event' occurred soon after the GPG (Rabassa *et al.*, 2000), during what is called post-GPG 1 and 2 (Coronato *et al.*, 2002a). It corresponds to the 'Daniglacial' (1.01 to 0.76 Ma) and "Gotiglacial" according to Caldenius, (1932) classification (Figure 1.11).



¹⁸ O stage	Glacial limits in Magellan Strait cal.ka BP	Glacial limits in Almirantazgo Sound cal.ka BP	Glacial limits in Lake Fagnano cal.ka BP	
MIS 12 (?)	● 1070-360 D. Cabo Virgenes	not recognized	● Daniglacial	Strike-slip fault scarp inferred fault
MIS 10 (?)	● 300-125 D. Punta Delgada	not recognized	● Gotiglacial/D. Rio Valdez	
MIS 4	● STAGE A 70.6 to 56.3	● A not recognized	● STAGE A >58	
MIS 2	● STAGE B 31.2 to 25-23	● B not recognized	● LGM [$<36.1>13.9$] (Finiglacial/Pescado pond)	
	● STAGE C 21.7-20.4	● C not recognized	● RP1 [$<36.1>13.8$] (recessions)	
	● STAGE D 18-17	last recessions: ● D-Boyd <i>et al.</i> 15.5 ● D-Hall <i>et al.</i> 17	● RP2 14.8 - 12.7 (recessions)	
ACR, Younger Dryas	● STAGE E 12.5-11.7	● not visible	● RP3 11.170* (recessions)	
	Bentley <i>et al.</i> , (1998, 2005) Clapperton <i>et al.</i> , (1995) Pelhier <i>et al.</i> , (2020) McCulloch <i>et al.</i> , (2005)a,b Rabassa <i>et al.</i> , (2000)	Boyd <i>et al.</i> , (2008) Fernandez <i>et al.</i> , (2011),(2017) Hall <i>et al.</i> , (2013), (2019)	*dated from core and sedim. rate Bujalesky <i>et al.</i> , (1997) Caldenius 1932 Coronato <i>et al.</i> , (2005),(2009) Rabassa <i>et al.</i> , (2000) Waldmann <i>et al.</i> , (2010)	

Figure 1.11: Paleo-glacial limits of Tierra del Fuego and Southern Patagonian Andes. Compilation of limits from (Caldenius, 1932; Clapperton *et al.*, 1995; Bujalesky *et al.*, 1997; McCulloch and

Bentley, 1998; Rabassa *et al.*, 2000; Rabassa, 2011; Coronato *et al.*, 2002a; Bentley *et al.*, 2005; McCulloch *et al.*, 2005; Waldmann, 2008; Boyd *et al.*, 2008; Coronato *et al.*, 2008; Coronato *et al.*, 2009; Waldmann *et al.*, 2010; Fernández *et al.*, 2011; Hall *et al.*, 2013; Fernández *et al.*, 2013; Peltier *et al.*, 2016; Fernández *et al.*, 2017; Hall *et al.*, 2017; Lozano *et al.*, 2018; Hall *et al.*, 2019; Soteres *et al.*, 2020). Abbreviations: ACC: Antarctic Circumpolar Current; ANT: Antarctic plate; A.P: Ainsworth Peninsula; A.T lobe: Alpine Tributaries lobe; CM: Caleta Maria; CW: Channel Whiteside; LF: Lake Fagnano; Last Glacial Maximum MFF: Magallanes-Fagnano Fault; PA: Punta Arenas; SAM: South American Plate; SCO: Scotia plate; RG: Rio Grande, Argentina; RP_{1,2,3}: Recessional phases; W.A.S.M: Western Arm Strait of Magellan;

1.3.5 Last Glacial period, MIS 4 to MIS 2

In Patagonia, the Last Glacial period corresponds to all the glacial deposits occurring post-Last Interglacial MIS 5 (125 ka). This period was defined as the 'Finiglacial' by Caldenius (1932). Five stages of advances have been recognized, and called stage A to E, from the outermost to the innermost margins with respect to the Andes (Clapperton *et al.*, 1995; McCulloch *et al.*, 2005) (Figure 1.11). The first ice-expansion was stage A (MIS 4) which has been recently dated between 70.6 to 56.3 ka along the western side of Magellan Strait (Peltier *et al.*, 2016; Soteres *et al.*, 2020).

The interglacial MIS 3 remains a controversial phase. Chronologies based on radiocarbon dates propose the MIS 3 was a recessional phase (Mercer, 1976; Laugenie, 1984; Rabassa and Clapperton, 1990; Clapperton *et al.*, 1995; Lowell *et al.*, 1995; Denton *et al.*, 1999; Porter, 2020). Along the Lake Fagnano southern shore, this phase is identified in proglacial delta deposits with interbedded peats dated at 39 cal ka BP and >50 cal ka BP. Authors suggest the delta was formed in a moderate recessional phase after MIS 4 (Bujalesky *et al.*, 1997) with proximal ice-contact. Using dated charcoals from the Peninsula Ainsworth in the Almirantazgo Sound, we will show in Chapter IV, that the recessional phase would have been more intense in this western region. On the other hand, Darvill *et al.* (2015) propose an extensive regional advance in the San Sebastian lobes between 45.6 ka (+139.9/-14.3) up to 30.1 ka (+45.6/-23.1). However, these ages afford dates ranging from MIS 6 to MIS 2. These hypotheses are not necessarily conflicting and can agree with a rapid retreat Early in MIS 3, followed by glacial advance during Late MIS-3.

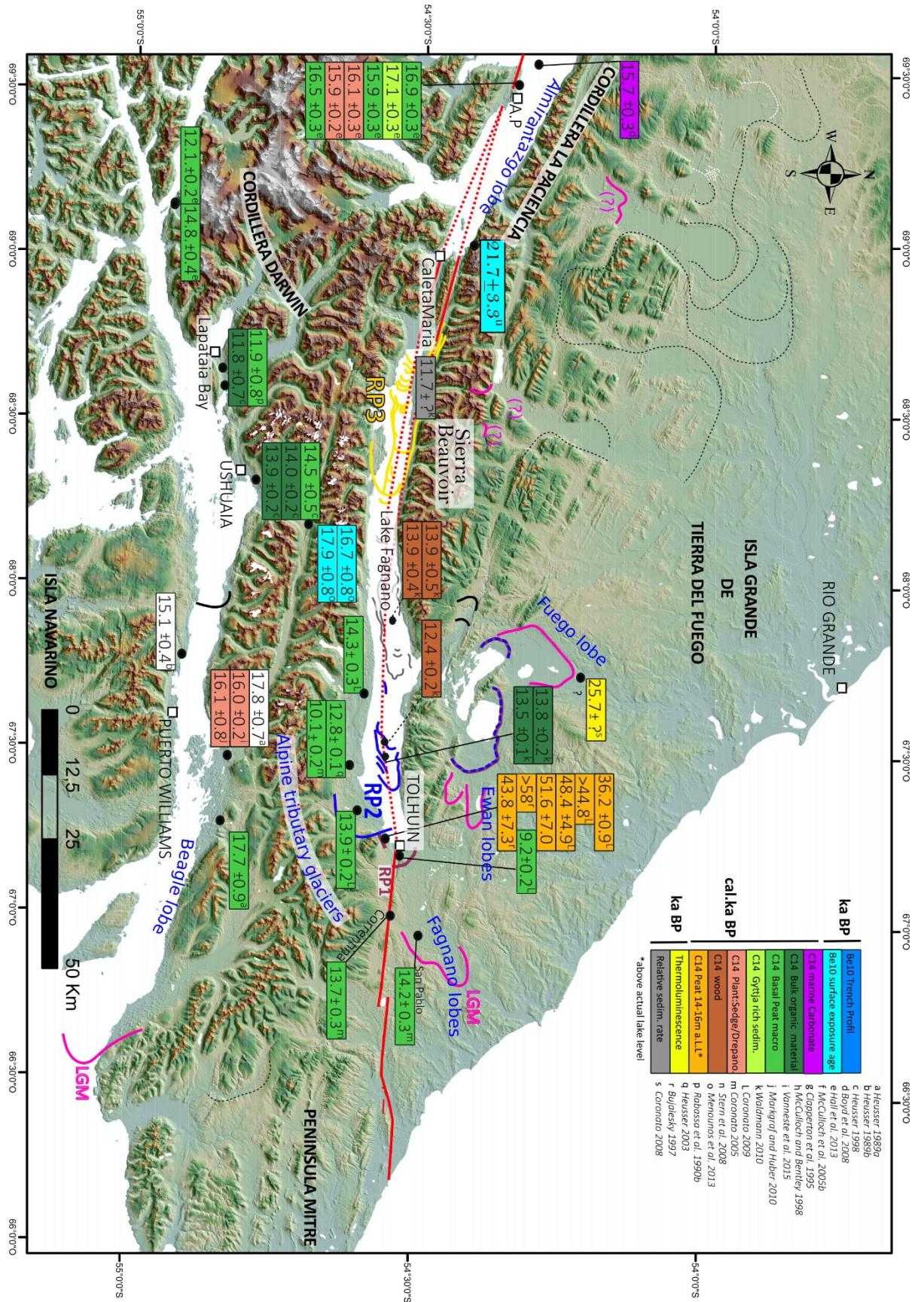
Stage B (late MIS 3 to MIS 2) is recognized as the Last Glacial Maximum (LGM). Despite near a century of scientific investigation about the Patagonian glaciations, the LGM limits remain poorly constrained in most of its extension. It is accepted that the Patagonian Ice sheet may approximately be grounded on the Pacific continental shelf edge and extended 350 km toward the east (Davies *et al.*, 2020). It was an ice band of 2090 km long, from 40°S to 56°S, unifying several ice fields: Isla de Chiloé ice-sheet, the Archipelago de Los Chonos, the Northern and the Southern Ice-sheets, the Grand Campo Nevado Ice-sheet and the Cordillera Darwin Ice-sheet (Figure 1.10). Along such a long latitude range, the LGM ice limits were reached at different times in Patagonia's different regions (Rabassa, 2011; Coronato *et al.*, 2004b; Davies *et al.*, 2020).

The global LGM (gLGM 38°- 48°S) stands between 33-28 ka (Davies *et al.*, 2020). The decay of the ice started about ~ 25 ka and stabilized soon after between ~ 21-18 ka. After 18 ka, the ice-lobes disintegrated rapidly and irreversibly and was lastly interrupted by five stages of glacial advances: 14 to 13 ka, 11 ka, 6 to 5 ka, 2 to 1 ka, and 0.5 ka. The LGM in the Magallanic region slightly differs from the north-central global Patagonian timing (gLGM).

The local LGM in Tierra del Fuego (lLGM) initiated at ~ 31.2 (McCulloch *et al.*, 2005; Kaplan *et al.*, 2008), or earlier (our study, Chapter IV), and culminated at ~25-23 ka. In the strait of Magellan, stages C, D, and E depict successive less extensive advancing fronts (Figure 1.11) at 21.7-20.4 cal ka BP, 18-17 cal ka BP and 12.5-11.7 ka BP, respectively. Ultra-local variations are described in the Almirantazgo Sound by Boyd *et al.* (2008) and Hall *et al.* (2013). They suggest the ice rapidly retreated in Brooks and Marinelli innermost fjords by 15-17 cal ka BP, without former evidences of readvance E. Fernández *et al.*, (2011, 2017) propose that the speed-retreat in these fjords could be mainly bathymetric-driven. In Eastern Tierra del Fuego, the LGM culminated at >25.7 ka in the Fuego lobes (Coronato *et al.*, 2009) and started to recess at ~20-18 ka (Roy *et al.*, 2020). All the final recessional morphologies are described in the Lake Fagnano as RP 1, 2, and 3, and account for progressive retreat in the Darwin Cordillera by 11.7 ka (Figure 1.12) (Waldmann *et al.*, 2010). However, because the final episode of retreat in the Darwin Cordillera was demonstrated in the Almirantazgo Sound to occur between 15-17 ka, the Fagnano lobe final retreat might have occurred earlier than the proposed age (before 11.7 ka).

The local LGM (ILGM) partially covered the Magallanes-Fagnano fault system. This period is associated with a sea-level fall of 150 m below the present-day level (Guilderson *et al.*, 2000). Accordingly, at the latitude of the eastern MFF (-54.5°), the land emerged farther east, extending the inland fault of about 170 km east of the actual coastline (Figure 1.10). While the eastern Magallanes-Fagnano fault remained free of ice, the western and central MFF was covered by large ice-lobes. Along the Cordillera Darwin northern flank, ice lobes were thicker than those in eastern Tierra del Fuego. Trimlines in Almirantazgo Sound evidence the highest imprint of the ice lobes standing about 600 – 800 m.a.s.l. Besides, the Almirantazgo Sound bathymetry (Fernández *et al.*, 2017) demonstrates the ice was grounded along the seafloor during LGM. The actual seafloor depth is -100 to -300 m (SHOA Chilean Navy, 1998) and may include glacial sediment units, then it suggesting a minimal ice mass thickness of > 700 -1100 m within the western MFF. In the mountains ranges Dientes del Dragón, Beauvoir and Valdivieso the trimlines in demonstrate maximum ice-mass > 600 m which rapidly decreases toward the east.

*(Next Page) Figure 1.12: Compilation of dated samples and their respective methods used to constrain the retreats of the Fuegian glaciers. Colour bars indicate the dating methods. Ages are calibrated radiocarbon and indices show the associated reference. Sources are: (Clapperton *et al.*, 1995; Bujalesky *et al.*, 1997; McCulloch and Bentley, 1998; Rabassa *et al.*, 2000; Coronato *et al.*, 2002a; McCulloch *et al.*, 2005; Coronato *et al.*, 2008b; Coronato *et al.*, 2004b; Boyd *et al.*, 2008; Stern, 2008; Coronato *et al.*, 2009; Waldmann *et al.*, 2010; Hall *et al.*, 2013; Menounos *et al.*, 2013; Roy *et al.*, 2020). For the glacial limits extent colours see Figure 1.9.*



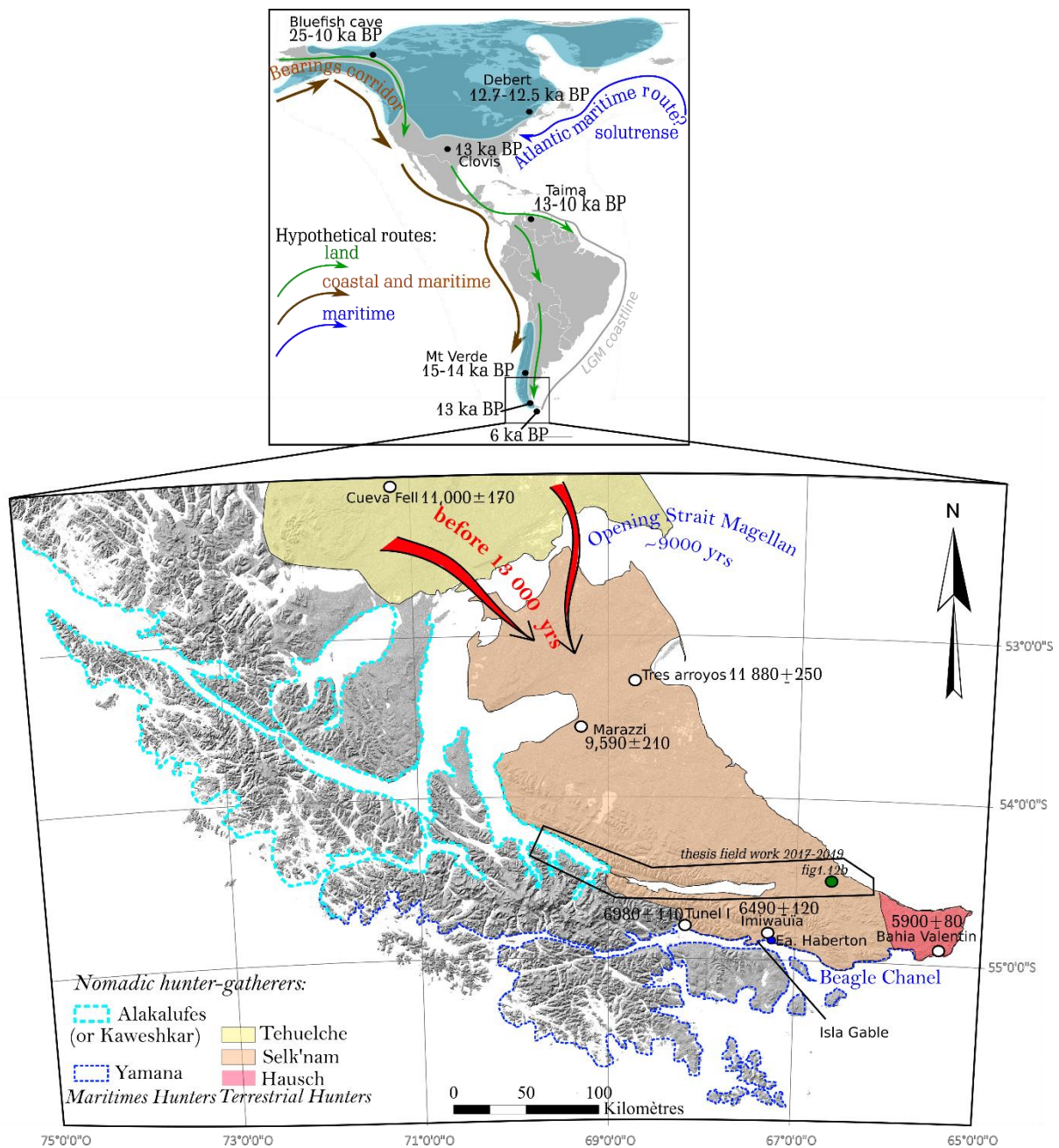
I.4 Twelve thousand years of fire in the Fuegian Andes

As a geologist, when I investigate for the first time an area, I am not only interested in the rocks and in the landscape morphology but also in the inhabitants and their history, who are part of the whole regional painting. Furthermore, when questioning about the paleoearthquakes in Tierra del Fuego, I cannot avoid wondering who was there, to feel, and to endure these tremendous quakes for the last 13 000 years.

I.4.1 The American migrations in the Late Pleistocene

The native groups, have migrated south, passing Monte Verde around 15 000 -14 000 yrs, and then the Strait of Magellan before its opening at 9 000 yrs (Miotti and Salemme, 2004; Salemme and Miotti, 2008; Legoupil, 2011). The oldest radiocarbon dates for human occupation available in Tierra del Fuego are located at Tres Arroyos site (Figure 1.11), and expose multiple evidences of occupation since 12 000 yrs (Massone, 1987, 1988, 2004). This cause a paradigm shift in archaeological thinking: the occupation at Monte Verde unequivocally demonstrates that the South America was colonized before the Clovis culture (Dillehay, 2000, 2003, 1999). Either it means an extremely rapid dispersal of humans from Bearings to South America, or that humans did enter the Americas long before 14 500 yrs and migrated more slowly toward the South (Dennell, 2015). At present, these possibilities remain two candidates, as there are still many substantial geographic gaps to fill (Dillehay, 1999). Heusser, (1994) suggested a hypothesized early occupation in South America, and notably near Monte Verde, based on paleofire charcoal layers at 33 000 yrs. Authors interpreted the absence of charcoal between 25 000 to 15 000 yrs due to human's migration stepping back to higher latitudes to shun the inhospitable austral lands and the Holocene glacial advances.

Figure 1.13: (a) The first settlements of the America and hypothesized routes. (b) Location map of the Native groups of Tierra del Fuego and Southern Patagonia, archaeological sites (white dots) and location of modern tepee in figure 1.13b (green dot). Sources: (Massone, 2004; Miotti and Salemme, 2004; Salemme and Miotti, 2008; Legoupil, 2009; Legoupil, 2011; Raff and Bolnick, 2014; Dennell, 2015). Base map is shaded mosaic relief image of the Southernmost Andes from SRTM ALOS Word 3D-30m (©JAXA).



These groups underwent giant earthquakes since their southward migration in the Fuegian archipelago at the end of Pleistocene, from 13 to 10.5 ka (Miotti and Salemme, 2004; Massone, 2004; Salemme and Miotti, 2008). Unfortunately, the European colonization irrevocably exterminated all of these groups, jointly with their knowledge of ancient temblors (Gusinde, 1951; Chapman, 1989; Peñaloza, 2015). The unique reference to an antique event originated from a Yagána tale mentioned by E.L. Bridges, son of Rev. T. Bridges, a first Salesian settler at Estancia Haberton, at the Beagle Channel northern coast:

«A long time ago the moon fell into the sea, [...] it rose in great tumult, just as the water rises from a bucket when a great stone falls inside. The only survivors of the flood were the fortunate inhabitants of Isla Gable [...]. The surrounding mountains soon submerged, and the people [...], looking around, saw nothing but the ocean to the edge of the horizon [...] ».

[Bridges, \(1952\) p166-167.](#)

Seemingly, the flood would have occurred over the Isla Gable and could be related to a meteorite falling or either to a tsunami from the adjacent fault in the Beagle Channel ([Cunningham, 1993](#)).

I.4.2 Selk'nam, Yagán, Haush and Alakalufes

Four native groups lived in the Isla Grande de Tierra del Fuego and the fjords: The Selk'nam (incorrectly call Onas), the Yagán (Yamanas english), the Haush, and the Alakalufes (Figure 1.14). The Selk'nam and the Haush were terrestrial seminomads, while the Alakalufes (or Kaweskar) and the Yamana were sea seminomads ([Chapman, 1989](#); [Gusinde, 1951](#)).

We owe our knowledge on Native inhabitants mainly through the prodigious works of Thomas Bridges (1842-1898, Anglican missionary), Martin Gusinde (1886-1969, Austrian priest and ethnologist), and Anne Chapman (1922 – 2010, French ethnologist and anthropologist). They lived decades with the natives, abandoned their own trends and religion, to investigate the indigenous culture, languages, beliefs, habits, and interactions. As they respectively lived with Selk'nam and Haush, only little is known on the Alakalufes and Yamana.

In 1880, the Selk'nam peoples were around 3000 to 4000 persons, and in 1930 there was only one hundred Selk'nam ([Chapman, 1989](#)). Individual counts were conducted in central Tierra del Fuego, that is why very few testimonies account for the decline of other groups. Each community formed smaller groups named Haruwen, which were either family and sometimes polygynous ([Bridges, 1879](#)). They lived in a wood hut or tepees (Figure 1.12 a, b).



Figure 1.14: (a) Selk'nam 1910-1920 (Alvarado et al. 2007, photo Agostini). (b) Modern tepee photographed in 2017 during thesis fieldwork in the remote easternmost land between Cabo Malengüena and the Irigoyen river (location green dot figure 1.11). (c) Men's dance in the Hain ceremonial tepee (Choza), photo Gusinde 1923. (d) Ulen spirit, Hain ceremonial Selk'nam in 1923, photo Gusinde (e) left to right: Selk'nams Elek, Angela Loij (center), Imshuta, prepare for the Kewanix dances in honour of Tanu spirit. Hain ceremonial in 1923, photo Gusinde. (f) 1914, Honte (Woman of the Haush group, mother of Luis Garibaldi Honte), unknown photographer, source Chapman 2002.

Each Haruwen had a vast territory passed on their descendants, in which they moved depending on the prey availability. They hunted with arch for guanaco, fox, rodents and multiple birds. For the costal Haruwen, they sometimes hunt for sea lion, seal or sea elephant. For terrestrial groups, they lived mostly on guanaco, in which they used all the parts (bones, tendons, leather) for crafting, tools, clothes and daily consumption items (Figure 1.14a).

These groups endured the Austral cold since generations, and would have developed significantly higher metabolisms than average humans. However, their veritable asset to fight the cold, was to cover their bodies with thick guanaco grease layer. During winters, they wrapped their foot in large piece of guanaco leather, whose woolly side enabled easy snowwalk with fair load-bearing capacity.

The Selk'nam and the Haush did not know the writing, and passed down their knowledge orally, with intergenerational discussion and numerous chants. In each generation, existed one "father of the word", who was the wise guard of the ancestral traditions.

Some Selk'nam words:

Haru, Earth | Jauje, fuego | Chowh, water | Shinká, sea waves

Huen, to laugh | Aska, family | Naa, woman | Chon, man

lHain, father | Mam, Madre | Yowen, guanaco.

Each Haruwen had a Chaman (named Xo' on), a healer who communicated with Nature (Brides, 1879). The Xo'on had a leading role in Hain ceremonies, in which the young adolescent gain access to the man status (Figure 1.14c) by numerous trials and wrestling. Based on oral

traditions, thereupon a time name Hoowin where women lead the Selk'nam, and the young girls were at the heart of the Hain ceremony (Chapman, 1989). Days before the Hain, the group prepared the costumes and painted their entire bodies with red and white clays and greases. Each person had well-determined role and embodied one of the ancient spirits (Figure 1.14d, e).

I.4.3 European arrivals, Dying in the Americas and early capitalism start

The 28 November 1520, almost 500 years ago, Magellan (and Pigaffeta) sailed through the Tierra del Fuego on behalf of King Charles I of Spain. As they noticed numerous smokes all over the coast, their name it "Tierra de Humos", successively amended by the King "Tierra del Los Fuegos" and later shortened Tierra del Fuego (Da Mosto and Allegri, 1894). The European settler groups were more and more to navigate through the Tierra del Fuego: 1616 Le Maire and Schouten (Dutch), 1624 Jacques l'Hermite (Dutch), 1699 Gouin and Beauchêne (French), 1774 Cook (British), 1787 Byron, Wallis and Carteret (British), 1828 Stoke, Skyring, Otway and Fitzroy (British HMS Beagle n°1), 1834 Fitzroy and Darwin (British HMS Beagle n°2), 1837 Dumont D'Urville (French). From the settlers account, we can perceive the general level of understanding, of curiosity, and empathy for the native Americans:

"Bearded, ugly and naked man with fire in each canoe to warm up themselves. So dirty to spoil any man appetite for Christmas dinner." J. Cook 23 December 1774 from (Cook, 1777)

"People try to steel the ship's auxiliary from HMS [...] we decided to take the family, and come back with them in England [1830]". Fitzroy, 1828 from (Fitzroy and King, 2018)

"The Fuegians are in a more miserable state of barbarism than I had expected ever to have seen a human being. [...] He who has seen a savage in his native land will not feel much shame, if forced to acknowledge that the blood of some more humble creature flows in his veins. [...] These were the most abject and miserable creatures I anywhere beheld". (Darwin, 1840, 1875)

The commerce and trade started soon after 1700 when the first Spanish settled in the Buenos Aires region. In Tierra del Fuego and Magallanic regions, the settlements occurred later in 1840. Various church missionaries often accompanied the expeditions and collectively converted, enforced European trends, and recruited the most resigned natives for wool or logging industries,

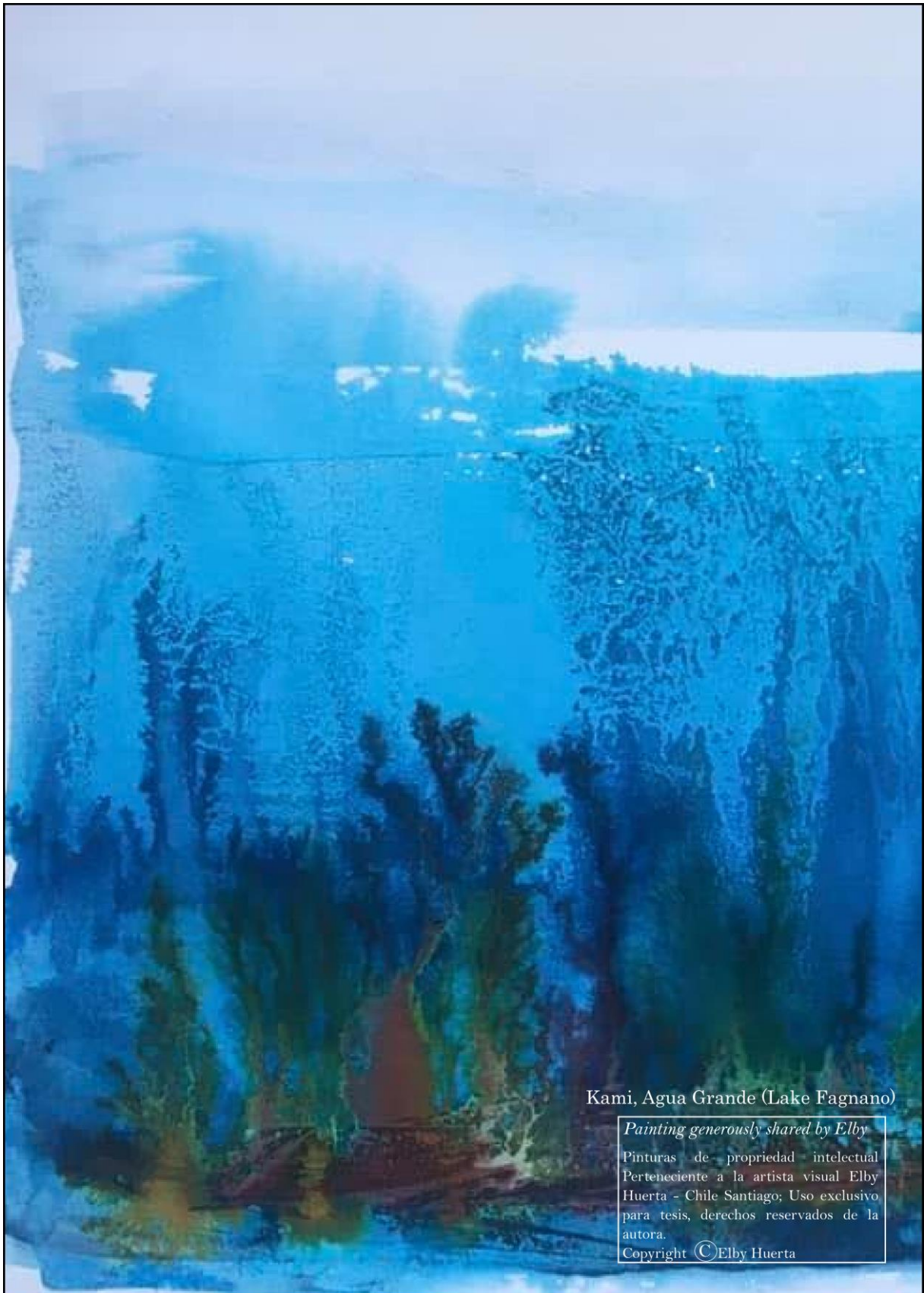
and gold quest (1880-1890) (García, 2013; García O, 2015; Casali and Manzi, 2017). In Tierra del Fuego, coastal gold-bearing alluvial deposits were exploited by the notorious J. Popper (Figure 12a,b), who had lead extermination campaigns in 1886 (Lothrop, 1928; Legoupil, 2009; Chapman, 2010). Besides, the replacement of the guanaco by the sheep breeding led to conflicting situation between Europeans and native hunters with a near eradication of terrestrial hunters in Tierra del Fuego by 1890 (Alvarado *et al.*, 2007; Legoupil, 2009). These missions predated the industrial capitalism and cumulated enormous capital gains on humans' back reduced to slavery or extermination.



*Figure 1.15: (a) Official photography of J. Popper gold quest and extermination campaigns in 1886 near Bahia San Sebastian (Alvarado *et al.*, 2007). (b) J. Popper after assault. (c) 1886, foreground Popper. Paris, 1889 Exposition Universelle. (d) Alakalufes or Yamanas compelled to wear European clothes in 1909. Notice in the legend, the author mistakes Onas from the genuine name Selk'nam, and most probably ignores that only the Alakalufes and the Yamanas are sea nomads.*

Contrary to what is often taught about the mythologized Columbus, Marco Polo, Magellan, and Darwin voyages, these European arrivals were before any Naturalist purposes, expansionist

and capitalist governmental missions. The Americas conquest is proposed to be the onset of the Anthropocene (Haraway *et al.*, 2016; Ferdinand, 2019). Although this epoch has not been officially approved yet as a recognized subdivision of geologic time, researchers have demonstrated the radical environmental changes in South America since the 15th century (Haraway *et al.*, 2016; Koch *et al.*, 2019). The European imprint has triggered significant epidemics, the continents' fauna and flora reunification, and land-use changes (Bonneuil and Fressoz, 2013). Koch *et al.* (2019) review pre-and post-1429 population loss and land-use, and they model the associated global carbon impact compared to natural carbon decline. They estimate the European epidemics removed 90% of the indigenous population over the 16th century representing 56 000 000 persons. The subsequent abandonment of 56 Mha of lands confined a large carbon amount, equivalent to 3.5 ppm decline, which triggered 47-67% of the global atmospheric decline between 1520 CE and 1600 CE (observed in Antarctic ice core records). It demonstrates that even centuries before the Industrial Revolution, human actions had global impacts on the Earth system. Interestingly, the European Colonialism that caused a relative carbon decrease, enabled to cumulated enormous capital gains, founding the modern capitalist societies. These same societies that are responsible of the exponential atmospheric carbon increase since the Industrial revolution.



Kami, Agua Grande (Lake Fagnano)

Painting generously shared by Elby

Pinturas de propiedad intelectual
Pertenece a la artista visual Elby
Huerta - Chile Santiago; Uso exclusivo
para tesis, derechos reservados de la
autora.

Copyright © Elby Huerta

Chapter II: Co-seismic deformation and post-glacial slip rate along the Magallanes-Fagnano fault, Tierra Del Fuego, Argentina

[TERRA NOVA WILEY - ROY et al 2019](#)

[TER-2019-0045.R1 - DOI: 10.1111/ter.12430](#)

[Received: 25 April 2019](#) | [Revised: 27 September 2019](#) | [Accepted: 2 October 2019](#)

Sandrine Roy^{1*}, Riccardo Vassallo¹, Joseph Martinod¹, Matías C. Ghiglione², Christian Sue^{1,3},
Pascal Allemand⁴

¹ ISTerre, Univ. Grenoble Alpes, Univ. Savoie Mont Blanc, CNRS, IRD, IFSTTAR, 38000 Grenoble, France |

² IDEAN-CONICET - Universidad de Buenos Aires – Argentina |

³ Université Bourgogne Franche-Comté, CNRS UMR6249, Besançon, France | ⁴ Université Claude Bernard Lyon 1, Laboratoire de Géologie

* Corresponding author: Sandrine Roy, Institute of Earth Sciences ISTerre
Université Savoie Mont Blanc 73376 Le Bourget-du-Lac
M|+336 37 37 03 17 E| sandrine.roy@univ-savoie.fr

Abstract

Across the extreme south of Patagonia, the Magallanes-Fagnano Fault (MFF) accommodates the left-lateral relative motion between South America and Scotia plates. In this paper, we present an updated view of the geometry of the eastern portion of the MFF outcropping in Tierra del Fuego. We subdivide the MFF in eight segments on the basis of their deformation styles, using field mapping and interpretation of high-resolution imagery. We quantify coseismic ruptures of the strongest recorded 1949, $M_w 7.5$ earthquake, and determine its eastern termination. We recognize several co-seismic offsets in man-made features showing a sinistral shift up to 6.5 m, greater than previously estimated. Using ^{10}Be cosmogenic nuclides depth profiles, we date a cumulated offset in post-glacial morphologies and estimate the long-term slip rate of the eastern MFF. We quantify a $6.4 \pm 0.9 \text{ mm.yr}^{-1}$ left-lateral fault slip rate, which overlaps geodetic velocity and suggests stable fault behaviour since Pleistocene.

KEYWORDS: strike-slip fault, slip-rate, coseismic deformation, Tierra del Fuego, Magallanes-Fagnano Fault

II.1 Introduction

The Magallanes-Fagnano Fault (MFF) accommodates the sinistral motion between the Scotia and South America plates along a 600 km fault system that crosses the Isla Grande de Tierra del Fuego from the western channel of the Magellan Strait to the Atlantic coast (Figure 2.1a). This active transform boundary continues eastward along the North Scotia Ridge toward South Georgia (Klepeis, 1994; Dalziel et al., 2013; Betka et al., 2016; Esteban et al., 2018). In Tierra del Fuego, GNSS data indicate that active deformations are localized on the MFF, and that present-day fault velocity ranges between $\sim 5.9 \pm 0.2 \text{ mm.yr}^{-1}$ (Mendoza et al., 2015) and $\sim 6.6 \pm 1.3 \text{ mm.yr}^{-1}$ (Smalley et al., 2003). The locking depth of the eastern MFF is estimated at about $11 \pm 5 \text{ km}$ (Mendoza et al., 2015).

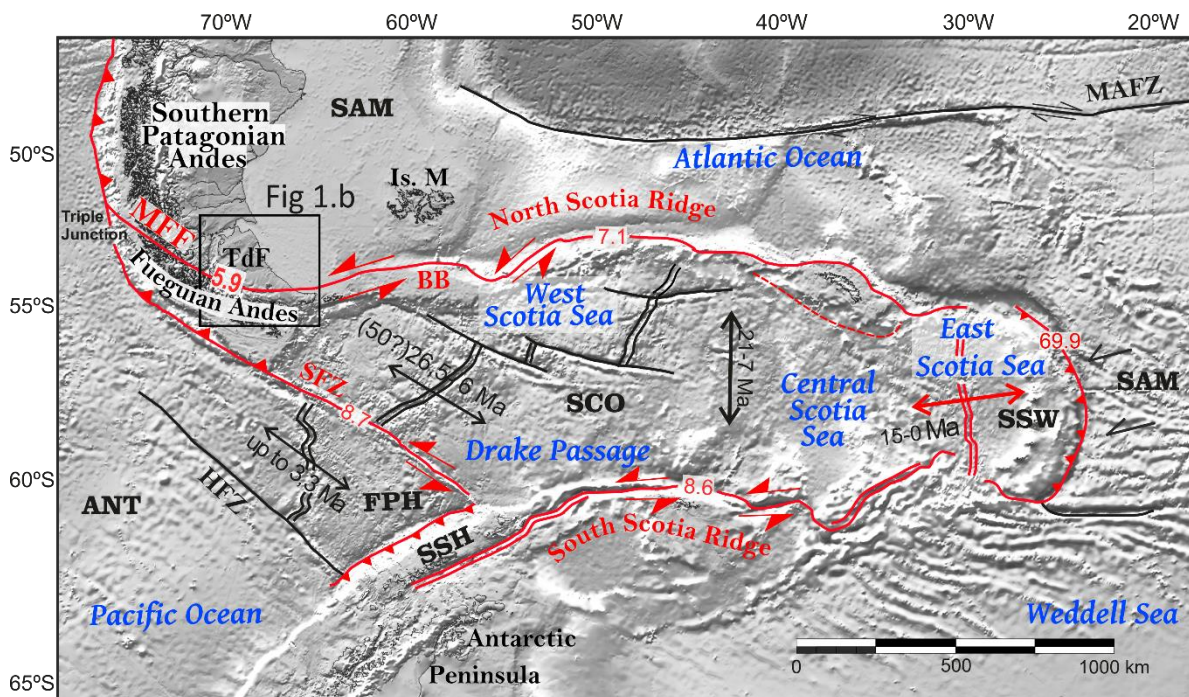


Figure 2.1 (a): Tectonic setting of southernmost Andes with plate boundary velocities (mm/yr) (from: Barker (2001); Ghiglione et al., (2010); Dalziel et al., (2013); Thomas et al., (2003)), superimposed on greyscale topography and bathymetry (Sandwell and Smith, 1997). Relative strike-slip motion of MFF from (Mendoza et al., 2015). Red lines are active structures; black lines are extinct tectonic features. ANT: Antarctic plate; BB: Burdwood Bank; FPH: Former Phoenix plate; HFZ: Hero Fracture Zone; Is. M: Islas Malvinas; MFF: Magallanes-Fagnano Fault; MAFZ: Malvinas-Agulhas

Fracture Zone; SAM: South America plate; SCO: Scotia plate; SFZ: Shackleton Fracture Zone; SSH: South Shetland plate; SSW: South Sandwich plate; TdF: Isla Grande de Tierra del Fuego.

In this work, we focus on the Eastern MFF between the Fagnano Lake and the Atlantic coast in Tierra del Fuego (Figure 2.1b). Two major seismic events occurred in 1879 and 1949. On the 1st February 1879, several European settlements reported an earthquake of intensity VII Modified Mercalli Scale (MMS) near Punta Arenas and VIII MMS in Tierra del Fuego (Cisternas and Vera, 2008), that was later estimated having magnitude 7-7.5 (Lomnitz, 1970). In 1949, two main earthquakes occurred on December 17 at 6:53 (GMT) (Mw7.75), and at 15:07 (GMT) (Mw7.5), followed by several aftershocks of unknown magnitude (Jaschek et al., 1982; Febrer et al., 2000). We report in Figure 2.1b the position of 1949 epicentres according to different authors. Co-seismic surface ruptures (Figure 2.2a) were described at Fagnano and Udaeta Lakes shoreline and in the Estancia La Correntina (Lodolo et al., 2003; Costa et al., 2006; Pedrera et al., 2014). The maximum horizontal component associated with the 1949 ruptures was estimated up to 4 m (Costa et al., 2006).

Intertwined with the tectonic activity, the landscape of Tierra del Fuego was shaped by the alternating advance and retreat of the Fuegian Patagonian ice-sheet (Waldmann, 2008; Glasser and Ghiglione, 2009; Coronato et al., 2009; Waldmann et al., 2010). A major glacial lobe flowed eastward from the Darwin Cordillera (Figure 2.1b) and carved a deep valley now partly occupied by the Fagnano Lake, while east of the lake, smaller tributary glaciers flowed northward above the fault, and eroded part of the pre-glacial strike-slip morphologies (Coronato et al., 2004b). Consequently, the reconstruction of the last deglaciation timing and the related deposit locations are crucial to understand when and where post-glacial strike-slip faulting were recorded. In our work, we built high resolution digital elevation model from Pleiades images combined with extensive field work to study the remarkable imprint of the tectonic activity left in the glaciofluvial deposits and analyse the geometry and kinematics of the fault ruptures.

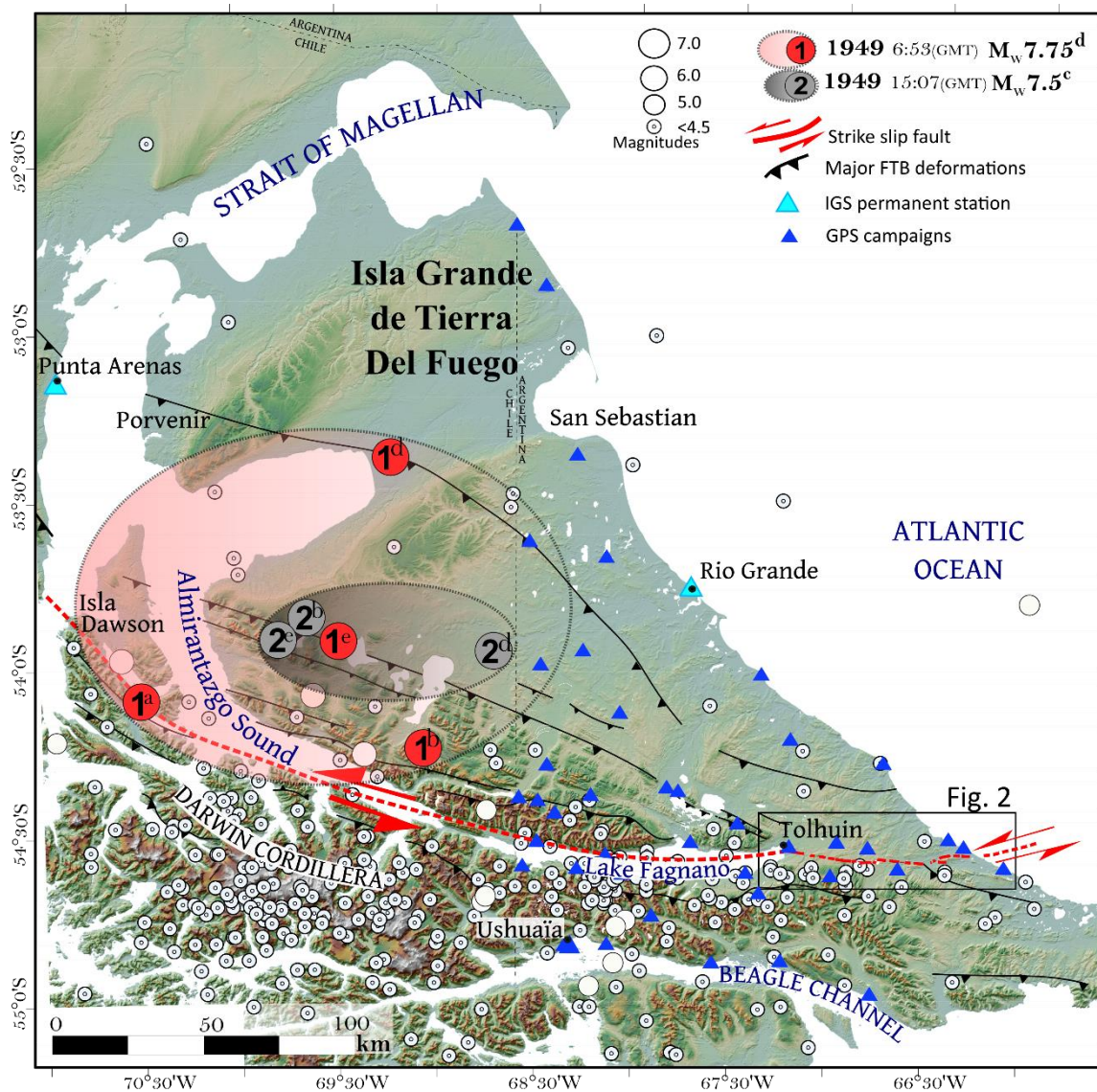


Figure 2.1 (b): Faults and seismicity of Tierra del Fuego. The trace of the MFF is shown with a red dotted line, and the major fold-thrust belt (from Glasser and Ghiglione, (2009) are shown with black lines. We reported historical 1949 earthquakes epicentre locations proposed by a-Castano, (1977); b-Jaschek et al., (1982); c- Lomnitz, (1970); d- Pelayo and Wiens, (1989); e- U.S. Geological Survey; Red and grey shaded ellipses refer to the most consistent region for epicentre location of the two main 1949 shocks. Catalog of earthquakes are from (Buffoni et al., 2009; Febrer et al., 2000; Flores Véliz, 2017; Pelayo and Wiens, 1989). Locations of GPS sites measured in Mendoza et al., (2015).

The Holocene activity of the MFF has been studied at some specific sites by Costa et al. (2006), Waldmann et al. (2011), Esteban et al. (2014), Onorato et al. (2016). In this paper, we

present a detailed description of the 65-km long onshore part of the fault located east of Fagnano Lake, including the previously unstudied 30 km-long segments located east of Udaeta Lake. We describe the 1949 rupture, and reassess the horizontal offset and the coseismic rupture length with new observations of unprecedented described features. Finally, we describe the geomorphic cumulated offset to constrain the average MFF long-term slip rate since the Late-Pleistocene.

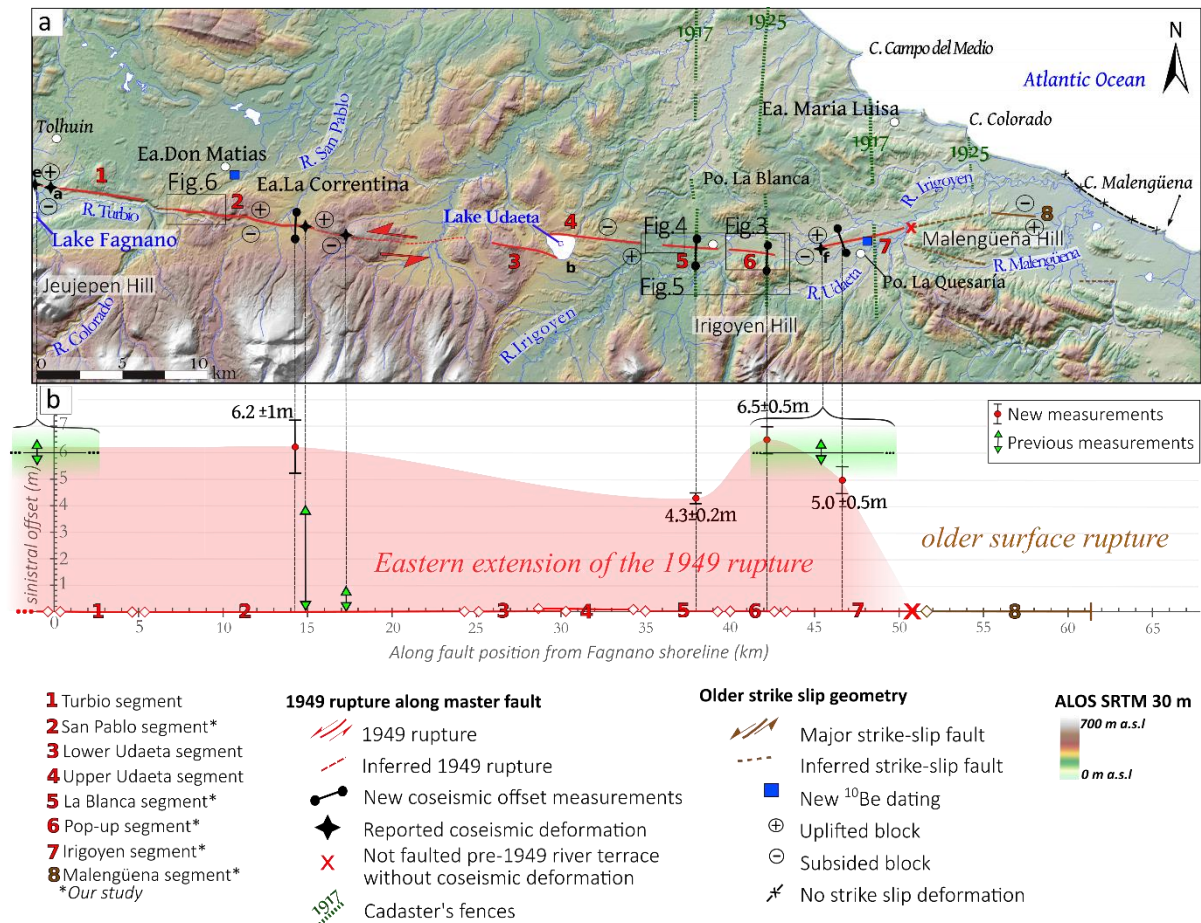


Figure 2.2 (a): Structural map of the eastern MFF. The 1949 surface ruptures are shown as red lines, and the segments with evidences of long-term slip are shown as brown lines. The red cross symbolizes the eastern termination of the 1949 surface rupture. Reported coseismic surface deformations: (a) sag pond and vertical scarp (~0.5–1 m) in Fagnano gravel bar (Lodolo et al., 2003); (b) liquefaction and truncated-tree line features (Onorato et al., 2016; Pedrera et al., 2014); (c) and (d) respectively 'San Pablo' and 'Oliva' disrupted fences mentioned by (Costa et al., 2006). (e) and (f) show two previous reported offsets by eyewitnesses without exact locations (Costa et al., 2006). The base map is DEM SRTM ALOS Word 3D-30m (© JAXA). (b) 1949 sinistral horizontal offsets along the eastern MFF. Red dots and their associated error bars correspond to measurements from this study.

Previous reported offset using green triangles and green shaded rectangles showing the range of possible locations. The 1949 surface rupture continues westward through the Fagnano Lake.

II.2 Eastern Magallanes-Fagnano Fault Geometry

East of Fagnano Lake, the MFF strike is $N90^{\circ}-95^{\circ}$, i.e. sub-parallel to the Paleogene structures that conform the Fuegian thin-skinned fold and thrust belt (Klepeis and Austin, 1997; Ghiglione and Ramos, 2005). We subdivide the fault into 8 segments with their singular geomorphic expressions (Figure 2.2). All segments are characterized by a main strike-slip kinematics, however a moderate dip-slip component results in the relative uplift of either the southern or northern block. The deformation style varies along the 65 km length of the fault and exposes both localized and more distributed patterns. We observe on most of the segments Riedel faults (Figure 2.3a) with a minor vertical component. Orientations indicate R-shear synthetic fractures ranging $N70^{\circ}-75^{\circ}$ (Figure 2.3).

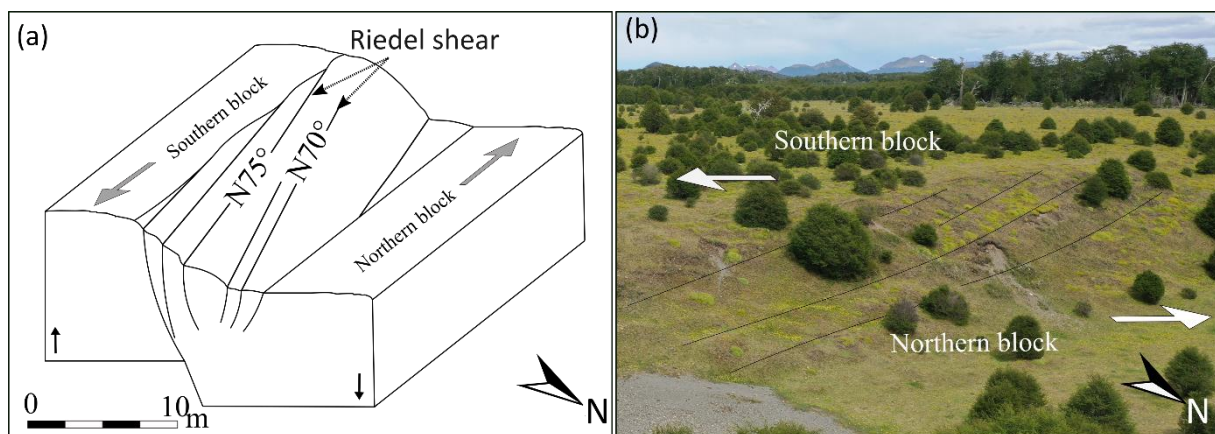


Figure 2.3: Deformation style of the segment 5. (a) Block diagram of Riedel faults with a long-term dip-slip component. (b) Field photography of the Riedel faults.

In other segments, the tectonic deformation is distributed off fault in a sheared zone. At the northern foothill of Sierra Irigoyen along segment 6, we identify a 3-km-long alignment of hectometres pop-up structures (Figure 2.4a). They consist in asymmetric 2-6 meters-high rhomboidal hills, elongated in their ENE, WSW axis. The inner part exposes $N80^{\circ}$ -striking Riedel faults (Figure 2.4b, d). On pop-ups, trees trunks of hundred years old are progressively tilted toward the external border, evidencing that the elevation of these structures amplified during the

last earthquake (Figure 2.4c, e). This particular expression of surface deformation, distributed on transpressive structures, is located in an active flood plain. The presence of unconsolidated sand material and water may favor this deformation style.

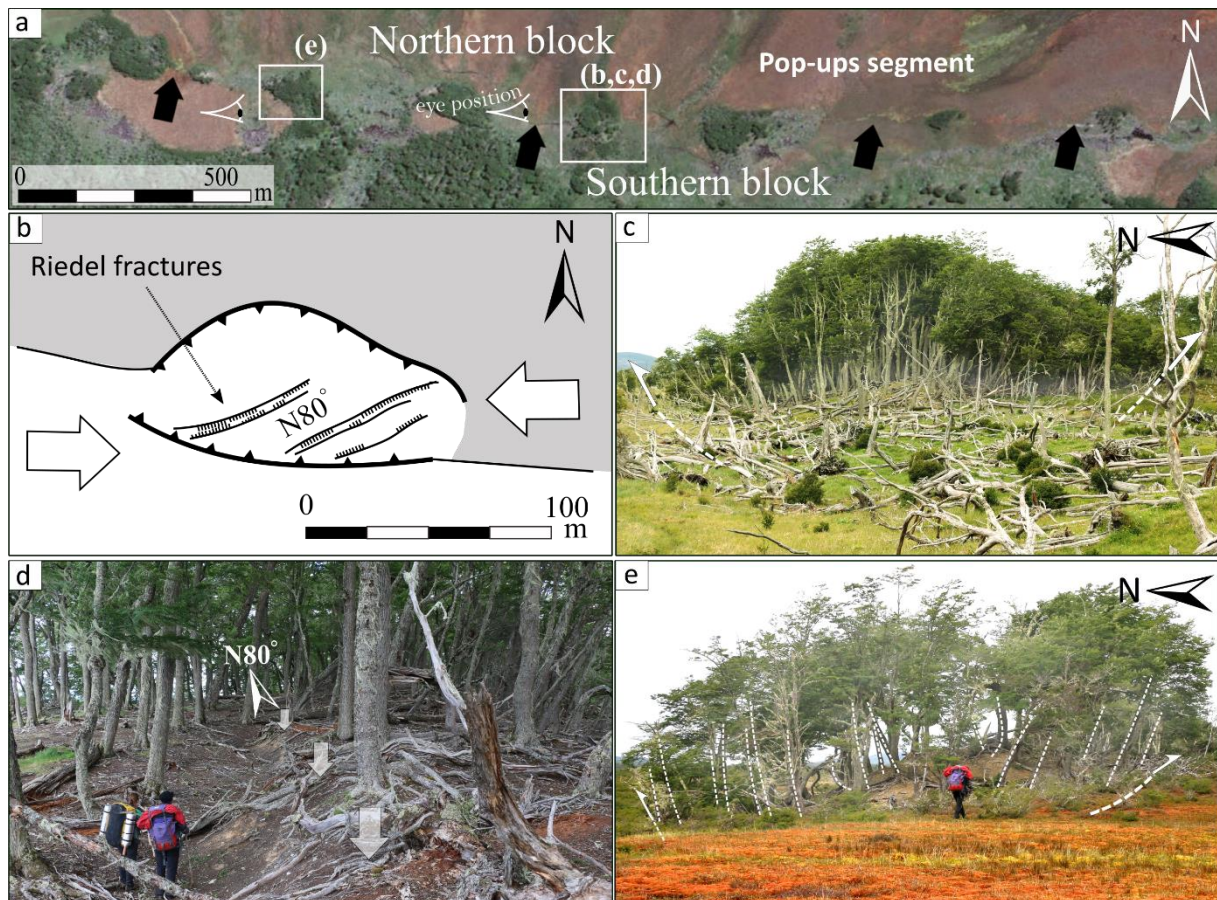


Figure 2.4: Geometry and style of the pop-up structures along segment 6. (a) General view of the pop-ups alignment (green forested patches). (b) Detailed structural sketch of one pop-up showing Riedel faults. (c) pop-up structure with fan shaped tilted trees. (d) Riedel fault within a pop-up; (e) pop-up structure with tilted tree.

II.3 The 1949 co-seismic rupture

Costa et al. (2006) interviewed several eyewitnesses of the 1949 earthquakes and concluded that the horizontal offset did not exceed 4 m. Some witnesses however reported lateral offsets as large as 6 m. Unfortunately, these observations are not supported by field measurements and their precise location is missing. A more exhaustive and accurate offsets estimation is therefore fundamental to improve earthquake scaling behaviour for this fault.

We observe many preserved markers of the co-seismic ruptures from the last earthquake sequence, some of them giving information on the 1949 sinistral offset. Two offsets have been measured (Figure 2.5) in sheep fences corresponding to the Argentinean land registers of the early XXth century (Casali and Manzi, 2017). These limits correspond to several tens of kilometres N-S straight wired connected fences which can easily be mapped from satellite images (Figure 2.5a). In segments 5 and 6, fence offsets evidence a 4 ± 0.2 m and a 6.5 ± 0.5 m sinistral shift, respectively (Figure 2.5b, c). However, it is not possible discriminating whether the offset originated from one or from the sum of the two successive shocks. No evidence of creeping has been noticed since the new fences replaced the pre-1949 ones (Figure 2.5d).

Another offset is measured at the segment 7 (Figure 2.2), where $N75^\circ$ lineament have been previously noticed (Ghiglione, 2003). The fault is crossed by a stream flowing southward which undergoes a sharp sinistral offset of $5 \text{ m} \pm 0.5 \text{ m}$. Besides, in the segment 2 a $6.2 \pm 1 \text{ m}$ sinistral offset is also visible in the foundations of an abandoned broken bridge that spanned over the fault line. These field measurements evidence the horizontal component of the rupture on different segments and show that largest offsets are up to 6-6.5 m. This value is higher than previously measured (4 m) and is consistent with observations noticed by eyewitnesses of the 1949 event.

The easternmost offset measured is localized within the segment 7. Eastward, no geomorphic evidence of the rupture could be observed in pre-1949 river terraces, suggesting that the surface rupture did not propagate farther east (Figure 2.2b). Along the segment 8, the fault trace is visible in a continuous 5 m-high scarp. However, this scarp is much more degraded than in the western segments. These characteristics are consistent with the occurrence of older ruptures along this segment. We did not observe any strike-slip evidence between the Colorado and Malengüeña Capes.

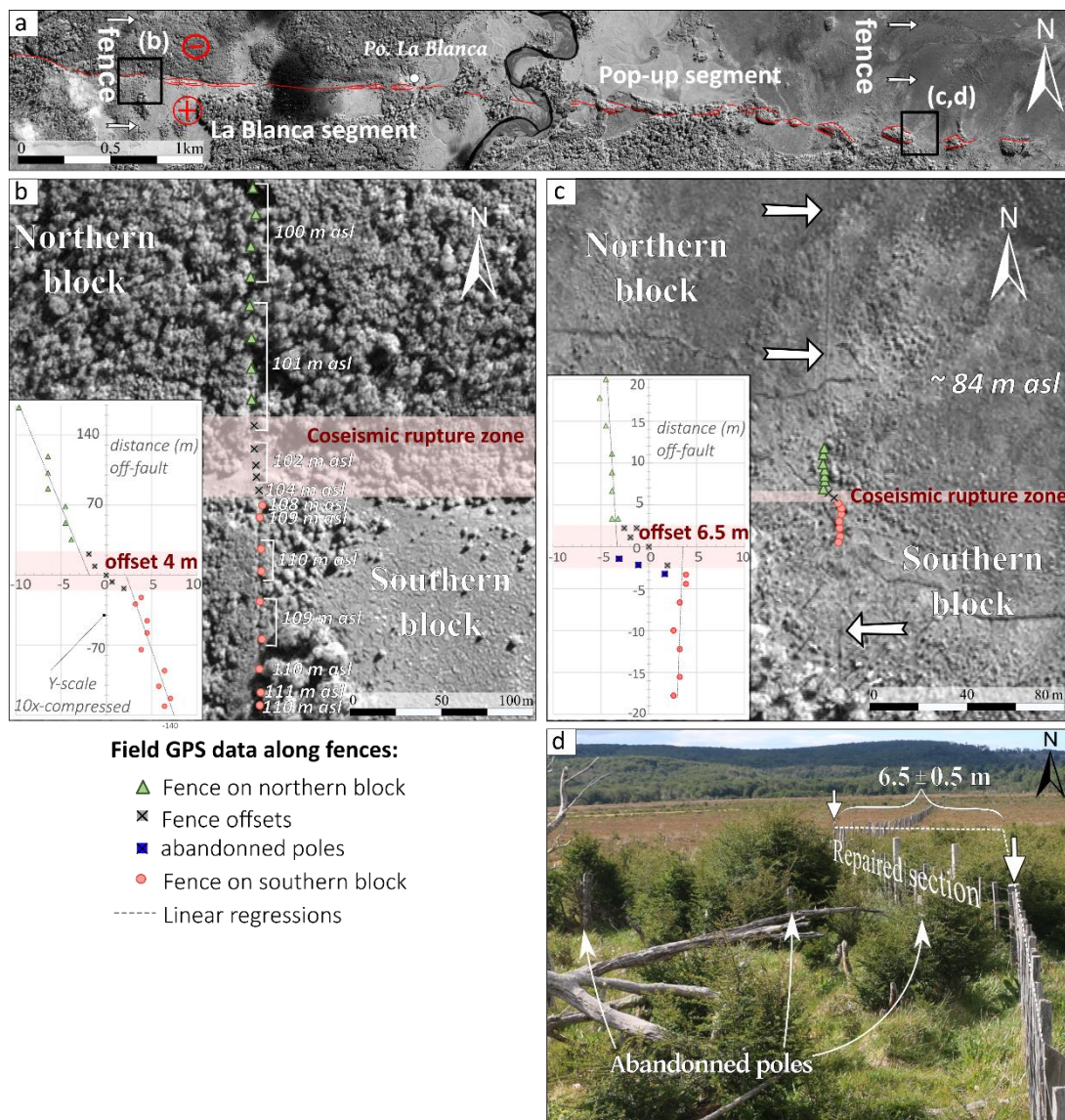


Figure 2.5: (a) Pléiade image above the fault segments 5 and 6 showing the location of offset fences. (b) and (c) GPS points along fences superimposed on Pléiade images respectively at segment 5 and segment 6. Note: on the figure (b) the NS scale of the lower graph has been compressed 10 times. White arrow in (c) highlight the trace of the fences away from the coseismic rupture zone. (d) Photography of measured sinistral offset along the segment 6, showing some of the disrupted fence abandoned poles.

Our observations show that 1949 co-seismic rupture zone ended at 50 km east of the Lake Fagnano shoreline. Westward of our study zone, the rupture continues across the Fagnano Lake parallel to its EW elongate geometry. It could die out somewhere along the 100 km of the lake or

continue further west in the Magellan Strait. Nevertheless, the lack of observation on the western part of the MFF prevent to identify the 1949 surface ruptures termination.

II.4 Post-glacial slip rate

Here, we use the changes in the hydrological network following the Fuegian glaciers retreat to assess the post-glacial long-term slip rate.

The segment 2 crosscuts four well-defined geomorphic markers within a 2 km-long zone (Figure 2.2a): a dead valley, its associated meander, one topographic depression, and one ridge (Figure 6a). We use the respective edges of the geomorphic markers (Figure 2.6b) to assess the left-lateral offset using the back-slip restoration technique (e.g. [McGill and Sieh, 1991](#); [Klinger et al., 2005](#)). The piercing points all match with the best correlation at 115 ± 5 m displacement (Figure 2.6c).

This restoration shows that these various markers are synchronous and probably related to a main landscape formation phase corresponding to the ice retreat. After restoration, the dead-valley recovers its characteristic shape before the abandonment. This valley was carved by meltwater streams following the retreat of tributary glaciers. Such glaciers have also been described further to the west in JeuJepen hill (Figure 2.2a) ([Coronato et al., 2002b](#)). Glacial and Glaciofluvial erosion erased previous strike-slip offset. Such markers fix the beginning of the tectonic surface deformation record in this segment, providing a relative slip chronometer.

By dating the exposure of the youngest sediments of the fossil drainage system, we date the abandonment of the valley and the onset of the subsequent tectonic deformation record. Sampling took place respectively near the Estancia Don Matias and the Puesto La Quesaria (Figure 2.2a) with established procedures ([Braucher et al., 2003](#); [Ritz et al., 2006](#)). We sampled quartz cobbles for cosmic ray exposure (CRE) dating using ^{10}Be along two vertical profiles. Surfaces are flat and underwent negligible erosion, thus we assume a zero denudation rate for age calculations. We use the least-square inversion to model theoretical curves on both profiles for ^{10}Be concentration measurements.

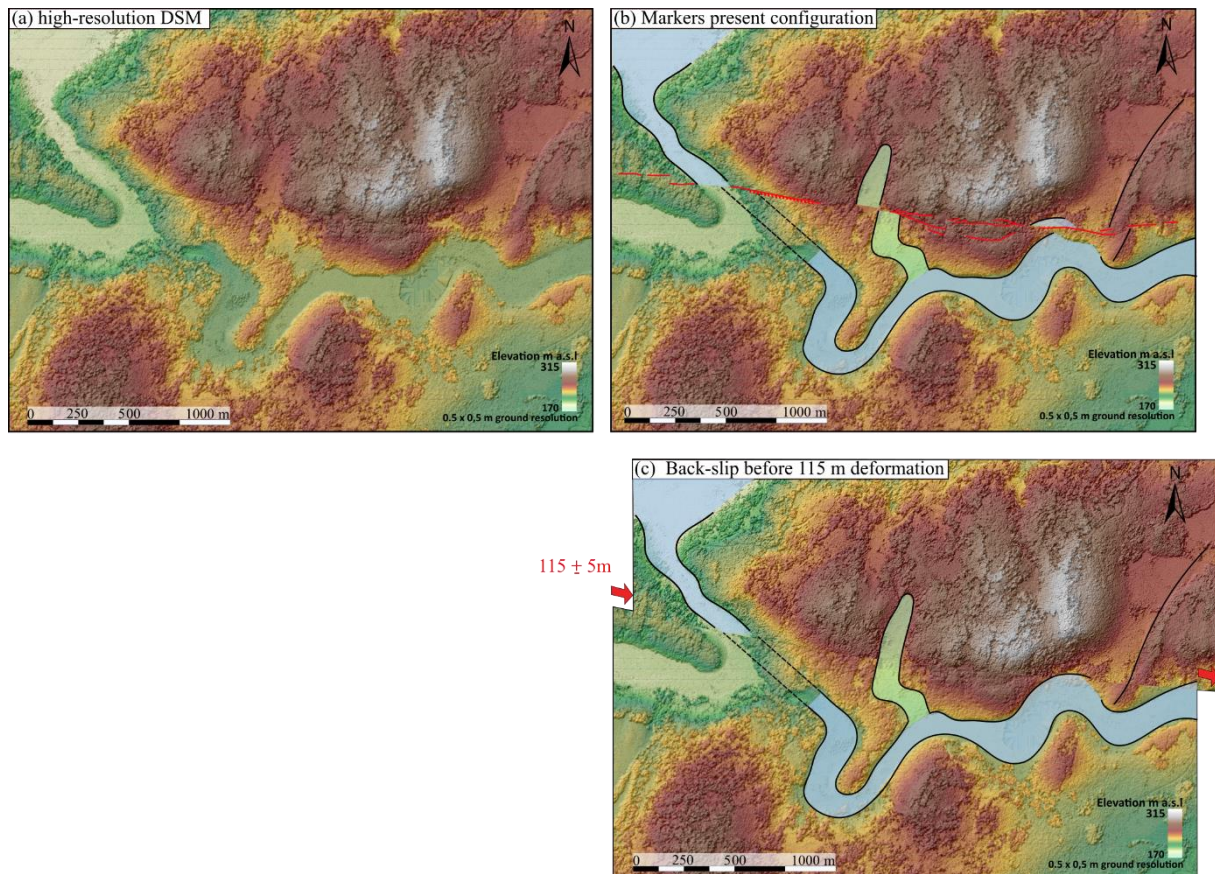


Figure 2.6: Back-slip deformation of post-glacial morphologies along segment 2. (a) High resolution DSM showing the dead valley drainage system. (b) Markers superimposed on DSM with strike-slip (red lines), and offsets in geomorphic markers (black lines): abandoned valley with associated truncated meander (blue cover), hanging valley (green cover) and a hill's ridge (single black line). Lines are used as piercing point crossing the fault trace. We projected each flank of the abandoned valley on the fault plane to identify piercing points. (c) Back slip deformation of markers, the piercing points match for $115 \pm 5\text{m}$ cumulated offset.

Estancia Don Matias's terrace stratigraphic log presents four faciès of well-sorted sandy gravel matrix with gradational contacts resulting from glaciofluvial depositions (Figure 2.7). The predominance of subangular and subrounded clasts in the two lower levels (unit 3 and 4) indicates a short glaciofluvial transport. The concentrations distribution does not decrease exponentially with depth, evidencing that sample may have two exposure sources: the common post-depositional cosmogenic nuclide production and their own pre-depositional production, which is responsible for an intrinsic ^{10}Be inheritance value. Based on these hypotheses, we apply the profile rejuvenation methodology (Le Dortz et al., 2012). We select the sample (DM5) with the

minimum ^{10}Be concentration normalized by depth. It has the lowest inherited concentration among all the profile samples. Its apparent exposure age is, therefore, the closest to the true post-depositional age of the valley. The ^{10}Be concentration of sample DM5 yields a maximum age of valley abandonment at $\sim 18 \pm 2$ ka. This age fixes the beginning of the tectonic deformation record. In the same area, age based on ^{14}C of basal peat bog grown on top of moraine deposits confirm that ice retreat in this region started before ~ 14 ka (Coronato et al., 2009).

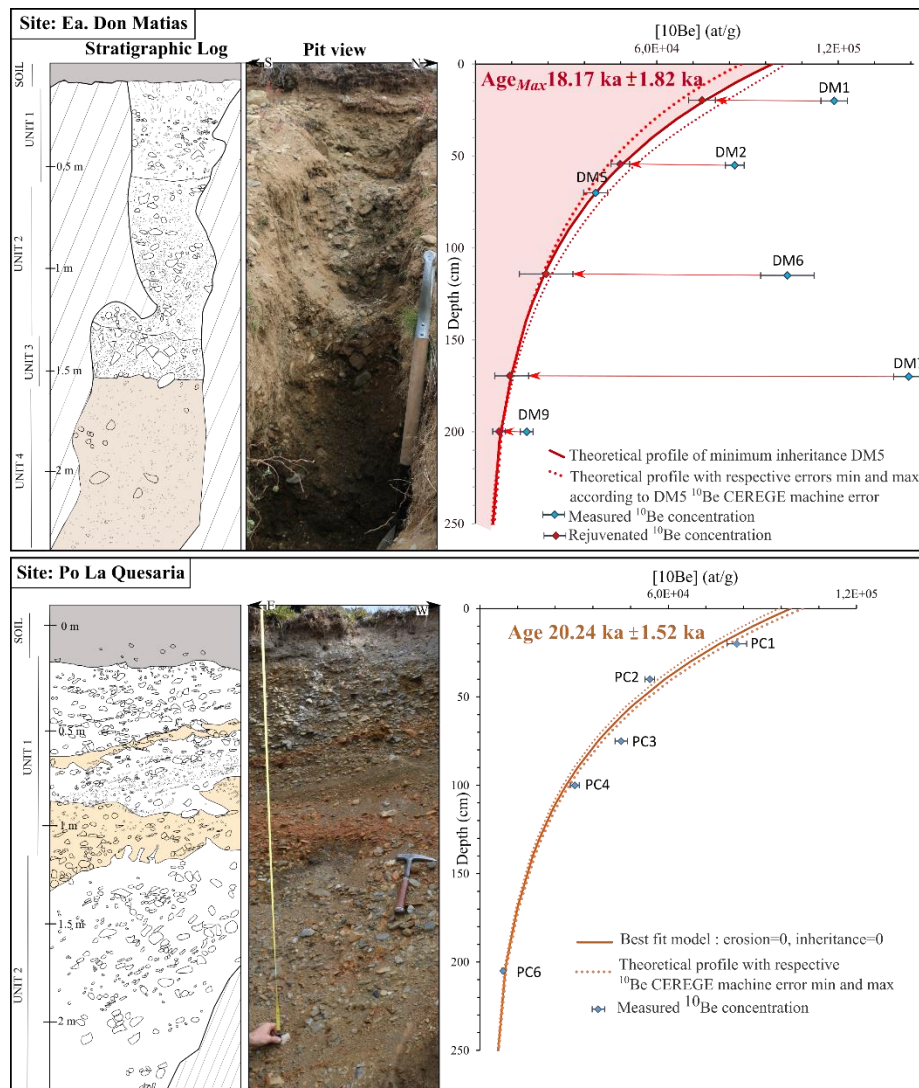


Figure 2.7: ^{10}Be depth profiles with respective stratigraphic log and pit view of site Estancia Don Matias and Puesto La Quesaria (see Figure 2.2 for location). ^{10}Be production rate has been calibrated for local latitudes and elevations (Stone, 2000), using the modified functions of (Lal, 1991), which stands in quartz production of 4.92 ± 0.43 at/g/yr at sea level and high latitude. Calculations were performed using attenuation lengths of 150, 1500 and 5300 $\text{g}\cdot\text{cm}^{-2}$ with associated relative

contributions of 97.85%, 1.50% and 0.65% (Braucher et al., 2003). We employ the currently accepted ^{10}Be half-life value of $1.387 \pm 0.012 \cdot 10^6$ yrs (Chmeleff et al., 2010; Korschinek et al., 2010; Nishiizumi et al., 2007). Measurements were completed at the accelerator mass spectrometry facility ASTER (Aix-en-Provence, France) after preparation at the ISTerre GeoThermoChronology platform (Grenoble, France).

At Puesto La Quesaria, we sampled the highest preserved alluvial terrace, whose formation is supposed to be synchronous of regional glacial retreat. The profile exposes pebble to gravel clasts in a sandy matrix characteristic of meltwater channel environment (Figure 2.7). Here, the distribution of ^{10}Be concentrations decreases exponentially with depth following the theoretical curve of ^{10}Be production (Brown et al., 1991; Dunai, 2010), suggesting that inherited cosmogenic concentrations are negligible compared to post-depositional concentrations. These concentrations yield a terrace exposure age of 20.2 ± 1.5 ka, overlapping the maximum age obtained near the Estancia Don Matias.

These ages characterize the main recession phase during which the tributaries glaciers retreated above the Southern Hills (Coronato et al., 2009; Waldmann et al., 2010; Rabassa et al., 2011). The abandonment of the glaciofluvial valleys resulting from ice retreat fossilized the associated drainage system allowing the preservation of fault activity in the landscape since 18-20 ka. The cumulated offset observed in the valley near by the Estancia Don Matias since this period yields a geomorphic slip-rate of 6.4 ± 0.9 mm.yr⁻¹.

II.5 Discussion and conclusions

We explore the main post-glacial deformations recorded along the eastern sector of the MFF from Lake Fagnano to the Atlantic coast and integrated previously documented geometries. Newly described strike-slip structures, pop-ups, and Riedel fractures are mapped with the relative vertical motion of blocks. The analysis of high-resolution topographic models and satellite images does not show any significant deformation on secondary structures, confirming that strike-slip motion concentrates along the master fault as already suggested by GPS data inversion (Mendoza et al., 2011).

We chart the 1949 surface primary ruptures and measured related sinistral slips. We document horizontal offsets up to 6.5 ± 0.5 m. Surface rupture can be followed along 50 km from the Fagnano Lake shoreline to the tip of the segment 7. According to the main shocks magnitudes the 1949 surface rupture probably continued beneath Fagnano Lake, but the lack of direct access to the western part of the MFF prevent to identify the 1949 western surface ruptures termination.

Back-slip restoration of offset glaciofluvial markers combined with ^{10}Be dating allow the first quantification of the geomorphic slip rate for this fault. The offset started to accumulate when the local glacial catchment source vanished and associated drainage system was abandoned $\sim 18 \pm 2$ ka ago. Our results yield a left-lateral Late Pleistocene slip rate of 6.4 ± 0.9 mm.yr $^{-1}$ over this period. This value overlaps the present-day velocity estimated using geodetic data. The unchanged fault slip rate over the different timescale suggests a stable fault behaviour since glaciers retreat.

Previous indirect attempts of major MFF earthquake recurrence estimations are divergent and possibly biased by the method used. The shorter proposed recurrence interval is about 350-850 years ([Waldmann et al., 2011](#)) while the longer is 3000-4500 years ([Costa et al. 2006](#)). The former study uses as a proxy the mass-wasting events in Fagnano Lake, which may integrate events triggered on other structures, while the latter is based on a single paleoseismological trench, in which sedimentary and tectonic record are not complete and some events may not be registered. Considering the 1949 co-seismic offsets in the area around the long-term slip-rate measurement, we obtained an average offset of 6 ± 0.5 m. With a geomorphic slip rate of 6.4 ± 0.9 mm.yr $^{-1}$, and based on the average co-seismic offset of 1949, we propose a frequency of large earthquakes event about 1000 ± 215 yrs.

Acknowledgement

This research is part of a bilateral scientific cooperation project between Argentinian Mincyt - Universidad de Buenos Aires, and the University Savoie Mont-Blanc (ISTerre) and the Besancon University, funded by the Argentinian-French ECOS-SUD under grant project A15U02. We acknowledge the French CNRS-INSU (project PICS and SYSTER). We address special thanks to J. Carcaillet (ISTerre GeoThermoChronology platform) for his guidance in cosmogenic dating and warmly thank F. Massot and O. Romeyer for their technical support. We are also deeply grateful to M. P. Escayola (UNTDF Universidad Tierra Del Fuego), M. Bauducco and C. Maure for their direct and efficient support in Tierra del Fuego. The authors thank J.L. Paños, E.S. Ampuero, K.A. Vargas Saldivia, and P.J. López, for kindly authorizing us to work on their lands. The manuscript was greatly improved due to careful reviews by F. Visini, P. Burrato and Associate Editor C. Chiarabba.

Annexe: Precise coordinates, and photo of trench location, and photographs of samples.



Painting generously shared by Elby
Pinturas de propiedad intelectual
Pertenciente a la artista visual Elby
Huerta - Chile Santiago. Uso exclusivo
para tesis, derechos reservados de la
autora.
Copyright © Elby Huerta

Ulen espíritu Selk'nam

Chapter III: New Insights into Paleoseismic records of the Magallanes Fagnano Strike-slip Fault, Argentina

Sandrine Roy^{1*}, Riccardo Vassallo¹, Joseph Martinod¹, Christian Sue^{1,2}

¹ ISTerre, Univ. Grenoble Alpes, Univ. Savoie Mont Blanc, CNRS, IRD, IFSTTAR, 38000 Grenoble, France|

² Université Bourgogne Franche-Comté, CNRS UMR6249, Besançon, France

* Corresponding author: Sandrine Roy, Institute of Earth Sciences ISTerre
Université Savoie Mont Blanc 73376 Le Bourget-du-Lac
M|+336 37 37 03 17 E| sandrine.roy@univ-savoie.fr

Key Points

- New records of five paleoearthquakes in the eastern Magallanes Fagnano Fault.
- New evidence of the last 3 major ruptures since 2 ka agree with a recurrence interval of 1000 yrs.

Abstract

The Magallanes-Fagnano fault (MFF) is an active sinistral strike-slip fault that cuts across Isla Grande de Tierra del Fuego, forming the plate boundary between South-American and Scotia plates. To improve Holocene earthquake's characterization of the MFF system, we conducted extensive fieldwork and neotectonic mapping. We excavated a paleoseismic trench across an 11-m-high fault scarp along the La Blanca segment. Using a scarp-derived colluvial wedge, cross-cutting relation, and 28-radiocarbon samples, we document evidences of five paleoearthquakes during the last 11 ka BP. The events are E₅ at 1949 and/or 1879 AD, E₄ at $\sim 788 \pm 122$ cal yrs BP, E₃ at $\sim 2165 \pm 155$ cal yrs BP and two events E₂, E₁ older than 10 776 cal yrs BP. Results yield an interseismic recurrence of ~ 1000 yrs in the last 2ka. We correlate and discuss our results with previous paleoseismic investigations. These findings improve the understanding of Tierra del Fuego's paleoearthquakes and provide a new frame for seismic hazard assessment at the South America – Scotia boundary.

Keywords Paleoearthquake records, Magallanes-Fagnano Fault, Strike-slip, Paleoseismology.

III.1 Introduction

Paleoseismic investigation allows analysis of a more extended history of major earthquakes than is possible from the historical record (Wallace, 1981). Surface fault geometries and disrupted stratigraphy constitute primary evidences and determining relics resulting directly from ancient seismic shocks (Sieh, 1981; McCalpin, 1996; Obermeier, 1996). In southernmost Patagonia (52°S), these archives are fundamental, especially as historical and instrumental records are scarce in this remote and highly tectonically active region.

Since the Early Miocene, the austral tip of South America has been affected by the left-lateral strike-slip Magallanes-Fagnano Faults (MFF) system cutting through the continent from the Pacific to the Atlantic (Winslow, 1982; Klepeis, 1994; Ghiglione, 2002; Lodolo et al., 2003; Torres-Carbonell et al., 2008; Tassone et al., 2005; 2008). The Tierra del Fuego represents the largest on-shore section of this boundary between the South American and the Scotia plates (Figure 3.1a). The Tierra del Fuego's recent tectonic history is closely intertwined with its glacial heritage, which offers an exceptional area for paleoseismic investigations (Figure 3.1b). The MFF disrupts the Pleistocene to Holocene surficial deposits transported by the last glacial and periglacial processes (Winslow, 1982; Klepeis, 1994; Lodolo et al., 2003; Costa et al., 2006; Waldmann et al., 2011; Onorato, 2018, 2020; Roy et al., 2020; Sandoval and De Pascale, 2020).

This paper offers new evidences of the MFF Late-Holocene activity using trench paleoseismological analysis and fault scarps geomorphology. Recently, studies have attempted to reconstruct 19 mass-wasting events over the last 11 ka using the lake sediment archives (Waldmann et al., 2011), and four paleoearthquakes from trench analysis in the eastern MFF (Costa et al., 2006). Our results improve the knowledge of paleoearthquake ages, magnitudes, and recurrence. This paper aims to integrate our data within previous paleorupture catalog, proposing a reviewed chronology of paleoearthquakes in Tierra del Fuego.

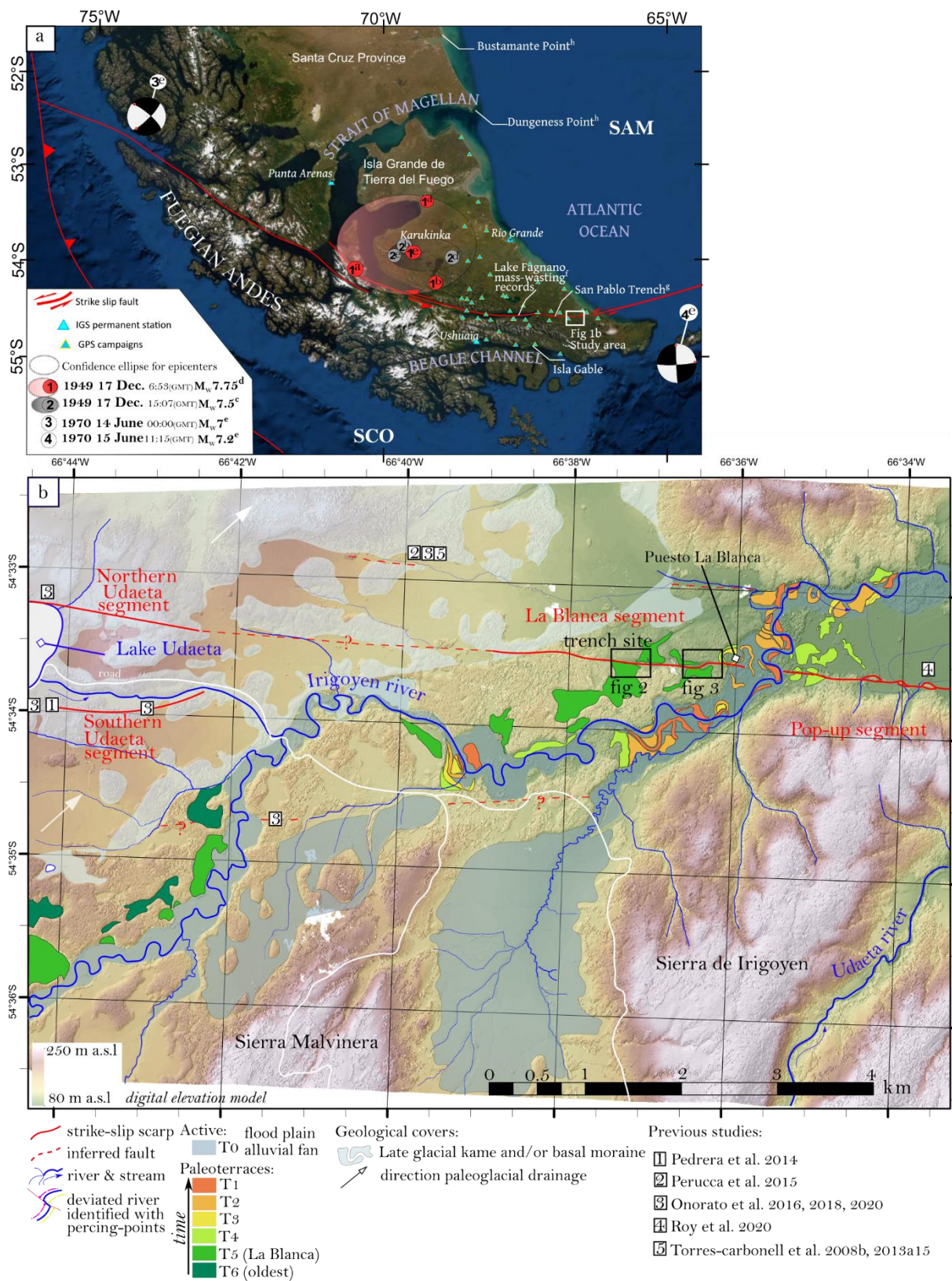


Figure 3.1 (a) Tectonic setting, previous paleoseismic studies, and instrumental records of $M \geq 7$ earthquakes of the Magallanes-Fagnano Fault. Focal mechanisms are from (Forsyth, 1975) and relative strike-slip geodetic-velocity from Mendoza et al. (2015) superimposed on World map ESRI.

References are (a) [Castano, \(1977\)](#); (b) [Jaschek et al., \(1982\)](#); (c) [Lomnitz, \(1970\)](#); (d) [Pelayo and Wiens, \(1989\)](#); (e) [U.S Geological Survey \(2017\)](#); (f) [Waldmann, \(2008\) and \(2011\)](#); (g) [Costa et al., \(2006\)](#); (h) [Bonorino et al., \(2012\)](#); SAM: South American plate; SCO: Scotia Plate. **(b)** Regional geomorphological map of the study area. The red lines refer to the fault scarps with cross-checked evidence of faulting in Pleistocene to Holocene surficial deposits. The red dashed lines show the inferred fault traces from satellite observations after ([Onorato, 2018](#); [Onorato et al., 2020](#); [Torres-Carbonell et al., 2008](#)). Background digital elevation model (DEM) generated from 2018-Pleiades images to topographic map 1 px = 2 m, with MicMac software from IGN French National Geographic Institute, and ENSG French national school for geographic sciences.

III.2 Historical Large Earthquakes

In 1879, the 1st February, several inhabitants and navigators reported a succession of shocks of great magnitude ([Serrano, 1880](#); [Simpson and Chaigneau, 1880](#); [Montessus de Ballore, 1912](#); [Bustos, 1931](#); [Dublé Almeida, 1938](#); [Brüggen, 1943](#); [Martinic, 1988](#); [Bridges and Canclini, 2001](#); [Martinic, 2008](#); [Cisternas and Vera, 2008](#); [Palacios R, 2013](#)). Based on these observations, the intensity was estimated at VII using the Modified Mercalli scale ([Lomnitz, 1970](#)). They is no reliable location, but the collected testimonies define a broad impacted zone from 50° to 54.5°S ([Martinic, 2008](#)).

Along the onshore MFF, the last instrumentally recorded event occurred in 1949. At 6:53 (GMT), on the 17 December, a magnitude Mw 7.75 earthquake struck off, soon followed by a second quake at 15:07 (GMT) of Mw 7.5 and several aftershocks of undetermined magnitude ([Jaschek et al., 1982](#); [Pelayo and Wiens, 1989](#); [Febrer et al., 2000](#)). Despite the attempts to establish the exact quake locations, these epicenters remain unclear. Indeed, substantial uncertainties are expressed ([Jaschek et al., 1982](#); [Adaros et al., 1999](#); [Febrer et al., 2000](#)), and to date, they are located in the region of the Karukinka natural park (Figure 3.1a). These shocks were widely felt across the entire Tierra del Fuego archipelago and in southern Santa Cruz Province ([La Prensa Austral, 1949](#); [Lomnitz, 1970](#); [Isla and Bujalesky, 2004](#); [Perucca et al., 2016](#); [INPRES, 2004](#)).

On the 14 of June 1970, an earthquake of Ms 7 (surface wave magnitude) occurred north of the Strait of Magellan's western arm (Figure 3.1a). A few hours afterward, an earthquake Ms 7.2

was recorded in the Atlantic offshore continuation of the MFF (Figure 3.1a), 54.476°S 64.499°W (Pelayo and Wiens, 1989). According to its size, the surface rupture unlikely reached the central Tierra del Fuego, or eventually, it would have affected the Atlantic coast ~ 150 km from the epicenter (Wells and Coppersmith, 1994).

III.3 Study site

III.3.1 The trench site

Our study area is located 40 km east of the Lake Fagnano. The La Blanca section is the eastern prolongation of the Northern Udaeta Fault, which bonds the active pull-apart basin Udaeta (Onorato et al., 2017). Our trench site (54°33'32.35" S, 66°37'17.32" W) is located 5 km east of the Lake Udaeta in the central part of the La Blanca section (Figure 3.1b). The study region accommodates most of the deformation along a single segment. However, several authors suggested the presence of sub-parallel lineaments east of Udaeta Lake (Torres-Carbonell et al., 2008; Onorato et al., 2020). Authors identified these structures on satellite images, describing them as discontinuous and inferred traces (Figure 3.1b). Due to the limited extension, and the lack of disrupted markers, we consider no or negligible Quaternary deformation accommodated on these sections.

Our study site, located along the main fault scarp, favors a possible long record of faulting in the subsurface. First of all, the site targets a paleo terrace level, whose sediments can record the ruptures since its abandonment. Secondly, the area experienced highly active deformation (Roy et al., 2020) indicated by remarkably preserved linear landform and offset fences attributed to the ultimate earthquake (Figure 3.2a, 3.2b). Finally, the nearby aligned pop-up structures (Roy et al., 2020), two aligned ridges, one pull-apart and several sag ponds (see annexe) show the imprint of the long-term seismic activity of the Magallanes Fagnano Fault in this region. Regarding this tectonic setting, the configuration favors a possible long record of faulting in the subsurface, making this site particularly relevant to the paleoseismic investigation (Burbank and Anderson, 2009).

This site cumulates left-lateral movement, along with a minor shortening component, that had uplifted the southern block relative to the northern block (Figure 3.2c). It had built a

continuous scarp in between them. In the trench site, this elevation gap forms a north-facing slope with moderate steepness of about $\sim 20\text{-}30^\circ$ and 11-m high. The two trenches were excavated perpendicular to the ridge (Figure 3.2 d, e). The excavated fault trace has noticeable surface expressions preserved in the topography. Among them, the surface shows four Riedel fractures labelled A, B, C, and D (Figure 3.2b). The three lowest Riedels (B, C, D) cross the trench n°1, and the Riedel A crosses the trench n°2. Orientation indicates R-shear synthetic fault ranging from $N70\text{-}75^\circ$. In the Riedel, the topography is slightly concave of about 10 -15 cm deep.

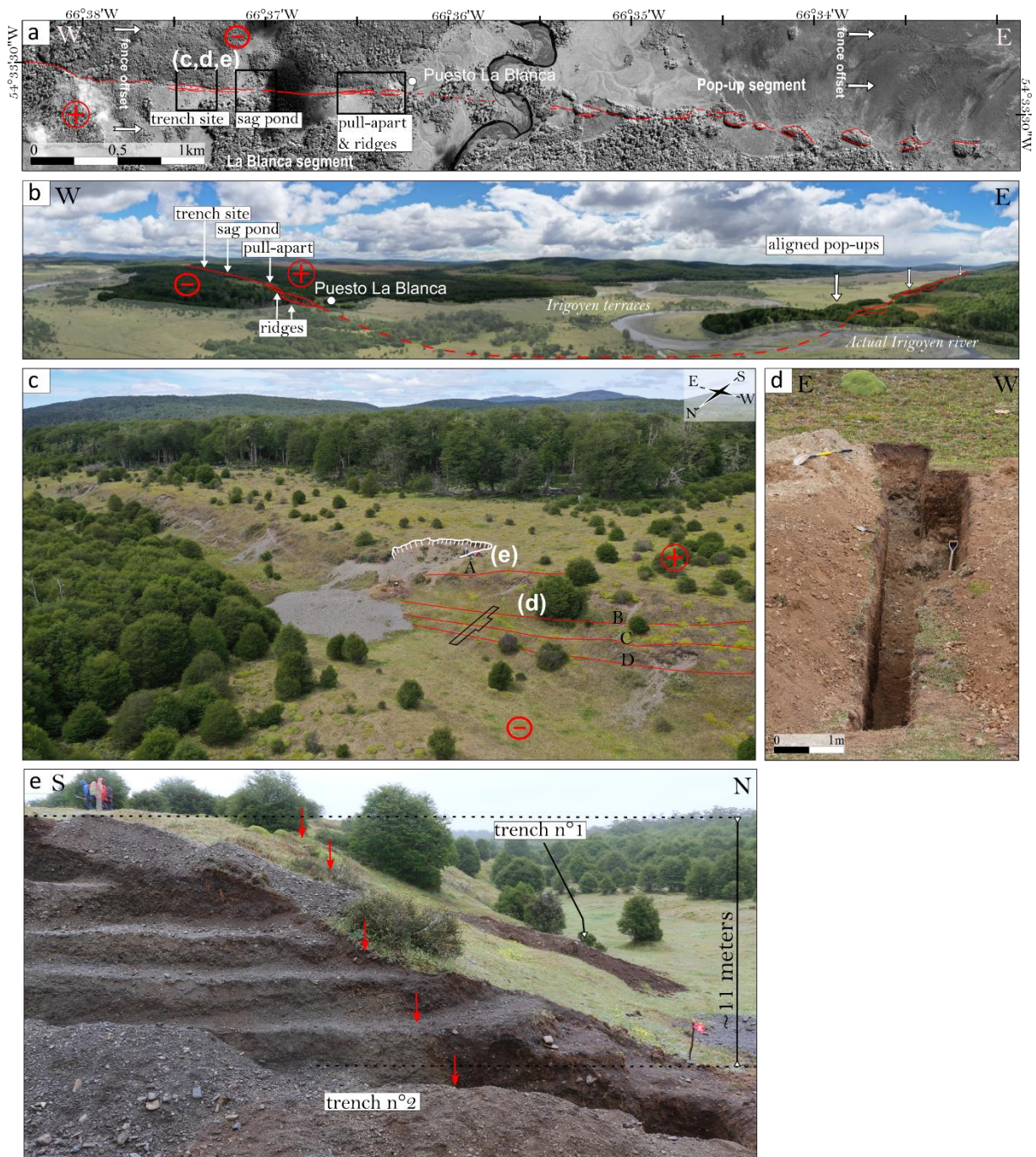


Figure 3.2: (a) Location map with Pleiades image. (b) Aerial photography of the study region. The photograph assemblage may distort the horizon and be responsible for the apparent bending of the fault trace. The red signs pinpoint the relative elevation changes between the blocks. The red lines refer to the fault scarps with evidence of faulting. The red dashed lines show the inferred fault traces with ambiguous faulting morphologies partially eroded by the floodplain. The lightened area indicates the Irigoyen paleo-floodplain and the actual meanders. We locate the near-by pop-up morphology and offset fences from (Roy et al., 2020). (c) Aerial photograph of the trench site. The black polygon marks out the trench n°1 edges. The white line demarcates the natural incision in which the trench n°2 was excavated. The red lines indicate the Riedels. (d) Photograph of the trench n°1. (e) Picture of the trench n°2 with persons for scale on the top of the ridge. The red arrows pinpoint the main fault of this trench FT2.

III.3.2 Methods

We map the fault scarps related to the MFF using Pléiade pictures, aerial photographs from unmanned aerial vehicle (UAV), high-resolution-DEM, and cross-checks these observations in the field. Figure 3.2a shows a synthesis of our observations along the La Blanca fault section.

The trench n°1 is located at mid-high of the scarp, and its northern end reaches the lowest part of the slope (Figure 3.2d). This trench is 9-m long and 1.50 m deep. The trench pattern is a single downslope slot with an additional westward enlargement of 80-cm wide and along 3-m.

The trench n°2 which is 13-m long 4.5-m deep, was dug into a natural incision in the southern block. The incision is associated with a massive colluvium fan that had facilitated the benched excavation of this trench on the upper part of the ridge (Figure 3.2e). A single fault crosses the scarp in the mid-slope dipping sub-vertically. It reinforced the assumption of a considerably localized deformation from the mid-slope to the ridge base. Unfortunately, the lack of datable terrestrial material in this trench does not allow quantitative paleoseismic study.

The trenches were gridded into 1 x 1-m squares. We pinpointed remarkable units and charcoals with flags to enable detailed and scale logging of structures, fault terminations, wedges, and stratigraphy. Each sample was selected in recognized units and originates from single charcoal.

Radiocarbon measurements were made at the Laboratoire de Mesures du Carbon 14 (CEA Saclay). The ages are calibrated using Oxcal version 4.3 (Ramsey, 2009; Ramsey, 2017) with southern hemisphere calibrating curve SHCAL13 (Hogg et al., 2013). The raw ^{14}C ages (yrs BP) and the calibrated ages (cal yrs BP) are available in Table 3.1 and registered online with the International Geo Sample Numbers (IGSN) at System for Earth Sample Registration (SESAR, <http://geosamples.org>).

The paleoseismic analyses are based on field log, macro photographs, high-resolution 3D models of the trench walls, and orthophoto mosaics. We determine the earthquake-related structure age using the radiocarbon ages from the deformed and undeformed layers. Alternatively, we analyze the rupture geometry, the stratigraphy, and the spatial distribution of dated coals to bracket the rupture ages. To correlate the ruptures with surface fault scarp we use the DEM and the 3D-models of trench walls (built with Agisoft PhotoScan).

Sample	N° SacA	IGSN	Nature	Mass spectrometry measurements (ages and error indicated in yrs BP)					Calibrated ages (cal yrs BP)		Unit
				Mg C	Delta C13	pMC	Age	Err	From	To	
C1 [#]	57475	IEROY0001	Charcoal	1,42	-31,30	88,32 ± 0,24	995	30	964	798	b
C2 [#]	57476	IEROY0002	Charcoal	1,26	-29,00	68,35 ± 0,21	3055	30	3 356	3 180	b
C3	57477	IEROY0003	Charcoal	1,07	-28,10	30,88 ± 0,16	9440	40	10 776	10 565	g
C4 [#]	57478	IEROY0004	Charcoal	1,71	-28,70	88,15 ± 0,22	1015	30	979	802	b
C5	57479	IEROY0005	Charcoal	1,55	-24,80	75,99 ± 0,21	2205	30	2 319	2 145	c
C6	57480	IEROY0006	Charcoal	1,67	-29,10	76,71 ± 0,21	2130	30	2 299	2 001	c
C7	57481	IEROY0007	Charcoal	1,41	-24,90	75,97 ± 0,21	2205	30	2 319	2 145	d
C8	57482	IEROY0008	Charcoal	1,56	-22,70	76,50 ± 0,22	2150	30	2 305	2 010	d
C9	57483	IEROY0009	Charcoal	1,32	-30,40	76,88 ± 0,22	2110	30	2 153	1 995	c
C10	57484	IEROY000A	Charcoal	1,51	-28,80	77,01 ± 0,22	2100	30	2 147	1 996	c*
C11	57485	IEROY000B	Charcoal	1,41	-23,90	76,83 ± 0,21	2120	30	2 294	1 999	c*
C12	57486	IEROY000C	Charcoal	1,34	-27,30	75,96 ± 0,21	2210	30	2 320	2 148	c*
C13	57487	IEROY000D	Charcoal	1,38	-26,80	76,74 ± 0,22	2125	30	2 297	2 001	c*
C14	57488	IEROY000E	Charcoal	0,63	-31,90	76,56 ± 0,22	2145	30	2 304	2 007	c
C15	57489	IEROY000F	Charcoal	1,53	-23,70	89,53± 0,23	890	30	910	733	b
C16	57490		Charcoal	0,96	-26,80	106,48 ± 0,25	Date out of range				
C17	57491	IEROY000G	Charcoal	0,29	-20,20	34,54 ± 0,21	8540	50	9 595	9 460	f
C18 [#]	57492	IEROY000H	Charcoal	0,38	-30,60	78,41 ± 0,22	1955	30	1 987	1 827	b
C20	57493			no coal							
C21 [#]	57494	IEROY000I	Charcoal	0,33	-28,50	31,89 ± 0,17	9180	45	10 490	10 240	g
C22 [#]	57495	IEROY000J	Charcoal	0,84	-28,10	31,98 ± 0,16	9160	40	10 478	10 233	g
C23	57499	IEROY000K	Charcoal	0,18	-20,90	36,63 ± 0,24	8070	50	9 130	8 768	f
C24	57500	IEROY000L	Charcoal	0,13	-22,90	45,21 ± 0,29	6380	50	7 424	7 180	f
C25	57501	IEROY000M	Charcoal	1,47	-27,00	76,25 ± 0,21	2180	30	2 310	2 117	c
C26	57502	IEROY000N	Charcoal	1,32	-26,00	76,67 ± 0,22	2135	30	2 300	2 004	c*
C27	57503	IEROY000O	Charcoal	1,34	-20,30	76,63 ± 0,22	2140	30	2 302	2 006	c*
C28	57504	IEROY000P	Charcoal	1,62	-21,00	76,33± 0,21	2170	30	2 309	2 065	c*
C29	57505	IEROY000Q	Charcoal	1,26	-23,10	76,57 ± 0,21	2145	30	2 304	2 007	c*
C30	57506	IEROY000R	Charcoal	0,88	-29,70	75,82 ± 0,22	2225	30	2 329	2 152	c*
C31	57507	IEROY000S	Charcoal	1,39	-22,30	76,68 ± 0,21	2135	30	2 300	2 004	c*

#Radiocarbons out of stratigraphic order

Note: [Measurements made at LMC14, CEA Saclay, France using the accelerator mass spectrometry \(AMS\) ARTEMIS, following preparation protocols \(Dumoulin et al., 2017, Moreau et al. 2013\). Radiocarbon ages are calculated using Mook and Van der Plicht \(1999\).](#)

The ages are calibrated using Oxcal version 4.3 (Bronk Ramsey, C. 2009, Ramsey, C. 2017) with atmospheric curve SHCal13 (Hogg et al., 2013). N°SacA: lab number; IGSN: International Geo Sample Numbers; Mg C: amount of carbon in mg ; Delta ¹³C: percent of isotope ¹³C; pMC: percent Modern Carbon.

Table 3.1:

Mass Spectrometry Measurements of Radiocarbon Samples.

III.4 Paleoseismic investigations

III.4.1 Stratigraphy

We identify 12 stratigraphic units labelled from the youngest unit-a to the oldest unit-j. A grey modern soil horizon labeled 's' caps the whole trench. The oldest exposed units-h, -i, and -j have the same composition but show entirely different structures. Generally, unit-j indicates the aggradation of river channels. Its coarse clasts size, the significant stratification, and the rounded cobbles evidence high energy transportation of material distal from its source. Conversely, the verticalized cobbles in-unit h and unit-i suggest they are reworked unit originating from the unit-j. These units are covered by unit-g, which contains charcoals with a maximum age range from 10 776 to 10 565 cal yrs BP (C₃) (Figure 3.3). The natural incision (trench n°2) exposed identical material to the fluvial unit-j, suggesting the southern block is a paleo-fluviatile terrace which is most probably older than 10 776 cal yrs BP.

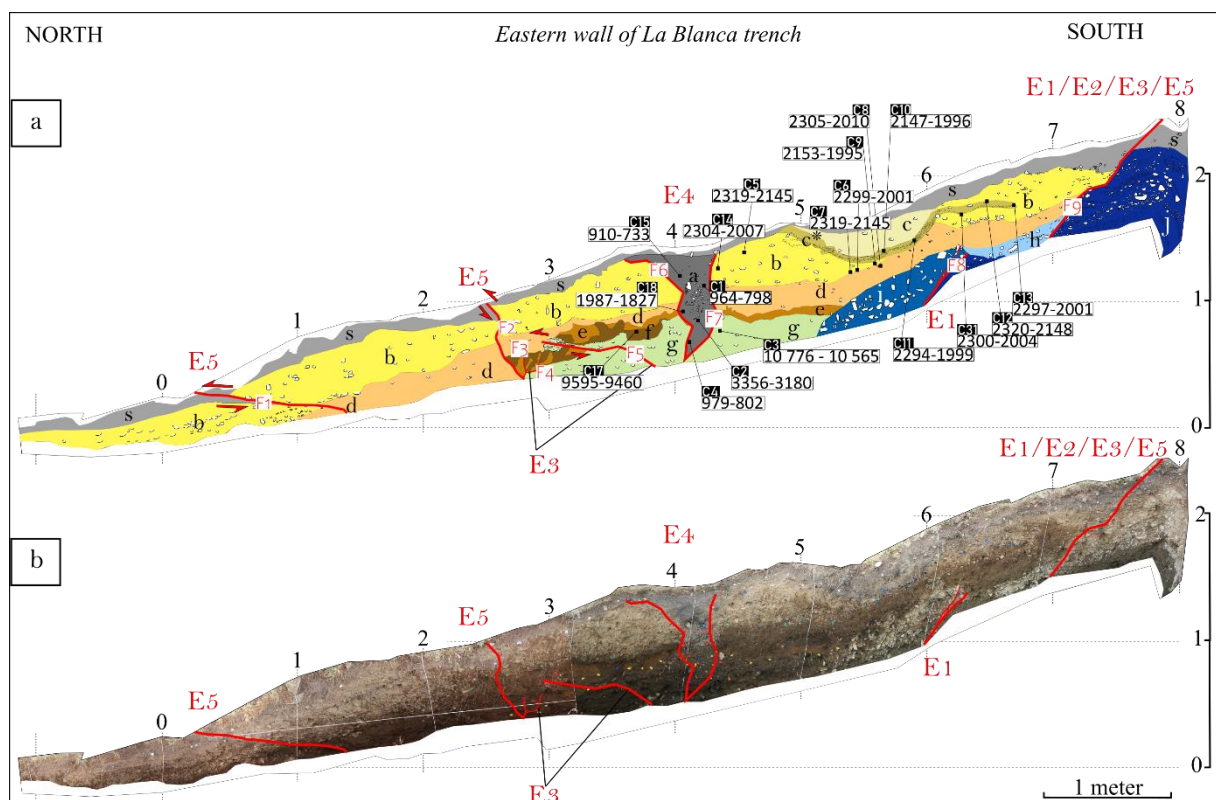


Figure 3.3: (a) Interpretation and (b) photogrammetry mosaic of the eastern wall of the La Blanca trench. Small black rectangles show the locations of radiocarbon samples, labeled by sample numbers and their corresponding calibrated radiocarbon ages (cal yrs BP). Seismic events (E), associated faults (F) and faulting movements (arrows) are shown in red. (See annexe for wider version).

The unit-g, -f and -e makes an angular unconformity with lateral onlaps on to unit-i which suggest an erosive phase before unit-g (Figures 3.3 and 3.4). The above units-e and -f are rich in silt and clay comparatively to the whole sequence. A change in environment transportation necessarily occurred post-unit-g and before unit-d to enable these fine sediments to settle down. Additionally, these two layers mark out the last water-transported alluvium materials. Indeed, the above material structure suggests a gravity-transportation. This environmental change is poorly constrained by radiocarbon ages and might have taken place after the deposition of unit-f ~7 424-7 180 cal yrs BP (C24) and previous to unit-d 2 319-2 145 cal yrs BP (C7).

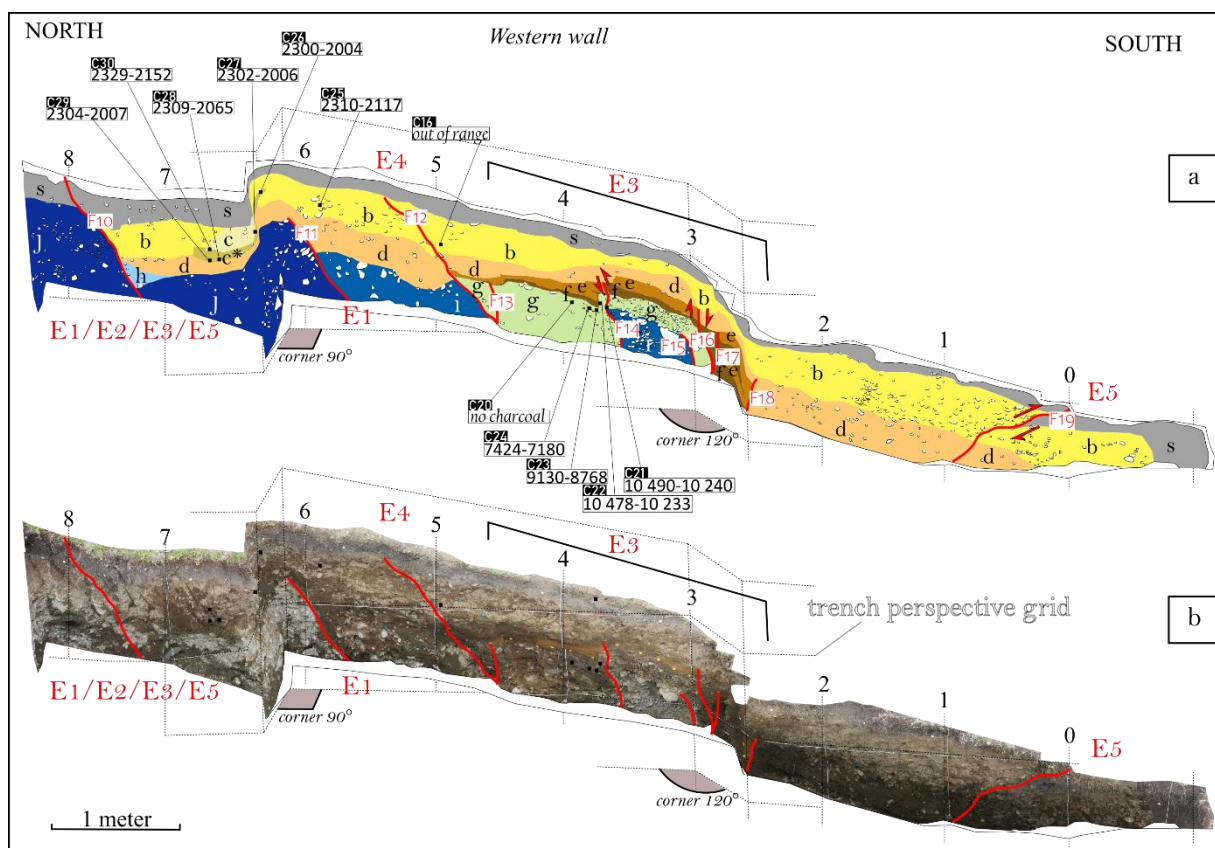


Figure 3.4: (a) Interpretation and (b) photogrammetry mosaic of the west wall of the La Blanca trench. The western trench wall is not flat, the perspective of the cutting is shown with dashed line grid and angles indicated in degree. (See annexe for wider version).

The lower unit-d age is poorly constrained because most of the charcoals are located in the upper unit-d or in the unit-c and -c* (Figure 3.3 and 3.4). Unit c* is very rich in thick charcoal and has a concave-shape recognizable on both side. According to the average age of the charcoals, it suggests a local fire event that took place ~ 2 ka. The oldest and the youngest radiocarbons of the unit-d, -c and -c* indicates a maximum age of ~2319-2145 (C7), and a minimum age of ~2153-1995 (C9) (Figure 3.4). In addition, the radiocarbons sampled in the upper unit-c (C5, C14) are in agreement with this age range. The whole sequence and the ages of various units have been constrained through ¹⁴C analyses and are summarized in Figure 3.5.

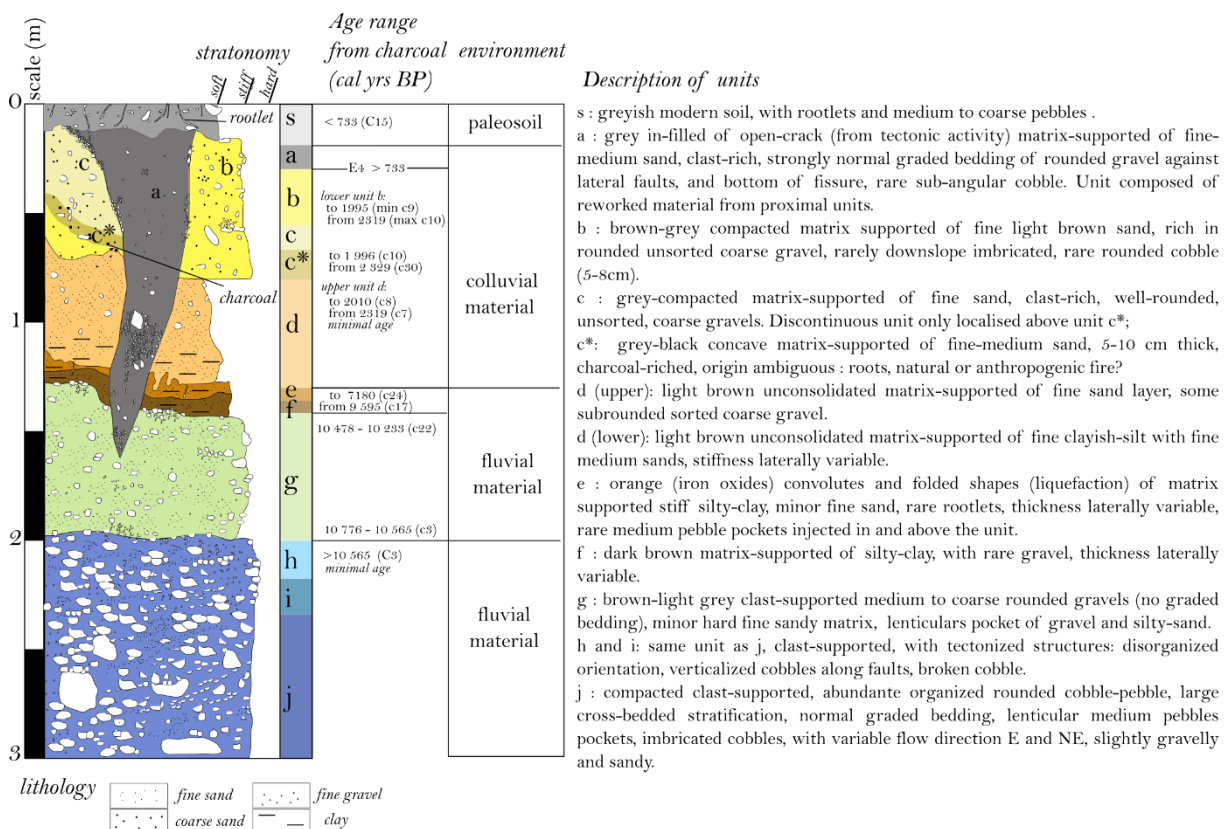


Figure 3.5: Synthetic log, associated faciès and environments of the La Blanca trench. Only unit j is shown in the log as the unit h and i are colluvial wedges originally from unit j. The unit j evidences the pristine structure of the floodplain and/or point bar deposits. We use the modified Udden–Wentworth grain-size scale (Blair and McPherson, 1999).

III.4.2 Reconstruction of paleoearthquake chronology

The disrupted structures are exposed on both walls of the trench n°1. Most of the faults are paired with their equivalent geometry on the opposite wall. The trench exposes nineteen ruptures truncating partially or entirely the section. They are grouped and interpreted in 5 seismic events. Figure 3.6 shows the chronological reconstruction of the tectonic and sedimentary episodes in this trench. The initial context is shown in stage A, and the actual state of the La Blanca trench is shown in stage H.

The faults F8, F9 on the east wall, and its counterparts F10 and F11 on the west wall cross-cut the fluvial unit-j. F8 is the downward extension of F9, like F11 is the extension of F10. This oldest event E1 is associated with the collapse of a first colluvial wedge (unit-i). A relatively younger event E2 might have reactivated the fault F9 and F10 and buried the unit-i under a secondary colluvial wedge (unit-h). Moreover, F8 and F9 are horizontally shifted downslope over 80 cm, as well as their counterparts F10 and F11 of ~1 m, which indicates a substantial amount of extension during the rupture E2. The multiple verticalized cobbles leaning against these faults and the disorganized structures confirm their tectonic origin. These two oldest events might have hit the Isla Grande de Tierra del Fuego before 10 776 cal yrs BP.

The third event E3 has markedly slashed both walls with numerous faults. This rupture is associated with multiple faults F3, F4, F5 in the eastern wall, and F13 to F18 on the other side. On the southern tips of the two walls, the unit-d forms a small wedge in which the clasts are disorganized with variable orientations. We suggest it corresponds to a colluvial wedge resulting from the re-activation of F9 and F10 during E3. On both walls, we log the cuts, the folds, and the irregular thickness of the dark brown unit-e, adjoining with the above flame-like structures of unit-f (Figure 3.7a). These two deformed horizons are richer in clay and silt than other units and are prone to liquefaction phenomenon. We recognize these convoluted features (Figure 3.7ab) as seismically-induced soft-sediment deformations structures (SSDS). These SSDS are typical water-escape structures due to shaking and subsequent liquefaction from the soft sediment horizon (Ojala et al., 2019). On the western wall, we notice that F14 and F15 are associated with a vertical uplift of 20-cm of the lower unit-g and possibly unit-i. It might indicate a slight reverse component associated with event E3.

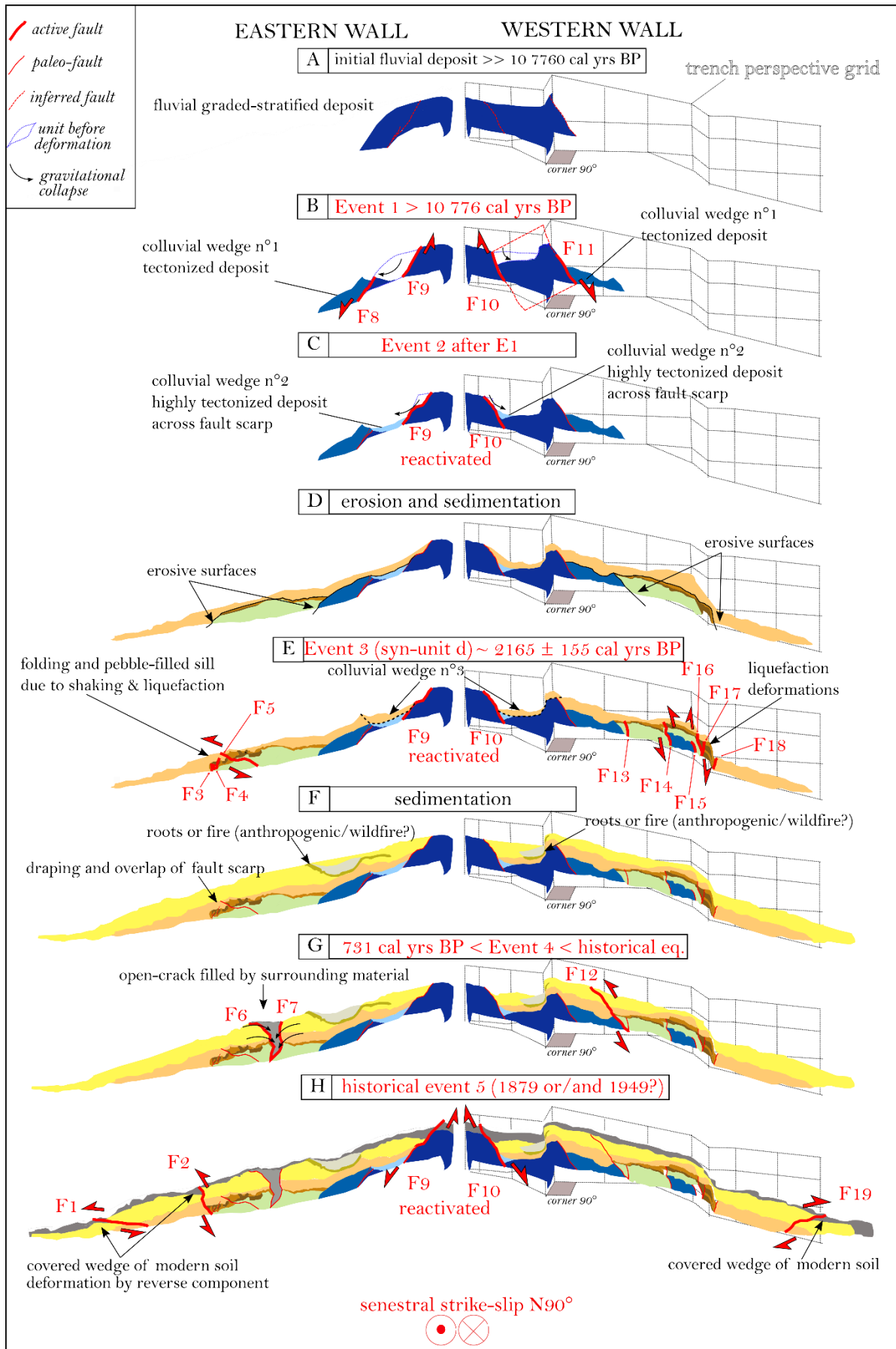


Figure 3.6: Reconstruction of tectonic activity recorded by deposits in the La Blanca trench and description of stratigraphic indices of faulting. Tectonic events and faults numbering are written in red.

Specific attention is drawn to the fault F₅ rooted in unit-g. Injection of medium pebbles along the fault F₅ crosses the unit-e and -f and deformed the unit-d (Figure 3.7c). The pebble orientations follow the upward movement in what appears as a sub-horizontal clastic-sill. The termination of the sill is a centimetric pebble-filled bowl-shaped intrusion. This clast-material is allochthonous, and may probably originate from unit-g at a distance of 1 meter from its present position. Interestingly, the SSDS drapes the pebble injection and follows the same convoluted shapes, indicating these two phenomena are coeval. The overlying undisrupted unit-b post-dates the intrusion. Consequently, the rupture might have taken place syn-deposition of unit-d. The age of the upper part of unit-d is constrained by the C₇/C₈ charcoals; therefore, it advocates an age from 2319 (C₇) to 2010 (C₈) cal yrs BP (Figure 3.6). Previous evidences of SSDS, convolute laminations, load structures and clastic dykes are exposed in the nearby Southern Udaeta section (Onorato et al., 2016), and along the Lake Fagnano (Onorato, 2018). These seismites did not affect the modern soil, suggesting they are older than the two historical earthquakes. Unfortunately, these structures are not timely-constrained, which prevent to corroborate them to any of our events.

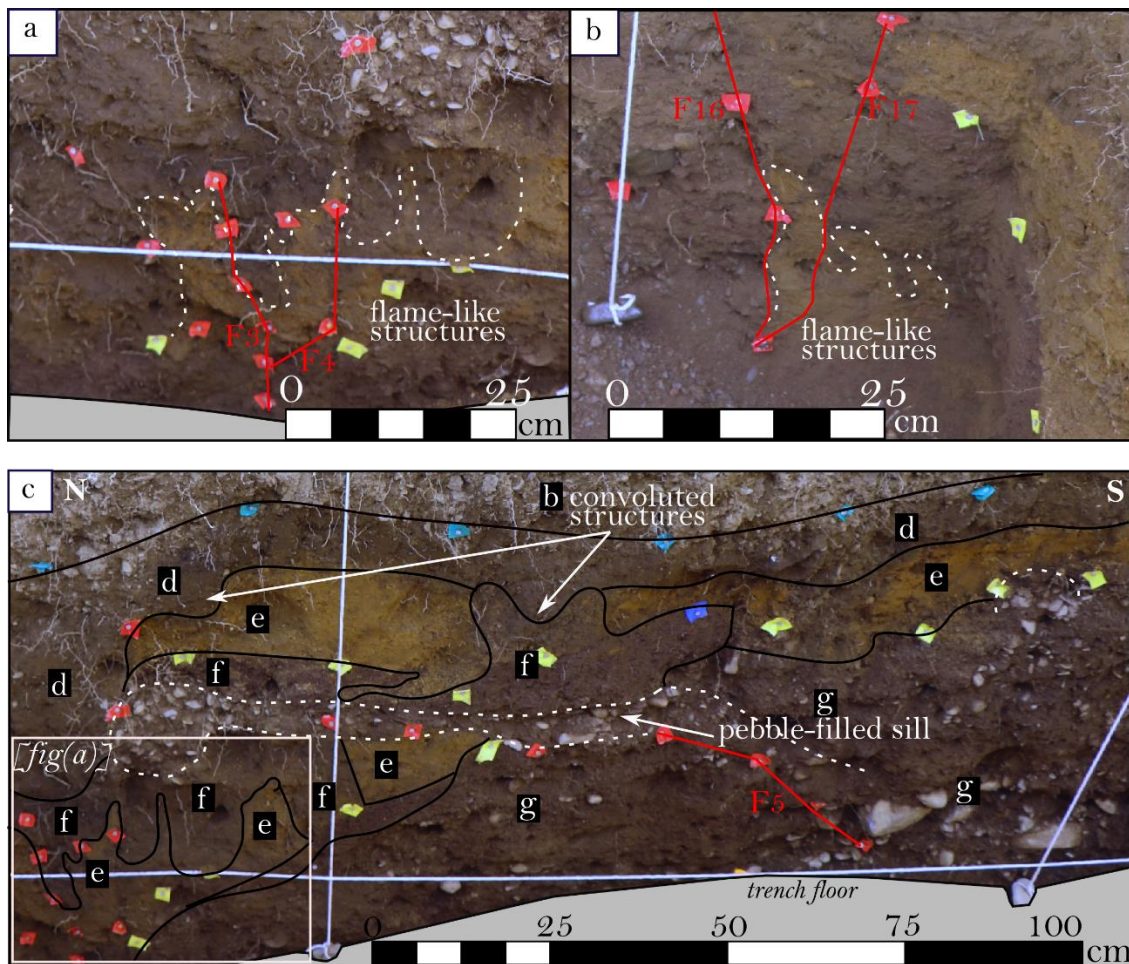


Figure 3.7: (a) Flame-like structure within the unit-e from the eastern trench wall. (b) Same features in the western wall. (c) Sub-horizontal pebble-filled sill from the eastern trench wall. Black rectangle letters refer to units. Note the lower unit d is deformed by the convolutes and the sill.

The following event E₄ produced the opening of a 70-cm wide and 1.30-m deep crack (unit-a) outlined by the faults F₆ and F₇. The charcoals ages and the disorganized structure suggest the open-crack was filled by the surrounding material at the time of the rupture. Large cobbles and smaller pebbles might have fallen first inside the fissure (Figure 3.3). Then the fining-up graded bedding against the inner fault sidewall is a characteristic feature of a sudden gravitational collapse. Three young charcoals from 979 up to 733 cal yrs BP are buried under very different depth from 0.3 m up to 1.20 m, supporting the chaotic nature of the deposit. The small soil deposit above the fissure remains undamaged and exposes pristine modern soil structure with rootlets and horizontal pebbles (Figure 3.3, see annexe for zoom-in). On the west wall, this event appears to be related to fault F₁₂ since the modern soil cap remains undamaged (Figure 3.4). The

rupture E₄ implies a vertical slip of about 10-20 cm along fault F₁₂, which had offset unit -g, -e, -f, -d and -b. Since the modern soil is not disrupted, the earthquake E₄ might have occurred before the last two historical earthquakes (1879 AD and 1949 AD) (Figure 3.6). We highlight three arguments in favour of constraining the event E₄ with the charcoal C₁₅: (1) The charcoal C₁₅ is located on the highest part of the stratigraphic filling; (2) Very few materials overlie the charcoal C₁₅, which suggests it is the youngest age of the material; (3) The presence of two additional charcoals (C₁, C₄) of almost the same age in various depths suggests this material was the most available unit by the time of the rupture, i.e., most available at the surface. On the other hand, this material could have been already available since a certain amount of time before the event and remobilized during event E₄. Thus one interpretation is that the youngest charcoal age represents the maximum paleoearthquake age of E₄ ≥ 910-733 cal yrs BP.

Lastly, the youngest rupture geometry E₅ is exposed symmetrically on both walls and impacts the entire ridge width. At the toe of the scarp, several reverse faults disrupt the entire section (F₁, F₂, F₁₉) and buried modern soil wedges. Along F₁ and F₁₉ a very small amount of sub-horizontal slip is measured ~ 5-10 cm. Along the sub-vertical reverse fault F₂, the downthrown side was dragged down of around 25 cm. The modern soil is clearly truncated also along the fault F₉ and F₁₀, which might have been re-activated (Figure 3.6). Furthermore, in the trench n°2, the fault FT₂ disrupts the surface and damages the modern soil (Figure 3.2e). In trenches, the geometries of the faults are consistent with what is observed in the surface morphology. The Riedels A, B, C, and D, crosscut the trench n°1 and n°2, and correspond respectively to the main fault FT₂ in trench n°2, and to the pair of faults F₉/F₁₀ (not apparent on western wall) and F₁/F₁₉ in trench n°1. Also, they are well-preserved on the topography which implies necessarily that they are relatively young morphologies. Accordingly, the event E₅ might be referred to the historical earthquakes in 1879 AD and/or 1949 AD.

To sum-up, the paleoseismic investigations in La Blanca section evidences five events (Figure 3.8) including the historical earthquakes 1879 and/or 1949. The two oldest events E₁ and E₂ are older than 10 776 cal yrs BP. The third event E₃ might have taken place between 2319 to 2010 cal yrs BP. The following rupture E₄ might have disrupted the La Blanca section after 910-733 cal yrs BP and before the historical earthquakes.

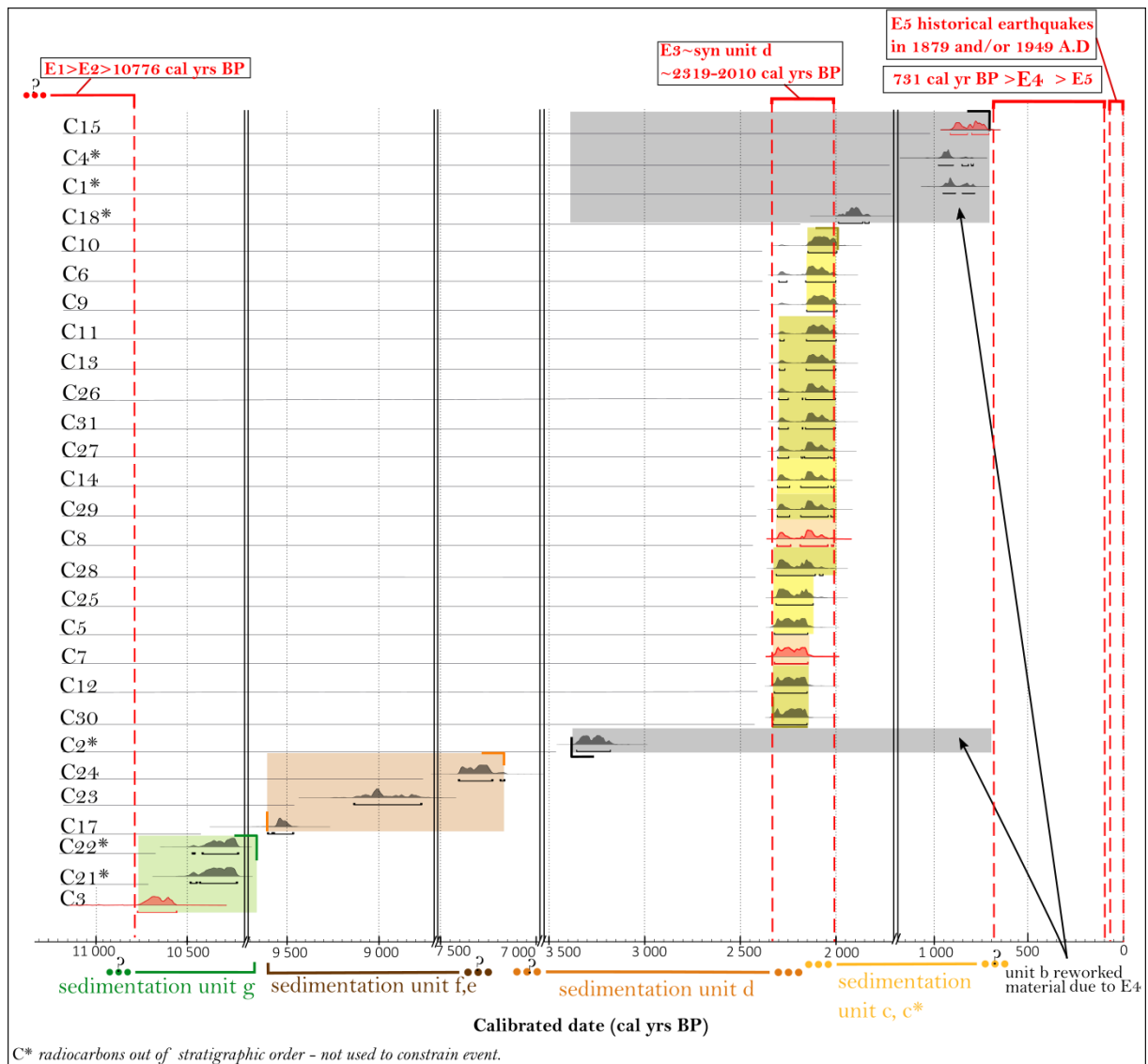


Figure 3.8: Histograms of ages model for samples in this study (the higher the histogram the more likely that age is). The rupture events are shown with red dashed lines. The possible age of the event is determined from the radiocarbon ages with red histograms. Age model are calculated for charcoals using OxCal v4.3.2 (Ramsey, 2009) and the Southern Hemisphere calibration curve SHCal13 (Hogg et al., 2013). Under the histogram, the black bars indicate the age range reported in table 3.1. Colored zones indicates the unit at which the charcoal belongs to. The ages of the units have been constrained through the youngest and the oldest charcoal ages belonging to the unit. Time is shown in calendar years before present (present refers to 1950). The double black bars in timescale are shorten time-cuts.

III.5 Discussion

III.5.1 Correlation with paleoearthquakes records

Comparing rupture histories in different areas several kilometers apart enable us to correlate the regional imprint of significant paleoearthquakes. We correlate our results in the La Blanca trenches with the paleoseismic investigations (Figure 3.9a) in the San Pablo section (Costa et al., 2006) and the chronology of mass-wasting events in Lake Fagnano (Figure 3.9b) associated with major paleoearthquakes in the Tierra del Fuego (Waldmann et al., 2011).

Costa et al. (2006) identified four seismic events in a trench excavated 24-km west of our study site. For comparison, we formulate its ages in cal yrs BP after recalibration using the calibration curve (SHCAL13). To avoid confusion in the rupture numbering, we label the events from Costa et al., (2006) Ea to Ed (oldest to youngest).

Waldmann et al. (2011) identified nineteen megaturbidites within the cores from Fagnano eastern sub-basin (Figure 3.9b). The dated buried materials should be treated as maximum ages for their corresponding unit. Indeed, slope destabilization can remobilize terrestrial material within the mass-wasting deposit, and dated material might be older than the seismic event. Using terrestrial materials and mass-wasting deposit thicknesses, the authors proposed an age model of sedimentation rate during Holocene and estimated the event chronology. Interestingly, in 2011, the authors preferentially used a constant sedimentation rate (Waldmann et al., 2011) even though substantial rate changes are expected resulting from the Holocene Fuegian glaciers retreat (Coronato et al., 2009; Waldmann et al., 2010). Consequently, this method extensively rejuvenated the rupture ages previously proposed by Waldmann in (2008).

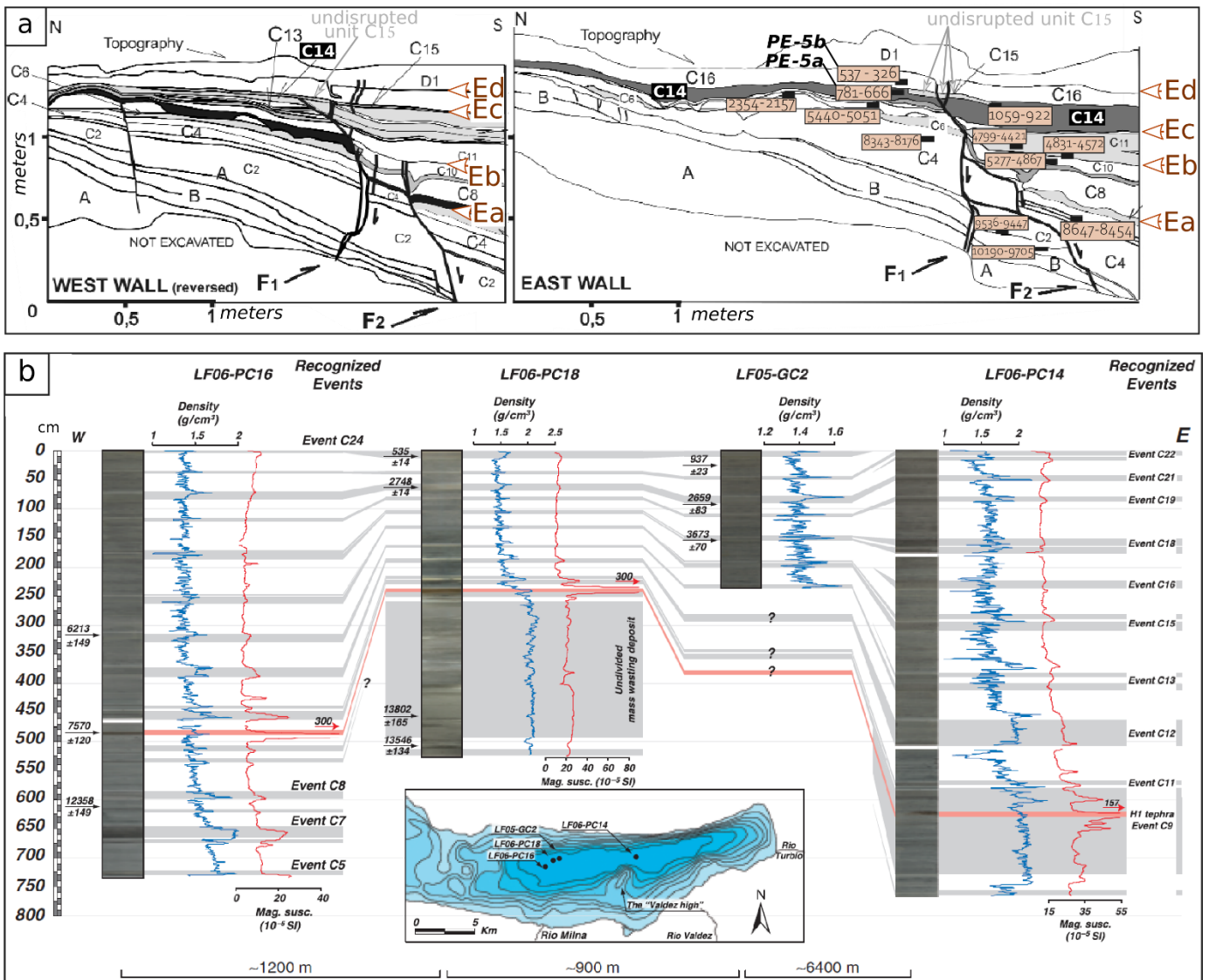


Figure 3.9 (a) San Pablo Trench from Costa et al. 2006. Sample locations are show with black rectangles, and radiocarbon ages are recalibrated using SHcal13 (Oxcal version 4.3). (b) Mass-wasting events stratigraphy (grey shade) and correlation among sedimentary cores, from Waldmann et al. 2003. Radiocarbon dating samples (macro terrestrial, pollen, wood and tephra) are shown with black arrow.

III.5.1.1 The two-historical earthquakes (E5)

The region was stroke by the last historical earthquakes, the 1 February 1879 and/or the 17 December 1949. The brief period between the two historical ruptures unable to discriminate the events with paleoseismic investigations. Nevertheless, south of the Lake Udaeta and only 6-km from our trench site, the work of Pedrera et al., (2014) shows the impacts of the two recent

earthquakes in the tree-rings. Therefore, it is more likely that the youngest rupture geometries observed in the La Blanca trench are resulting from the two last earthquakes.

III.5.1.2 The penultimate earthquake pre-1879 (E₄)

We show that one rupture had opened a wide fissure filled with material of same age (unit a). The three charcoals in the fissure have ages ~ 910-733 cal yrs BP, and are widely distributed over the fissure depth. This age is therefore a maximum age for the event E₄.

Costa et al. (2006) used the ages (PE-5a, PE-5b) of a disrupted unit and a modern peat bog to constrain this event (E_c, in Figure 3.9a). It is worth noting an undamaged layer, unit C₁₅ located under the dated peat deposit, that suggests this paleoearthquake might be older than previously proposed (Costa et al., 2006). The authors showed the fault termination disrupted a unit called C₁₄, dated from 1 059-922 cal yrs BP to 781-666 cal yrs BP. However, it remains unclear where the fault termination stops due to the severe asymmetry of the stratigraphy (Figure 3.9a). Importantly, the authors identified this event in the west wall, but collected the constraining radiocarbons in the east wall which lacks of clear evidence of this event. The interpretation is therefore delicate, and this rupture could have occurred during the layering of unit C₁₄.

The sedimentary core LF05-GC2 (Waldmann et al., 2011) show a thick megaturbidite layer located right below dated pollen at ~937±23 cal yrs BP (Figure 3.9b), which should be used as a maximum age for this event.

Based on our maximum age of the open-crack in the La Blanca section and considering the minimum age of unit C₁₄ in the trench of San Pablo, we proposed to bracket E₄ after 910-733 cal yrs BP and before 781-666 cal yrs BP, being 788±122 cal yrs BP (Figure 3.10).

III.5.1.3 Third Youngest paleoearthquake (E₃)

We identify the event E₃ ~2164 ± 155 cal yrs BP, that can be correlated to the mass-wasting event C₂₁ associated with the third youngest paleoearthquake recorded (Waldmann, 2008; Waldmann et al., 2011) (Figure 3.10). The thick megaturbidites of event C₂₁ has recovered two radiocarbons of ~2 762-2 734 cal yrs BP and 2 742-2 576yr BP (Figure 3.9b). These radiocarbon

ages are maximum ages, pre-dating the E₃ paleo-rupture, and are consistent with our result of one event E₃ that occurred post-2700 BP.

III.5.1.4 Isolated Events (E₂) and (E₁)

We evidence E₂ and E₁ events, which are earthquakes before $10\,670 \pm 106$ cal yrs BP, but that are not correlated to another record yet. These events are not identified in Costa et al., (2006) study, whose trench investigation took place on a secondary trace, and implied part of the deformation was possibly lacking. Two additional isolated events (E_a, E_b) were previously recognized in the San Pablo Trench (Costa et al., 2006). E_a and E_b are ruptures confirmed by direct and unambiguous geometries but not recognized in our trench. Isolated events do not account for smaller temblors. Indeed, it is common for strike-slip faults to splay into several branches as they reach the surface, sometimes tens or hundreds of meters apart (Burbank and Anderson, 2009).

III.5.1.5 Paleo-earthquake chronology

Our results precise the timing of the last three major paleo-earthquakes E₅, E₄, E₃. The chronology includes additional events E₂, E₁ and previously described ruptures E_a and E_b, which are reported respectively to 6697 ± 1646 cal yrs BP, and 4924 ± 353 cal yrs BP (Figure 3.10).

We compare the chronology with the mass-wasting events from the Lake Fagnano before and after rejuvenation (Waldmann, 2008; Waldmann et al., 2011). We highlight the seven thickest events which may represent the major paleoearthquakes, and that are supported by dated units bracketing the ages. For these reasons, we proposed the corrected chronology for the most recent earthquakes in Eastern Tierra del Fuego shown on Figure 3.10.

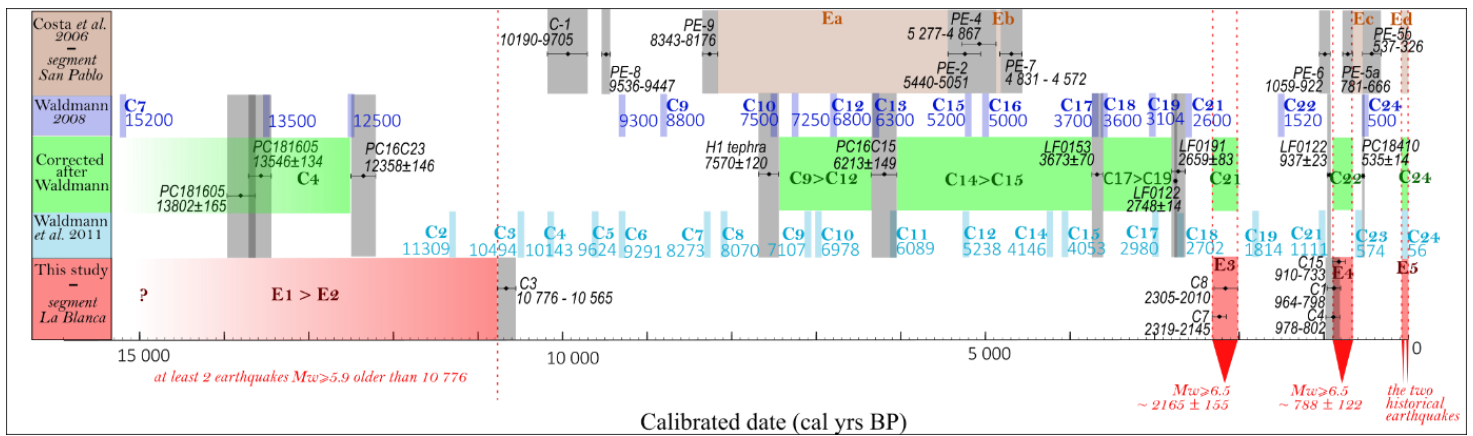


Figure 3.10: Correlation of the paleoearthquakes during the late Holocene in eastern Tierra del Fuego. Colors bars show the reported events according to several studies. Costa et al. (2006) refer to earthquakes constrained by paleoseismological trench at San Pablo section; Events from Waldmann et al. (2008) and (2011) indicate significant mass-wasting deposits in the eastern sub-basin of Lake Fagnano. Note in these studies (1) in 2008 the study is based on a model age with variable sedimentation rates over time; (2) in 2011, the study takes into consideration the Hudson H1 tephra radiocarbon ages and a fixed background sedimentation rate of 0.54 mm/yr which had rejuvenated the mass-wasting events; (3) Associated errors of the event are not available. Black bars and black diamonds indicate radiocarbon ages. We recalibrate the radiocarbon ages from Costa et al. (2006) using OxCal v4.3.2 and calibration curve SHCal13. Time is in calendar years before the present (present refers to 1950).

III.5.2 Earthquake recurrence

Our results are compatible with the previous chronology of mass-wasting events (Waldmann et al., 2011), only if it is assumed that the Lake Fagnano underwent a variable sedimentation rate during the Holocene (Waldmann, 2008). The paleoseismic investigations in Tierra del Fuego, including ours, present multiple evidences of the three major events occurring in the last two thousand years (Figure 3.10). Our data determined a recurrence interval of ~1000 yrs in the Late Holocene that agrees with previous estimates (Waldmann et al., 2011). Furthermore, this recurrence interval is consistent with the number of high magnitude earthquakes required to lead

geomorphic slip-rates of 6.4 ± 0.9 mm/yr up to 7.8 ± 1.3 mm/yr along the study area (Roy et al., 2020; Sandoval and De Pascale, 2020).

III.5.3 Paleoearthquake magnitudes

Our results evidence five seismic events with clear faulting imprinted at surface and subsurface. Such events may account for one or several events cluster in time. In the case of two overlapping earthquakes in less than a century, it is hardly possible to distinguish them in a paleoseismic trench. For instance, in our trench, the two major earthquakes of 1879 and the 1949 events appear as one single event (E5).

However, as we previously estimated both the average recurrence interval (~ 1000 yrs) and the Holocene minimal slip-rate (~ 6.4 mm/yr) (Roy et al. 2020), it requires on average 6.4 meters of slip per event. Thereby, using Wells & Coppersmith's scaling relations, the associated paleoearthquake magnitudes reveal to be equivalent to earthquakes of around $M_w 7.6$ (Wells and Coppersmith, 1994).

In addition, the Lake Fagnano mass-flow event archive does not pinpoint the extent of the paleoearthquake surface ruptures, and it only indicates the associated slope destabilization. The authors suggest a magnitude of $M_w \geq 7$ is required to generate such megaturbites and dominate the shallow sedimentary record (Waldmann et al., 2011), which would agree with our estimation.

III.5.4 Conclusion

Our work strengthens the knowledge of the paleoearthquakes in Tierra del Fuego. We summarize the results from this study in the following points:

The stratigraphic sequence recorded five earthquakes constrained by AMS ^{14}C dating: E5 at 1949 and/or 1879 AD, E4 at $\sim 788 \pm 122$ cal yrs BP, E3 at $\sim 2165 \pm 155$ cal yrs BP and two events E2, E1 older than 10 776 cal yrs BP. The three youngest events suggest a recurrence interval of 1000 yrs for major earthquakes along the Magallanes-Fagnano strike-slip fault.

Our study puts in evidence one more event in the last ~2 ka in comparison with Costa et al. (2006), and allows to better constrain the earthquake ages for the Lake Fagnano record in Waldmann et al (2011).

The event E₃ ~ 2165 ± 155 cal yrs BP is associated with soft-sediment deformation structures. The recognition of the seismites in the La Blanca trench demonstrates the fluvial material is prone to liquefaction. We highlight the necessity of absolute dating of that secondary paleoseismic evidences, which are widely outcropping in Tierra del Fuego (Borrello, 1962; Schmitt, 1991; Ghiglione, 2002; Perucca and Bastias, 2008; Onorato et al., 2016; Onorato, 2018). Marine mass-wasting archives and new paleoseismological records in the Magallanes Regions could yield efficient Holocene rupture cross-correlation across southernmost Patagonia.

Acknowledgments

This work is part of the Ph.D. thesis of Sandrine Roy funded by the French Ministry of Higher Education and Research. The Labex@OSUG2020 (Sandrine Roy) and the French CNRS-INSU (Christian Sue - project PICS and SYSTER) provided additional supports. ¹⁴C ages were measured by the Plateforme Nationale LMC14 (LSCE (CNRS-CEA-UVSQ)-IRD-IRSN-MC) Service National de l'INSU. We would like to kindly acknowledge Cristian Maure and Marina Baudduco from Ushuaia for their hospitality and direct support in the field. This research is part of a new bilateral scientific cooperation project between Universidad de Tierra del Fuego (Ushuaia) and the University Savoie Mont-Blanc (ISTerre). We are grateful to Mónica P. Escayola and Dr. Daniel A. Fernández (CONICET, Instituto de Ciencias Polares, Ambiente y Recursos Naturales-ICPA, Universidad Nacional de Tierra del Fuego) for the discussions and the logistical help in Tierra del Fuego. We warmly thank Fabien Massot for his precious and unswerving administrative support.



Fuegos de la Tierra Selk'nam

Painting generously shared by Elby

Pinturas de propiedad intelectual
Pertenciente a la artista visual Elby
Huerta - Chile Santiago; Uso exclusivo
para tesis, derechos reservados de la
autora.

Copyright © Elby Huerta

Chapter IV: Paleoseismology and dendroseismology applied on the active western Magallanes-Fagnano Fault, Chile

Sandrine Roy^{1*}, Riccardo Vassallo¹, Laurent Astrade², Joseph Martinod¹, Christian Sue^{1,3}, Pablo Morales Vasquez⁴

¹ ISTerre, Univ. Grenoble Alpes, Univ. Savoie Mont Blanc, CNRS, IRD, IFSTTAR, 38000 Grenoble, France

² Laboratoire EDYTEM – Univ. Savoie Mont Blanc, CNRS – Campus scientifique, 73376 Le-Bourget-du-Lac, France

³ Université Bourgogne Franche-Comté, CNRS UMR6249, Besançon, France

⁴ Universidad de Concepción, Chile

* Corresponding author: Sandrine Roy, Institute of Earth Sciences ISTerre
Université Savoie Mont Blanc 73376 Le Bourget-du-Lac
M|+336 37 37 03 17 E| sandrine.roy@univ-savoie.fr

Key Points

- Tree-rings analysis shows 1879 and 1949 Mw>7 earthquakes in Ainsworth Peninsula, Chile.
- Primary evidence of post-LGM deviated drainages of 315 ± 15 m in Almirantazgo Sound, Chile.
- Fast western Magallanes-Fagnano strike-slip fault up of 19.5 ± 4.2 mm/yr.

Abstract

We present results of extensive field surveys, paleoseismological trenching, ^{10}Be dating, and dendroseismology study that investigate the western Magallanes-Fagnano Fault at the foothill of the Darwin Cordillera. We review and map the remarkable terrestrial record of strike-slip in the Chilean territory. In the south of Almirantazgo Sound, we identify multiple deviated postglacial drainages in the remote Peninsula Ainsworth. Using high-resolution Pléiade imagery, we propose their back-slip restoration and determine a maximum sinistral offset of 315 ± 15 m. Based on our ^{10}Be dating, we find that the Peninsula irreversibly deglaciated $\sim 16.7 \pm 2.8$ ka BP. Combining glacial and tectonic cross-cut relations and trench investigation, we suggest the sinistral displacement began to cumulate after the last glacial maximum, which implies a post-LGM slip-rate of 19.5 ± 4.2 mm/yr. Based on primary faulting evidences we characterize the Quaternary and the modern activity of the western MFF. Old *Nothofagus Pumilio* trees growing on the Ainsworth section recorded the effects of two major earthquakes in 1879 and 1949 in their annual ring-width patterns. Our results and previous paleoseismic data in Tierra de Fuego demonstrate the 17 December 1949 Mw7.5 earthquake's rupture length exceeded 200 km.

Keywords: Andes, Strike-slip, Dendroseismology, Ruptures, Glacial retreat, Cordillera Darwin.

IV.1 Introduction

In the southernmost Andes, the glacial and tectonic imprints are tightly intertwined. The Magallanes-Fagnano strike-slip Fault (MFF) is located in a tectonically complex region, where the South American, Scotia, and Antarctic plates meet. Global Positioning System (GPS) measurements, concentrated on the Argentinian Tierra Del Fuego, provide a relative South American - Scotia plates motion of 6.6 ± 1.3 mm/yr with a near-vertical fault locked at 15 km depth (Smalley *et al.*, 2003). In western Tierra del Fuego, and in the Magallanes fjords, sites are extremely remote, and mostly recovered with saturated unconsolidated glacial deposits or peat, which considerably limits geodetic studies and Interferometric synthetic aperture radar monitoring (InSAR). Scarce GPS-network does not allow to constrain the motion in Chile, and fails to resolve second-order deformation associated to the MFF curvature (Smalley *et al.*, 2003; Mendoza *et al.*, 2011; Mendoza *et al.*, 2015).

The major MFF intersects the Chile Trench at $51^{\circ}30'S$, and bends along the Patagonian Orocline, crossing the Fuegian Batholith. The main MFF structures change from a NW-SE trend in southern Patagonia to a W-E in Tierra del Fuego (Figure 4.1). In the Magallanes regions, numerous fjords and seaways follow the strike-slip lineaments and ice-carved valleys. During the Last Glacial Maximum (LGM), the multiple massive ice-lobes originating from the Darwin Cordillera reached the Strait of Magellan up to $52^{\circ}45'S$ (Caldenius, 1932) (Figure 4.1). Studies from erratic boulder fields and lateral moraine systems evidence five stages of retreat from A to E, i.e., outer to inner with respect to the Andes (Clapperton *et al.*, 1995; McCulloch and Bentley, 1998; Bentley *et al.*, 2005; McCulloch *et al.*, 2005; Sugden *et al.*, 2005). Stage B (MIS 2) represents the local LGM, which appeared less extensive than the pre-LGM limit A (MIS 4) (Peltier *et al.*, 2016). Last glacial-interglacial transition timing from Marine Oxygen Isotope (MIS) 4 to 2 remains under debates in Southern Patagonia. Considering the large uncertainties of stage A cosmogenic depth-profiles dating (Darvill *et al.*, 2015b), this limit could have been deposited during a late MIS 3 glaciation and more likely prior (Soteres *et al.*, 2020). In the Strait of Magellan, the LGM onset sometimes after 31,2 ka BP and culminated at c. 25,2–23,1 ka BP (Clapperton *et al.*, 1995; McCulloch *et al.*, 2005; Kaplan *et al.*, 2008; Rabassa, 2011). Marine and terrestrial sediment cores from Almirantazgo Sound indicates a rapid, irreversible retreat in the Cordillera between 17 to 15.5 ka (Boyd *et al.*, 2008; Hall *et al.*, 2013; Fernández *et al.*, 2017; Hall *et al.*, 2017; Hall *et al.*, 2019).

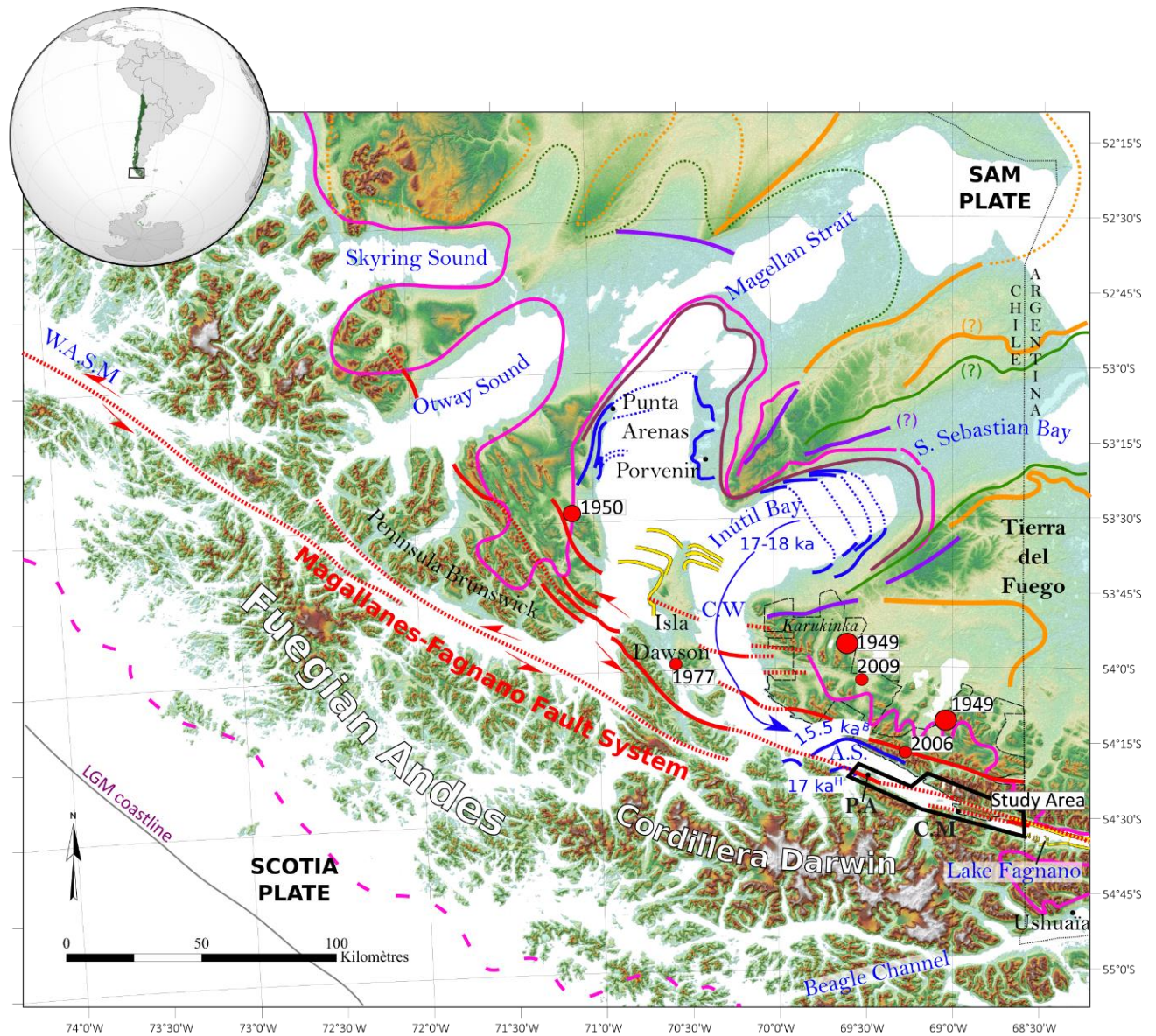
Recognition of strike-slip faults is made difficult by the near parallelism between glacial lineations, lithological strikes, and fault trends. Strike-slip Quaternary evidences are now well-documented in the region of Peninsula Brunswick, western Fagnano Lake, and in Chilean Tierra del Fuego (Winslow, 1982; Cunningham, 1993; Klepeis, 1994; Klepeis and Austin, 1997; Lodolo *et al.*, 2003; Betka *et al.*, 2016; Asenjo Fernandoy, 2020; Sandoval and De Pascale, 2020). However, in the central Almirantazgo Sound, in the Azopardo and Jackson valleys, many lineaments are suspected to be active but have only been little ground-studied, and limited to secondary faulting evidences.

The oldest historical seismic activity occurred in the 1st February 1879, and was reported from 50° down to 54°30'S (Serrano, 1880; Simpson and Chaigneau, 1880; Montessus de Ballore, 1912; Bustos, 1931; Dublé Almeida, 1938; Brügggen, 1943; Martinic, 1988; Bridges and Canclini, 2001; Cisternas and Vera, 2008; Martinic, 2008; Palacios R, 2013). The intensity was estimated at VII using the Modified Mercalli scale (Lomnitz, 1970). Earthquake instrumental records on the same day two major earthquakes of Mw 7.75 and Mw 7.5 the 17 December 1949 (Jaschek *et al.*, 1982; Pelayo and Wiens, 1989). These epicenters remain unclear and are located in the Karukinka natural park (Figure 4.1) (Adaros *et al.*, 1999; Febrer *et al.*, 2000; Jaschek *et al.*, 1982). In 1950, one foreshock was recorded south of Punta Arenas of Mw 6.8. In the 14 and 15 June of 1970, two shocks of magnitude Mw 7 occurred, respectively located in the MFF Atlantic continuation (52°1'22,8" S, 74°4'12" W), and north of the Magellan Strait western arm (54°18' S, 63°36' W). In our study area, three proximal earthquakes of moderate magnitude Mw 4.6 to 4.9 were recorded in 1977, 2006 and 2009 (Figure 4.1). Modern seismicity shows a cluster of epicenters which related to the strike-slip faulting zone, with a seismicity found suggesting a rather continuous release of energy in low magnitude events (Febrer *et al.*, 2000). Recent study along the Patagonian Andes suggests the present moderate seismicity would be mostly due to isostatic rebound following the retreat of the Patagonian Ice (Ammirati *et al.*, 2020).

Understanding the Quaternary fault activity should be determined through intrinsic characteristics like the cumulated displacement and major earthquakes dating (Wood and Mallard, 1992). Moreover, the fault activity may be determined over time that includes several earthquake cycles (Machette, 2000). The main purpose of this work is to acquired strike-slip faulting at surface due to relative plate motion deformation. Here we review observations and

evidence for strike-slip in the Western MFF from Lake Fagnano to the western arm of the Magellan Strait. We present the first mapping of glacial and strike-slip morphologies where the cumulated deformation onshore shows the best expression. Using extensive field work, high-resolution imagery, dendroseismology analysis, ^{10}Be and ^{14}C dating, we assess the strike-slip displacement in this area. Our motivation is to identify the successive imprints of glacial shaping and tectonic deformation to characterise the Quaternary and present-day MFF behaviour in Chile.

(Next page) Figure 4.1: Structural map of the Chilean MFF system with the major glacial limits and ice advance chronology. Black rectangle shows the location of the study area. The red lines indicate the recognized fault sections, and the dashed red lines indicate the interpolated traces after (Winslow, 1982; Cunningham, 1993; Klepeis, 1994; Klepeis and Austin, 1997; Fernández et al., 2011; Lodolo et al., 2003; Smalley et al., 2003; Fernández et al., 2013; Esteban et al., 2014; Betka et al., 2016; Fernández et al., 2017; Sandoval and De Pascale, 2020; Asenjo Fernandoy, 2020). Historical earthquakes are shown with red dots. Earthquake locations from (Jaschek et al., 1982; Febrer et al., 2000) The glacial limits are shown with coloured lines. The grey line indicates the pacific coastline at Last Glacial Maximum (LGM). Abbreviations as follows: ACR: Antarctic Cold Reversal; A.S: Almirantazgo Sound; C.M: Caleta María; C.W: Channel Whiteside; D: drift; SAM: South American; P.A: Peninsula Ainsworth; W.A.S.M: Western Arm Strait of Magellan. The base map is shaded mosaic relief image of the Southernmost Andes from SRTM ALOS Word 3D-30m (©JAXA).



¹⁸ O stage	Glacial advances in Magellan Strait cal.ka BP	Glacial advances in Almirantazgo Sound cal.ka BP	Glacial advances in Lake Fagnano cal.ka BP	
MIS 12 (?)	1070-360 D. Cabo Virgenes	not recognized	— Daniglacial	— Strike-slip fault scarp
MIS 10 (?)	300-125 D. Punta Delgada	not recognized	— Gotiglacial/D. Rio Valdez	— inferred fault
MIS 4	STAGE A 70.6 to 56.3	— A not recognized	— STAGE A >58	● M _w >6.9
MIS 2	STAGE B 31.2 to 25-23	— B not recognized	— LGM [$<36.1>13.9$] (Finiglacial/Pescado pond)	● 4.6<M _w <5
	STAGE C 21.7-20.4	— C not recognized	— RP1 [$<36.1>13.8$]	
	STAGE D 18-17	last recessions:	— RP2 14.8 - 12.7	
		— D-Boyd et al. 15.5		
		— D-Hall et al. 17		
ACR, Younger Dryas	STAGE E 12.5-11.7	— not visible	— RP3 11.170*	
	Bentley et al., (1998, 2005)	Boyd et al., (2008)	*dated from core and sedim. rate	
	Clapperton et al., (1995)	Fernandez et al., (2011),(2017)	Bujalesky et al., (1997)	
	Peltier et al., (2020)	Hall et al., (2013), (2019)	Caldenius 1932	
	McCulloch et al., (2005)a,b		Coronato et al., (2005),(2009)	
	Rabassa et al., (2000)		Rabassa et al., (2000)	
			Waldmann et al., (2010)	

IV.2 Western Magallanes-Fagnano Fault Geometry

Here, we review the MFF geometry from the east to west, starting at the Northern Fagnano section and ending at the Chile Tripe Junction. We recap observations of markers associated with Quaternary to Late Cretaceous deformations. The modern markers will be discussed in the following section.

IV.2.1 Northern Fagnano Faults

The Magallanes fault zone between the western Lake Fagnano and the eastern Almirantazgo Sound is divided into a series of narrow strike-slip faults and fault splays that bound the Sierra de Beauvoir and the Sierra Dientes del Dragón (Figure 4.2a).

All the strike-slip related deformation mapped within this region is superimposed on contractional structures from the Magallanes foreland fold and thrust belt (FTB). For instance, in Sierra Dientes del Dragón, the Cerro Verde anticlinal is dissected on its northern side by the MFF parallel to fold axis. The authors described a thrust contact between the Upper Jurassic volcanoclastic rocks and the Upper Jurassic to Lower Cretaceous tuffs (Figure 4.2a), which accommodated 6-km sinistral displacement and several hundred-meter vertical uplift (Klepeis, 1993; Klepeis, 1994). The rocks evidence here intense cataclasis and brecciation (Klepeis, 1994). Esteban et al., (2014) propose the eastern continuation of this section along the Sierra Beauvoir (Figure 4.2a).

Recent active faulting structure have been mapped North of Sierra Beauvoir. Authors identified the Deseado fault (DF) thanks to truncated vegetation and disrupted the alluvial Quaternary cover (Klepeis, 1994; Perucca and Bastias, 2008; Sandoval and De Pascale, 2020).

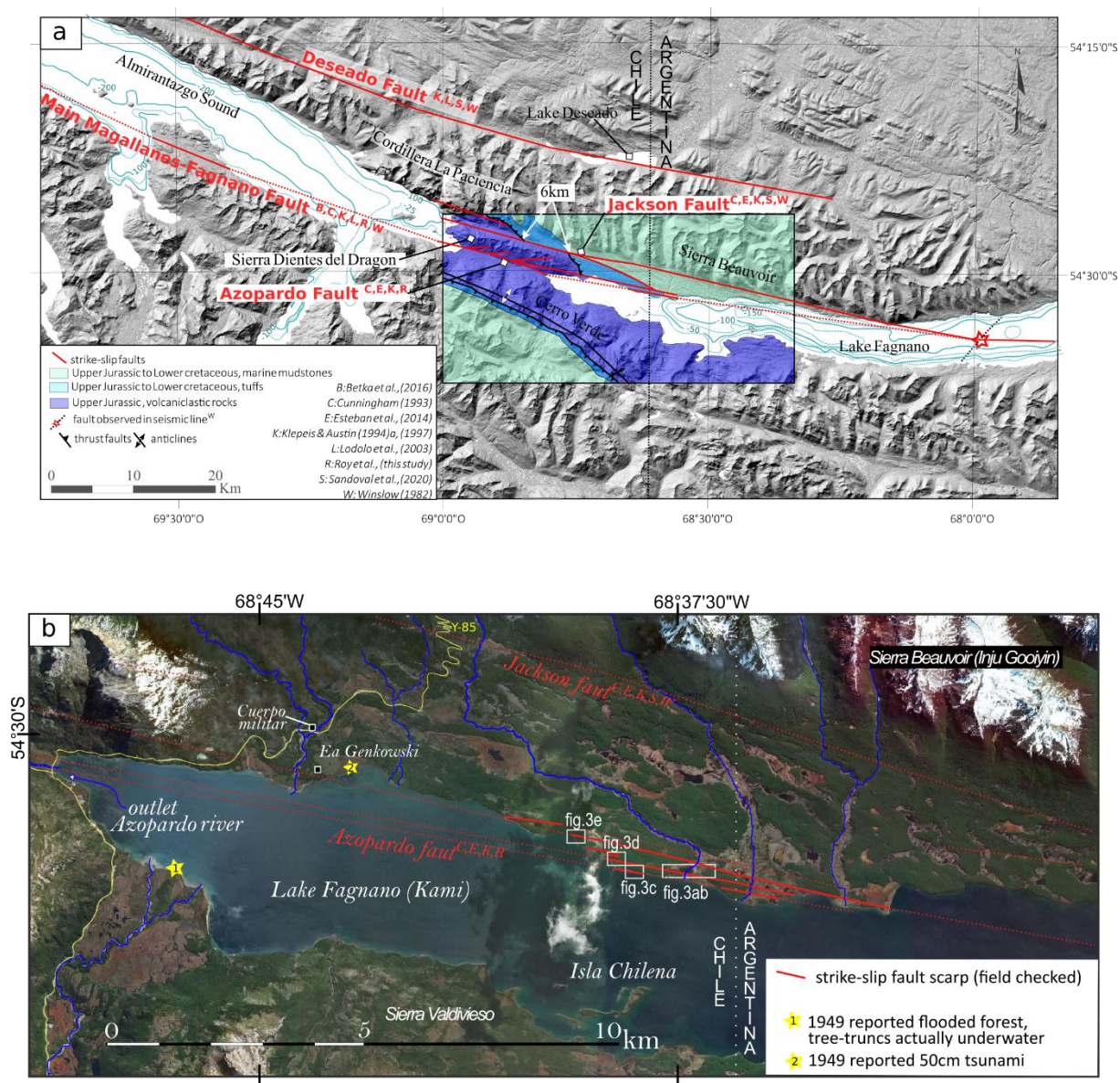


Figure 4.2: (a) Structural map of the central MFF. The exact locations of field surveyed faults are shown in red line, and associated studies are cited in the legend. The inferred faults are indicated in dashed red lines. The geology of Sierra Dientes del Dragón is shown to evidence the sinistral 6 km offset (Klepeis, 1994; Rojas and Mpodozis, 2006). References are as follow: B: Betka et al., 2016; C: Cunningham, 1993; E: Esteban et al., 2014; K: Klepeis, 1994; Klepeis and Austin, 1997; L: Lodolo et al., 2003; R: Roy et al., (this study); S: Sandoval and De Pascale, 2020; W: Winslow, 1982. The base map is the shaded DEM SRTM ALOS Word 3D-30m (©JAXA). Bathymetry of Almirantazgo Sound with a 50-m contour interval is the Esri, GEBCO, NOAA (2014) grid. Bathymetry of Lake Fagnano with a 25-m contour interval is from Lodolo et al., (2003). (b) Detailed structural map of the central Magallanes-Fagnano Fault near the western outlet of Fagnano Lake. The base map is satellite Bing™ Maps.

We carry out extensive field survey on the Fagnano Lake northern bank, from the Argentinian/Chilean border to the Azopardo river. This area was alternatively shaped by faulting and the action of Almirantazgo-Fagnano ice lobe. The last subglacial environment deposited multiple elongated lateral moraines N110-N115° disrupted by several ridges N°95-98 (Figure 4.2b).

We map at least four sub-parallel scarps up to 7-km long (Figure 4.3a, b). Locally, several scarps take the form of ridges, that several shallow grabens separate. Often, the graben' bottom is disrupted by meters-scale ridges. The southernmost ridge is visible in the proximal under-water morphology (Figure 4.3c). The easternmost fault location beneath the lake is unclear. Still, the alignment of these ridges combined with the central Fagnano (68°W) faulted zone interpreted in the seismic line ([Waldmann et al., 2011](#)), suggests that the main fault splays are located along the northern Fagnano shore. The western continuation of these ridges run toward the Azopardo river (Fagnano outlet).

In this region, we notice there is not relative elevation changes between the northern and the southern blocks. However, along these ridges, we measure prominent local vertical components up to 10 m (figure 4.3d, e). At the kilometers scale, these moderate topographic uplifts and subsidences may appear as restraining bends resulting from the local fault geometry. Besides, profuse tilted trees and uprooted trees evidence the recent severe motion of the ground surface (Figure 4.3b, c, d).

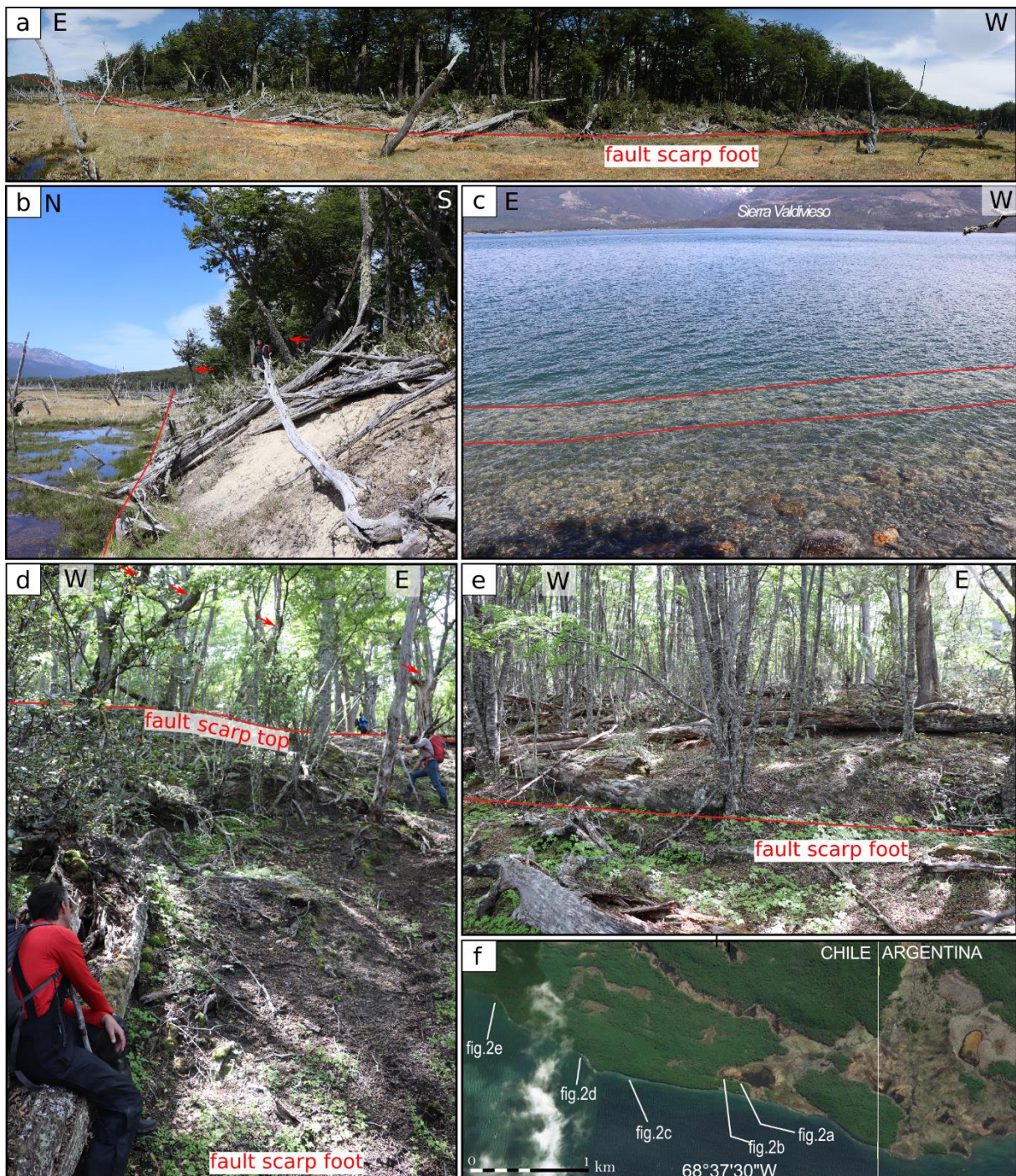


Figure 4.3: (a) Panorama of one scarp of several hundred meters long. (b) Tilted and uprooted trees along the ridge. (c) Underwater ridge in the northern shore of Lake Fagnano. (d) Highest fault scarp with tilted trees on its slope. (e) Well-defined ridge of 1-meter high. (f) Location of faulting structure on satellite Bing™ base map.

IV.2.2 Azopardo and Jackson faults

At the western end of Fagnano Lake ($68^{\circ}51'W$), the MFF splits into two fault zones north and south of the Sierra Dientes del Dragón, named the Azopardo fault and the Jackson fault (Figure 4.4). This mountain range is the northern flank of the Cerro Verde anticlinal with Upper Jurassic volcanoclastic rock (Thomas, 1949; Rojas and Mpodozis, 2006). Early geostructural studies described the two fault zones arranged in an extensive graben system with orientation $N108^{\circ}$ (Winslow, 1982; Klepeis, 1994). None of these valley floors exposed clear sinistral strike-slip morphology likely due to the reworking of their respective watercourse.

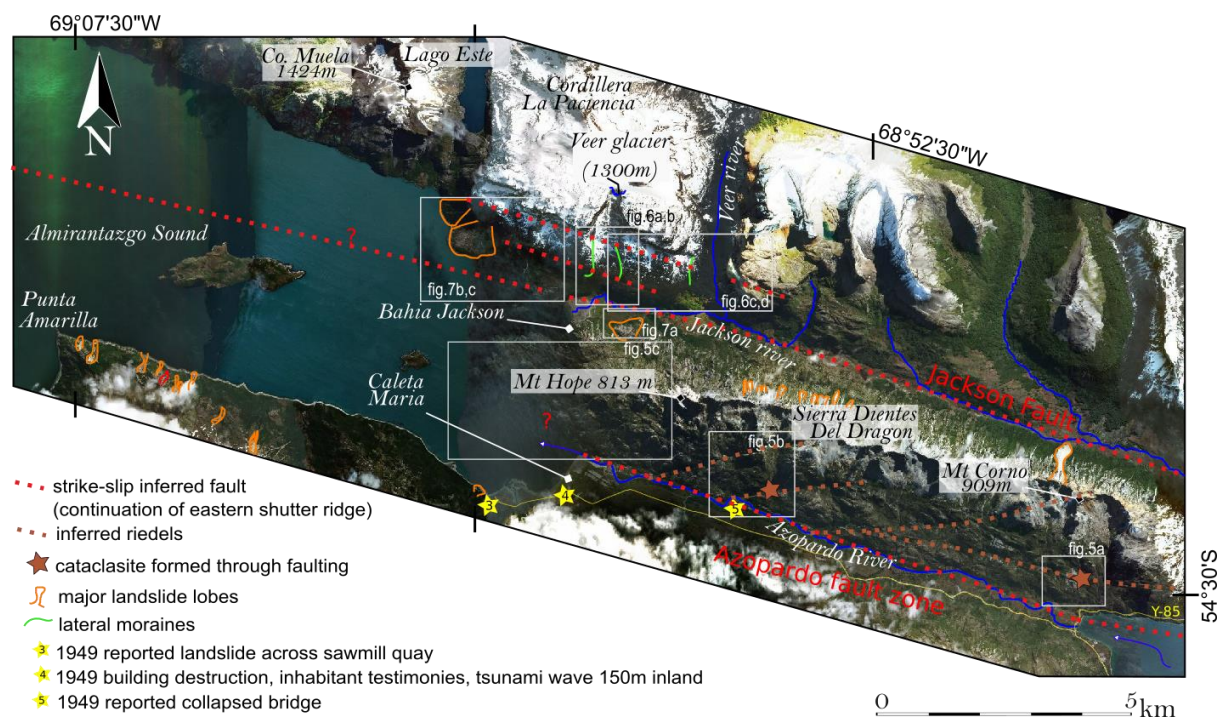


Figure 4.4: Detailed structural map of the western MFF. The base map is satellite Bing™ Maps.

However, along the Azopardo northern flank, we observe four failure zones. We examine two cataclastic areas up to 70 m wide south of Mt Corno and Mt Hope (Figure 4.4). We identified the easternmost cataclasite, located in a failure zone with $N97^{\circ}$ orientation (Figure 4.5a). This lineament results from the northern Fagnano shore ridge. The western cataclasite and two other failure zones trend $N79^{\circ}$ - $N84^{\circ}$ (Figure 4.5b) and correspond to the Riedel orientation. In these two zones, the Upper Jurassic silicic volcanic rock (Tobífera formation) breaks down to cataclasites and has been pulverized in situ (Figure 4.5 a, b). From the western outlet of Lake Fagnano, the MFF bends of $\sim 30^{\circ}$, from an E-W trending in Tierra del Fuego to a WNW-ESE trending

Magallanes regions. Consequently, in these two adjacent valleys, the fault scarps have been obscured, and are confounded with parallel glacial landforms (Figure 4.5c).

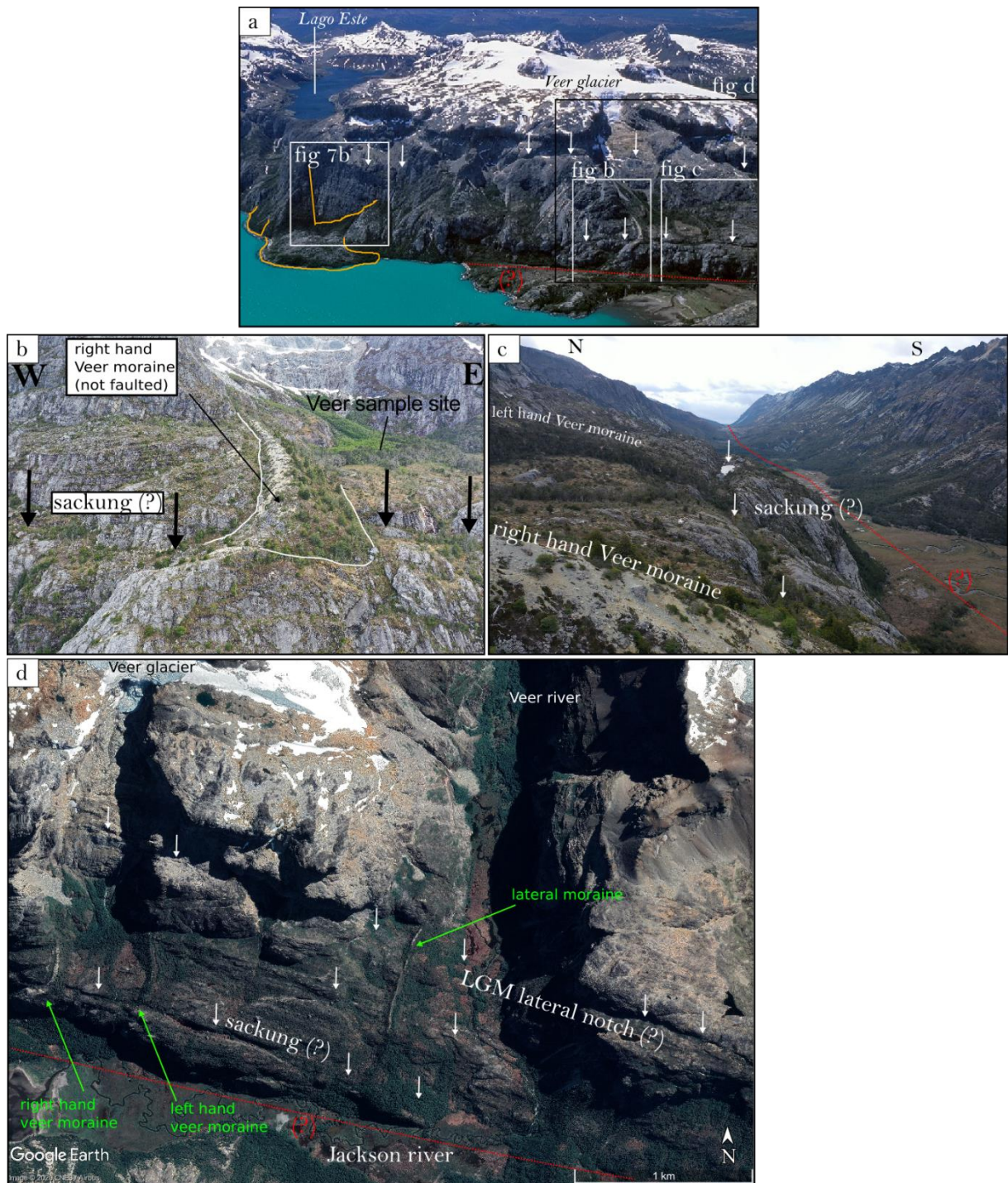


Figure 4.5: Photographs in the Azopardo valley. (a) Cataclasite below the Mt Corno. Yellow star indicates the subsided area subsequent to the 1949 earthquakes. (b) Cataclasite zone below the Mt Hope. Yellow star marks the 1949 crushed bridge over the Azopardo river. (c) View of the riedel fault zones (brown dashed lines) on the Sierra Dientes del Dragón from the Caleta María. The white dashed line evidence the roches moutonnées.

Seemingly, the Jackson valley does not expose unequivocal faulting morphology on its floor. The northern Jackson catchments comprise several well-preserved lateral moraines from the

Veer glacier and the adjacent valleys (Figure 4.4). We conduct field mapping along the Veer moraines, which are westward bent (Figure 4.6a, b). These bends indicate not only the past ice-direction, also the moraines were not affected by recent strike-slip after their deposition. All the moraines are not recently horizontally disrupted, but they partially fill up a spectacular uphill-facing scarps 20-m wide (Figure 4.6b, c, d) that seems to be markedly old. The anticarp creates a large depression of 4-km-long elongated in N^o108 direction, and divides the mountain flank into two parts. The lowest rock mass is sagging; we identify this geomorphic feature as the Jackson sackung (i.e., sackungen, or deep-seated gravitational slope deformation DSGSD).

(Next page) Figure 4.6: Photographs of the Jackson Valley. (a) Location maps on an aerial photograph of the Bahía Jackson and Cordillera La Paciencia (photographer @GuyWenborne). The white arrows indicate the sackung scarp and possible fault plane. (b) Aerial photograph of the Veer moraine. The white line delineates the right-hand moraine, and the black arrows indicate the sackung scarp. (c) Aerial shot of the Jackson valley toward the Fagnano Lake. The white arrows show the uphill-facing scarp with a pond in the counterscarp. The red line indicates the possible trace of Jackson fault. (d) Satellite image of the Veer glacier and the Veer river catchments. The green lines indicate the preserved moraines that are slightly deformed by the sackung scarp. The white arrows indicate the sackung and a possible lateral glacial notch from the last glacial maximum. (next page)



Two kilometers west of the Jackson sackung, we identify a mega-debris cone originating from a 1-thousand meters high sub-vertical rockwall (Figure 4.7a, b). We measure the main discontinuity plane ($N^{108}/67^{\circ}S$, strike/dip), which corresponds to the same orientation of the Jackson sackung (Figure 4.7b, c). The debris deposit spread over the steep coastline of the Almirantazgo Sound with approximately 1.5 km width and 60 m high. The deposit represents a

spectacular volume of about $\sim 3 \cdot 10^9 \text{ m}^3$, which is a minimal approximation because it does not consider the rock volume underwater.

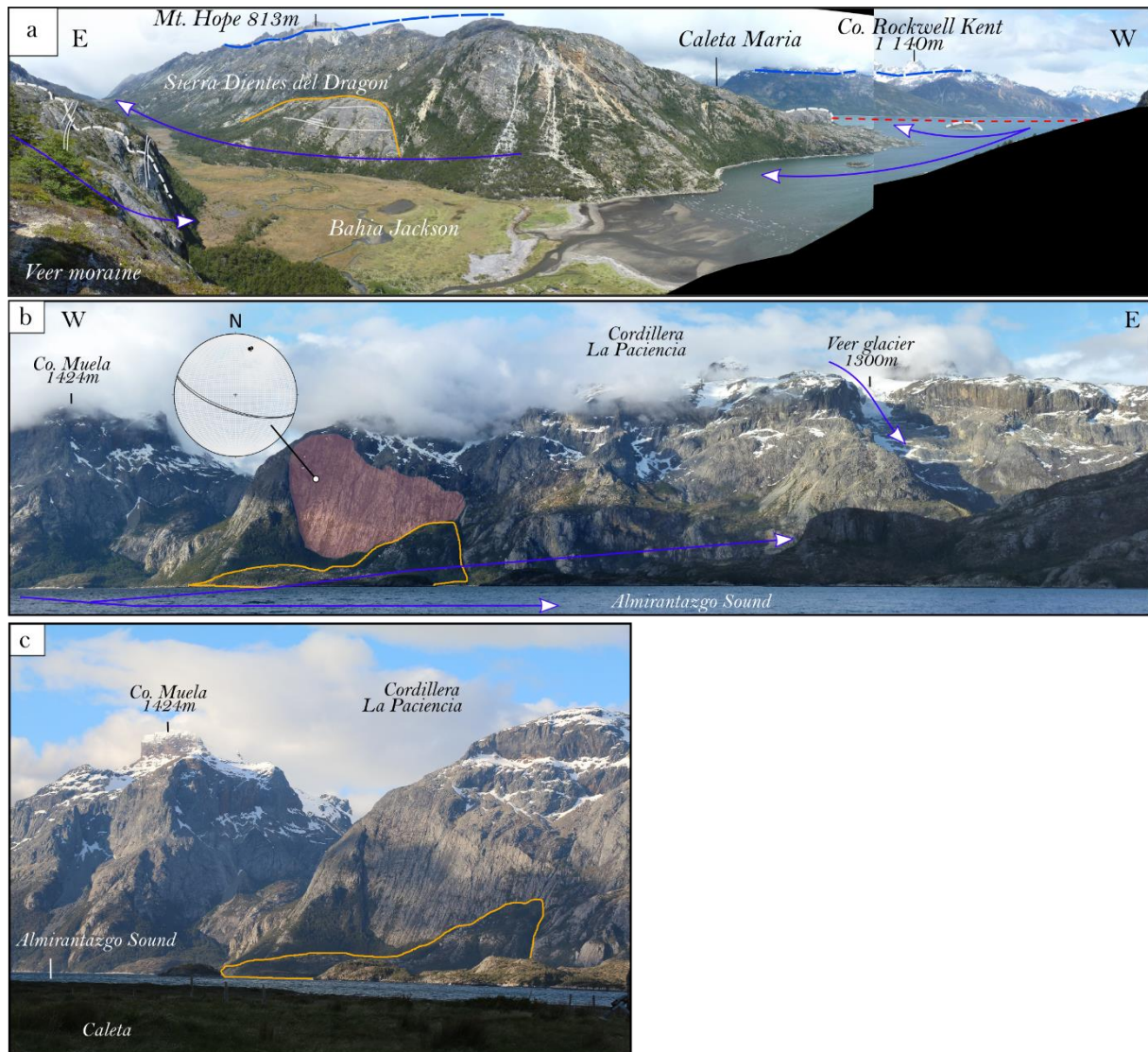


Figure 4.7: Photographs of spectacular rockslides. **(a)** Rockslides at Jackson Valley. Blue dashed lines indicate trimline and the maximum thickness of the paleo-Almirantazgo-Fagnano lobe and the blue arrows show the paleo-flow directions. The white line indicates glacial lineation and glacial notches. Note the rockslide on the northern flank of Sierra Dientes del Dragón marked with the orange line. **(b)** Rockslide of Cordillera La Paciencia. The red areas indicate the same fault plane orientation. The orange line indicates the debris cone. Blue arrows show the paleo-flow directions of the Almirantazgo-Fagnano paleo-lobe, which flowed from west to east, and split into two lobes in the Jackson Valley and the Azopardo valley. **(c)** The same rockslide with a detailed view of the fault plane and the orange lines indicates the debris cone.

IV.2.3 Ainsworth Section

The Ainsworth section is located at the Cordillera Darwin's foothill between the Fjord Parry and the Ainsworth Bay. A previous study based on swath bathymetry localized the Jackson fault's western continuation describing one submarine ridge north of the Peninsula Ainsworth (Asenjo Fernandoy, 2020). Thus, the author proposed the Ainsworth section is the continuation of the Azopardo fault.

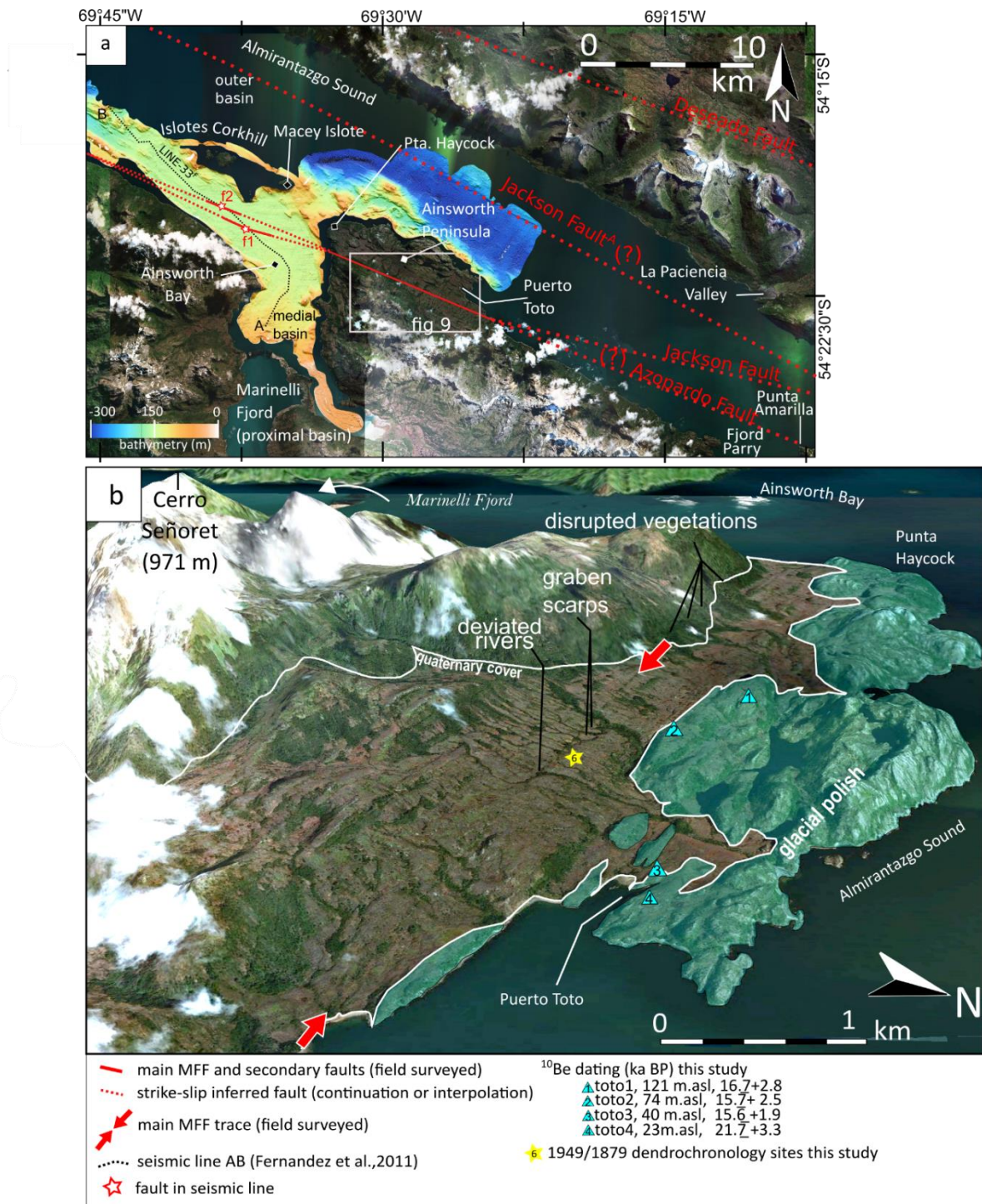


Figure 4.8: (a) Detailed map of the Ainsworth section. The red lines indicate the surveyed fault trace. The red dashed lines indicate the interpolation of the fault trace. The star shows the dendrochronology and paleoseismology sites (this study) with damaged trees in 1879 and 1949 earthquakes. The bathymetry is from Hallet (2016), with raw ship-based multibeam sonar data acquired during R/V Nathaniel B. Palmer expedition NBPO505 (2005) (<http://www.marine-geo.org>) and data processing (MB-system) is from (Fernández et al., 2011). The base map is satellite Bing™ Maps. (b) Ainsworth segment geometry. The base map is satellite Bing™ Maps with 2 x exaggerated relief.

We identify the Ainsworth segment consisting of one single scarp that crosses the entire Peninsula along a N112 trend (Figure 4.8a). A continuous scarp stretches over 10 km, disrupts the last glacial moraine deposits and deviates the drainages. The drainage system of Cerro Señoret catchment flow downhill orthogonally to the scarp, and incise the Quaternary cover (Figure 4.8b). At the scarp horizon, these channels make a double right angle (bayonet-shaped), exhibit significant offsets. The fault sharply left-laterally deviates the whole network (Figure 4.8b). Near the coast, the rivers bypass the glacial polishes and flow into the Almirantazgo Sound. We map the scarps' exact location, deviated rivers, disrupted vegetation, and tilted trees (Figure 4.8b). We sample trees for dendrochronology study and the glacial polishes for ^{10}Be dating's (Figure 4.8b). The scarp offsets the principal river channel in a spectacularly sinistral displacement of ~315 m (Figure 4.9a). Along the shutter ridge, the southern block is relatively higher than the northern block, which has enclosed sag ponds and peat bog. The fault disrupts eskers and Quaternary cover. We develop the dendrochronology results, trenching, and drainage offsets respectively in section III and IV.

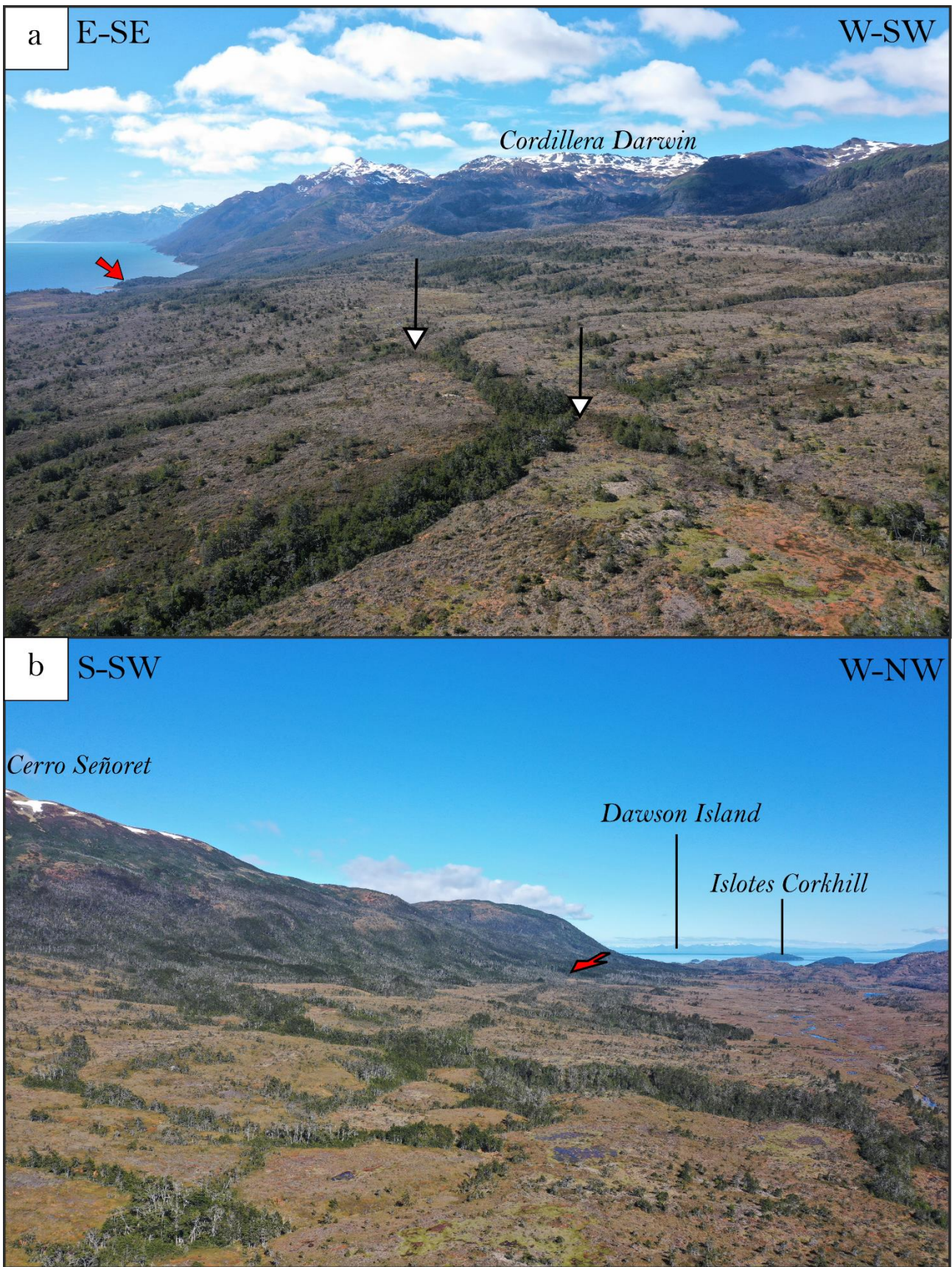


Figure 4.9: (a) Aerial view of the stunning sinistral offset on the Peninsula Ainsworth. The red line indicates the kilometeric scarp. Black arrows target the main sinistral bayonet deflection of one post-glacial river. Red arrows indicate the fault trace. The distance between the two indicators is ~300 meters. In the right lower corner, note the field of eskers. (b) Aerial view of the western continuation of the Ainsworth section toward the Isla Dawson.

We interpolate the western continuation of the Ainsworth section through the Ainsworth Bay. The Ainsworth bay corresponds to the medial basin of the Marinelli glacier (Figure 4.8a). Previous seismic investigations were conducted in this area (Koppes *et al.*, 2009; Fernández *et al.*, 2011; Hallet, 2016) and across the fault (Figure 4.8a). Figure 4.10a shows the 17 km long seismic line along the thalweg from Marinelli medial basin (left) to the ice front outer basin (right) (Fernández *et al.*, 2011). The authors define three sediments units (Figure 4.10b), the basal unit GFU (gravity flow unit), the middle unit (GMU, glacimarine unit), and the youngest unit (HPU, hemipelagic unit). The first two units are estimated around the age of the Marinelli glacier retreat from the outer basin to the medial basin around 12.5 ka (Boyd *et al.*, 2008). The modern unit HPU has ages from 364 cal yrs BP to the present.

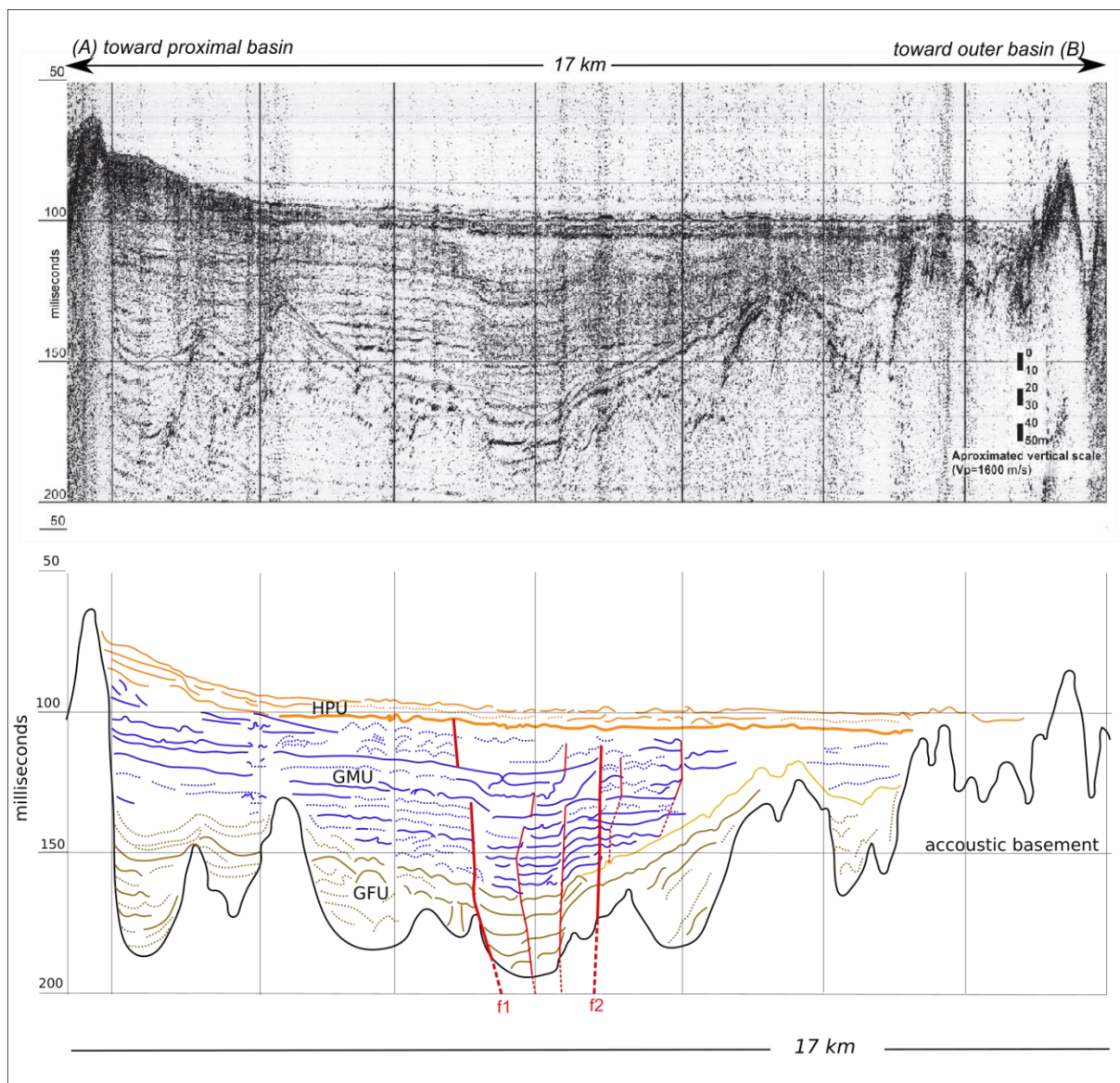


Figure 4.10: (a) Seismic line 33. The profile AB is from Marinelli medial basin (left) to the outer basin in Almirantazgo Sound (right). Data is from (Fernández et al., 2011; Hallet, 2016) acquired during R/V Nathaniel B. Palmer expedition NBPO505 (2005). (b) Interpretation of seismic line 33 from (Fernández et al., 2011). Red lines indicate the fault splays after (Fernández et al., 2011). F1 and F2 are the faults reported in Figure 4.8. Abbreviations as follow: GFU: gravity flow unit; GMU: glacimarine unit; HPU: hemipelagic unit.

The GFU and GMU (115m thick) are disrupted by fault splays (Figure 4.10b). The lowest part of the modern unit exposes disrupted reflectors. We interpreted these fault splays as the western continuation of the Ainsworth segment (Figure 4.8a). This interpretation disagrees with the previously fault geometry of the Ainsworth Bay proposed by Asenjo Fernandoy, (2020). Using

the bathymetry of Ainsworth Bay, this author suggests the lineament circumvents the medial basin toward Punta Haycock and through the Islotes Macey and Corkhill. Additionally, previous studies defined this morphology as the medial basin excavated during the last glacial advance of the Marinelli frontal moraine between 12.5-15.5 ka BP (Boyd *et al.*, 2008; Izagirre *et al.*, 2018). As the inland fault morphology is a sharp straight trace, we do not believe the offshore continuation suddenly curves out to the north, passing the coastline.

IV.2.4 Western Magallanes Faults

In the literature, the main MFF was described in Almirantazgo Sound, crossing the Isla Dawson and bending toward the Indio Bay (Winslow, 1982; Cunningham, 1993; Klepeis, 1994; Klepeis and Austin, 1997; Lodolo *et al.*, 2003; Betka *et al.*, 2016). In the Brunswick Peninsula, two sub-parallel segments crosscut or reactivates reverse faults and folds of the Late-Cretaceous-Eocene Fold and Thrust Belt (FTB) (Betka *et al.*, 2016). Therefore, authors proposed the strike-slip deformations postdate the FTB.

We note the alignment between this lineament and the fault crossing the Peninsula Ainsworth. We suggest there are both parts of one single main MFF fault (Figure 4.11). Recent characterisation of glacial and strike-slip morphologies in the Strait of Magellan, in the Whiteside Channel, and the Almirantazgo Sound recognized faults in seismic lines (Fernández *et al.*, 2017; Asenjo Fernandoy, 2020). They demonstrated the offshore continuations of the Karukinka fault, the Deseado Fault, and two fault splays in the western Almirantazgo Sounds (Figure 4.11). Authors proposed these faults splays separated several pull-apart basins localised east and west of the Isla Dawson (Lodolo *et al.*, 2003; Betka *et al.*, 2016; Fernández *et al.*, 2017; Asenjo Fernandoy, 2020). The fault splays reactivated the pre-Jurassic suture zone between basement Fuegian foreland terranes of Tierra del Fuego and the Cordillera Darwin metamorphic complex (Hervé *et al.*, 2010).

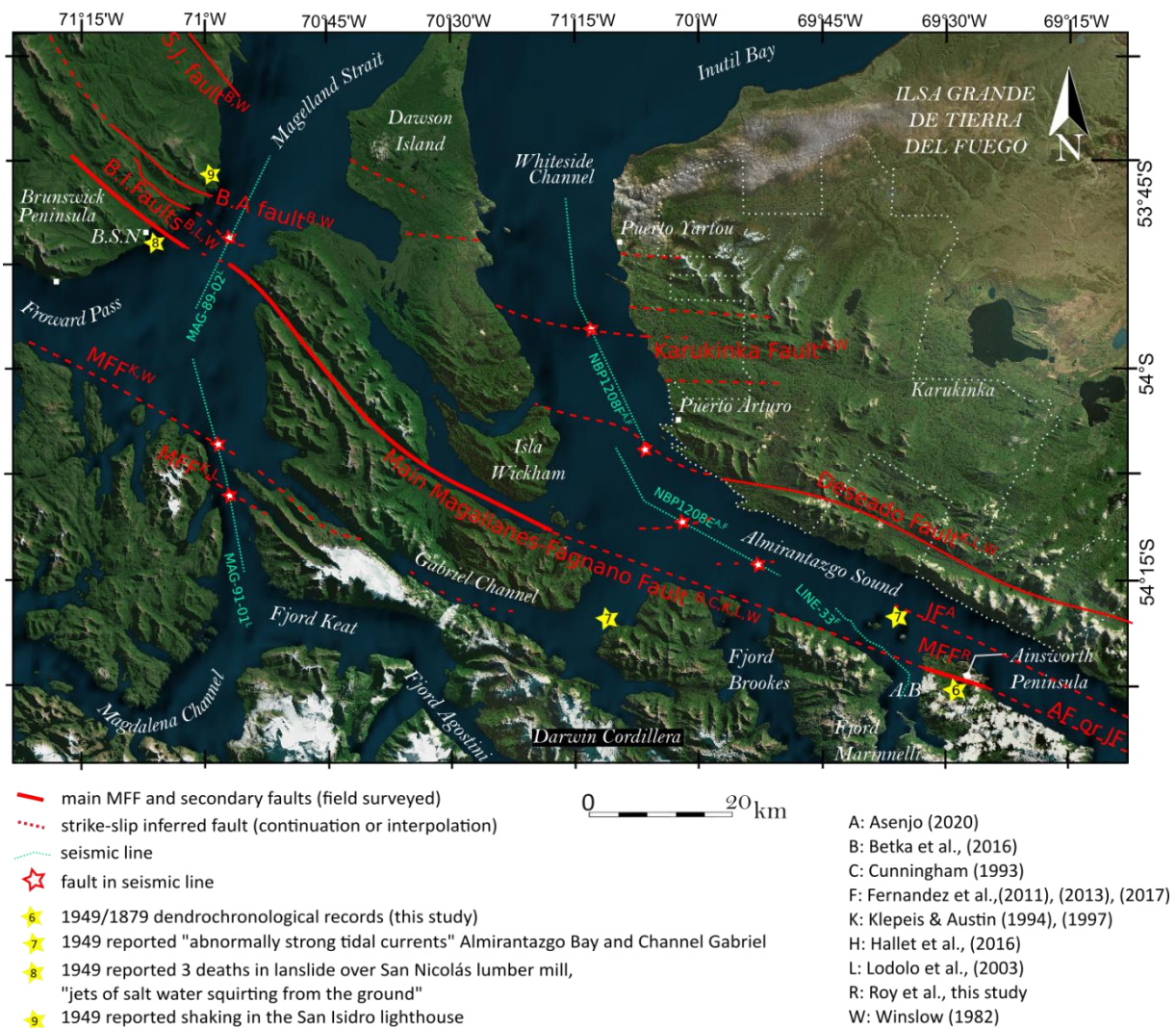


Figure 4.11: Detailed map of the Western Magallanes Fagnano Fault system. White dashed line delimits the Karukinka Natural Park. Abbreviations as follow: A.B: Almirantazgo Bay; B.A: Bahía del Aguila; B.I: Bahía del Indio; B.S.N: Bahía San Nicolás; S.J: San Juan (Rio); MFF: Magallanes-Fagnano Fault; The base map is satellite Bing™ Maps. References of cited literature are shown in the figure.

IV.3 Fault rupture over the past two centuries

IV.3.1 Dendroseismology

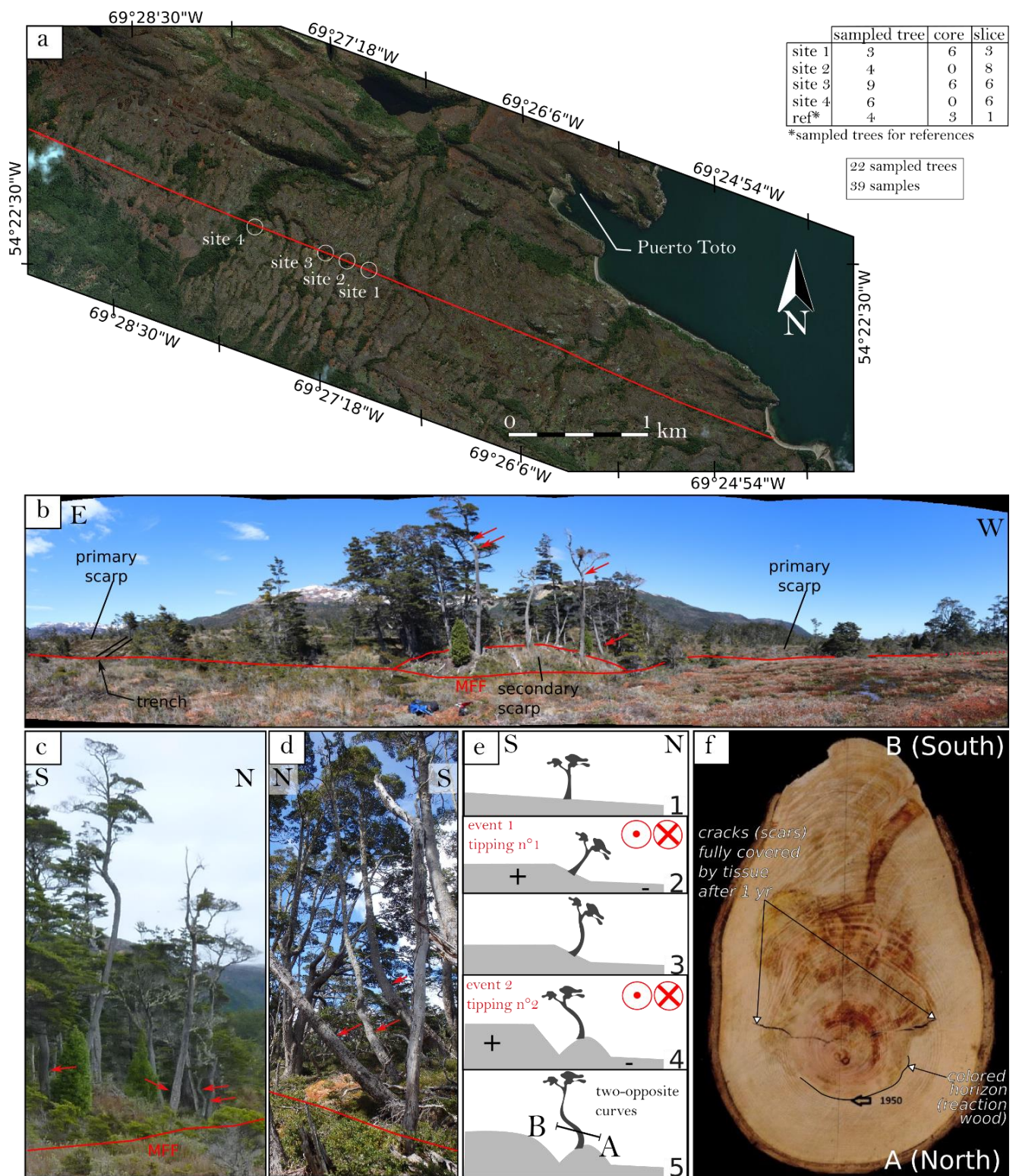
In the Peninsula Ainsworth, we carry out a dendroseismological study to characterise MFF's recent activity. The MFF scarp crosses the entire Peninsula in a N112 direction, with a southern block continuously higher than the northern block (Figure 4.12a). This ridge defines a north-

facing slope up to 10-m high. The topography comprises several local ridge adjoining the prominent fault scarp (Figure 4.12 b).

Evaluation of active faulting using dendrochronological indices can provide crucial quantitative data for evaluating seismic hazards (Fritts, 1976). Pioneer investigators in dendroseismology have successfully used trees to study earthquakes (Page, 1970; Meisling and Sieh, 1980; Jacoby and Ulan, 1983). Indeed, a site's disturbance by rupturing faults can injure or tilt a tree stem and may cause changes visible in the tree-rings (Jacoby *et al.*, 1988; Yamaguchi and Hoblitt, 1995; Yamaguchi *et al.*, 1997; McCalpin, 2009). The subsequent trauma in the cell structure is called reaction wood. Past events are dated with yearly precision by analyzing the radial growth of trees (narrow or wide annual rings), the cell anomalies (reaction wood, modification of cell structure) and the tree-ring morphology (scarps, tilting) (Astrade *et al.*, 2012). The damaged trees by large earthquakes are a criterion for assigning shaking intensity above VIII (Mercalli intensity Scale) and usually limited within a few kilometers of the seismic source (Jacoby *et al.*, 1988).

(Next page) Figure 4.12: (a) Location of sites and numbers of trees sampled per sites. The red line indicates the Magallanes-Fagnano Fault. (b) Site 1. The red lines indicate the MFF ridges. (c) Group of trees in site 1. The red arrows show the two characteristic opposite curves. (d) View of site 4 showing the several northward tipped tree-trunks. (e) N. pumilio slice from site 1. The profile AB indicates the reaction wood orientation (rings squeezed in the tilt direction) in response to the northward tilt coeval to the 1949 earthquake. Notice the color change (lighter) after 1950 and the two scars that cross the heartwood, including the 1950 ring. (f) Steps development of the two opposite curves: (1) Normal vertical growth; (2) 1st earthquake, formation of the primary shutter ridge, and northward tilt of the tree. (3) The tree tends to grow vertical and makes the 1st curve. (4) 2nd earthquake with coeval faulting, and formation of a secondary ridge. The tree tilts southward; (5) Vertical growth making the 2nd curve in the opposite direction.

IV.3 Fault rupture over the past two centuries



We sampled trees in four sites along the Magallanes-Fagnano fault in the Peninsula Ainsworth (Figure 4.12a). We collected cores and slices from 22 tilted living-trees located on the fault scarp and four reference trees located away from the fault. The comparison with control-trees allows us to differentiate the climatic signal from the faulting disturbances. We collected

slices and cores of the species *Nothofagus pumilio*, an endemic winter-deciduous tree of the Southern Andes, which has a characteristic vertical axis (Puntieri *et al.*, 1999; Puntieri *et al.*, 2003). Sampling always took place at the tree base or trunk curvatures.

Numerous trees located at sites 1 and 4 expose a specific morphology with two opposite curves (Figure 4.12 c, d). These double opposite curves may have originated from the successive vertical recoveries by phototropism following two events (Lopez Saez and Corona, 2015). Various circumstances can cause such changes in the morphology: adjustment of the drainage, landslides, crawling, avalanche, rockfall, torrential flow, and disrupted topography during earthquakes (Lopez Saez and Corona, 2015). In this configuration, the trees may have tilt northward during a first event along the prominent fault scarp (Figure 4.12e). During a second event, part of the scarp may have slipped or been disrupted, creating a secondary ridge and tilting the tree on the counter side (Figure 4.12e). Alternatively, the second curve could originate from a new growing bough, from a second tilt due to local topographic and drainage adjustment (gravitational instability, pond).

For this angiosperm trees, a tilt produces an asymmetric tree-ring growth with a compression wood in the sloping side A and broader rings on the opposite side B (Figure 4.12 f) (Kaennel and Schweingruber, 1995; Lopez Saez and Corona, 2015). The compression wood has thicker cell walls than the surrounding tissue, resulting in darker colouring (Shroder and Butler, 1986; Stoffel *et al.*, 2010). Cores and Slices were sanded, sharply cut, and analysed at the Edytem Laboratory. We examine both the cells (reaction wood color, ring scarp) and the growth curve data.

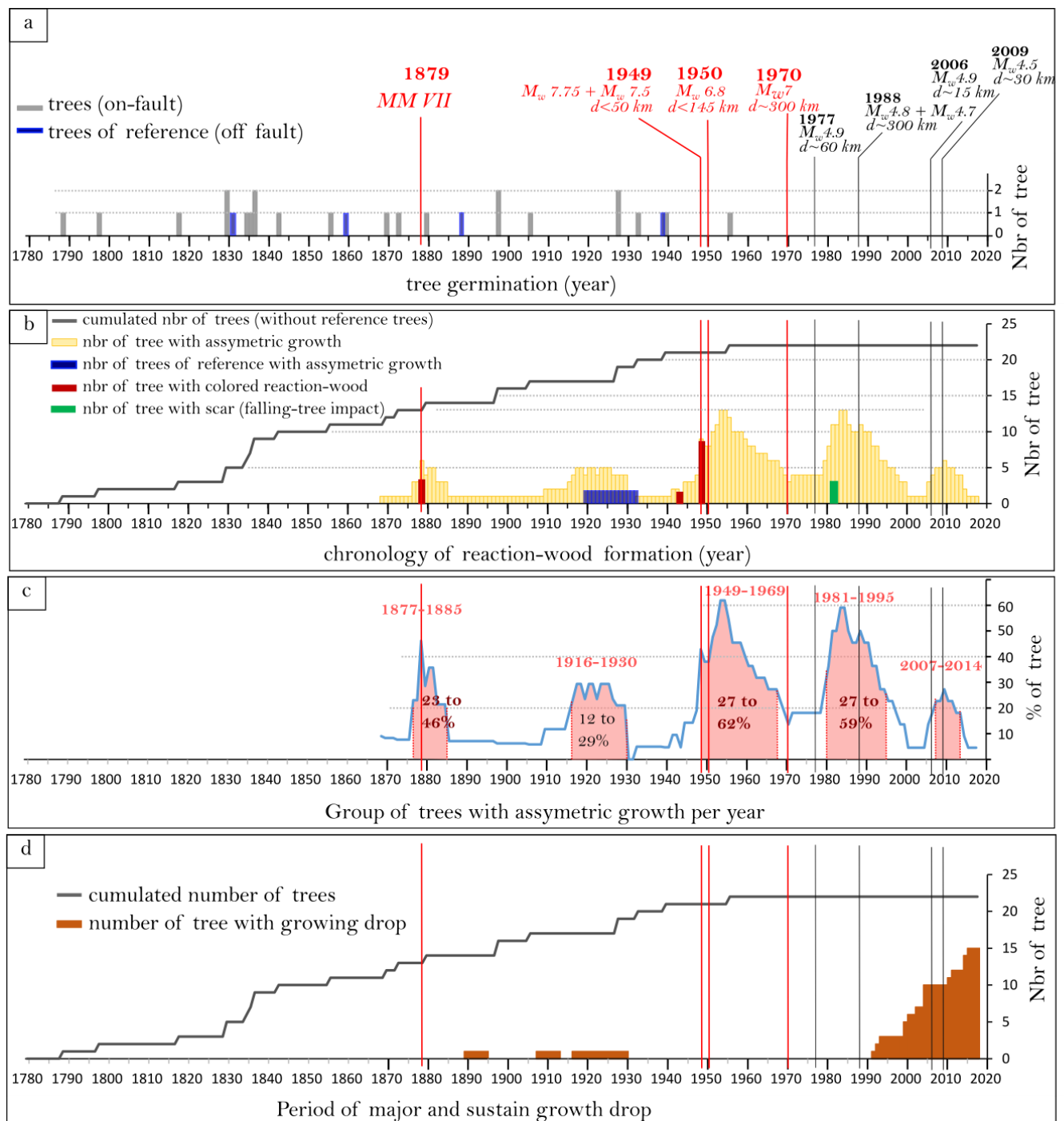


Figure 4.13: Dendrochronological synthesis. The red lines indicate the major historical earthquakes, and the black lines indicate local moderate earthquakes. (a) Numbers of trees in function of their year of germination. (b) The number of trees showing reaction wood in function of the reaction wood ring age (asymmetrical growth, colored ring, scar). The total number of tree (grey curve) does not include the four control-trees. (c) Percentage of trees with asymmetric growth versus time. (d) The number of trees showing a sustained period of growth drop.

We determine past disruptive events using the number of trees affected in a particular year. We report the percentage of trees affected using the number of trees alive at that time (It) (index number [Shroder, \(1978\)](#)). The germination ages range from 1956 back to 1789 (tree on fault scarp), and reference trees ages range from 1939 to 1831 (Figure 4.13a). We use the colored reaction-wood, which is manifest and narrow changes in the tree-ring sequences. This method allows to unequivocally date the event's year ([Lopez Saez and Corona, 2015](#)). We identify two events (Figure 4.13b red bars) that impacted the rings in 1879 (3 trees out of 9 alive, It 33%), in 1949 (8 trees out of 15 alive, It 53%). We associate these events to the two major historical earthquakes. We exclude one event marked in a single tree in 1944 ($It < 5\%$).

The examination of tree-ring eccentricity is mandatory to reinforce the results from reaction wood coloration analysis. This characteristic remains indiscernible on the cores. Because several trunks were only cored, we may miss the eccentricity changes and underestimate the true number of impacted trees. We identify groups with a span onset of asymmetric growth, which defines 5 phases from [1877-1885], [1916-1930], [1949-1969], [1970-1995], and [2007-2014]. Two of the control-trees show broader tree-rings associated with the phase 1919 to 1933, suggesting this phase might be triggered by global climate-driven change in the area (Figure 4.13b). Therefore, we can exclude this event from our paleoseismic record.

We focus on the distribution of the impacted tree number (asymmetry). We notice that for the 1879's event the maximum number of trees damaged occurred in the year 1879 (Figure 4.13b yellow histogram). Interestingly, the highest number of impacted tree does not necessarily match the other event's date. There are nine trees (It 42%) with asymmetric growth in 1949, and up to 62 % show an eccentricity growth in the two decades following the 1949 earthquakes. We observe a delay in the eccentricity growth onset up to 20 years following the 1949 quake (Figure 4.13c). The numerous historical aftershocks ([Jaschek et al., 1982](#)) justified perhaps co-seismic topographic changes until late in 1950. Variable parameters can explain the extended phase of eccentricity onset: post-event topographic adjustment, or topographic changes caused by the drainage system adaptation newly disrupted morphology ([Astrade et al., 2012](#)).

From 1970 to 1995, we identify 27% to 59% of the trees with asymmetric growth and note two peaks in 1982 and 1984-1985. In addition to asymmetric growth, we observe cracks in the

three *N. pumilio* stems on the ring 1982 (Figure 4.13b). The cracks are radial splitting which are quickly recovered by tissue after one year. Importantly, there are not associated with colored reaction wood, which implying that this event was not necessarily accompanied by wood-cell compression. The trees affected are spread over the four sites, and the crack is absent on the control-trees. Therefore, it invalidates a hypothetical dryness or cold episode causing respectively drought cracks or frost cracks (Kaennel and Schweingruber, 1995). Besides, it implies this event might have affected only trees on the fault scarp. Most likely, these cracks may have formed by the impact of one tree falling over another trunk. From these informations, it is not possible to conclude about the 1982's cracks origins. Trees fell over either caused by a wind storm or ground-shaking. However, there is not earthquake by that time near the Peninsula. The interpretation of this event is not straightforward, especially as the number of tree with asymmetric growth is distributed over 1970 to 1995. We exclude the major earthquakes in the 80's that occurred along the Shackleton Fracture Zone and the West Scotia Ridge as they were extremely distal (>400 to 800 km) and pertained to different tectonic setting. In 1970, there are two major earthquakes: the 14 June (-52.035°, -74.097°; distance from site 400 km) of magnitude Mw7, and the 15 June (-54.3°, -63.6°; distance from site 300km) of magnitude Mw7.2 (Pelayo and Wiens, 1989; Febrer *et al.*, 2000; U.S. Geological Survey). They are both far from the Peninsula Ainsworth to potentially disrupt the local morphology. The 15 October 1977 occurred a moderate quake of Mw 4.9 with an epicenter located in the Isla Dawson (-53.973°, -70.515°). It is unlikely that such magnitude would cause surface rupture at 60 km away from the epicenter (Hanks and Kanamori, 1979; Wells and Coppersmith, 1994).

The most recent phase of impacted trees occurred between 2007 and 2014, with 18 to 27% the trees damaged. At that time, only two proximal earthquakes occurred in 2006 (09 January; -54.292°, -69.274°; ~15 km) and 2009 (06 November; -54.083°, -69.534°; ~30km). According to their respective magnitude, Mw 4.6 and 4.5, their mean rupture lengths are estimated << 3 km (Hanks and Kanamori, 1979; Wells and Coppersmith, 1994), thus it is improbable these events affected the Peninsula.

Curiously, four trees (It 40%) show an early asymmetric growth in 1877, 1878. Seemingly, previous the 1949 earthquakes, four trees in 1947 (It 19%) start to create eccentric tree-rings. Uncertainties in tree-rings analysis might be introduced by a ring suppression (lack of growth

after damaged), miscount, unfavorable climate, or restricted lighting early in the life of the tree (competition) (Shroder, 1978). Here, the control-trees do not evidence a significant period of growth drops or climatic changes during these phases (Figure 4.13d). Moreover, damaged trees are present in all sites, which prevents the effect of a possible individual artefact. Because their percentage are high, further investigations must discriminate the methodological uncertainty against the potential low magnitude foreshocks. Additional study of the regional climatic signals may contribute to understand the sustain growth drop since 1990 (Figure 4.13d), but this is beyond the thesis questions.

The dendrochronological study leaves no doubt that the MFF ruptured along the Peninsula Ainsworth in 1879 and 1949. Perhaps, this section ruptured as well in 1950. One additional event in 1982 is not consistent with the instrumental seismic record. Further investigations are required to infer the disturbance mechanism triggering the 1982's cracks and 2007 to 2014 eccentricity growth.

IV.3.2 Secondary rupture evidences

Knowledge of a region's seismicity is a crucial key to estimate the earthquake hazards. To investigate the regional seismicity [McCalpin \(2009\)](#) further distinguishes primary and secondary evidence of recent fault activities, with secondary being landslides, tsunami, or liquefactions. In Chile, the recent earthquake secondary evidences are extensive and well expressed. Following the 17 December 1949 earthquakes, numerous testimonies were reported all around the Southern Chile. Several inhabitants described a 50-cm tsunami over the Estancia Lago Fagnano land (personal discussion German Genskowski) (Figures 4.2) and mentioned the sea that suddenly drained away in Caleta María (Figure 4.4). In Gabriel Channel, in Porvenir and Almirantazgo Bay, several navigators observed abnormal strong tidal wave. South of Punta Arenas in the San Nicolás Bay, jets of salt-water squiring from the ground were noted (Figure 4.11) ([La Prensa Austral, 1949](#); [Lomnitz, 1970](#); [Isla and Bujalesky, 2004](#); [INPRES, 2004](#); [Perucca et al., 2006](#); [Martinic, 2008](#)). Two specular examples are the subsided delta along the Fagnano's southern bank (Figure 4.14a), and the historical photographs of the destroyed pier in Caleta María before (Figure 4.14b) and after (Figure 4.14c) the 1949 earthquakes. However, the timing and the

localisations of the former scarp remains ambiguous from these secondary ground-shaking evidence.



Figure 4.14: (a) Lake Fagnano's southern bank was subsided near the Betbeder river mouth coeval to the 1949 earthquakes with numerous half-submerged tree trunks. (b) The 1945 pier of Caleta María sawmill, from García, (2013), a photograph of Lucio Genskowski.P. Note the Islote Albatros in the background for reference point. (c) The pier after the 17 December 1949 earthquake. Note the same background reference point and the debris cone, from García, (2013), photo Lucio Genskowski.P.

Sharp surface fault geometries, paleoseismological trenches, and disrupted trees constitute hard data and primary evidence to understand the most recent fault activity (McCalpin, 1996; Obermeier, 1996; Sieh, 1981). In southernmost Patagonia, these archives are fundamental, especially as historical and instrumental records are scarce. In the study area of Azopardo and Jackson faults, there is not hard data yet to support whether they are, or are not, active in the last century. Contrarily to the recent conclusions (Sandoval and De Pascale, 2020), we propose these two faults are two potential candidates to be two master faults along with their northern counterpart, the Deseado Fault.

IV.4 Quaternary activity along Peninsula Ainsworth

IV.4.1 Offsets from high-resolution digital topography

Here, we use the changes in the hydrological network of the Peninsula Ainsworth catchment to assess the long-term slip. We investigate a twelve rivers, including ten active channels and two fossil channels (Figure 4.15). They are all characterized by a linear flow toward the NE, sharp offset by the fault scarp, and 90° to 80° of obliquity angle between channel orientation with respect to the fault trace. This configuration represents a highly reliable quality geomorphic measurement site (McCalpin, 2009; Salisbury *et al.*, 2012; Madden *et al.*, 2013; Zielke *et al.*, 2015).

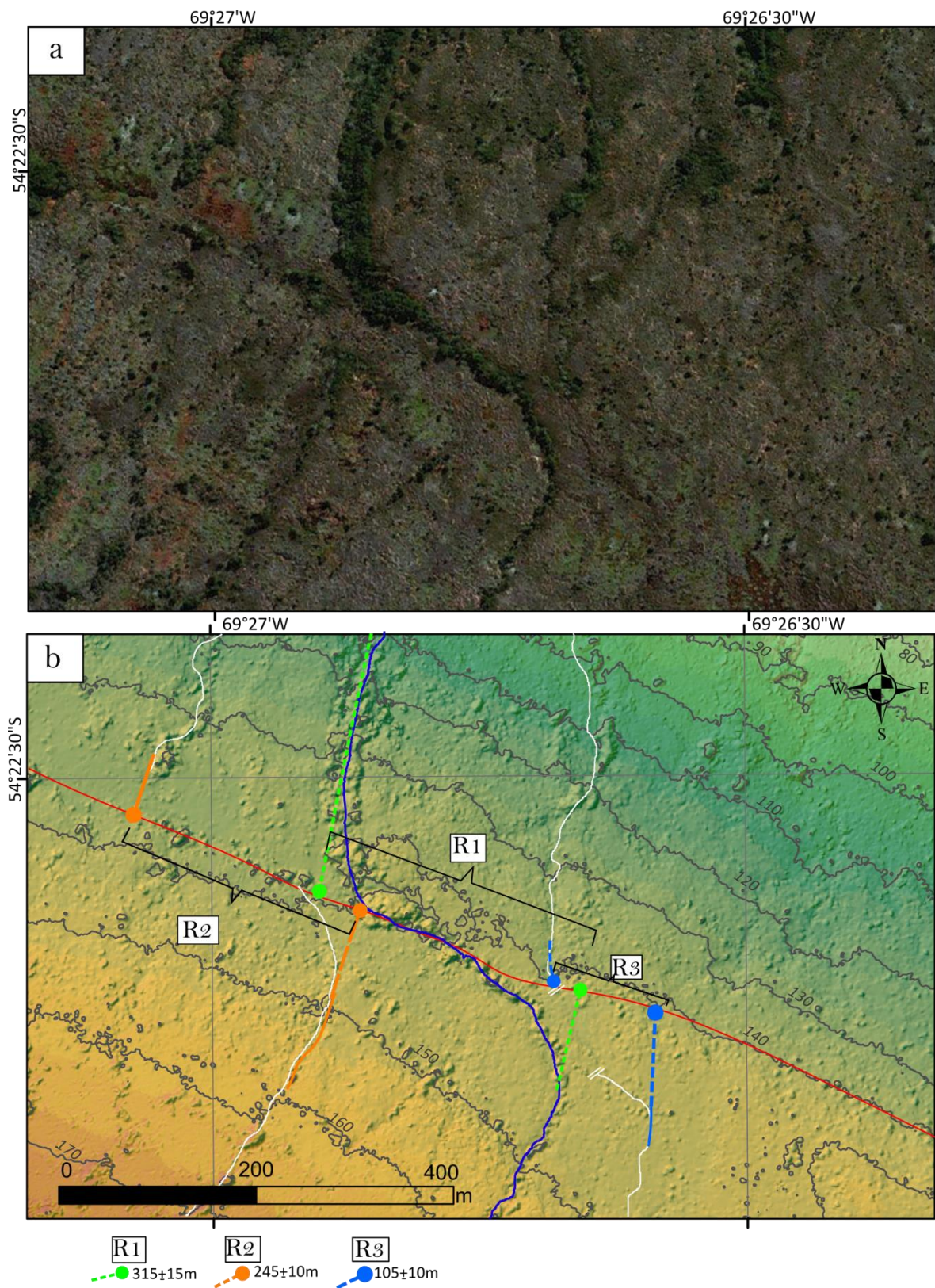
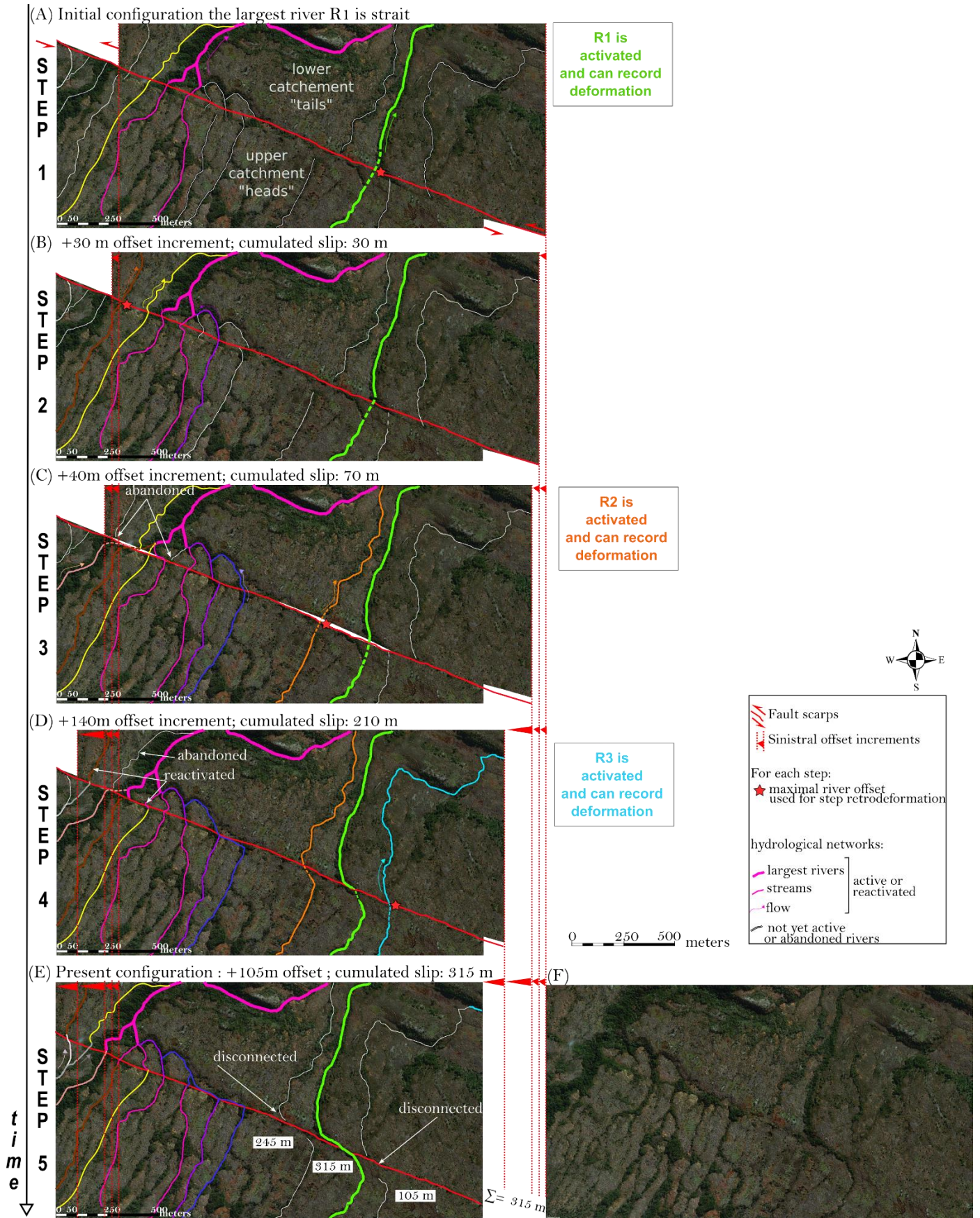


Figure 4.15: Three offset measurements. (a) the Site's view without interpretation. The base map is satellite Bing™ Maps. (b) Displaced river channels (dark blue line), fossil channel (white line) and idealized fault plane (red line) on 2m grid resolution Pleiades DSM data set. The distance

measurements are projected onto an idealized planar fault (indicted by dashed line with dot on the fault planes). Contour plots with 10-m above sea level interval.

The sinistral displacement is particularly well-expressed in three river channels (Figure 4.15a). We used aerial photographs with a high-resolution digital surface model (DSM) from Pleiades images using MicMac (free, open-source photogrammetric suite, IGN, ENSG). We identify the channel heads and their associated channel tails, with their respective unique match. We projected the linear drainage heads and tails on to the fault plane. We measure the respective maximal offset of River 1, 2 and 3 of about $315 \text{ m} \pm 15 \text{ m}$, $245 \pm 10 \text{ m}$, and $105 \pm 10 \text{ m}$.

(NEXT PAGE) Figure 4.16: Retro-deformed landscape by the determined offset amount to assess reconstruction reliability and offset range. The colored lines indicate the active streams. Note that each stream keeps its original color corresponding to its activation, which facilitates the displacement monitoring. The white lines show the inactive channels (not yet incised). We mention the stream state: active, abandoned, or disconnected. Retro deformation is developed in 5-steps (A) to (E). Step A is the initial setting with river R1 in its pristine form with a straight channel. Step E is the final configuration that matches the existing hydrological network. We specify the additional offset increment and the amount of cumulated slip since the deformation begins. (F) Same step as step E (actual configuration) without interpreted lines.



These measurements suggest the three rivers have recorded a different amount of sinistral displacements, which correspond to a differential beginning of their hydrological development. The deepest and largest river bed R₁ records the maximum shift. We interpret R₁ as the oldest hydrological network capable of recording the earliest deformation while deepening its active channel. The rivers R₂ and R₃ are narrower and shallower. They may have developed later and recorded less amount of sinistral movement. We use the whole hydrological catchment to understand the backslip along the scarp (Figure 4.16). In step 1, we restore the initial configuration based on the hypothesis that the oldest river, R₁, was linear and undisrupted at that time (Figure 4.16a). In this configuration, three western head streams match with three tail streams. The other streams are not yet developed by that time. In step 2, we applied a 30-m left-lateral increment (Figure 4.16b). The previously activated streams remain connected (Figure 4.16b). Because one new tributary matches with one tail stream, we consider this river is activated at that time. We apply the same reasoning for the entire restoration.

In step 3, the cumulated sinistral displacement of 70 m shifts the river R₂ matching with its former tail (Figure 4.16c). The river R₂ starts to incise and acts as a 'chronometer' of the deformation. Note that in fine, in step 5, the river R₂ has cumulated a total amount of ~245 m corresponding to the maximal distance R_{2max}. In step 4, we increment 140 m of the sinistral slip, which results in the alignment of R₃'s head and tail (Figure 4.16d).

In step 5, the fault has offset the R₁, R₂, and R₃ rivers of their respective maximal sinistral displacement R₁ ~ 315 m, R₂ ~245 m, and R₃ ~105 m (Figure 16e). The cumulated sinistral displacement to reconnect all the actual rivers is 315 ± 15 m, and it constitutes the largest offset of Peninsula Ainsworth across the moraine deposit.

IV.4.2 Trench analysis

We excavated a trench (54.375606°S, 69.449923°W) across the 4-m fault scarp, in a single slot of 6-m long and 2.5 m deep. We collected five samples in the Ainsworth Trench. Each piece was selected in recognized units and originates from single charcoal. Radiocarbon measurements were made at Laboratoire de Mesures du Carbon 14 (LMC14, CEA Saclay, France). The ages are calibrated using Oxcal version 4.4 (Ramsey, 2017; Ramsey, 2009) with the southern hemisphere calibrating curve SHCAL20 (Hogg *et al.*, 2020). The raw ¹⁴C ages (yrs BP)

and the calibrated ages (cal yrs BP) are available in Table 4.1. Specific attention was drawn onto samples C1 (N°SacA 60318) and C2 (N°SacA 61164). These sample activities (pMC) are close to the background activity, meaning that they are at the limit of datable ¹⁴C method. However, sample C1 can be dated because its activity is higher than twice the standard deviation σ (Stuiver and Polach, 1977). Besides, the activity of C2 differs from the background between 1 and 2 σ . Therefore, the LMC14 laboratory reported this age as “apparent” (Mook and Plicht, 1999; Stuiver and Polach, 1977). This apparent age is a minimum age. The C2’s apparent age is reported in yrs BP as the calibration method is not applicable in this case.

Sample	N° SacA	IGSN	Nature	Mass spectrometry measurements (ages and error indicated in yrs BP)					Calibrated ages (cal yrs BP)		
				Mg C	Delta ¹³ C	pMC	¹⁴ C Age	Err	From	To	Unit
C1	60318	IEROY000T	Charcoal	1,66	-22,10	0,567 ± 0,141	41 600	2000	51 139	42 276	U5
C2*	61164	IEROY000U	Charcoal	0,96	-18,30	< 0,41094 *	> 44 100	NA	NA	NA	U5
C4	60319	IEROY000V	Charcoal	0,89	-33,60	68,168 ± 0,232	3 080	30	3 370	3 212	U2
C5	60320	IEROY000W	Charcoal	1,29	-24,30	62,078 ± 0,209	3 830	30	4 402	4 097	U1
C6	60321	IEROY000X	Charcoal	1,35	-26,20	64,336 ± 0,213	3 545	30	3 959	3 718	U1

*Apparent age close to background : $1\sigma < \text{measured sample activity} < 2\sigma$. Error on ¹⁴C age, and calibration not applicable (NA).

Note: Measurements made at LMC14, CEA Saclay, France using the accelerator mass spectrometry (AMS) ARTEMIS, following preparation protocols (Dumoulin et al., 2017, Moreau et al. 2013). Radiocarbon ages are calculated using Mook and Van der Plicht (1999).

The ages are calibrated using Oxcal version 4.4 (Bronk Ramsey, C. 2009, Ramsey, C. 2017) with atmospheric curve SHCal20 (Hogg et al., 2020). N°, field name; SacA: lab number; IGSN: International Geo Sample Numbers; Mg C: amount of carbon in mg ; Delta ¹³C: percent of isotope ¹³C; pMC: percent Modern Carbon.

Table 4.1: Mass Spectrometry Measurements of Radiocarbon Samples.

The trench walls expose a clear stratigraphic record of successive lake, glacier and peat bog deposits. A progradation sequence with unlithified sediments (unit 8 to unit 3) is capped by recent peat bog (unit 1 and 2) (Figure 4.17). The lowest unit 8 (not apparent on the mosaic) is a massive blue clay covered by fine clay-silt bottomsets (Unit 7). These units could be deposited in a paleolake in paraglacial environment. The alternating light-coloured, coarse-grained and dark-coloured, fine-grained suggested they could represent rhythmites (Figure 4.18a) (Ashley, 1975; Menzies, 1996; O’Sullivan, 1983). Figure 4.18a shows climbing ripples above wavy laminations, which indicates not only an increase in bed sediment load (Jopling and Walker, 1968) but also the current direction toward the north. The gradational contact between units 8, 7, and 6, joined with

the increasing grain size, expresses the energy increase due progressive progradation of river or ice advance into the paleolake (Figure 18 b, c).

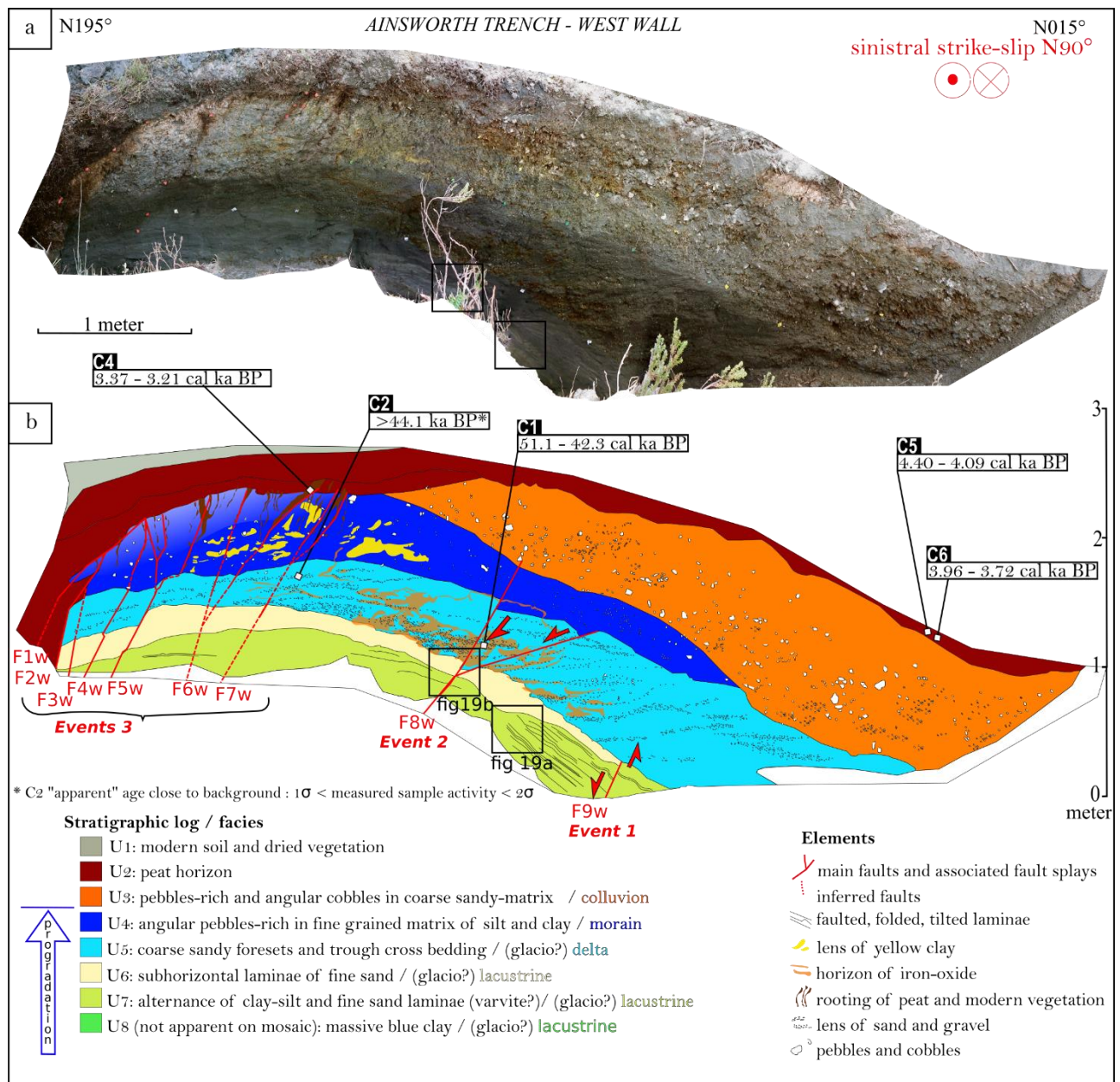


Figure 4.17: Mosaic views of the trench's (-54.375606, -69.449923) western wall across the Ainsworth section (a) photographic mosaic; (b) with interpretative logs and sample locations. Details on ^{14}C samples are given in Table 4.1 (all the ages are calibrated, excepting the sample C2). The ages are calibrated using Oxcal version 4.4 (Ramsey, 2017; Ramsey, 2009) with southern hemisphere calibrating curve SHcal20 (Hogg et al., 2020). We use the modified Udden–Wentworth grain-size

scale (Benn and Evans, 2014; Blair and McPherson, 1999). *The units U8 to U4 show the gradual facies shifts during period of ice advance*

This vertical profile is a typical of progradation into a paraglacial lake (Benn and Evans, 2014; Brodzikowski and Loon, 1990; Menzies, 1996). The lack of transition between units 6 and 5 suggests part of the sequence may have been eroded. This sharp erosional contact and the coarse grain size of unit 5, suggest a substantial (meltwater?) energy increase (Figure 4.19 b, c). The upper units evidence an environmental change from ice-distal to ice-contact system. The rapid ice-advance is shown by the succession of a sandy-gravelly foresets (unit 5 delta) covered by clast-supported diamict (unit 4 moraine ice-contact). Samples C1 and C2 were collected in the terminoglacial unit 5. A lacustrine environment, probably associated with a paraglacial context, was therefore present at this place between 42 and 51 ka. Considering the lithofaciès mentioned above, we propose that units 8 to 5 correspond to the last interglacial, and unit 4 is associated to the last MIS 2 glacial advance.

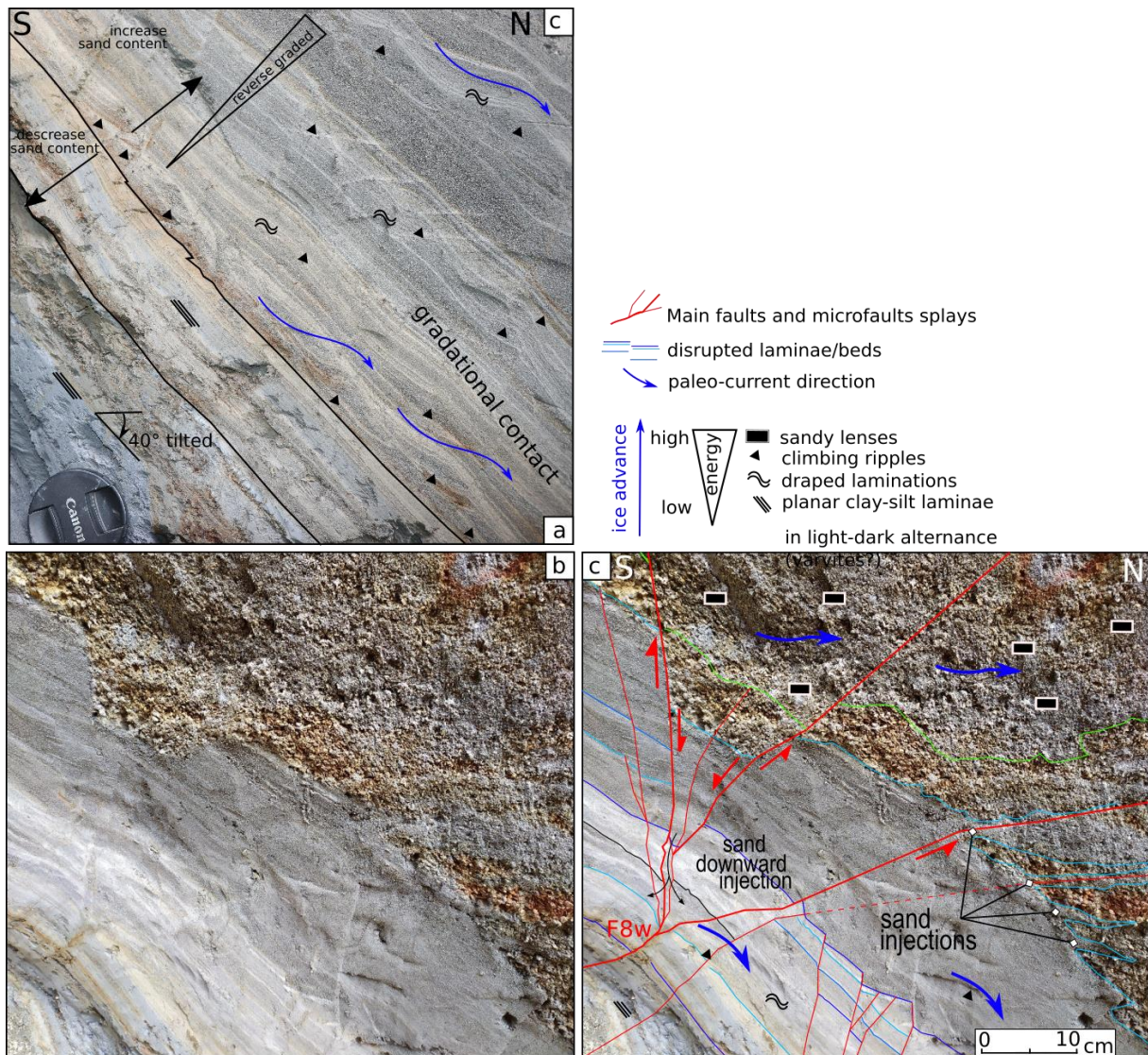


Figure 4.18: (a) Zoom in the unit 8 to 6 in the lower western wall. Note the sequence with succession of wavy laminations, climbing ripples, and upward increase in sand content. (b, c) Zoom in the lower western wall showing the sharp erosional contact between units 6 and 5.

Brittles structures cut this unlithified sequence. Faults 1 to 7 have disrupted the unit 8 to 2, and opened cracks, which were fed by peat bog dated to $3\,290 \pm 80$ yrs (Figure 4.19). These faults are associated with the most recent ruptures event 3. The fault F8 ends in the colluvium layer unit 3 and is related to a rupture E2 younger than units 5 and 4. The most ancient rupture identified is event 1, and is associated with the fault F9. F9 stops in unit 6 and is eroded by unit 5. In addition to faulting, the units 8 to 6 are affected by a 40° tilt that occurred prior to the deposition of unit 5 (Figure 4.18). Therefore, event 1 might have triggered severe uplift and faulting with a minimum age > 42.3 cal ka BP.

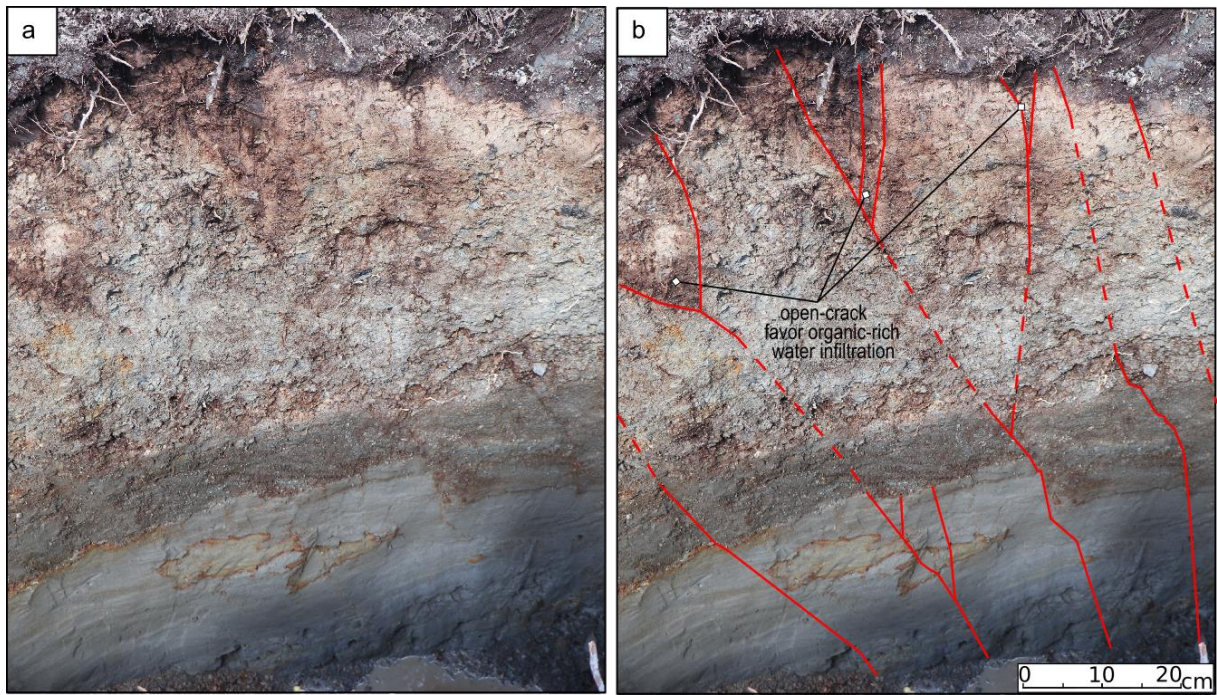


Figure 4.19: Zoom in the eastern wall showing the brittle faults in unlithified sediments connected to sub-surface open-cracks.

All the faults are rooted probably deeper than unit 8 (Figure 4.20 a, b). The dipping of these faults suggests they converge at depth. We suppose the trench's faults are comprised in a flower structure (Figure 4.21). The cumulated vertical movement along these faults is relatively small compared to the scarp morphology. Due to the trench limited extents limits, determined by the presence of water in the sediments, we may miss several splays north and south of the trench. These major fault splays may explain the cumulated vertical displacement. The flower structure defined here the kilometeric scarp, a linear antiform, that is bounded longitudinally along its flanks by the upward and outward diverging strands (Harding, 1985) (Figure 4.21).



Figure 4.20: (a, b) Zoom in the bottom of the trench showing the fault *g* in the western wall (*F_{gw}*) and in the eastern wall (*F_{ge}*) that connect at depth, and disrupt the lowest unit 8.

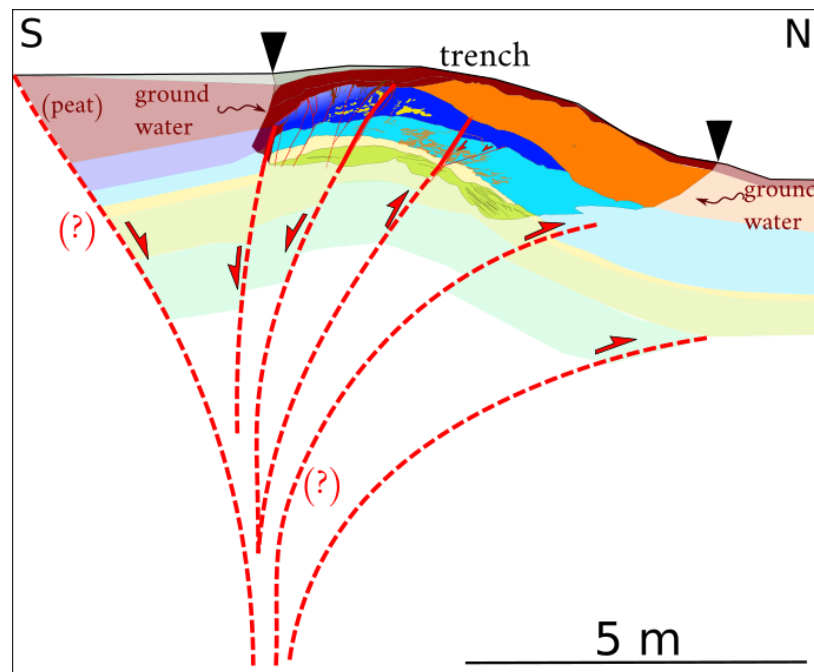


Figure 4.21: Interpretation of the trench site as a flower structure. Black triangles point the trench.

IV.4.3 Dating last glacial retreat to constrain long-term offset

To identify the potential complexities between glacial and tectonic deformations, we map the glacial morphologies and the rupture traces (Figure 4.22a). We report our dated samples, datings available in literature, and associated dating methods. This provides a reliable framework for assessing velocity from offset values (Zielke *et al.*, 2015). In the peninsula, the systematic smooth western stoss-end and the sharp eastern lee-side of the roches moutonnées suggest a paleo ice-flow toward the east (Figure 4.22b). It implies that the ice-sheet that covered the entire Peninsula was mostly fed by the paleo-glaciers Cerro Señoret, Marinelli and Ainsworth grounded on the Darwin Cordillera northern flank. On the peninsula Ainsworth the glacier merged in the Almirantazgo lobe in an eastward motion.

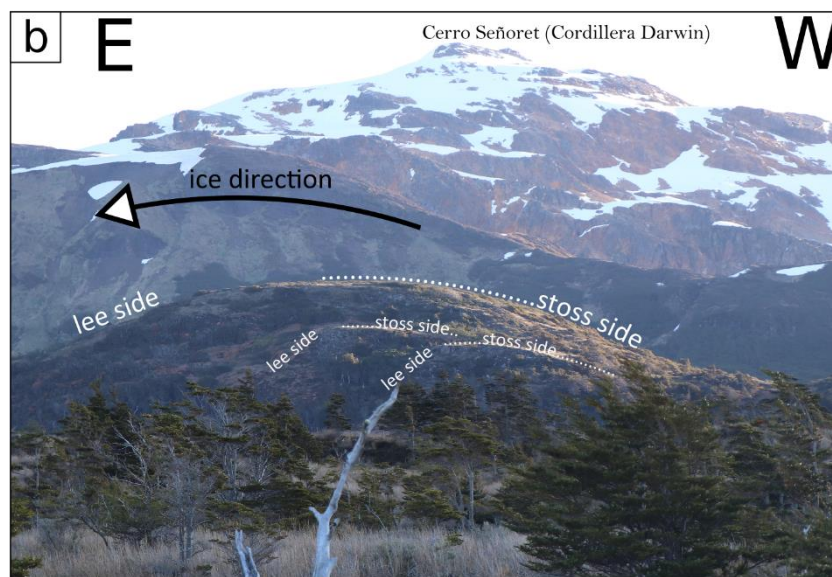
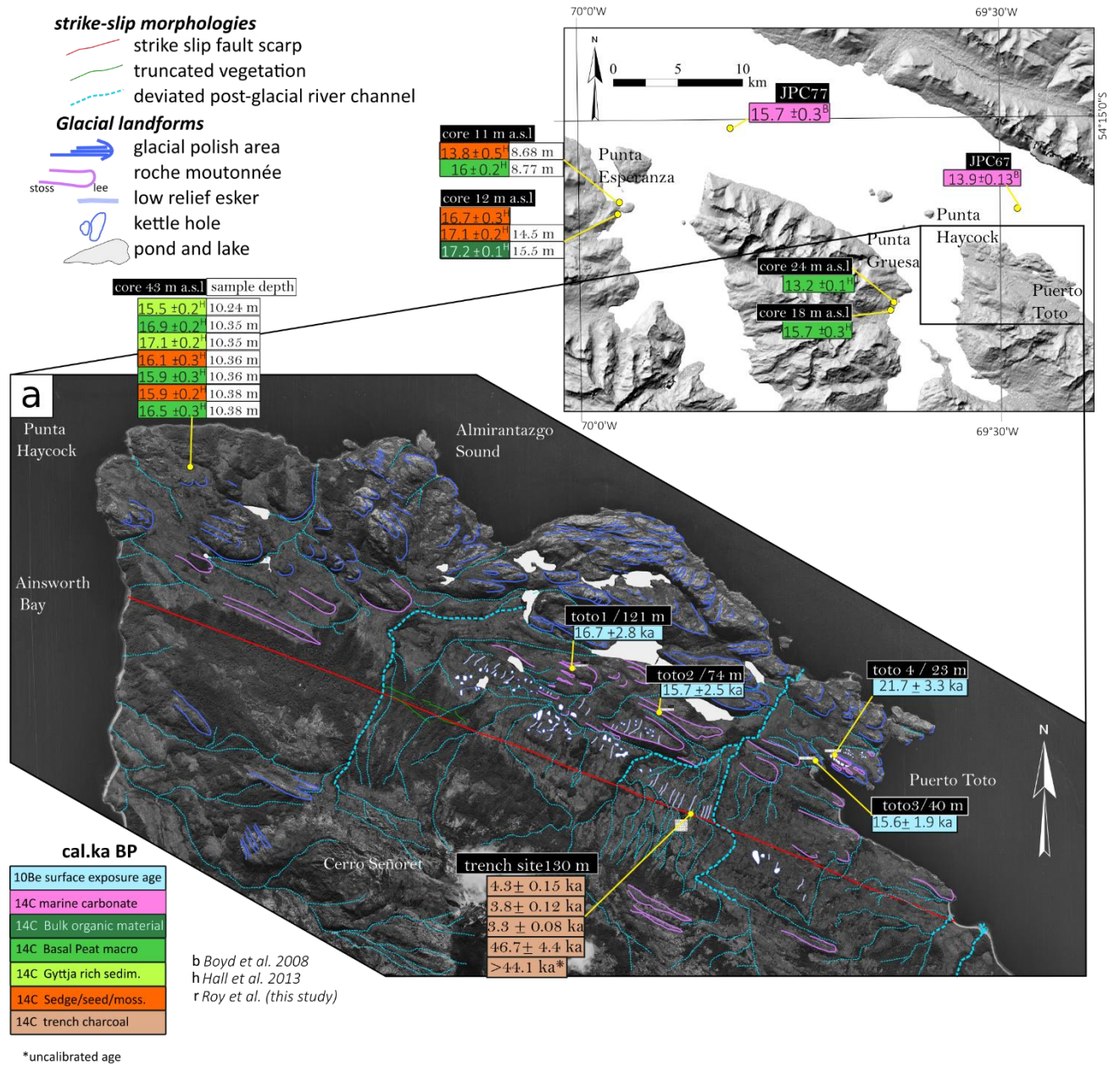


Figure 4.22: (a) Glacial and strike-slip geomorphology map of Ainsworth Peninsula. Inset shows the location regional dating available. (b) A roche moutonnées hillock on the Cordillera Darwin northern foothill, on which smallest scale roches moutonnées are shown. These features differ from bedrock glacially polish due to their asymmetric shape related to the ice-action. On side is moulded (stoss-side) and the other is steepened (lee-side) (Sugden and John, 1976).

We sampled two roches moutonnées and two glacial polishes in Peninsula Ainsworth. We collected an additional sample of Cordillera La Paciencia's foothill (see table 2 for locations). Samples were prepared at ISTERre following the chemical procedures described by Brown et al. (1991). The Laboratoire National des Nucléides Cosmogéniques (LNMC, Cerege, Aix-en-Provence, France) performed the ^{10}Be analyses. We detail in Table 4.1 the methods used for calculating of the production rate and the shielding factors. With this method we date the time by which the rock became exposed to cosmic rays starting the cosmogenic nuclide production (Dunai, 2010; Nishiizumi et al., 1989). Regarding the smooth shape sampled surfaces, it leaves only little doubt that the last ice–bedrock interface was erosive, and erased the cosmogenic memory of eroded bedrock surfaces. Such surface found on glacially over-ridden bedrock usually provide reliable deglaciation ages (Briner et al., 2006; Dunai, 2010; Fabel et al., 2002).

Sample	Lat (°S)	Long(°W)	Nature	Altitude (m.asl)	$^{10}\text{Be}^1$ (at/g)	Err, $^{2\ 10}\text{Be}$ (at/g)	Prod. rate ³ (at/g/yr)	Err. prod. rate (at/g/yr)	Shielding ⁴	Age (yrs)	Err (yrs)
CP01	54,42522	69,01570	polished surface	41	56 972	3 039	4,50	0,39	0,929809	12 815	1 786
toto-1	54,36083	69,47073	Roche moutonnée	121	86 488	7 266	5,25	0,45	0,998799	16 715	2 817
toto-2	54,36493	69,45719	Roche moutonnée	74	77 489	6 016	5,01	0,43	0,998799	15 685	2 547
toto-3	54,36978	69,43087	polished surface	40	74 765	2 698	4,84	0,42	0,999604	15 613	1 912
toto-4	54,36924	69,42814	Roche moutonnée	23	101 718	6 646	4,75	0,41	0,999161	21 697	3 272

¹Measurements made at Laboratoire National des Nucléides Cosmogéniques LNMC (Cerege, Aix-en-Provence, France) using the accelerator 5 MV ASTER and following procedure Braucher et al., (2015).

²Uncertainty includes: measure (number of count), standard (certification), average standard measures (machine), systematic error (machine external error 0.5% Arnold et al., (2010).

³Production rate have been calculated following Stone et al., (2000) using modified scaling function Lal et al., (1991).

⁴Topographic shielding calculator Stoneage.ice-d.org Version 2 http://stoneage.ice-d.org/math/skyline/skyline_in.html

Table 4.2 ^{10}Be measurements

Excepting the totō₄ sample, discussed later, our data set describes age-equivalent around 16 ka BP which agrees with literature datings available in the area. Indeed, in Punta Haycock, Hall et

al. (2013) dated organic materials in cores originating from peatbog above glacial sediments, ranging from 17.1 ± 0.2 to 15.5 ± 0.2 cal ka BP. In Punta Esperanza and Gruesa, the same method was used to date the Ainsworth Fjord deglaciation from 16.4 ± 0.5 to 13.8 ± 0.5 cal ka BP, and Brook Fjord deglaciation 17.2 ± 0.2 to 16.1 ± 0.2 yr BP (Hall *et al.*, 2019). Furthermore, Boyd *et al.*, 2008 cored marines sediments in the Almirantazgo Sound evidencing a major transition from ice-proximal to ice-distal facies between 15.5 to 12.5 ka BP. Therefore, based on our results and previous contributions, we can reasonably propose a minimal limiting deglaciation age of the Ainsworth Peninsula at 16.7 ± 2.8 ka BP (totō₁).

Despite the samples totō₄ and totō₃ are distant of <200 m, they belong to two distinct hillocks. The age uncertainty of totō₄, makes it slightly older than the other samples. This sample could have undergone less glacial erosion, which could have preserved inherited cosmogenic component from previous exposures. According to the local data set, we cannot use this sample to constrain the ice recession in this area.

This result evidences the Almirantazgo lobe irreversibly retreated in the Darwin Cordillera by 16.7 ± 2.8 ka. In contrast, at the same period in the eastern region, authors suggest that the Fagnano lobe was standing near the limit RP₂ (Figure 1.10). (Coronato *et al.*, 2009; Waldmann *et al.*, 2010), with a final retreat occurring about 11.7 ka (Waldmann *et al.*, 2011). Because the Fagnano and the Almirantazgo lobes were both fed mainly by the Darwin Cordillera ice-sheet (secondary fed by alpine glaciers), it is difficult to explain how their respective final retreats would have occurred at such different times. Our result strongly suggest the final retreat of Fagnano Lobe occurred earlier than the proposed age.

IV.5 Discussion and Conclusion

Our study evidences the modern activity along the Ainsworth fault section and identifies the two last major ruptures in 1879 and 1949 using tree-ring and trenching analyses. The 1879 and 1949 ruptures have been recorded in tree-rings 170 km further east in Tierra del Fuego (Pedrera *et al.*, 2014). Paleoseismic trench investigation evidences one or two of these ruptures disrupted the La Blanca section 190 km farther east (Roy *et al.* 2020, Chapter 3). Also, the 1949 rupture was identified in disrupted fences 195 km east of Ainsworth Peninsula, and survey in the morphology suggested this rupture ends 10 km before the Atlantic coastline (Roy *et al.*, 2020). Consequently,

based on these primary evidences, our results demonstrate a minimal subsurface rupture length (RLD) of ≥ 170 km in 1879, and of ≥ 200 km in 1949. It implies two giant earthquakes in less than one century in Tierra del Fuego.

Following the empirical relationships between RLD and magnitude, and using the regression coefficient for strike-slip configuration (Wells and Coppersmith, 1994), we estimate the moment magnitude of 1879 $M_w \geq 7.66 \pm 0.24$ and 1949 $M_w \geq 7.76 \pm 0.24$. Our estimate of 1949's magnitude is consistent with the instrumental record $M_w 7.75$ (Lomnitz, 1970) and with a coseismic horizontal offset of 6.5 meters in Argentina (Roy et al., 2020).

On one hand, our result on 1879's earthquake propose the first direct estimate of its magnitude and rupture length, which agree with previous intensity value MM VII (Lomnitz, 1970). On the other hand, our results imply that two giant earthquakes occurred in less than a century in Tierra del Fuego. It disagrees with the accepted recurrence interval of major earthquake ~ 700 to 1000 years (Costa et al., 2006; Roy et al., 2020, and this thesis Chapter III; Waldmann et al., 2011).

The peaks of tree-ring eccentricity between 1970 to 1995, and 2007 to 2014, remain not understood, and uncorrelated with significant earthquakes. Also, if moderate earthquakes or wind-storms can disturb the trees environment, impacting tree-rings, then it necessarily challenges the dendroseismological method. To overcome this unknown, it is mandatory to study climate-driven events on this time-scale, and to sample additional trees localized off- and on-fault.

Using high-resolution imagery, field mapping, ^{10}Be and ^{14}C dating, we measure the long-term offset, and propose two hypotheses for the displacement onset. The deviated rivers incise the Quaternary cover, consisting of eskers field and roches moutonnées from the last glacial maximum. It is unlikely that the eastward paleo-ice-sheet carved channels with an orthogonal flow direction. Indeed, under subglacial conditions, only ice-directed meltwater channels are likely to incise parallel to ice-movement or sub-parallel to its ice margins (Sugden and John, 1976; Menzies, 1996). Contrary to the measured rivers, a meltwater channel is usually characterized by an abrupt inception and termination in bedrock (Sugden and John, 1976; Walder and Hallet, 1979; Bennett and Glasser, 2011). These rivers crosscut the Quaternary cover, which were formed in

an outwash plain by retreating glaciers. Thus, we postulate that these rivers are developed during the deglaciation following the local LGM. Furthermore, our ^{10}Be ages and previous contributions, in the Peninsula Ainsworth indicate a minimum limiting age for irreversible ice retreated at 16.7 ± 2.8 ka BP. Considering a 315 ± 15 m sinistral offset, it implies a postglacial slip-rate of 19.5 ± 4.2 mm/yr.

A less likely hypothesis is that the rivers were carved during the last interglacial phase, implying that the drainage may have remained activated under the LGM ice-sheet. Based on our radiocarbon dating, the last interglacial maximal age in the Peninsula is $> 46.7 \pm 4.4$ cal ka BP, which results in a minimal long-term slip-rate of $> 6.8 \pm 0.8$ mm/yr. At first glance, this rate is akin to the Argentinian MFF geomorphic slip-rate of 6.4 ± 0.9 mm/yr ([Roy et al., 2020](#)). However, two significant inconsistencies remain. Firstly, the drainage system cuts both the last interglacial sequence and the LGM moraine deposit observed in our trench. Therefore, the cross-cutting relation suggests these rivers cannot be older or coeval to the ultimate interglacial. Finally, the hypothetical river preservation under LGM ice-sheet conflicts with contemporary orthogonal polishing of extensive bedrock surfaces. The conservation of these depressions is especially unusual under one 1-km thick LGM ice lobe running on the Darwin Cordillera northern flank ([Hulton et al., 2002](#)).

Our data suggest that the glacial and tectonic imprints are tightly intertwined in the Peninsula Ainsworth. Based on our analysis, the Western MFF long-term slip-rate is considerably faster than its eastern counterpart in Tierra del Fuego. Interestingly, the postglacial slip-rate is moderate to the east, whose LGM-ice-sheet was thinner and less extensive ([Rabassa et al., 2000](#); [Coronato et al., 2008](#); [Coronato et al., 2009](#); [Waldmann et al., 2010](#); [Rabassa, 2011](#)). These findings suggest that the Magallanes Region of Chile's strike-slip fault is broadly active since the Last Glacial Maximum. The intriguing coincidence between the onset of fast slip accumulation on the Magallanic strike-slip fault and the end of the last ice age strongly suggests an external forcing. Future efforts should evaluate postglacial unloading as a potential cause for increased strike-slip-rate in the Chilean Territory.

Acknowledgments

We would like to deeply acknowledge Captain Fredy Moreno Azua, Camilo Uribe Padilla, Andrés Fabián Huenchueo Ruiz (Nativo Expediciones) and Annemie Eyer for their direct and encouraging support in the field in 2018 and 2019. We warmly thank Ivette Martínez, and Cesar for their help in Caleta María. We are very appreciative of the precious testimonies on the regional history that German Genskowski and Maricela Díaz offered to us. We would like to thank Matías C. Ghiglione for bringing us on the right track in Tierra del Fuego (IDEAN Instituto de Estudios Andinos). This work is part of the Ph.D. thesis of Sandrine Roy funded by the French Ministry of Higher Education and Research. The French CNRS-INSU (Chrisitan Sue - project PICS and SYSTER) provided additional supports. ^{14}C ages were measured by the Plateforme Nationale LMC₁₄ (LSCE (CNRS-CEA-UVSO)-IRD-IRSN-MC) Service National de l'INSU. We thank the LMC₁₄ analyse group Lucile Beck, Jean-Pascal Dumoulin, Emmanuelle Delque-kolic and Christophe Moreau for the fruitful discussions. We are grateful to the EDYTEM laboratory for dendrochronology expertise and tree-ring art work. We warmly thank Fabien Massot for his precious and unswerving administrative support.



Halaháches ou Kotais,
Espíritu de la Ceremonia del Hain

Painting generously shared by Elby

Pinturas de propiedad intelectual
Pertenciente a la artista visual Elby
Huerta - Chile Santiago; Uso exclusivo
para tesis, derechos reservados de la
autora.

Copyright © Elby Huerta

CHAPTER V:

Numerical modeling of strike-slip fault during icecap growth and melting

Abstract

This chapter is dedicated to the modeling of strike-slip faults response to climate-driven changes in ice volumes on Earth's surface. We first introduce the history of the glacial isostatic concept and the birth of subsequent scientific questioning on glacially induced seismic activity. A complete review of recent modeling approaches is formulated and their implications on the understanding of the Quaternary seismic activity of Fennoscandia, Northern America, Basin-and-Range, and the Polar regions. The Magallanes-Fagnano fault is an exceptional object for studying glacial unload and pulse of tectonic activity. Indeed, at Last Glacial Maximum, the Chilean part of the fault was under 1-km thick ice-sheet, contrary to the eastern Argentinian section, which was almost free of ice. The comparison of the long-term slip rate of these regions suggests that the western MFF moved significantly faster than the eastern section since the glacier retreat. Here, we use analytical and finite element models to investigate the fault response to glacial (un)loading. Several earth models and glaciation scenarios are experimented. We explore the effect of (1) the obliquity of the ice-sheet comparatively to the fault position (2) duration of glacial period (3) retreating velocity of the ice and (4) the influence of plate velocities. Our results show the loads applied on Earth surface exert a significant control on the rate of strain accumulation on strike-slip fault. The Earth material rheologies, the load history and the obliquity of the fault with respect to the icecap, are the primary parameters which govern the fault response. Glaciation favors fault locking and mutes the fault's rupture, and the deglaciation implies a slip pulse. However, the predicted cumulated slip delayed is negligible compare to the observed slip-rate contrast between east and west Magallanes-Fagnano Fault.

V.1 State-of-the-Art

V.1.1 A concise history of glacio-seismotectonics

Glacio-seismotectonics refers to the past and continuing effects of ice sheets and glaciers (Stewart *et al.*, 2000) on contemporary crustal deformation and seismicity. It primarily implies the glacial isostatic adjustment (GIA) and subglacial erosion.

The oldest questioning on GIA dates from 1491, in the Swedish town of Östhammar, when it has been noticed that harbor was no longer possible to reach by the fishing-boats. Although the profusion of the Swedish investigations about land uplift – looked upon as a water decrease during the 16th and 17th centuries, it is only in 1865 that the Scottish geologist Thomas Jamieson first formulated:

“It is worthy of remark that in Scandinavia and North America, as well as in Scotland, we have evidence of a depression of the land following close upon the presence of the great ice-covering [...] It has occurred to me that the enormous weight of ice thrown upon the land may have had something to do with this depression. [...] Then the melting of the ice would account for the rising of the land, which seems to have followed upon the decrease of the glaciers.” (Jamieson, 1865)

Later, T. Jamieson described the uplift as a crustal rebound due to the ice covers unloading, i.e., he suggested the crust having an elastic behavior (Jamieson, 1882). Without proof of the upper crust's elasticity and the lack of significant local earthquake at this epoch, the idea defended by Jamieson did not receive any support until the 1890s. The first map of Fennoscandia uplift (De Geer, 1890) stated that firstly, the phenomenon was not latitude-dependant. A massive uplift could not be explained by regional water decrease but only by a land uplift.

“The immense loading of the ice gradually caused a local depression of the Earth's crust which is supposed to be in a fairly sensitive state of equilibrium, and that the area after the deglaciation slowly raised again although it has scarcely succeeded in fully reaching its original level.” (De Geer, 1890)

This view was later reinforced by De Geer and his colleagues (De Geer, 1940), who produced a master chronology of varves* series in Sweden, which presented clear evidence of glacial

adjustment depression and subsequent uplift of Fennoscandia. Moreover, De Geer hinted at the possibility of deglaciation associated with large earthquakes that fractured the bedrock and shattered the ice, which resulted in breaking the sub-surface to very bouldery seismic moraines (De Geer 1940, p. 113-132).

“It seems as if the symbiosis between boulder-producing earthquakes and moraine-building oscillating ice-boulders commenced about at the year —1050 before the end of the Ice Age, or 9640 years before A.D. 1900”. [p158]

“But now we find indications of such more intense earthquakes at the very end of the Ice Age. At exactly the same epoch, it is well-known that especially the central parts of Scandinavia have been subjected to a very considerable upheaval of land”. [p177](De Geer, 1940)

or readers with historical interest in understanding glacial isostatic adjustment, we refer to the excellent papers (Bergsten, 1954; Ekman, 1991; Ekman, 2013; Whitehouse, 2009; Mörner, 2014) and other references cited thereafter.

V.1.2 Glacially induced earthquake in stable continent cratons

V.1.2.1 The Scandinavian paradox

Afterward, the northern Scandinavia was the classical region for glacial isostatic adjustment studies. The key point of this part of the world lies in the existence of multiple large superficial faults in a stable continental craton (Kinck *et al.*, 1993). Consequently, earthquakes with large magnitudes are generally not expected in these areas. This paradox yielded to introduce a new aspect: the possible linkage of seismic activity with changes in stress during glacial isostatic adjustment (Mörner, 1969; Mörner, 1972). Soon after, intense faulting and fracturing were documented in Finnish Lapland (Kujansuur, 1964), southern Norway (Feyling-Hanssen, 1966), Swedish Lapland (Lundqvist and Lagerbäck, 1976), and southern Sweden (Lagerlund, 1977), mostly on normal and reverse faults.

The recognitions of postglacial fault scarps and glacially induced earthquakes infiltrate into the mainstream with the Pärve fault studies. The Pärve fault is an imposing example of a 150 km long thrust, which disrupts the Late Weichselian (25 ka) glacial markers, including eskers,

drumlins, meltwater channels outwash plains (Figure 5.1). It delineates a vertical displacement of up to ~30 meters. Seismic activity is interpreted as a result of decreased normal stresses which migrated from northeast to southwest as the deglaciation proceeded (Lundqvist and Lagerbäck, 1976). For the authors, it appears indubitably that the rapid post-glacial rebound may in itself be the reason for sudden breaks. Thereby, the supposed inactive segments are described as active contemporaneous to the maximum glacial isostatic uplift at 9 000 – 8 500 years old (Mörner, 1978). If the Pärve fault segments are interpreted as a single post-glacial fault, in that case, a single major event of moment magnitude $M_w \sim 8$ may have shaped the entire fault scarp (Arvidsson, 1996).

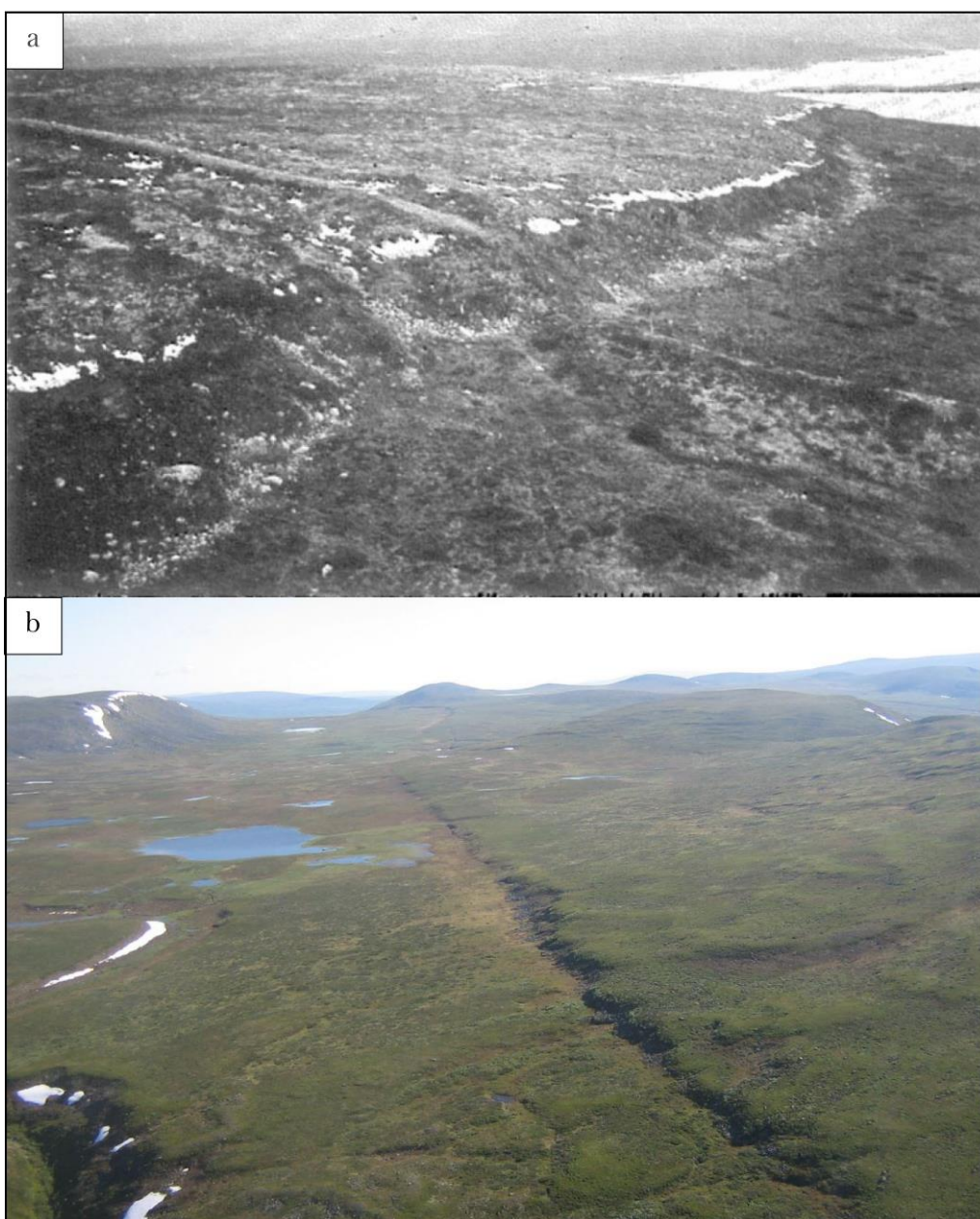


Figure 5.1: Photographs of the Pärve Fault, Sweden. (a) The Pärve fault cross-cuts an esker abruptly north of Lake Langasthe (lake in the background). Fault is the steep vertical scarp of several meters high, located from the lower-left to the upper-right corner. The esker is the small light-grey line offset in the picture center. Photograph by K. Lagerback (1975) from (Lundqvist and Lagerbäck, 1976). (b) The central Pärve by Björn Lund (Lindblom et al., 2015)

Several authors agree with Arvidsson's hypothesis that glacial isostatic adjustment in this region plays a significant role in triggering earthquakes of moment magnitude $M_w \sim 6-8$ (Muir-Wood, 1989; Stanfors and Ericsson, 1993; Lambeck et al., 1998; Ojala et al., 2019). In Scandinavia, the off-loading stress field is dominating over the stress from the plate tectonics during deglaciation (Muir-Wood, 1989; Gregersen, 2002). The ruptures have been interpreted due to decreased normal stresses on steeply dipping reverse faults (Wu et al., 1999; Turpeinen et al., 2008) during glacial, post-glacial, and late-glacial periods, and have been called glacially-induced faults. Since then, glacially induced faults are widely investigated in northern Scandinavia (Dehls et al., 2000; Gregersen, 2002; Lagerbäck and Sundh, 2008; Kukkonen et al., 2010; Palmu et al., 2015; Ojala et al., 2019) in central Sweden and Finland (Figure 5.2) (Smith et al., 2014; Malehmir et al., 2016; Ojala et al., 2019), as well as outside the formerly glaciated area in southern Sweden (Jakobsson et al., 2014), and in the southwest Baltic region (Al Hseinat and Hübscher, 2014; Brandes et al., 2018).

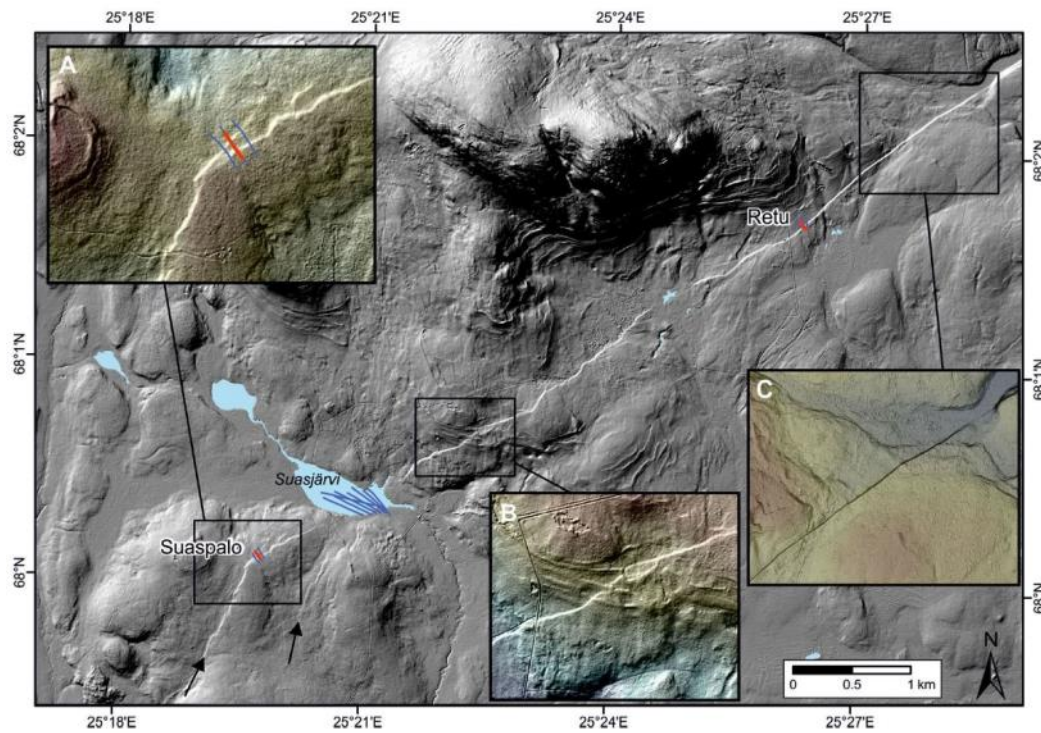


Figure 5.2: LiDAR-based digital elevation model of the Suasselkä post-glacial fault complex, Finland. Re-activated fault cross-cuts (a) a lateral drainage channels, and (b) a paleo proglacial lake shorelines (c) trench site of the study (Ojala et al., 2019).

Nowadays, the Weichselian Fennoscandia Ice Sheet is well known. It represented at its maximum of $\sim 2 - 3$ km ice thick (Patton et al., 2016). The Fennoscandia, Celtic Sea, and the Barents Sea Ice Sheets formed the Eurasian Ice Sheet Complex. The rebound of the earth's crust in response to ice sheet disintegration depends on the mantle's viscosity. Usually, the total rebound's magnitude is taken as about a third the ice thickness, so that a 2 - 3 km ice thickness load would produce a $\sim 0.7 - 1$ km vertical crustal response (Domack and Powell, 2018). During the Late Weichselian from 13 000 to 9 000 years BP, the slow warming period induced progressive melting of the ice sheets and yielded about 500 m of regional uplift (Aber and Ber, 2007). In 9 500 - 8 000 ka, the rapid temperature climb caused a fast retreat. Since 9 000 years BP, another 300 m of rebound took place in Scandinavia (Aber and Ber, 2007). Currently, the Scandinavia region is still experiencing crustal uplift with a maximum apparent rate about $8 \text{ mm}\cdot\text{yr}^{-1}$ (Dehls et al., 2000; Fjeldskaar et al., 2000) located in the central region of Sweden (Figure 5.3).

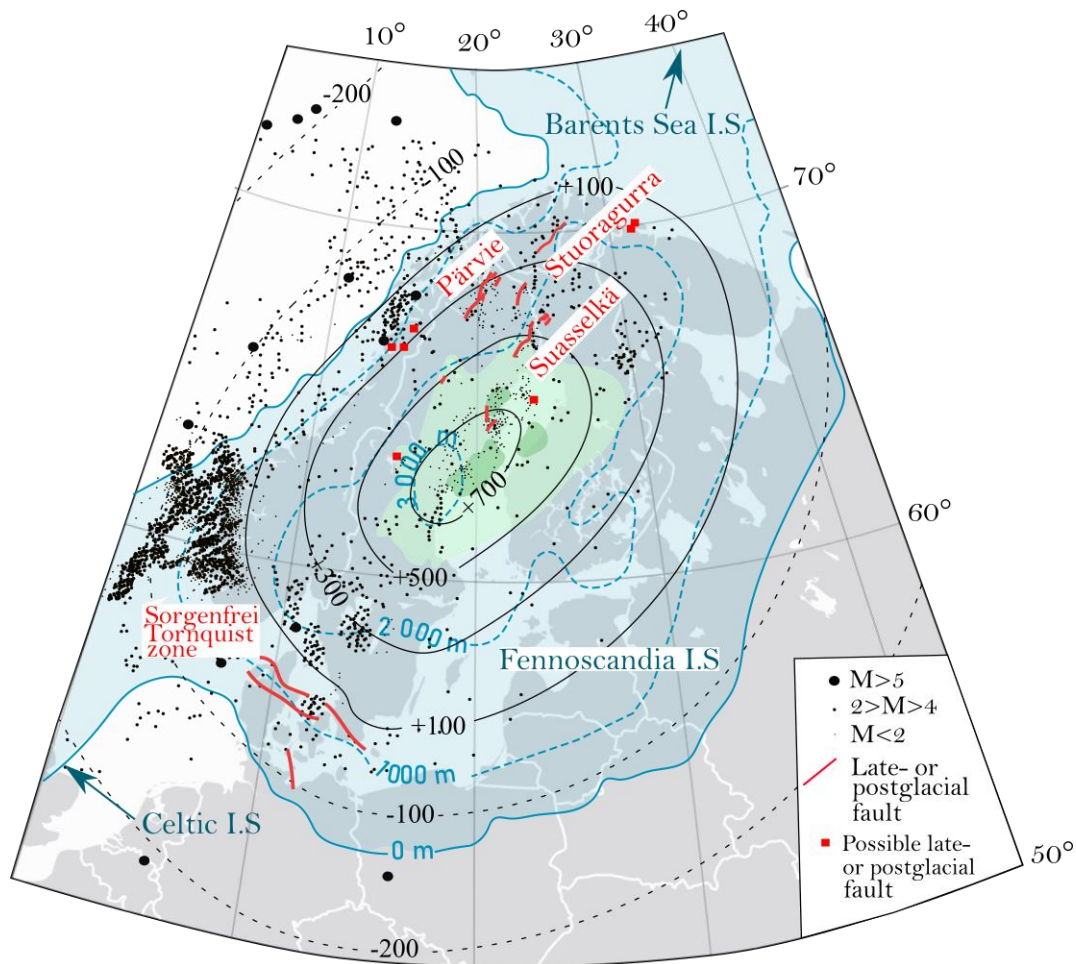


Figure 5.3: Influence of deglaciation on the deformation of Fennoscandia. Major faults are mentioned in red. The red lines indicate the location of late- or postglacial faults (PGF) and reactivated faults, and red squares show possible PGFs (Al Hseinat and Hübscher, 2014; Brandes et al., 2018; Muir-Wood, 1989; Lagerbäck and Sundh, 2008). The Late Weichselian (LGM) extension of the Fennoscandia Ice Sheet is shown as a blue cover (Patton et al., 2017). The blue dashed lines indicate ice-thickness at 20 ka in meter from interpolated ANU-ICE (Craig et al., 2016). The black contours show the cumulated rebound and subsidence since the LGM in meter (Gregersen and Voss, 2010; Möner, 1979). The light and dark green zones indicate patterns of maximum current uplift rates, respectively of 8 mm.yr⁻¹ and 9 mm.yr⁻¹ from present-day GPS data (Craig et al., 2016; Dehls et al., 2000; Kierulf et al., 2014). Seismicity records are from (Dehls et al., 2000; Gregersen and Voss, 2010; Lagerbäck and Sundh, 2008). Record of $M_w > 5$ since 1977 are from <http://www.globalcmt.org>.

V.1.2.2 The North American craton

The occurrence of glacially induced faults in stable intraplate interiors has requested interest in northern Europe and eastern Canada and northern U.S (Shilts *et al.*, 1992; Wu and Johnston, 2000; Steffen *et al.*, 2012). Though the early investigations focused on tiny faults in the Canadian Shield and the northern Appalachians, a similar concept emerged about the glacially induced faults. Small throws were first recognized in 1894 (Figure 5.4) in the striated glacial pavement in Saint John, New Brunswick (Matthew, 1894).

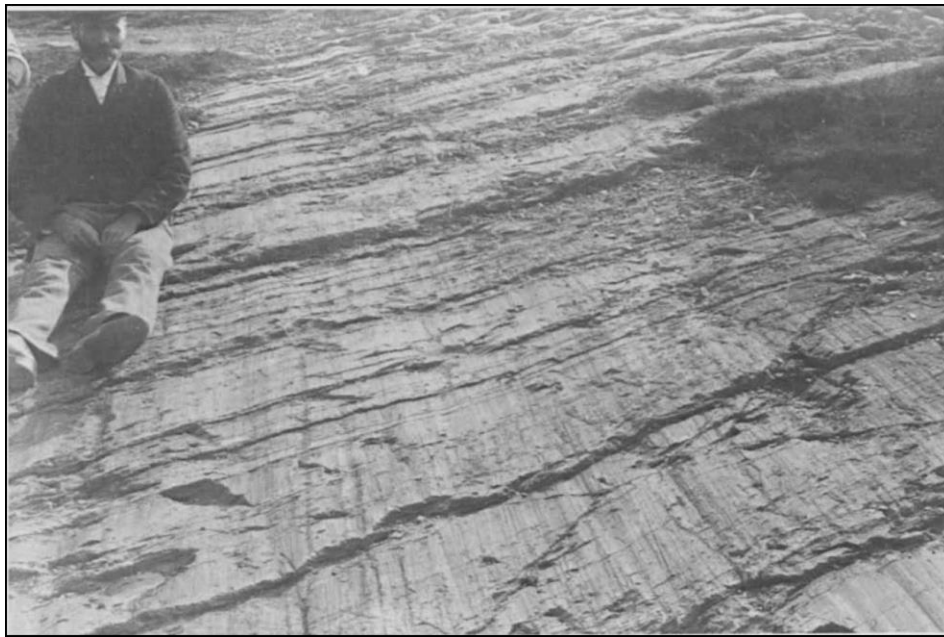


Figure 5.4: Small offsets in the striated glacial pavement from Saint John, New Brunswick photograph taken in 1890. Glacial striae are the thin lineaments intersected by the prominent offset, which crosses the picture from lower left to centre-right. Multiple small offsets are visible parallel to the main offset. Photograph by Geological Survey of Canada photograph GSC-204595 (1894) from (Adams, 1989; Aber and Ber, 2007).

The striae in bedrock are attributed to the last flow direction of the Laurentide ice sheet's southern margin at the end of the Wisconsin glaciation (Broster and Burke, 1990). The offset in these striae formed very soon after the Laurentide ice sheet retreated (Adams, 1989), with a few of them rounded which formed earlier contemporaneous with the glaciation (Broster and Burke, 1990). Authors concluded that it seems unlikely these small individual reverse faults were strongly seismogenic and represent only the response from stress release and flexural deformation of the

upper crust due to glacial loading and unloading. On the other hand (Shilts *et al.*, 1992; Broster *et al.*, 1994) presented considerable evidence for post- and Late-glacial paleoseismic events in the region like massive boulder rock-avalanche deposits, along with disturbed sediments and mass-flow deposits in local lakes. Taken these diverse features together, only earthquakes could produce these structures within southeast Canada (Aber and Ber, 2007).

The maximum extent of the Laurentide ice sheet covered North America from the 40° latitude up to Greenland (Figure 5.5), and the grounded ice occupied part of the Atlantic continental shelf (Stokes, 2017). The maximum ice limits were reached at different times in different regions of the Laurentide (Dyke, 2004; Clark *et al.*, 2009; Stokes, 2017). Nevertheless, it is generally admitted that the Laurentide attained its maximum position around 26-25 ka (MIS 2) and remained in this position until 18 ka (Stokes, 2017; Margold *et al.*, 2018). At that period, ice thickness varied from 50 m up to 3.4 - 3.6 km in the west of Hudson Bay (Simon *et al.*, 2016). Depending on the region, the rebound associated with this load would produce a vertical uplift ranging from 16 m up to 1 200 m (Domack and Powell, 2018). The average ice thickness was about 2.5 km (i.e., associated vertical stress was ~ 25 MPa), and the flexural stresses exceeded 50 MPa (Wu and Hasegawa, 1996). Authors conclude that depending on the rate of relaxation, the rebound induced stresses that can trigger seismic activity in these regions (Wu and Hasegawa, 1996). Ice-cores recorded in Greenland indicate progressive warming from 18 ka to 14.5 ka (Johnsen *et al.*, 1992; Dyke, 2004), which initiated a slow retreat of the north-eastern Laurentide (Clark *et al.*, 2009). Rapid deglaciation occurred around 12-10 ka, and melting was almost completed by 8 ka (Clark *et al.*, 2009). Today, the uplift rate of cm/year is still ongoing near the Hudson Bay, where the greatest ice thickness was located (Domack and Powell, 2018).

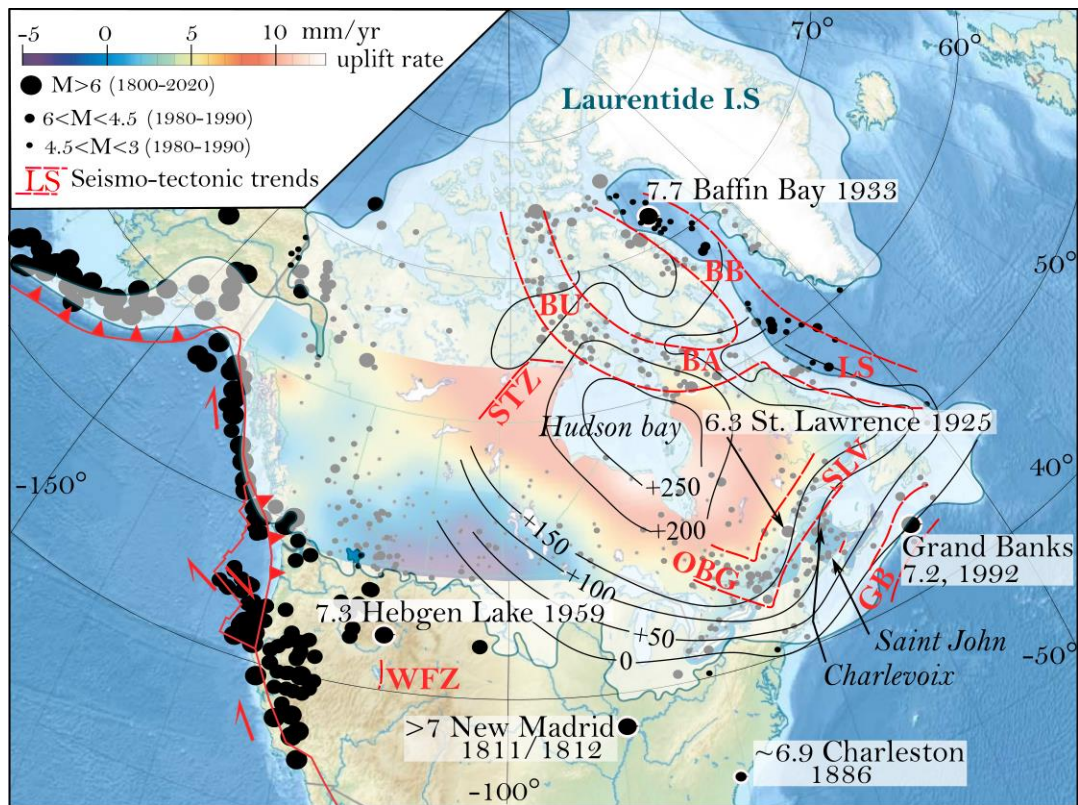


Figure 5.5: Relative location of the Laurentide Ice-sheet at Last Glacial Maximum with possible re-activated basement fault. The dashed red lines indicate seismotectonic zones in the North America craton from (Wu, 1998; Steffen et al., 2012) BA: Bell Arch; B: Baffin Bay; BU: Boothia Uplift; GB: Grand Bank; LS: Labrador Sea; OBG: Ottawa Bonnechere Graben; SLV: St. Lawrence Valley; S: Snowbird; WFZ: Wasatch Fault Zone. The extend of the Last Glacial Maximum is from (Patton et al., 2016; Margold et al., 2018). The black contours indicate the cumulated rebound and since the LGM in meters. The color bar suggests that Canada's uplift rates from CBN regional solutions are consistent with the post-glacial rebound signal (Henton et al., 2006). Record of earthquakes are: $M > 6$ from USGS; $6 < M < 4.5$ from (Wu, 1998); $4.5 < M < 3$ from (Hunt and Malin, 1998; Wu, 1998; Steffen et al., 2012).

Northeast America is supposedly a stable continental region. However, it contains several intense seismicity zones with large intraplate earthquakes of M_w 7-8 within the craton. Three examples of events occurred in 1811 in New Madrid M_w 7.2-8.2, in 1929 on Grand Banks M_w 7.2, in 1933 on Baffin Bay M_w 7.7, affecting the eastern margin of the continent. Looking at the event locations (Figure 5.5), while the New Madrid event is located in a region outside the Laurentide ice sheets, the last two sites are in areas that were right beneath the ice-load. According to

(Walcott, 1970) and (Stein *et al.*, 1979)'s model, the last two events mentioned above are related to Pleistocene deglaciation reactivating of basement faults. These faults are remnants of the Labrador Sea opening. Regarding the New Madrid event, Wu and Johnston (2000) show that the postglacial stress is too small to trigger a severe earthquake in this area because rebound stress decays rapidly away from the ice margin. Authors conclude that crustal failure may preferentially occur in a zone several hundred kilometers inside the maximum ice margin.

V.1.3 Glacially induced earthquakes along active plate margins

While deep tectonic processes are usually considered the primary cause of earthquakes in active margins, investigations highlight the impact of nontectonic processes such as ice-load, erosion rate, and water-level fluctuation in the last decade.

V.1.3.1 Effect of glacial erosion and current glacier retreat: the case of Alaska

Surface processes like the erosion rate may directly modulate tectonic deformation (Stewart *et al.*, 2000; Steer *et al.*, 2014). Along the Pacific plate boundary of central Alaska, the effect of unloading due to bedrock glacial denudation is superimposed on to the uplift mechanism from glaciers wastage (Meigs and Sauber, 2000; Stewart *et al.*, 2000; Sauber and Molnia, 2004). In glaciated mountainous terrains, the glacial erosion that resets the orogenic topography provides an additional compensatory uplift mechanism and may impact the Earth's response (Stewart *et al.*, 2000).

Southcentral Alaskan glaciers experience massive retreats and thinning at a rate of 1 to 5 m/yr. Models predict an associated vertical uplift about 0 to 50 mm.yr⁻¹ and horizontal displacements of 0-10 mm at variable orientations (Sauber and Molnia, 2004). The horizontal velocity of southern Alaska relative to stable North America is 10 to 40 mm.yr⁻¹ (Meigs and Sauber, 2000; Sauber *et al.*, 2000). Even though tectonics forces are the primary forces responsible for major earthquakes, ice-wastage forces are now considered an essential aspect for interpreting geodetic results (Sauber and Molnia, 2004). The same authors show the number and size of earthquakes increased in regions where glaciers retreated quickly between 1993 and 1995, in the eastern Chugach Mountains.

These observations are also supported by the Laur16 model (Simon *et al.*, 2016) of long-term glacioisostasy of the central and northern Laurentide Ice Sheet. The vertical land motion rates may contain a significant component attributable to the lithosphere's elastic responses to changes in present-day regional ice cover. In Greenland, for instance, the current post-glacial rebound is small $\sim 3.4 \text{ mm.yr}^{-1}$. Compared to central Canada $\sim 12 \text{ mm.yr}^{-1}$, the estimated present-day mass loss effect is unusually large with 2.9 mm yr^{-1} (Simon *et al.*, 2016).

V.1.3.2 Effect of water-level: The Basin & Range, and the Dead Sea examples.

In the Basin and Range Province (West U.S.), the active east-west extension is responsible for forming normal faults. The most prominent example is the Wasatch Fault zone (Figure 5.5). Late Pleistocene/Early Holocene paleoseismological records of the Wasatch fault show an increase in the slip-rate (McCalpin and Nishenko, 1996; McCalpin, 2002). A causal relationship is suggested with the synchronous regressions of Lake Bonneville and Lake Lahontan nearby the Wasatch fault (Hetzl and Hampel, 2005; Hampel and Hetzel, 2006). This desiccation removed 100-meters of water from the Wasatch fault zone's hanging wall over the time window 10 to 16.5 cal ka (McCalpin and Forman, 2002).

The effects of fluctuation in the water reservoir above active faults are documented in Dead Sea strike-slip Fault (Bartov *et al.*, 2002; Bartov and Sagy, 2004; Kagan *et al.*, 2011). Prediction of stress due to water volume changes superimposed on the pre-existing Dead Sea fault tectonic stress field show that water-level variations could have triggered changes in the paleoseismic rates (Belferman *et al.*, 2018).

V.1.4 Models of fault behavior underneath icecap

The growth in our understanding of icecap effects has been driven by the emergence of tectonic modeling constrained by new field observations. The stress changes due to surface (un)loading have been analyzed using Mohr diagrams and numerical models (Johnston, 1987; Johnston, 1989; Wu and Hasegawa, 1996; Wu *et al.*, 1999; Sauber and Molnia, 2004).

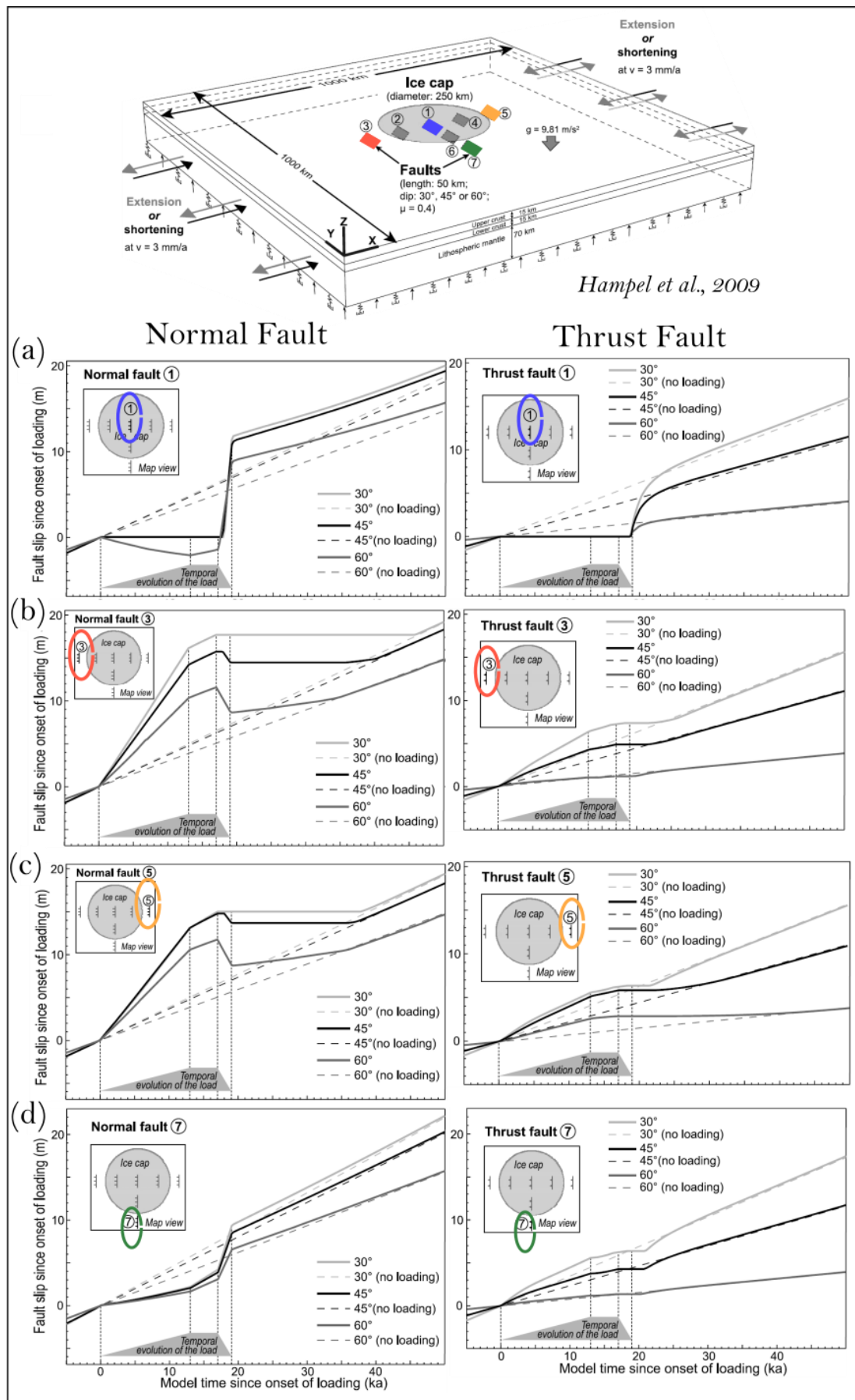
Authors agree that ice-sheet loading generally tends to reduce faults activity during glaciation because normal stresses on fault planes increase. For instance, the current seismicity

of Antarctica and Greenland are shadowed by their respective ice sheets, which reduce the differential stress $\sigma_1 - \sigma_3$, and result that faulting is inhibited (Johnston, 1987; Wu and Hasegawa, 1996; Turpeinen *et al.*, 2008).

In Antarctica, this stress shadowing is amplified by a thick elastic lithosphere of the order of 150–240 km. It creates an extended lagged stress response from the glacial isostatic adjustment. This process may cause present-day earthquakes many hundreds of kilometers seaward of the former Last Glacial Maximum grounding line (Ivins *et al.*, 2003). As suggested by (Wu, 1998; Hampel and Hetzel, 2006), the time lag between the changes in loading and the fault's reaction is determined by the viscosity.

In recent years, models of fault slip underneath icecap have shown that during glaciation, the locked lithosphere gradually accumulates elastic deformation and stores plate-tectonic stress. Removal of the ice mass allows this stored stress to be released and superimposed on the isostatic stress (Gregersen, 2002). Deglaciation periods promote earthquakes within and outside the formerly glaciated regions (Wu, 1998; Wu and Mazzotti, 2007). Nevertheless, these model setups do not include faults.

Development of finite element models, including discrete fault planes in the upper crust, allow the prediction of slip-rate evolution through time (Hetzel and Hampel, 2005; Hampel and Hetzel, 2006; Hampel *et al.*, 2007; Turpeinen *et al.*, 2008). Three-dimension modeling quantifies the response of isolated fault underneath and outside the load during a glacial-interglacial cycle. Authors suggest that the rate of load removal, fault strength, and the lithosphere's thickness plays a minor role in controlling fault response (Hampel and Hetzel, 2006). These experiments are restricted to extensional and compressional settings but do not evaluate the transform tectonic setting's response.

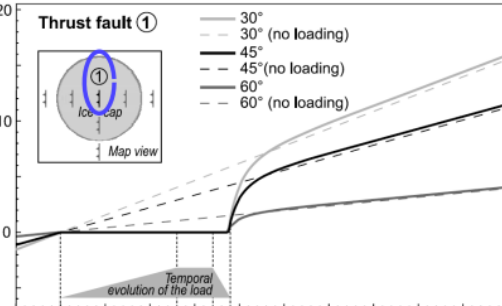
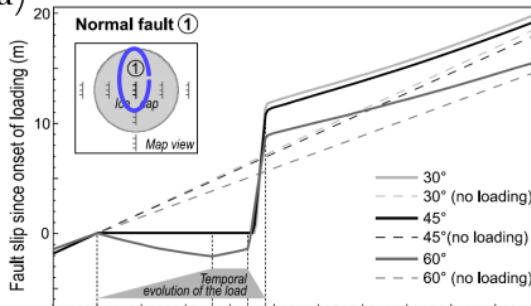


Hampel et al., 2009

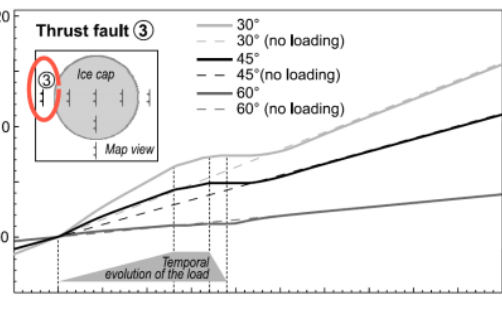
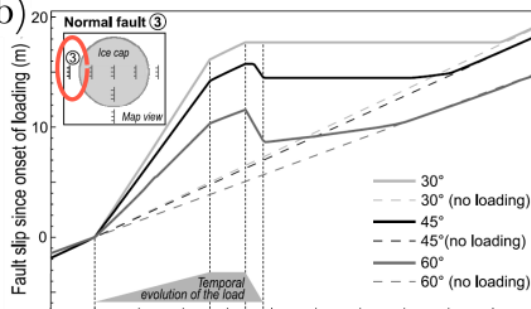
Normal Fault

Thrust Fault

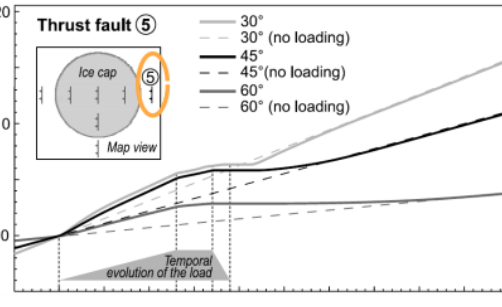
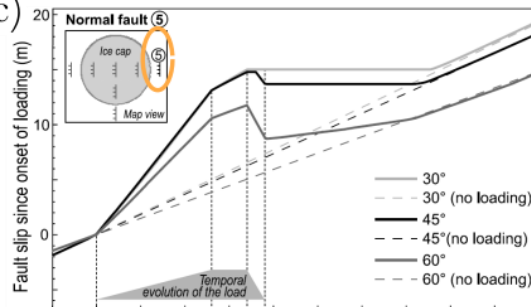
(a)



(b)



(c)



(d)

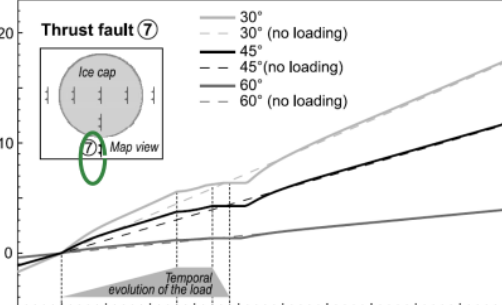
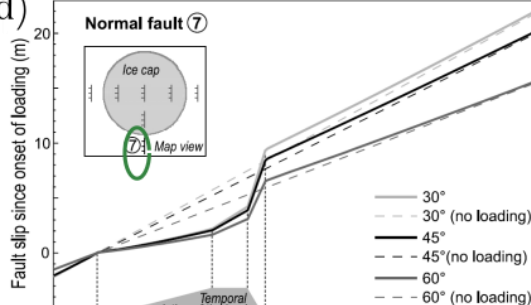


Figure 5.6: Results of normal and thrust fault experiments from Hampel et al., (2009). (a) Faults beneath icecap. (b) Faults outside icecap, and load on the footwalls. (c) Faults outside icecap, and load on the hanging walls. (d) Faults outside icecap, and load on fault's tips (i.e., loading both hanging and foot walls). The experiments are carried out with fault dips of 30°, 45°, and 60°. The grey polygon indicates the load's temporal evolution (loading 0-13ka, stable load 13-17, unloading 17-19, post-loading >19ka).

In the last decade, model predictions compared to paleoseismological records established a clear link between Fennoscandia Ice-sheet melting and the slip evolution of normal and thrust faults in Scandinavia (Hetzel and Hampel, 2005; Hampel and Hetzel, 2006; Hampel et al., 2007). Concerning the fault right beneath the ice-sheet (Figure 5.6 a), a general analysis states that when ice-sheet grows, it generates a period of seismic quiescence, while during ice-sheet melting it yields to a period of seismic burst (Hetzel and Hampel, 2005; Hampel and Hetzel, 2006). The magnitude of the weight is the primary factor controlling the timing of fault response. Asthenosphere's viscosity determines the delay between loading and fault reactions (Hampel and Hetzel, 2006). For faults outside the formerly glaciated area, the behavior is controlled by the ice-load location relative to the fault. With a load on either the footwall or the hanging wall, normal and thrust fault slip-rates have same pattern: an increase at loading, a decrease at unloading (Figure 5.6 b, c). Conversely, with a load on the fault tip, patterns of slip-rate are the opposite (Figure 5.6 d). At loading, the normal fault is almost 'locked' while the thrust fault slips at a faster rate than before loading (Hampel et al., 2009).

V.1.5 Strike-slip fault and glacial unloading in Tierra del Fuego

The recognition that post-glacial crustal deformation and tectonic strains are potentially intertwined have not been considered outside the Antarctica, Eurasia, Greenland, or North American regions. Very few studies investigate the interaction between icecap stress fields and a strike-slip configuration.

V.1.5.1 Reverse and strike-slip: compressive tectonic configurations

Muir-Wood (2000) described these interferences for post-glacial rebound in a compressive (strike-slip and reverse fault) tectonic field using the Fault Stability Margin (FSM) approach. In

the Mohr-Coulomb diagram, the FSM defines the distance of the semi-circular arc joining the maximum and the minimum principal stresses from the failure envelope. The tectonic stresses orientations relative to the rebound stresses determine the interference. For deglaciation of a circular icecap Muir-wood determined quadrants where the interference is constructive and reduces FSM (closer to rupture = seismic), or destructive and increases FSM (away from rupture = aseismic) (Figure 5.7a). In the unloaded region, the two quadrants which favor earthquake nucleation are located perpendicular to the maximal principal tectonic stress. Conversely, in the two other quadrants, seismicity is “muted” because the rebound stress orientation is the opposite of maximal principal stress (destructive interference). Outside the unloaded region, i.e., in the forebulge, the seismogenic quadrants are in the opposite configuration. Note that the whole quadrant is impacted only when the rebound stress overwhelms the tectonic stress. Otherwise, when the rebound stress is comparable to tectonic stress, for instance, in the Laurentide region, the area of interference is reduced to the quadrant's central patches (Figure 5.7b). In the northeast American craton, the predominant cause of intraplate deformation is the glacial isostatic adjustment. Around the Laurentide, the contractional belt of the Laurentide forebulge induces a $1\text{-}2\text{ mm.yr}^{-1}$ far-field horizontal motion directed toward the ice sheet (Kremer et al., 2018). The constructive patches mentioned by (Muir-Wood, 2000) in the Laurentide forebulge (Figure 5.7b) fit most of the potentially post-glacially reactivated zone of the Baffin Bay and Labrador Sea region. However, elsewhere it is difficult to define where these quadrants should be localized, as they are not consistent with the observed seismicity (Grand Banks, Wasatch Fault).

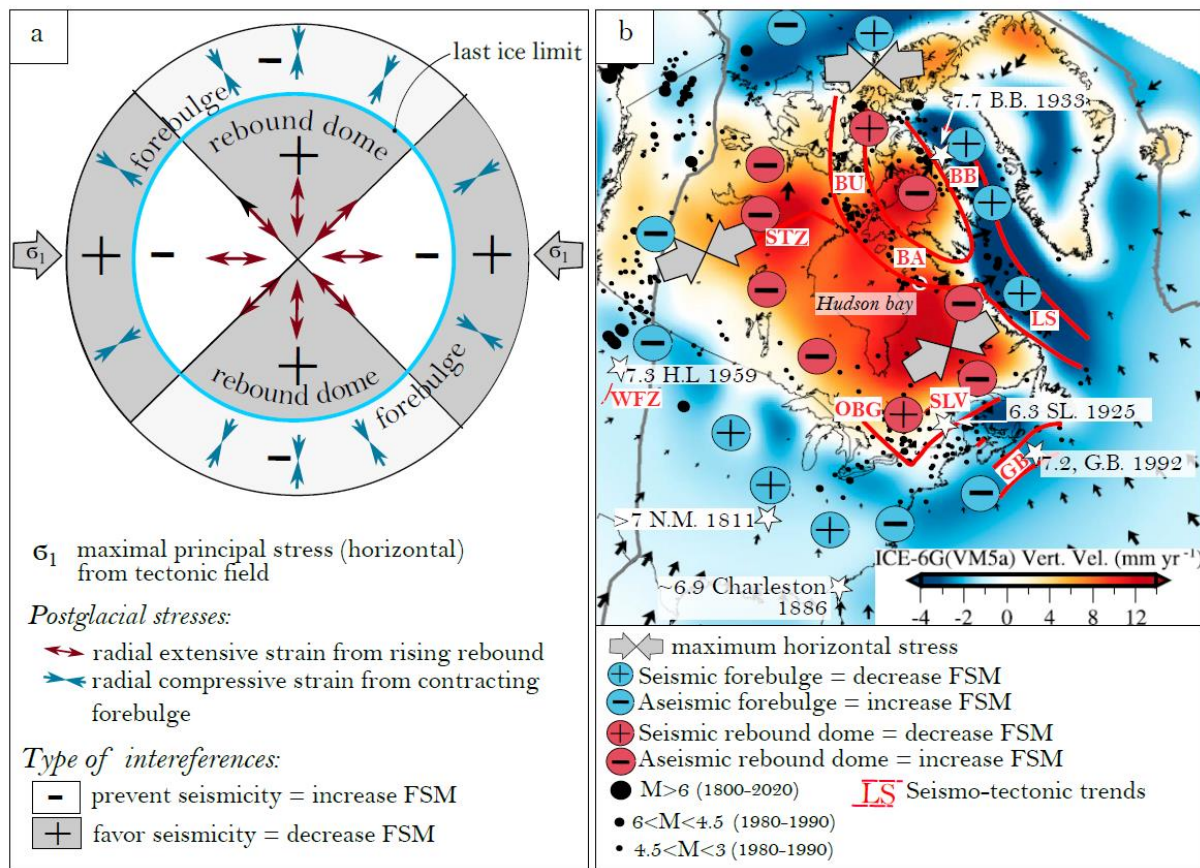


Figure 5.7: (a) The constructive (+) and destructive (-) interferences between the maximal principal stress and post-glacial rebound and forebulge (blue and red arrows) from (Muir-Wood, 2000). Only the horizontal maximal principal stress σ_1 is represented to include both compressive, and strike-slip configuration. (b) Comparison between interference patches locations from (Muir-Wood, 2000) and predicted vertical/horizontal velocities, and observed seismicity of the Laurentide rebound dome. Color bar indicates vertical uplift rate and vectors are horizontal velocities predicted by the ICE-6G_C (VM5a) model (Kreemer et al., 2018). The red lines indicate seismotectonic zones from (Steffen et al., 2012; Wu, 1998). Record of earthquakes are M>6 (USGS); 6<M<4.5 from (Wu, 1998); 4.5<M<3 from (Steffen et al., 2012; Hunt and Malin, 1998; Wu, 1998), Abbreviations are: BA: Bell Arch; BB: Baffin Bay; BU: Boothia Uplift; GB: Grand Bank, HL: Hebgren Lake; LS: Labrador Sea; NM: New Madrid; OBG: Ottawa Bonnechere Graben; SLV: Saint Lawrence Valley; S: Snowbird; WFZ: Wasatch Fault Zone.

V.1.5.2 Faster Chilean Magallanes-Fagnano Fault and ice-sheet unloading

This Chapter evaluates the postglacial unloading as a potential cause for increased strike-slip-rate in the Chilean Territory. As developed in Chapters 2 and 4, the Magallanes Fagnano

Fault long-term slip-rate is considerably faster in the western region. In the Argentinian Tierra del Fuego, the long-term slip-rate is estimated at 6.4 ± 0.9 mm/yr (Roy *et al.*, 2020) up to 7.8 ± 1.3 mm/yr (Sandoval and De Pascale, 2020) since 18 ± 2 ka (Figure 5.8). The postglacial slip-rate is assessed in the Chilean MFF, ranging from 12.41 mm/yr up to 23.36 mm/yr (Roy *et al.* 2020, chapter 4, this study). The western sinistral offset was identified in a post-LGM drainage system about 15.6 ± 1.9 cal ka BP.

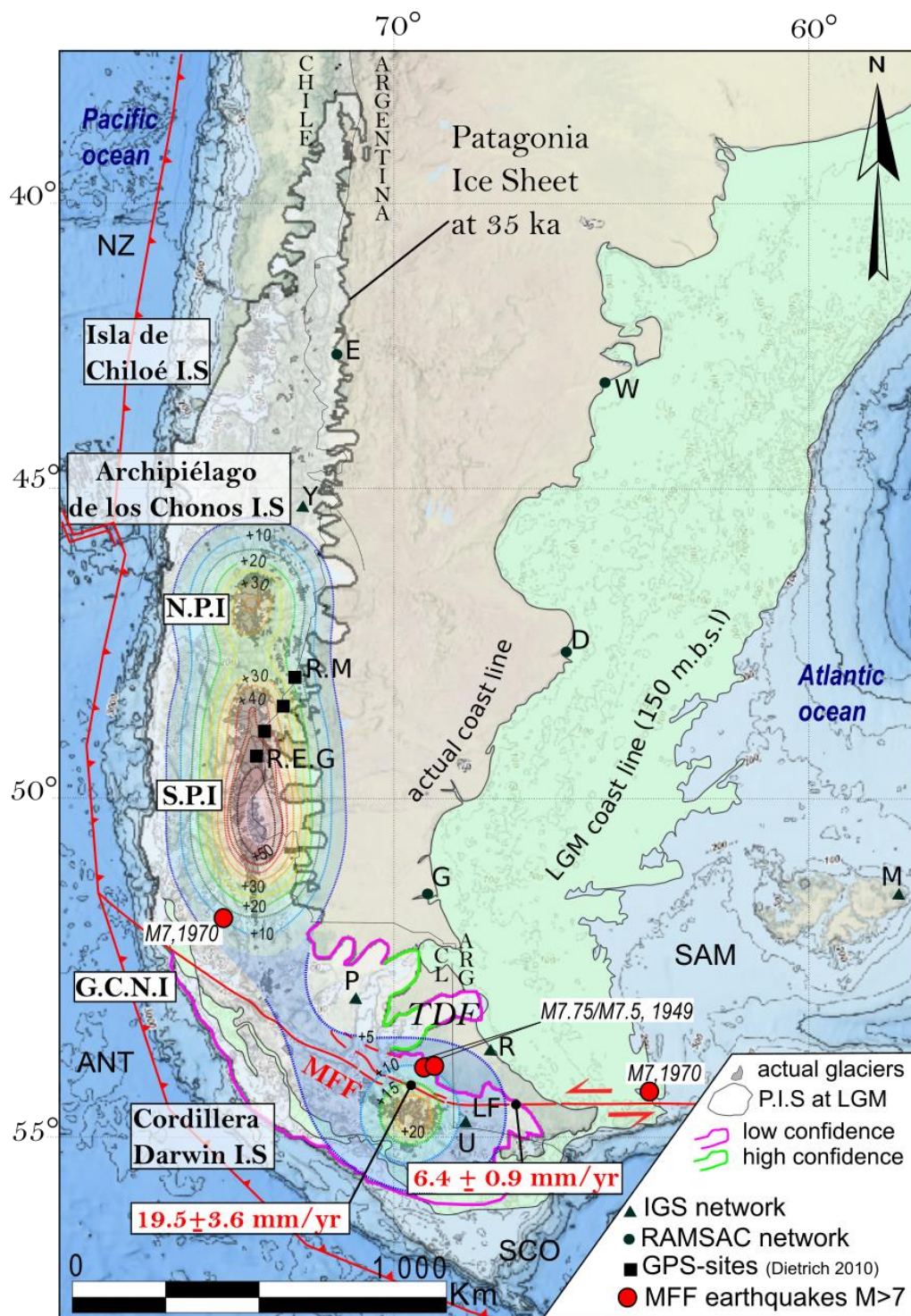


Figure 5.8: Maps of the Patagonian Ice-sheet (PIS) at 35 ka (Davies et al., 2020) above the Magallanes-Fagnano Fault system (MFF). Major faults are mentioned in red. The colored zones with dashed contours indicate the predicted present-day uplift due to ice-mass changes in mm/yr. This data are from (Dietrich et al., 2010) for the SPI, and from (Ivins and James, 2004) for the TDF. Abbreviations as follow: AR: Argentina; CL: Chile; D: Puerto Deseado; E: Esquel; G: Rio Gallegos; G.C.N.I.: Gran

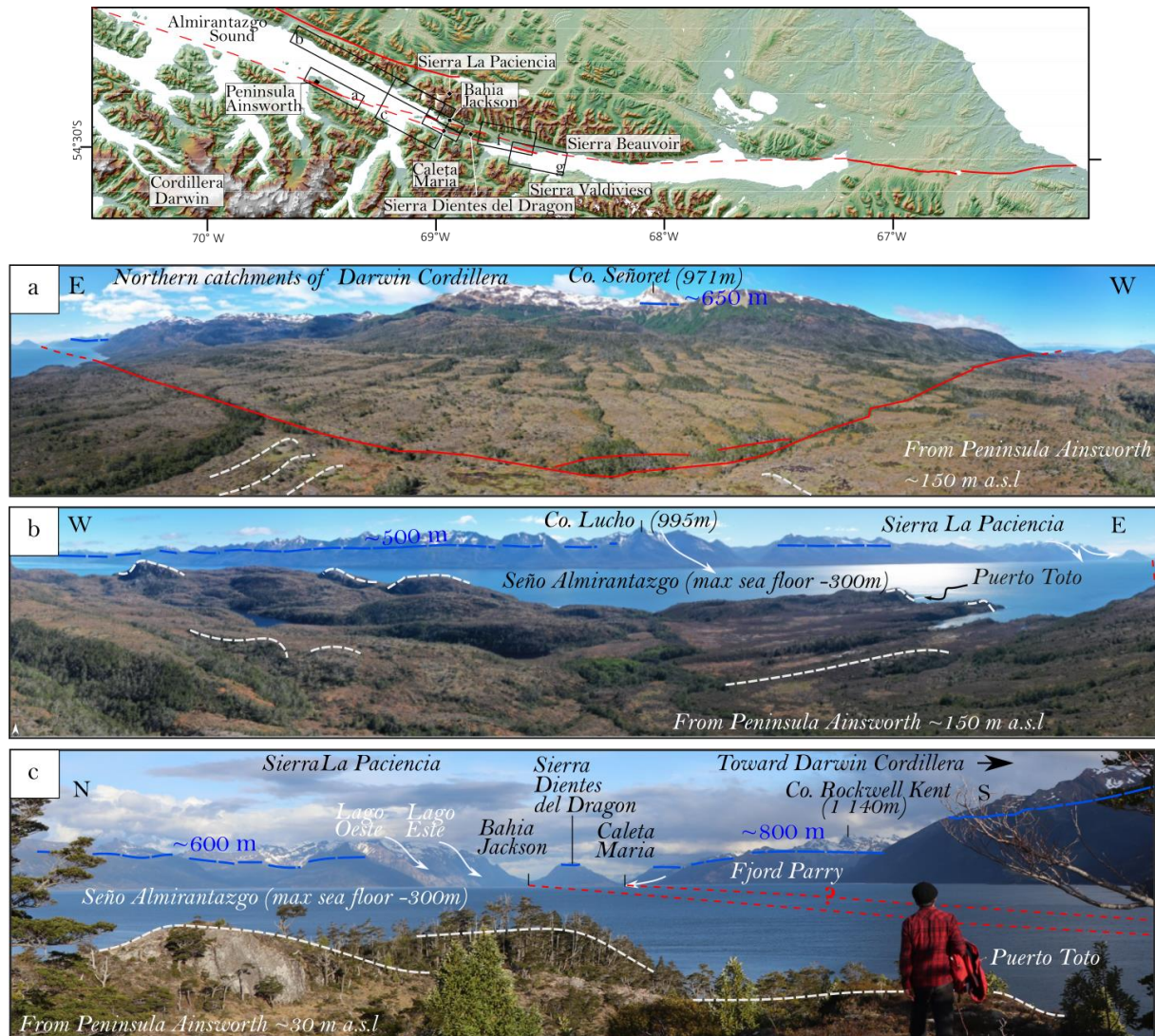
Campo Navedo Ice-sheet; LF: Lago Fagnano; M: Malvinas Islands; NPI: Northern Patagonian Ice-sheet; P: Punta Arenas; NZ: Nazca plate; R: Rio Grande; RAMSAC: Argentine Network for Continuous Satellite Monitoring; R.M: Rio Mayer; R.E.G: Refugio Eduardo Garcia; SAM: South American plate; SCO: Scotia plate; SPI: Southern Patagonian Ice-sheet; U: Ushuaia; Y: Coyhaique; W: Rawson. The base map is general bathymetric chart of the oceans (GEBCO 2014; National Centers for Environmental Information NCEI, NOAA). with 100 meters' interval below sea level).

One of the Fuegian Andes singularity lies in the uneven LGM-ice extents, which was massive along the west's MFF and limited in the east (Figure 5.8). The southernmost tips of the Patagonian Ice-sheet partially covered the MFF system (Figure 5.8). The LGM was associated with a sea-level fall of 150 m (Guilderson *et al.*, 2000). Accordingly, the land emerged farther east of the MFF, extending the inland fault of about ~170 km (Figure 5.8). At the LGM, while the eastern MFF remained free of ice, the western and central regions were covered by large ice-lobes. After the LGM, the sea level rises progressively of 100 m relatively to the LGM coastline and irreversibly loaded the eastern MFF. This eastern marine transgression (loading) and the coeval massive western ice-wastage (unloading) are to stress changes that may have affected the strike-slip motion.

The ice-sheet changes involved in the last glacial events are poorly constrained, and even less in the western fjord margins. The eastern and southernmost sides are better mapped and dated. However, there are very few age controls available (Bujalesky *et al.*, 1997; Rabassa *et al.*, 2000; Coronato *et al.*, 2002b; Coronato *et al.*, 2008; Coronato *et al.*, 2009; Waldmann *et al.*, 2010; Rabassa, 2011; Roy *et al.*, 2020). Most of the north-western limits are inferred from studies of dated glacial moraines and glacial deposits (Figure 5.8) (Clapperton, 1993; Peltier, 2004; Bentley *et al.*, 2005; McCulloch *et al.*, 2005; Sugden *et al.*, 2005; Boyd *et al.*, 2008; Kaplan *et al.*, 2008; Fernández *et al.*, 2011; Fernández *et al.*, 2017; Hall *et al.*, 2019).

Dynamic ice sheet modeling suggests the Fuegian Andes-Tierra del Fuego LMG ice thickness was ~ 800-1200 m (Hulton *et al.*, 2002). The trimlines in Almirantazgo Sound (Figure 5.9 a, b, c), Caleta Maria, and Jackson Bay (Figure 5.9 d, e) evidence the highest imprint of the ice lobes standing about 600 – 800 m.a.s.l. Besides, the Almirantazgo Sound bathymetry (Fernández *et al.*, 2017) demonstrates the ice was grounded along the seafloor during LGM. The actual seafloor

depth is - 100 to -300 m (SHOA Chilean Navy, 1998), suggesting the ice mass was ~ 700 -1100 m thick within the central MFF. In Sierra Dientes del Dragón, Sierra Beauvoir, and Sierra Valdivieso, the trimlines demonstrate a maximum ice-mass of 700 m, which rapidly decreases toward the east (Figure 5.9 f, g).



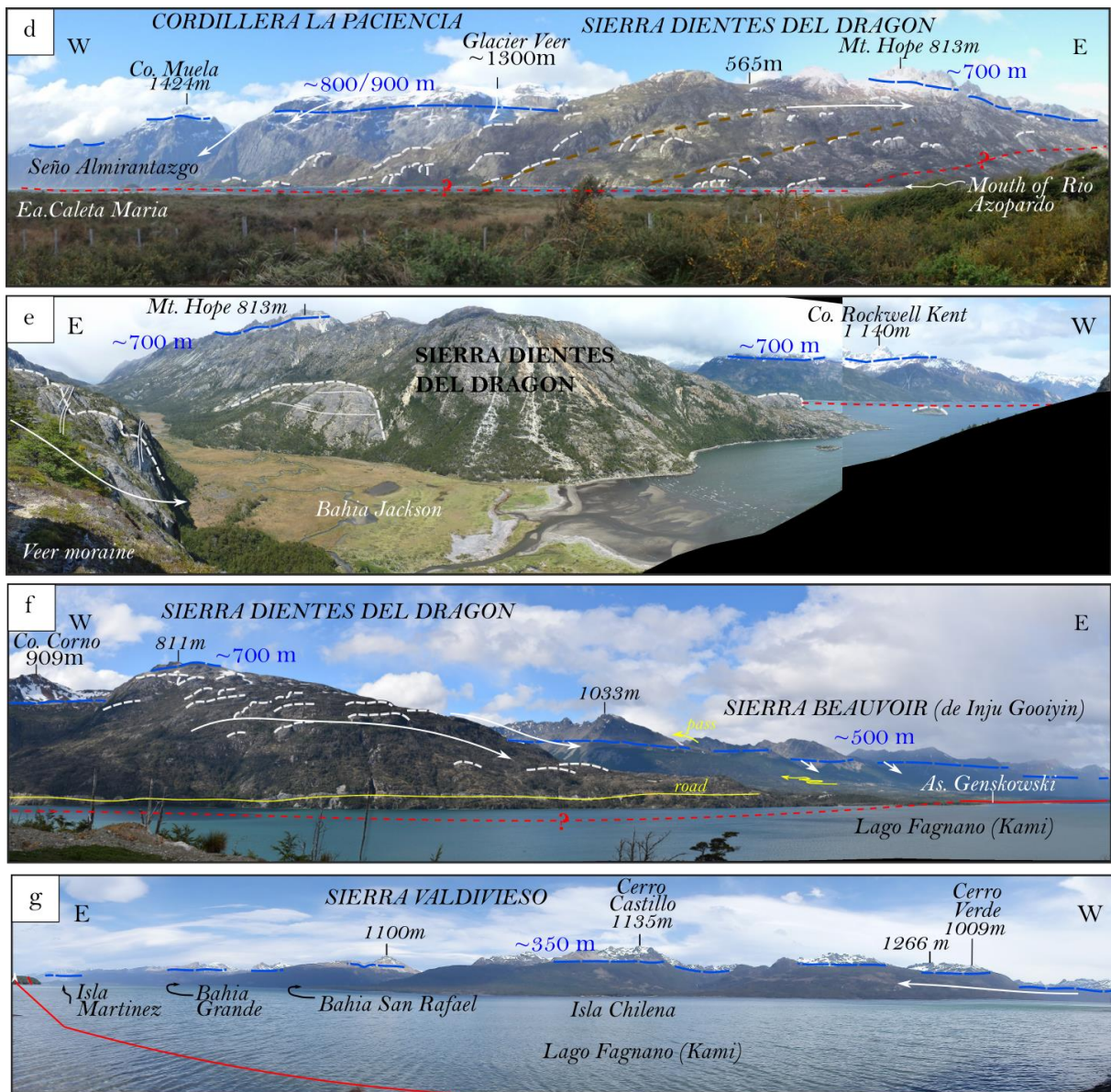


Figure 5.9: Overview of the trimlines from studied sites, shown with dashed blue lines. White arrows indicate ice flow direction. Glacial morphologies, such as drumlins, kettles, kames, back whales, roches moutonnées, are enhanced with dashed white lines. Red lines mark MFF faults that we surveyed, while red dashed lines show the suggested traces. (a) View from Peninsula Ainsworth of the central arm of the Strait of Magellan along the Almirantazgo Sound. Photographer is facing north. (b) Same location, but photographer is facing south. (c) View of the eastern Almirantazgo Sound. Photographer is on the east peninsula cap. (d) View from Caleta Maria of the northern catchment of Azopardo valley. (e) View of Jackson Bay and Sierra Dientes del Dragón taken from Veer moraine. (f) Western Fagnano Lake. (g) View of the southern bank of Fagnano Lake.

Geodetic studies of the Southern Patagonia Icefield (SPI) evidence the largest glacial isostatic rate ever recorded in the world (Dietrich *et al.*, 2010; Lange *et al.*, 2014). The dome-shape uplift center is located in the Viedma glacier's Nunatak and shows a vertical velocity measurement up to 39 mm/yr at Refugio Eduardo García station (Figure 5.8). In Tierra del Fuego, models evidence a smaller, disconnected rebound dome centered in the Cordillera Darwin (Ivins and James, 2004). Predicted uplift rates for the center, varies between 12 up to 21 mm.yr⁻¹, depending on the model's asthenospheric thickness (Figure 5.10). A smoother uplift decay toward the central Lake Fagnano is expected to be ~6-9 mm/yr. This E-W uplift gradient is visible in GPS measurements, but the predicted rate is twice as the observed one $\sim 3.1 \pm 0.4$ mm/yr (Mendoza *et al.*, 2010; Mendoza *et al.*, 2011). Ivins *et al.* (2004) assumed a particularly low asthenosphere viscosity over Patagonia, caused by the underlying subducted slab windows, which is a fair assumption for the Northern region, but perhaps not as realistic for the Tierra del Fuego. Also, the study evidences significant tectonic shortening in the western Fagnano Lake, therefore additional analysis is required to quantify the neotectonic contribution from a regional GIA process (Mendoza *et al.*, 2011). In the Atlantic coast and the Beagle Channel, dated shells obtained from elevated beaches indicate a post-glacial isostatic rebound calculated rates about 0.09 and 2.9 mm/yr (Gordillo *et al.*, 1992; Bujalesky *et al.*, 1997).

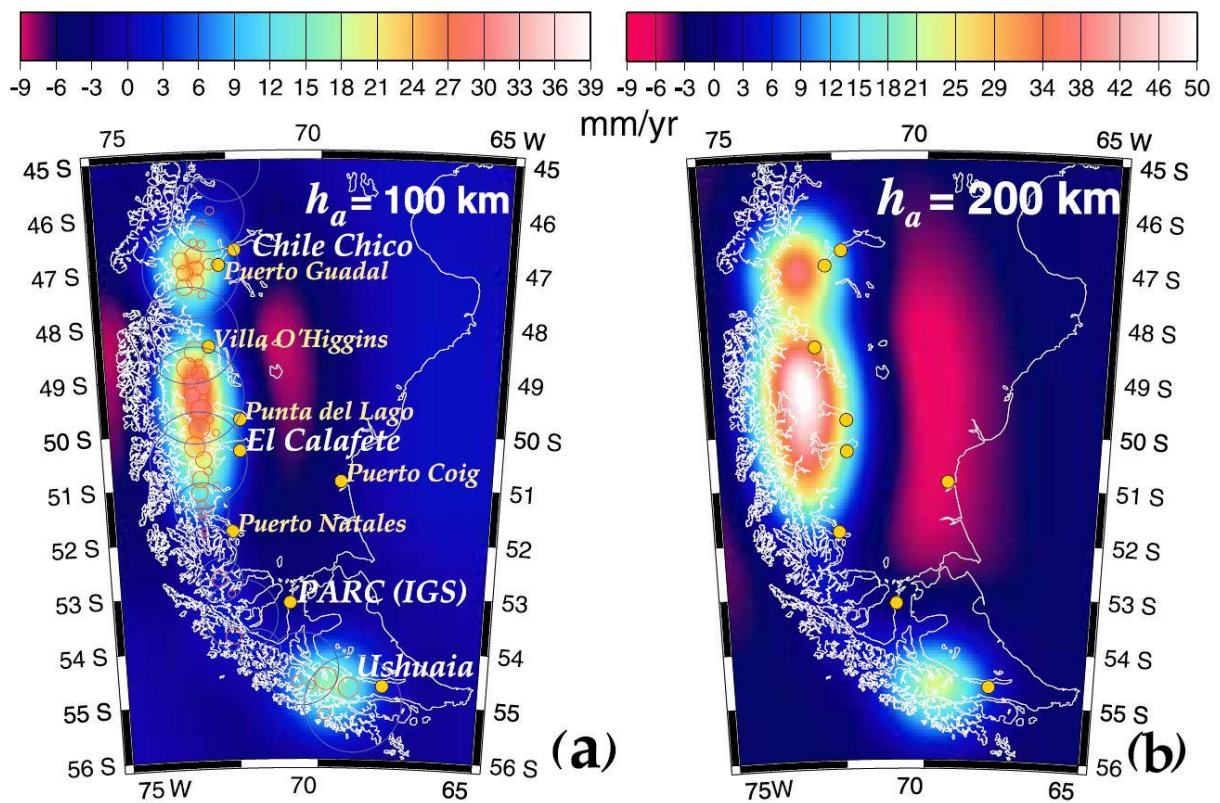


Figure 5.10: Present-day predicted uplift for two asthenospheric thicknesses and with a low viscosity = 1×10^{18} Pa s, and elastic lithosphere thickness 35 km from (Ivins and James, 2004). (a) Asthenosphere thickness of 100 km. (b) Asthenosphere thickness of 200 km.

The intriguing coincidence between the fast slip accumulation on the Magallanic strike-slip fault and the end of the last ice age strongly suggests an external forcing. This Chapter is the first study to evaluate the icecap effects above a strike-slip fault configuration. Using basic analytical model and a finite-element model, we aim to assess the slip proportion related to the ice-mass changes in the Chilean Territory.

V.2 Analytical evaluation of the glacial loading effect on strike-slip fault

Here, we set down an elementary 2D bending problem to evaluate the lithosphere behavior under a linear load representing the glacier that grew above the Southern Andes. We wish to determine roughly the effect of the obliquity of the load above a strike-slip fault. Note that the following demonstrations are deliberately simplified to focus only on the first order. Thus we assume several strong approximations.

Firstly, we estimate the maximum deflection of the lithosphere under a line-load. Then we calculate the plate curvature, and evaluate the corresponding stress change under the load. Lastly, we determine at first order the effect of the position of the load relative to a strike-slip fault. This section offers a basic first-order approximation of expected results in section with 3D finite element modeling.

V.2.1 Definition

Stress can be resolved into two components: normal stress (σ_n) and shear stress (σ_τ). The total stress can also be subdivided into three orthogonal components labeled σ_1 , σ_2 and σ_3 , corresponding to the maximum, intermediate, and minimum principal stresses. When, $\sigma_1 = \sigma_2 = \sigma_3$, it means, horizontal stresses and vertical stress are equal, it is called lithostatic state of stress. Conversely, when $\sigma_1 \neq \sigma_2 \neq \sigma_3$ the stresses generally involve faulting, and are named deviatoric stress $\Delta\sigma$. The deviatoric stress can cause strain (ϵ , deformation) of the rock, such as dilatation or distortion. Tectonic processes are continually straining the Earth's surface, and typical values for deviatoric stresses in the continents are of the order of 10 to 100 MPa. The strain can directly be measured in rocks or on Earth's surface by geodetic techniques like Global Positioning Systems (GPS) or Short Aperture Radar interferometry (InSAR), while the amount of stress can only be inferred from the strain (Burbank and Anderson, 2009). Strike-slip faulting occurs in a triaxial stress field with the principal stresses define such as $\sigma_1 > \sigma_2 > \sigma_3$ with σ_1 and σ_3 horizontal (Figure 5.11).

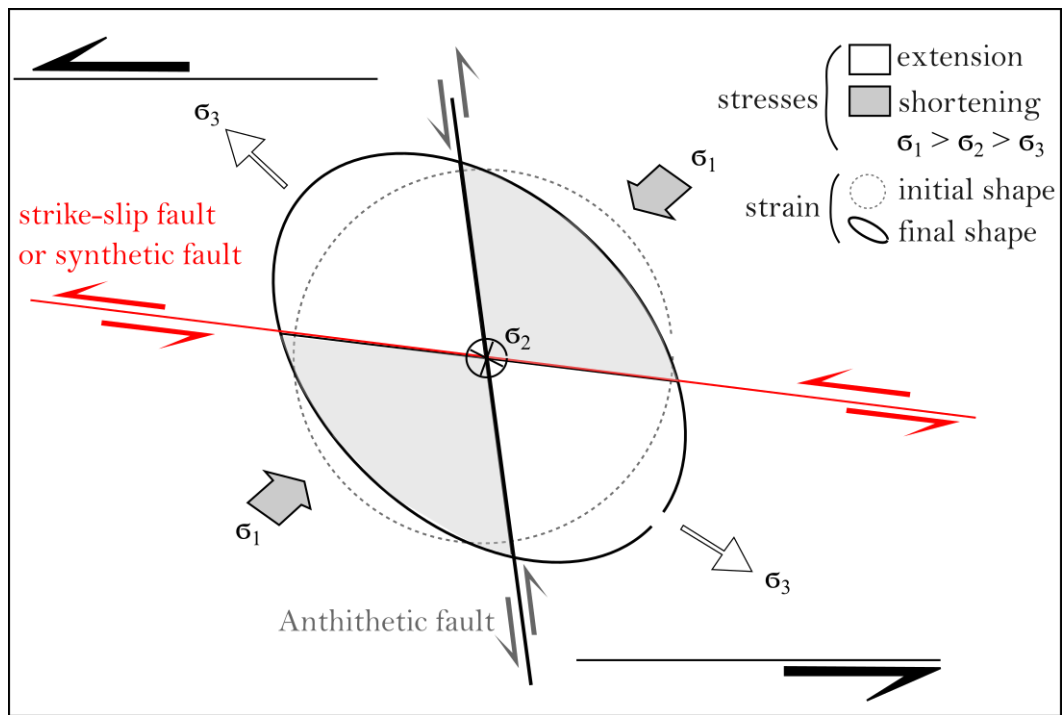


Figure 5.11: Map view of the strain and stress ellipsoid for a sinistral strike-slip fault. The principal stresses are σ_1 (horizontal) $>$ σ_2 $>$ σ_3 (horizontal).

V.2.2 Setup: bending of the lithosphere beneath a linear glacial load

Here, we assume an elastic lithosphere infinitely long in the x and y directions, of height H , characterized by its density (ρ), Young modulus (E), and Poisson's ratio (ν) (Figure 5.12). Young's modulus of rocks varies from about 10 to 100 GPa, and Poisson's ratio varies between 0.1 and 0.4 (Turcotte and Schubert, 2014).

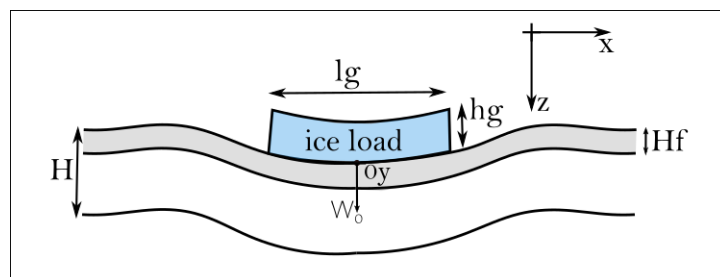


Figure 5.12: Sketch illustrating the two-dimensional bending of the lithosphere by the icecap.

V.2 Analytical evaluation of the glacial loading effect on strike-slip fault

The lithosphere contains a brittle upper crust of height H_f . The downward force of the gravity acceleration is $g = 9.82 \text{ m}\cdot\text{s}^{-2}$. The load is an icecap of high h_g , it has an infinite length ($L_g \rightarrow \infty$) in the y -direction, l_g is the icecap width along the x -axis, and ρ_g its density. We assume the icecap width is relative small, and thus we consider the icecap load is a line load V_o applied at $x = 0$. The plate bends under the line load. The line load is:

$$V_o = \rho_g \cdot g \cdot l_g \cdot h_g$$

To describe the bending, we use the flexural parameter α defined as:

$$\alpha = \left(\frac{4 \cdot D}{\rho \cdot g} \right)^{1/4}$$

(see [Turcotte and Schubert, 2014](#) eq [3.127])

with D , the flexural rigidity (stiffness) in $\text{N}\cdot\text{m}$ of the plate as:

$$D = \frac{E \cdot H^3}{12 (1 - \nu^2)}$$

The plate deflection is $W(x)$ in meters and is negative downwards. In this configuration, the deflexion $W(x)$ for $x \geq 0$ is:

$$\text{Equation (1)} \quad W(x) = -\frac{V_o \cdot \alpha^3}{8D} \cdot e^{-x/\alpha} \cdot \left[\cos \frac{x}{\alpha} + \sin \frac{x}{\alpha} \right]$$

(see [Turcotte and Schubert, 2014](#) eq [3.130])

The maximum deflexion located in the center of the load, at $x=0$, is given by:

$$W(0) = -\frac{V_o \cdot \alpha^3}{8D}$$

Taking a lithosphere of $H = 100 \text{ km}$, $\rho = 3300 \text{ kg/m}^3$, $\nu = 0.25$, $E = 5 \cdot 10^{10} \text{ Pa}$, and the ice load of $\rho_g = 920 \text{ kg/m}^3$, $l_g = 100 \text{ km}$, $h_g = 1000 \text{ m}$, we find from Equation (1) that $\alpha \sim 153 \text{ km}$; $D \sim 4.44 \cdot 10^{24} \text{ N}\cdot\text{m}$; $V_o = 9.2 \cdot 10^{11} \text{ N}\cdot\text{m}$; and maximal deflexion is $W(0) \sim -91 \text{ m}$.

V.2.3 Amplitude of plate curvature and glacier perpendicular strain of the plate

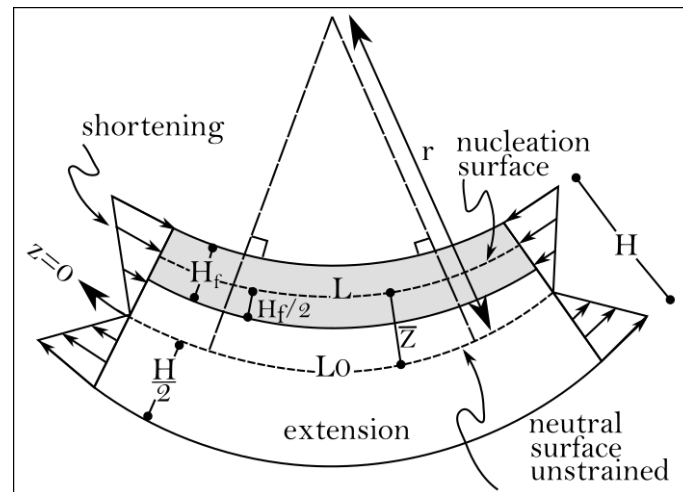


Figure 5.13: Cross section of curved elastic lithosphere. Arrows shows the normal stresses. The curvature of the plate is exaggerated.

To relate curvature with the strain of the lithosphere, we proceed as follows. The plate is deflected downward (Figure 5.13), and its radius of curvature is r such as:

$$\frac{1}{r} = \frac{\partial^2 z}{\partial x^2} = \left(\frac{V_0 \cdot \alpha}{4D} \right) \cdot e^{-x/\alpha} \cdot \left[\cos \frac{x}{\alpha} - \sin \frac{x}{\alpha} \right]$$

The upper half of the plate is shortened along the x -axis, and the lower half is extended. The associated longitudinal strain is a contraction in the upper half and is an extension in the lower half. We assume that there is no strain ϵ_{xx} in the middle of the plate, which is the neutral unstrained surface located at $H/2$ (Turcotte and Schubert, 2014).

Generally, the nucleation of earthquakes is confined to the shallowest brittle crust. Usually, this seismogenic layer is no deeper than 15-20 km in the case of a strike-slip fault. In Tierra del Fuego, the regional model suggests the fault is locked at 11 km \pm 5 km (Mendoza et al., 2015). Thus, we focus on the nucleation surface strains and stresses located in the middle of the brittle crust at $Hf/2$. The distance \bar{Z} between the neutral unstrained surface and the nucleation surface

is $\bar{Z} = \frac{H-Hf}{2}$ (Figure 5.13). The deformed length L of the plate along the nucleation surface can be expressed in function of its initial length L_0 and in function of the plate curvature radius r such as:

$$L = \frac{L_0}{r} \left(r - \frac{H-Hf}{2} \right) = L_0 \left(1 - \frac{H-Hf}{2r} \right)$$

The strain ϵ_{xx} of the nucleation surface can be expressed as:

$$\epsilon_{xx} = \frac{L - L_0}{L_0} = \frac{L_0 \times \left(1 - \frac{H-Hf}{2r} \right) - L_0}{L_0} = \frac{H-Hf}{2r}$$

$$\text{Finally the strain is, } \epsilon_{xx} = \frac{(H-Hf)Vo\alpha}{8D} e^{-x/\alpha} \left[\cos \frac{x}{\alpha} - \sin \frac{x}{\alpha} \right]$$

Given the same numerical application than in the previous section, and taking $Hf = 30$ km, the line-load triggers a surface of nucleation shortening of ϵ_{xx} . The maximum deformation of the nucleation surface is located right under the load. On the nucleation surface, and right under the load in $x = 0$ the deformation is $\epsilon_{xx}(0) = 2,72 \cdot 10^{-4}$. At 50 km away from the line-load, in $x = 50$ km, the deformation is smaller and is $\epsilon_{xx}(50) = 1.23 \cdot 10^{-4}$. Notice that the deformation magnitude at the icecap border ($x=50$ km) corresponds to ~ 45 % of the maximum deformation $\epsilon_{xx}(0)$. At 120 km away from the line-load, in $x=120$ km, ϵ_{xx} is almost null.

This crustal contraction under the icecap is accompanied by outward mantle flow from beneath the icecap. Outside the former icecap, the extension and the uplift lead to creating a budge shape of the lithosphere, called forebulge. Indeed, far away from the line load, after $x > 120$ km, the strain ϵ_{xx} has the opposite sign.

V.2.4 Stress evolution under a line-load

We wish to determine the stress evolution in the x direction $\Delta\sigma_x$, and in the y direction $\Delta\sigma_y$. ε_{xx} is calculated above. $\varepsilon_{yy} = 0$ since deformations under a linear load is 2D. And $\Delta\sigma_{zz} = \rho_g \cdot g \cdot h_g$

We can apply the Hooke's Law:

$$\begin{cases} E \cdot \varepsilon_x = \Delta\sigma_x - \nu\Delta\sigma_y - \nu\Delta\sigma_z \\ E \cdot \varepsilon_y = \Delta\sigma_y - \nu\Delta\sigma_x - \nu\Delta\sigma_z = 0 \\ E \cdot \varepsilon_z = \Delta\sigma_z - \nu\Delta\sigma_x - \nu\Delta\sigma_y \end{cases}$$

$$\begin{cases} E \cdot \varepsilon_x = \Delta\sigma_x (1 - \nu^2) + \Delta\sigma_z(-\nu^2 - \nu) \quad [1] \\ \Delta\sigma_y = \nu(\Delta\sigma_x + \Delta\sigma_z) \\ E \cdot \varepsilon_z = \Delta\sigma_z (1 - \nu^2) + \Delta\sigma_x(-\nu - \nu^2) \end{cases}$$

we obtain:

$$\Delta\sigma_x = \frac{1}{(1 - \nu^2)} \Delta\sigma_z(\nu^2 + \nu) + \frac{E \cdot \varepsilon_x}{(1 - \nu^2)}$$

Consequently, the stress $\Delta\sigma_x$ can be divided into two components. The first component is controlled by the term $\Delta\sigma_z$ which represents the stress due to loading. The second component is governed by the term ε_x , which describes the strain due to the bending of the lithosphere.

$$\begin{cases} \Delta\sigma_x = \frac{1}{1 - \nu} \cdot \left[\frac{E \cdot \varepsilon_x}{1 + \nu} + \nu \cdot \Delta\sigma_z \right] \\ \Delta\sigma_y = \nu [\Delta\sigma_x + \Delta\sigma_z] \end{cases}$$

with $\Delta\sigma_x =$ component due to bending + component due to loading

We take the same numerical application than the previous section, and obtain:

$$\text{Principal stresses at } x = 0 \text{ are } \left\{ \begin{array}{l} \Delta\sigma_x(0) = 14.5 \text{ MPa (bending)} + 3 \text{ MPa (loading)} \\ \qquad \qquad \qquad = 17.5 \text{ MPa} \\ \qquad \qquad \qquad \text{and} \\ \Delta\sigma_y(0) = \nu \cdot \Delta\sigma_x + \nu \cdot \Delta\sigma_z \\ \qquad \qquad \qquad \sim 6.6 \text{ MPa} \\ \Delta\sigma_z(0) = 9.03 \text{ MPa} \end{array} \right.$$

V.2.5 State of Stresses - Mohr-Coulombs analysis

Now let's consider a fault plane located under the icecap. We wish to express the stress changes in the Mohr-Coulomb representation. We consider a fault with a local coordinate system $(\vec{n}, \vec{\tau})$. This orthogonal system is defined by \vec{n} the unit vector perpendicular to the fault plane, and $\vec{\tau}$ the horizontal tangential unit vector (Figure 5.14 a). The fault is a sinistral strike-slip fault. The fault can have an angle θ relative to the (\vec{e}_x, \vec{e}_y) coordinate system. In other words, the fault can be oblique relative to the ice-load axis. Ice-load remains fixed along the y-axis. If the angle $\theta = 0^\circ$, then the fault is parallel to the icecap, and the local coordinate system $(\vec{n}, \vec{\tau})$ has the same orientation as the coordinate system (\vec{e}_x, \vec{e}_y) .

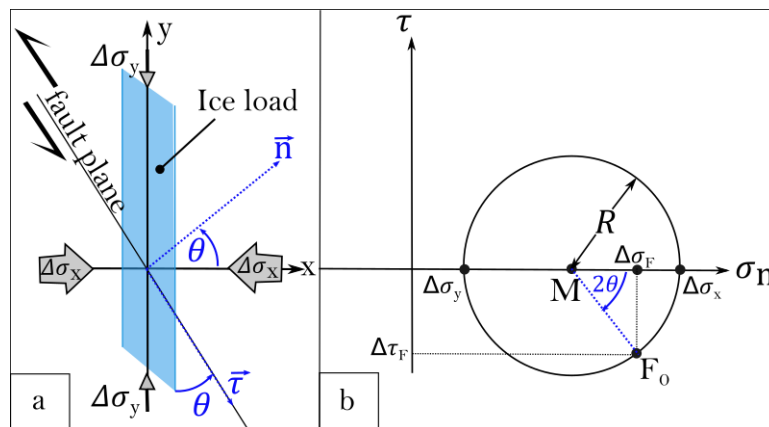


Figure 5.14: (a) Map view of the orientation of the fault relative to the ice load. (b) Illustration of the Mohr diagram with R is the Mohr's circle radius, M the Mohr's circle center, $\Delta\sigma_x$ and $\Delta\sigma_y$ correspond respectively to the maximal principal stress and the minimal principal stress.

Because in a strike-slip fault, the principal stresses σ_1 and σ_3 are horizontal, we will see that the angle θ has primary importance in controlling the failure. Indeed, under a load, the lithosphere's induced cylindrical curvature will favor or prevent slip to occur depending on the orientation of the associated horizontal stresses to the fault.

The coordinate system $(\vec{n}, \vec{\tau})$ is defined such as :

$$\vec{n} = \cos(\theta) \cdot \vec{e}_x + \sin(\theta) \cdot \vec{e}_y$$

$$\vec{\tau} = -\sin(\theta) \cdot \vec{e}_x + \cos(\theta) \cdot \vec{e}_y$$

Rotation of an angle θ in the coordinate system (\vec{e}_x, \vec{e}_y) corresponds to a rotation of -2θ along the Mohr circle. The circle, which has a radius R , represents the evolution of the normal and tangential components of the stress in function of the angle θ . The center and radius of Mohr circle are defined by:

$$\Delta M = \left(\frac{\Delta\sigma_x + \Delta\sigma_y}{2} \right) \text{ and } \Delta R = \left(\frac{\Delta\sigma_x - \Delta\sigma_y}{2} \right)$$

In our problem, instead of considering the intrinsic tectonic stress of the fault (i.e., σ and τ), we focus on the changes in stress which occur during loading. Therefore, we use $(\Delta\sigma_G)$ and $(\Delta\tau_G)$ corresponding to the changes in normal and tangential stresses on the fault plane, such as:

$$\begin{cases} \Delta\sigma_G = \Delta M + \Delta R \cdot \cos(2\theta) \\ \Delta\tau_G = -\Delta R \cdot \sin(2\theta) \end{cases}$$

The Mohr circle enables the visualization of the relationships between the normal (abscissa) and shear (ordinate) stresses and allows the determination of rupture planes' orientation. There are two domains controlled by the Coulomb's criterion: failure and a stable domain. A slip occurs when the Mohr's circle reaches the Coulomb's criterion, that is when Mohr's circle intersects the straight line of Coulomb's criterion. The Coulomb's criterion defines the shear stress τ required to (re)activate failure as:

$$\tau = C_0 + \sigma_n \cdot \tan(\varphi)$$

τ Resolved shear stress on the fault

σ_n Normal stress on the fault

C_0 : coefficient of friction

φ Friction angle

Let's consider an active sinistral strike-slip fault, which at time t_0 is close a failure condition. The tectonic conditions applied on the fault correspond almost to the stresses required for a rupture (Figure 5.15 a). At this time t_0 , we consider the point F_0 of the Mohr's circle that almost intersects the failure envelope. At time t_1 , we assume the icecap loads instantaneously the fault (Figure 5.15 b). The vertical load increases the horizontal stresses. Point F_0 generally moves away from the failure envelope to the new position F_1 . The load makes it harder for the rupture to occur,

which prevents earthquakes from happening. The new position F_1 is determined by the changes in stresses on the fault plane ($\Delta\sigma_G$) and ($\Delta\tau_G$) due to the ice load (Figure 5.15 b).

$$\text{For a fault parallel to the load } \theta = 0^\circ \begin{cases} \Delta\sigma_G = \Delta\sigma_x \\ \Delta\tau_G = 0 \end{cases}$$

Numerical application in $x = 0$:

$$\Delta M = 12.1 \text{ MPa}; \Delta R = 5.4 \text{ MPa}$$

$$\text{with } \theta = 0^\circ \begin{cases} \Delta\sigma_G = 17.5 \text{ MPa} \\ \Delta\tau_G = 0 \text{ MPa} \end{cases}$$

The distance between the failure envelope and the point F_1 , is known as the 'fault stability margin' (FSM), which translate the fault ability to rupture or to be stable. An increase of FSM reduces the potential for earthquake generation, while a decrease of FSM favors failure. During the existence of the ice sheet, the FSM increases due to vertical loading. Meanwhile, the permanent tectonic stresses will reduce this distance; the longer the ice sheet is in existence (Muir-Wood, 1989). Therefore, after a certain amount of time, the tectonic stresses bring the fault close to failure conditions (FSM decreases), and the rupture occurs at time t_2 (Figure 5.15 c). This period (t_1 to t_2) can be compared to the interseismic phase, in which surface slip accumulates away from the fault plane. We propose to determine this amount of stress required to induce failure of the fault. Accordingly, we define the ΔR the distance from F_1 to the new position of potential rupture F_2 . If the circle radius ΔR grows of $+\Delta R$, the Mohr's circle reaches the rupture, and the fault slips. We can define the stresses change as follow:

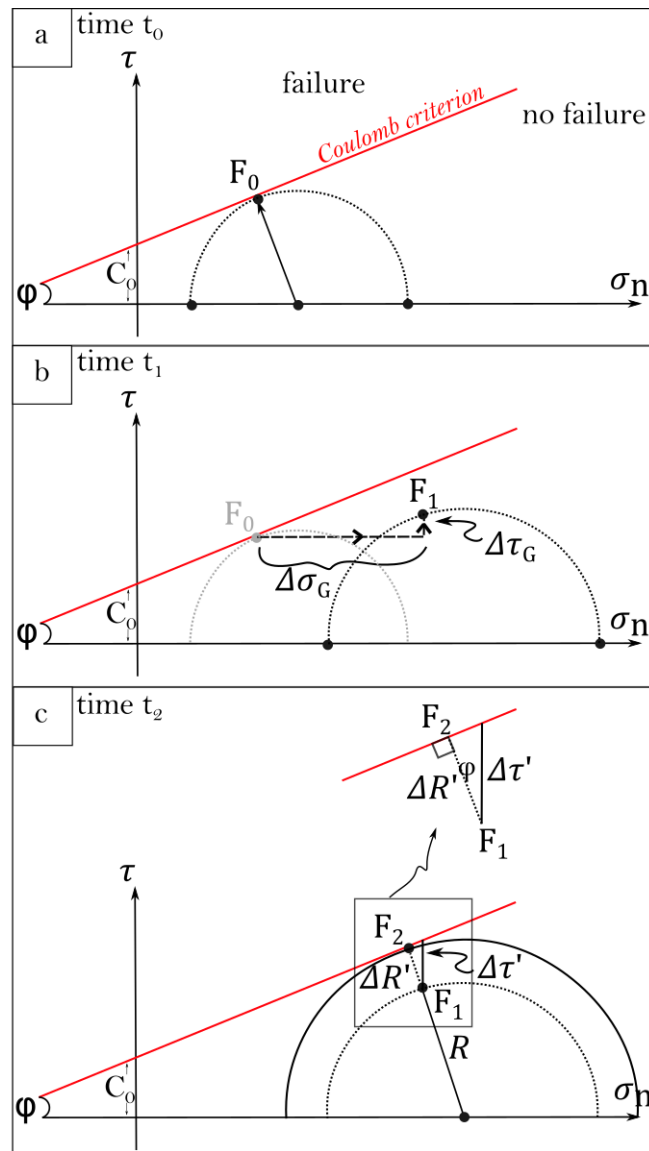


Figure 5.15: Mohr's circle (a) at time t_0 before loading, (b) at time t_1 during loading, (c) at time t_2 when the fault is reactivated.

$$\begin{cases} \Delta R' = \Delta \sigma \cdot \sin(\varphi) - \Delta \tau \cdot \cos(\varphi) \\ \Delta R' = \Delta M \cdot \sin(\varphi) + \Delta R [\cos(2\theta) \cdot \sin(\varphi) - \sin(2\theta) \cdot \cos(\varphi)] \\ \Delta R' = \Delta M \cdot \sin(\varphi) + \Delta R \cdot \sin(\varphi - 2\theta) \end{cases}$$

with φ the friction angle, and θ the obliquity of the fault.

We can estimate the cumulated slip d required to increase the Mohr's circle of $\Delta R'$, i.e., to reach failure conditions. During the interseismic phase, while the fault plane is locked, the tectonic movement's stress continues to apply, and the lithosphere accumulates strain away from the fault plane. The distance at which the maximum displacement is cumulated away from

V.2 Analytical evaluation of the glacial loading effect on strike-slip fault

the fault is the locked distance l (Figure 5.16). The cumulated displacement d (Figure 5.16) is the relative movement between the two plates required to cause a rupture. When the cumulated strain d is reached, it exceeds the frictional and cementing forces opposing motion along the fault plane, driving slip to occurs instantaneously (Kearey *et al.*, 2009). The locked distance to the Magallanes-Fagnano Fault (Figure 5.17) at which the maximum rate of deformation is located is $l \sim 30$ km (Mendoza *et al.*, 2015).

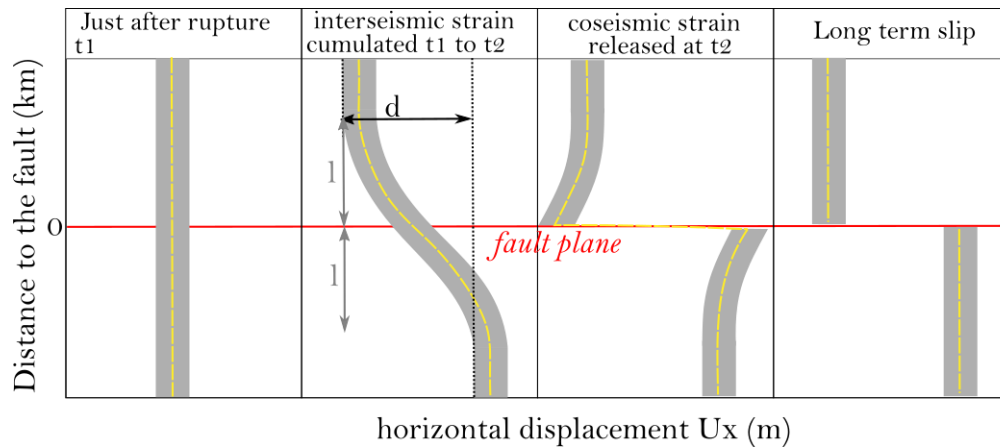


Figure 5.16: Model of deformation during the interseismic phase from time t_1 to t_2 . The locked distance is l . The displacement between the two blocks required to start a rupture is d .

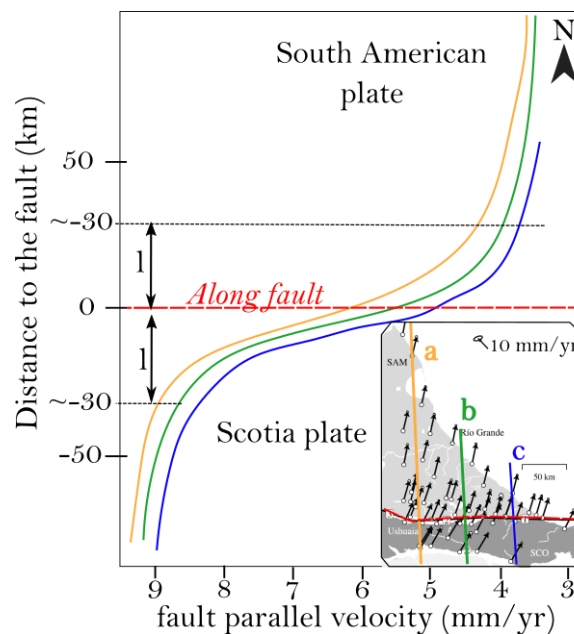


Figure 5.17: Three profiles of the Argentinian MFF interseismic velocities from Mendoza et al. (2015) compared to the fault distance. The profiles integrate the observed regional GNSS velocities and the predicted interseismic fault parallel velocities with respect to the reference frame IGS08

We propose to estimate the displacement d :

In the interseismic phase, the fault is locked : $d(y) = \frac{d}{\pi} \arctan\left(\frac{y}{Hf}\right)$

The strain is $\varepsilon_{xy}(y) = \frac{d}{\pi Hf} \times \left[\frac{1}{\left(1 + \left(\frac{y}{Hf}\right)^2\right)} \right]$

On the fault $y=0$: $\varepsilon_{xy(0)} = \frac{d}{\pi Hf}$

$$\Delta\tau' \sim \frac{E}{1+\nu} \varepsilon_{xy} = \frac{E \times d}{(1+\nu)\pi Hf}$$

When the fault ruptures, at t_2 we have:

$$\Delta\tau' = \frac{\Delta R'}{\cos(\varphi)}$$

And cumulated displacement is $d = \frac{(1+\nu)\pi \times Hf \times \Delta R'}{E \times \cos(\varphi)}$

Numerical

$$\text{with } \begin{cases} v = 0.25 \\ E = 5.10^{10} \text{ Pa} \\ D \sim 4.44 \cdot 10^{24} \text{ N.m} \\ \alpha \sim 153 \text{ km} \end{cases} \begin{cases} \Delta\sigma_x(0) = 17.5 \text{ MPa} \\ \Delta\sigma_y(0) = 6.6 \text{ MPa} \\ \Delta M = 12.1 \text{ MPa} \\ \Delta R = 5.4 \text{ MPa} \end{cases} \begin{cases} H = 100 \text{ km} \\ \rho = 3300 \text{ kg/m}^3 \\ l_g = 100 \text{ km}; h_g = 1000 \text{ m} \\ \rho g = 920 \text{ kg/m}^3 \end{cases}$$

application in $x = 0$:

Friction angle ϕ (degree)	Orientation will favor ice-cap effect which locks the fault			Orientation: fault parallel to ice cap			Orientation will reduce ice-cap effect which unlocks the fault		
	θ_{max} (degree)	$\Delta R'$ -max (MPa)	Cumulated slip d (m)	θ (degree)	$\Delta R'$ (MPa)	Cumulated slip d (m)	θ_{min} (degree)	$\Delta R'$ -min (MPa)	Cumulated slip d (m)
30°	-30°	11,43	31,10	0°	8,72	23,73	60°	0,60	1,64
10°	-40°	7,50	17,95	0°	3,03	7,25	50°	-3,32	-7,95
0,1°	-44,95°	5,43	12,81	0°	0,03	0,07	45,05°	-5,39	-12,71

Here we use $\nu=0,25$; $E = 5,10^{10}$ Pa; $D \sim 4,44 \cdot 10^{24}$ N.m ; $\alpha \sim 153$ km ; $\Delta\sigma_x(0) = 17,5$ Mpa ; $\Delta\sigma_y(0) = 6,6$ MPa ; $\Delta M = 12,1$ MPa; $\Delta R = 5,4$ MPa; $H = 100$ km ; $\rho = 3300$ kg/m₃ ; $l_g = 100$ km : $h_g = 1000$ m ; $\rho_g = 920$ kg/m³

Table 5.1 Stress and displacement required to reactivate the strike slip fault

V.2.6 Conclusion

[1] The icecap makes the faulting harder to occur.

[2] The tectonic stress orientations relative to the icecap deflexion determine the interference. The icecap's orientation relative to the fault primarily controls this quiescence effect's amplitude, as shown in Table 5.1.

[3] During glaciation, the quiescence effect is maximal for 'well'-orientation, which favors locking the fault and prevents earthquake nucleation. In this case, the interference is destructive and increases the stability of the fault. This configuration is similar to the interseismic phase in which the strike-slip faulting carries on way longer before reaching the rupture condition. The plates can 'store' and cumulate a large amount of slip away from the fault before rupture. Then when a rupture occurs, the fault releases the cumulated slip in one or several events. The maximum slip pulse is estimated from ~23 m up to ~31 m in orientations that favor icecap effect.

[4] The quiescence effect is minimized for the antithetical orientation, and the icecap does not efficiently prevent the fault from rupturing. In this configuration, the tectonic stresses orientations relative to the icecap deflexion stresses have constructive interference, reduce the fault stability.

[5] In situ stress measurement consistent with measured stress states in the upper crust are frequently found to be approximately equal to those predicted by Coulomb frictional failure theory review by Townend and Zoback (2000), using laboratory derived coefficients of friction of

0.6–1.0 (i.e., angle of friction 30–45°) (Byerlee, 1978). Realistic value of friction angle for the upper crust ranges from 30° to 45°. With a friction angle of 30°, the icecap quiescence effect is maximal for a fault with an angle of -30° relative to the icecap. In this configuration, during the interseismic phase, the maximum cumulated displacement before rupture is ~ 31 m. The locking effect is almost non-existent when the icecap has angle of +60° relative to the fault. Using a friction angle of 10°, the icecap quiescence effect is maximal for a fault with -40° angle relative to icecap. Under the load, the fault is locked, and cumulates a maximum displacement of ~ 17.95 m (Table 5.1). If these slips are released in one event, the associated earthquake magnitude may exceed Mw8 (Wells and Coppersmith, 1994). If the icecap has an antithetic angle of + 50°, then the icecap favors the rupture. Even the fault is loaded, the rupture can occur with a cumulated slip of ~ 7.95 m.

[6] This analytical experiment enables to evaluate roughly the amount of extra displacement cumulated slip under an icecap before to reach the rupture. The results show a slip-delay, which depends only on the initial ice-mass. As a reminder, the regional difference of cumulated slip since the glacier retreat is ~ 200 m, between the eastern (115 m) and the western MFF segment (315 m) MFF segments. The analytical approach shows the maximum slip-delay (31 m) represents no more than $\leq \sim 15\%$ of the difference. However, the experiment has a simplistic set-up, which includes an elastic lithosphere. It implies the slip-delay is time-independent, whatever is the glaciation duration. This method allows for targeting the effect of the rheological properties of the lithosphere on the fault behavior beneath an icecap. it is an oversimplified approach, and in nature, the slip-delay is depending on the deglaciation rate and on the underlying complex Earth's rheology.

V.3 Setup of the 3D-finite element model

Based on the analytical results, we proposed here a refine experiment in which various Earth's material rheology can be incorporated. To investigate the response of a major strike-slip fault such as the Magallanes Fagnano Fault system to glacial loading and subsequent unloading, we perform numerical modeling using the code ADEL (Hassani *et al.*, 1997; Chéry *et al.*, 2001) in the three-dimensional edition. ADEL is a finite element software developed in FORTRAN 77. Space is discretized using linear tetrahedrons elements (Figure 5.18). ADEL uses a dynamic relaxation method for time discretization (Underwood, 1983; Belytschko, 1983; Cundall and Board, 1988; Poliakov *et al.*, 1993).

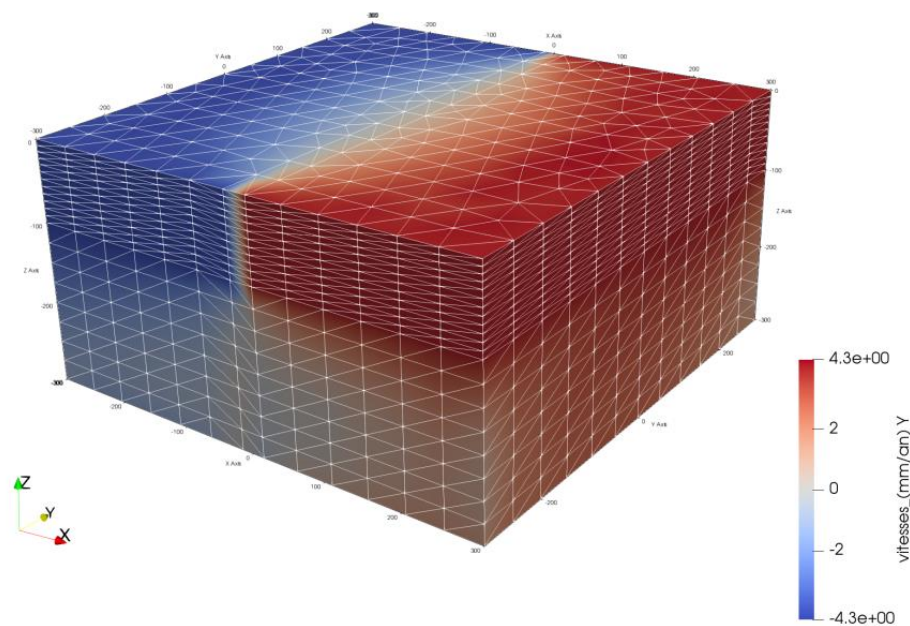


Figure 5.18: 3D view of the model mesh. Edges of tetrahedron elements are in white. Color bar correspond to velocities of the blocks in the case of a left-lateral strike-slip fault with a slip-rate of 8 mm. yr⁻¹

To improve our knowledge of strike-slip fault behavior during loading and unloading phases, we investigate the following questions:

1. How does horizontal fault velocity evolve through time during glacial loading and subsequent unloading?
2. What is the effect of the position of the fault relative to the icecap?
3. Does the duration and the intensity of the loading phase control the post-unloading slip size?
4. Does the fault velocity control the magnitude of the fault response to glacial unloading?

V.3.1 General setting and constitutive laws

ADELI enables to study the strain and the stress field induced by a finite fault embedded into the continental crust. Following this approach, [Grosset et al., 2019](#) use ADELI to model a 50-km-long fault, representing the Belledonne fault (Alps, France) as a finite dextral strike-slip fault located outside a formerly glaciated area. However, in our study, we model a transform plate boundary of a thousand of kilometers long, which separates the Scotia Plate and the South American Plate. Consequently, instead of using a finite fault, we assume a fault zone with a specific width, which cross-cuts from end to end the model. In this way, the Magallanes-Fagnano Fault (MFF) is modeled as a shear zone embedded in the Earth's crust with its proper rheology parameters different from the nearby Earth's crust materials.

The model simplifies the natural setup of the Magallanes-Fagnano Fault. The Earth is modeled as a portion of flat-earth of 600 x 600-km width and 300-km depth, divided into two blocks from end to end by a 30-km-wide fault zone. The code models a maximum of 200 000 tetrahedron elements with an element edge size of 50 km. The top face of the model is the Earth's surface, and the origin of the reference frame is located on the center of this surface. The x-y plane is horizontal, and z (upward) increases when elevation increases. The x, y, and z-directions correspond to north, west, and zenith. In this way, the fault zone is orientated in the east-west axe, and separates the northern block (South American plate) from the southern block (Scotia plate).

Our model loads the strike-slip fault with a rectangular icecap of 150 x 500 km. The model's surface holds the pressure of the glacial load of 10 MPa, equivalent to 1080 m of ice with a density

of 930 kg.m^{-3} . Experiments test three orientations of the fault positions relative to the icecap. In all experiments, the icecap remains centered in the model. We change the model mesh to implement three fault positions: centered fault, asymmetric fault, and oblique fault (Figure 5.19).

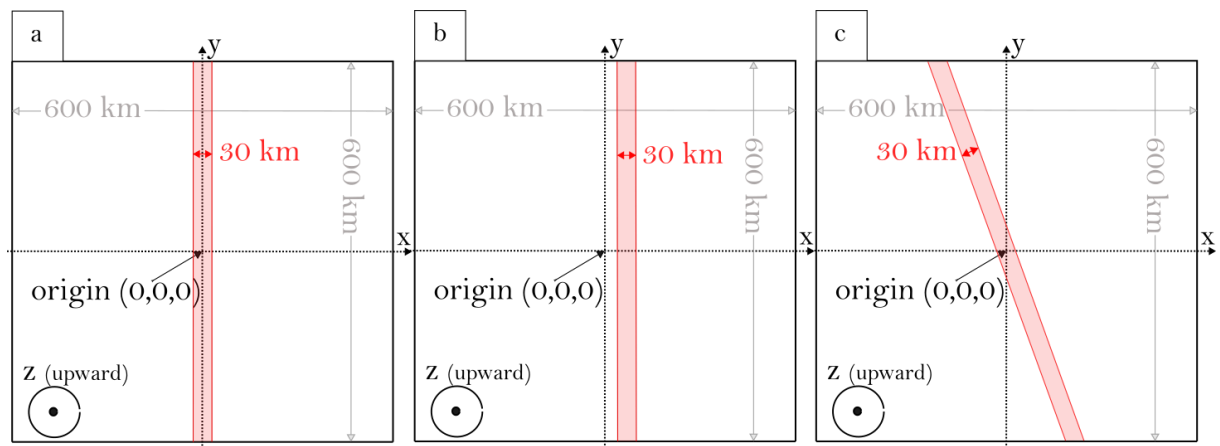


Figure 5.19: Map views of the three fault orientations. (a) Centered fault. (b) Asymmetric fault. (c) Oblique fault.

There are two sets of experiments: 2-layers and 3-layers earth model (Figure 5.20). The 2-layers setup is composed of the 100-km-thick elastic lithosphere on top of the 200-km-thick viscoelastic asthenosphere. The 3-layers setup is divided into 30 km-thick lithospheric crust, 70 km thick lithospheric mantle, and 200 km thick asthenosphere. Each layer is homogeneous and isotropic, except along the fault zone whose mechanical properties differ. Four rheologies are used to mimic Earth's rheologies: linear elastic, Maxwell viscoelastic, and time-independent elastoplastic.

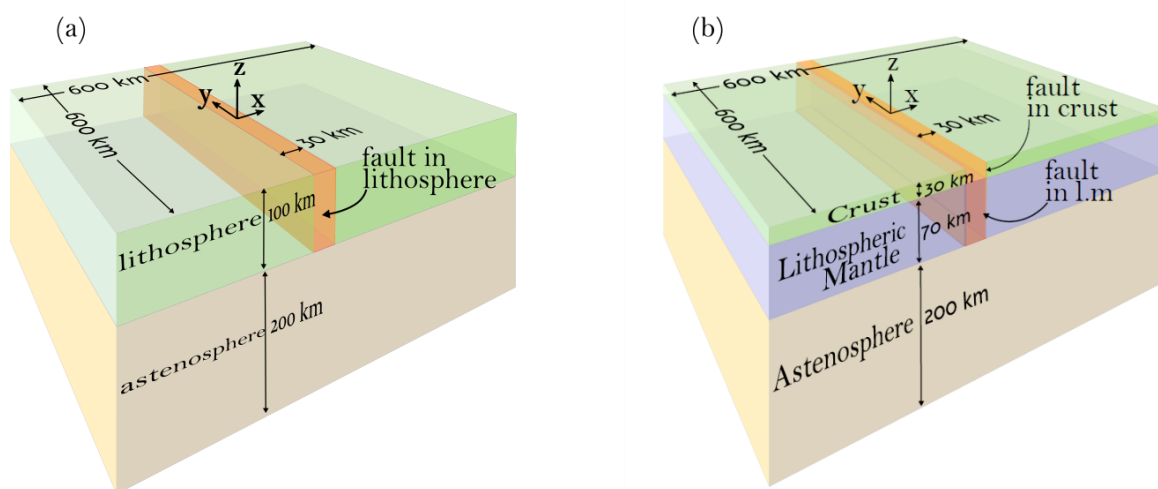


Figure 5.20: 3D sketch of the Earth models. (a) The 2-layers model: green layer is the crust (100 km); Orange layer is the asthenosphere (200km); Red layer is the fault zone (30 km-wide), which is embedded in the lithosphere. (b) The 3-layers model. Green layer is the crust (30 km thick); Purple layer is the lithospheric mantle (70 km thick); Orange layer is the asthenosphere (200 km thick); The fault zone is 100 – km thick and 30 km wide. The fault zone is divided into two volumes of different rheology. The dark orange volume is the fault embedded in the lithospheric crust; the dark purple volume is the fault in the lithospheric mantle

V.3.1.1 Elastic lithosphere

The lithosphere is considered purely elastic, except in the fault zone whose rheology is elastoplastic. Consequently, this means the rigid lithosphere bends under the icecap weights and acquires a reversible flexure. The elastic bending of the lithosphere yields to regional vertical movements of uplift and subsidence. It is a simplified setup, as it is generally valid only for the first ~30-km of the Earth's crust. The elastic materials follow constitutive Hooke's law. The lithosphere of the 2-layers model has a density of $\rho = 2\,800\text{ kg}\cdot\text{m}^{-3}$. This value is plausible for the continental crust (depth 3-24.4km) (Dziewonski and Anderson, 1981). However, for 2-layers model, which was to set a simple Earth model, we assume the same density for the whole lithosphere (100 km thick). The 3-layers model takes into account this complexity with a 30 km-thick crust with a density $\rho = 2\,800\text{ kg}\cdot\text{m}^{-3}$ and with a lithospheric mantle of 70 km thick with a density of $\rho = 3\,300\text{ kg}\cdot\text{m}^{-3}$. In all experiments, the Poisson's ratio $\nu = 0.25$ (Turcotte and Schubert, 2014). The Young modulus is $E = 1.0 \times 10^{11}\text{ Pa}$ in the 2-layers experiment and is $E = 0.6 \cdot 10^{11}\text{ Pa}$ in the 3-layers model. These values are realistic earth's crust properties (Turcotte and Schubert, 2014).

V.3.1.2 Elastoplastic fault zone

The fault zone of the 2-layers model is strictly located in the lithosphere and corresponds to one single volume. While in the 3-layers model, there are the fault zone in the lithospheric crust and the lower fault zone in the lithospheric mantle. For fault in the lithosphere (2-layers), and fault in the lithospheric crust (3-layers), we assumed an elastoplastic behavior. Thus, beyond the elastic domain, these zones are characterized by a pressure-dependent law. Slip initiation on the

fault is governed by the Drucker-Prager criterion defined as Equation 2 (Desai and Siriwardane, 1984; Hassani *et al.*, 1997). Therefore, at the beginning of each experiment, this material has elastic behavior and gradually reaches the plasticity threshold to evolve in fully plastic behavior. We assume a weak zone with an $E = 5 \cdot 10^{10}$ Pa, $\nu = 0.25$, and a cohesion C of $1 \cdot 10^6$ Pa. We first take a friction angle φ of 1° in the simplistic 2-layers experiment, and then of 10° in the 3-layers model. Smaller friction angle allows reaching faster the fully plastic behavior in the fault zone, thus it

with:

$$J'_2(\sigma) \text{ the second invariant of the deviator stress} = \left[\left(\frac{3}{2} \right) s : s \right]^{1/2}$$

$$J_1(\sigma) \text{ the mean pressure} = \frac{1}{3} \sigma \text{ [Pa]}$$

enables to initiate earlier the strike-slip faulting.

$$\text{Equation (2)} \quad F(\sigma) = J'_2(\sigma) + \left(\frac{6 \sin \varphi}{3 - \sin \varphi} \right) J_1(\sigma) - \left(\frac{6 \sin \varphi}{3 - \sin \varphi} \right) \times \left(\frac{C}{\tan \varphi} \right)$$

Viscoelastic asthenosphere

The asthenospheric mantle is assumed to be viscoelastic, as defined in equation 3. When the elastic limit is exceeded, the material either deforms plastically or ruptures and causes a permanent change in shape.

$$\text{Equation (3)} \quad \dot{\sigma}_{ij} + \frac{\mu}{\eta} \left(\sigma_{ij} - \frac{1}{3} \sigma_{kk} \delta_{ij} \right) = \lambda \varepsilon_{kk} \delta_{ij} + 2\mu \dot{\varepsilon}_{ij}$$

With: σ_{ij} and ε_{ij} are the stress and strain tensors

δ the identity matrix written here as the Kronecker delta notation

V.3.1.3 Elastoplastic or viscoelastic fault zone

The lower fault zone embedded in the lithospheric mantle (3-layers model) is either Drucker-Prager elastoplastic, either a Maxwell viscoelastic material according to the current stress state. The rheological parameters of the different materials are defined in Table 5.2.

Table 2a : 2-layers model parameters

	Lithosphere	Asthenosphere	Fault in lithosphere
N° volumes	1, 3	4, 5, 6	2
rheology	elastic	viscoelastic	elastoplastic
Young modulus (Pa)	1,0E+11	1,0E+11	5,0E+10
Poisson coefficient	0,25	0,25	0,25
density (kg.m ⁻³)	2 800	3 300	2 800
Viscosity (Pa.s)	na	5,0E+19	na
power law exponent	na	1	na
cohesion (Pa)	na	na	1,0E+06
friction angle (°)	na	na	0,1

Table 2b : 3-layers model parameters

	Crust	Lithospheric mantle	Asthenosphere	Fault in crust	Fault in mantle lithosphere
N° volumes	1, 3	4,6	7,8,9	2	5
rheology	elastic	viscoelastic	viscoelastic	elastoplastic	visco-elastoplastic
Young modulus (Pa)	6,0E+10	1,5E+11	1,1E+11	5,0E+10	1,5E+11
Poisson coefficient	0,25	0,25	0,25	0,25	0,25
density (kg.m ⁻³)	2 800	3 300	3 300	2 800	3 300
Viscosity (Pa.s)	na	1,0E+23	1,0E+19	na	1,0E+23
power law exponent	na	1	1	na	1
cohesion (Pa)	na	na	na	1,0E+06	1,0E+06
friction angle (°)	na	na	na	10	10

Table 5.2a Parameters used in model with 2 layers and 5.2b Parameters used in model with 3 layers.

V.3.2 Velocity setup and evolution

Velocity boundary conditions are enforced on the outer face of the mesh. During the first thousand years, the velocity increases linearly to its maximum value. After 1 000 years, the maximal speed is applied until the end of the experiment. Using a velocity boundary conditions to the model faces in the xz-plane toward +y for the northern block, respectively toward -y for

the southern block, the model mimics the left-lateral strike-slip movement in the lithosphere of the MFF (Figure 5.21).

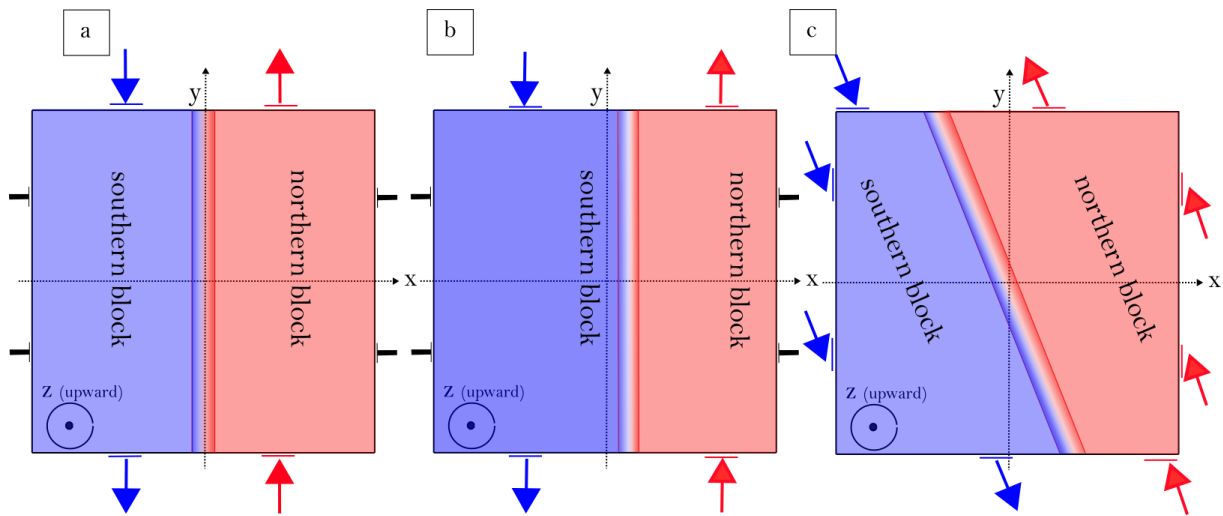


Figure 5.21: Map views of the velocity boundary conditions for the experiments with: (a) centered fault, (b) asymmetric fault and (c) oblique fault.

In the 2-layers model, the velocity boundary conditions are only applied to the lithosphere (Figure 5.22a). In the 3-layers model, these conditions are applied to the lithospheric crust and lithospheric mantle. Note that the velocity boundary conditions are not applied to the asthenosphere mantle (Figure 5.22b). The model sides in the yz plane are fixed in the x-direction and move freely in the y and z –directions. The bottom of the model is fixed in the z-direction. The other sides are free to move in the x, y, and z-directions.

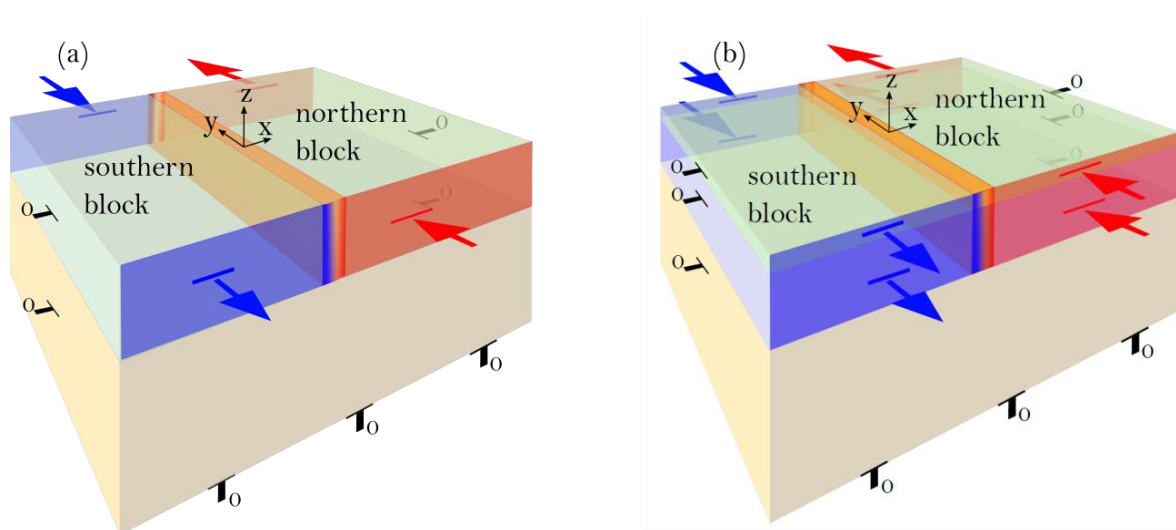


Figure 5.22: 3D sketch of the velocity boundary conditions (a) in the 2-layers mode and (b) in the 3-layers model.

The velocity boundary conditions along the xz face of the fault zone are defined by a parametric variation along the x-axis to induce a smooth transition between the two blocks. It means the velocity changes gradually in the fault zone. At the southern fault limit, the movement is toward the east, whereas in the northern boundary the motion is toward the west.

V.3.3 Pressure setup and evolution

We imposed the pressure boundary conditions on the mesh outer faces. The model is submitted to a constant gravity field, included as a body force of 10 m.s^{-2} . We applied the lithostatic pressure on the asthenospheric mantle xz-sides. The model's surface holds the pressure of the glacial load. To model the icecap, we apply a pressure of 10 MPa on the top faces, which is equivalent to 1080 m of ice with a density of 930 kg.m^{-3} . The icecap has a rectangular shape of $150 \times 500 \text{ km}$. Even though the ice body is simple, the proportions are conformed at 1st order with the local LGM (36.1-25 ka) of the Cordillera Darwin ice-sheet, which was $\sim 125\text{-}200 \text{ km}$ wide $\sim 600 \text{ km}$ long for an ice elevation about $\sim 700\text{-}1100 \text{ m}$. This shape does not attempt to model the LGM Fuegian ice-sheets spatial complexity neither its thickness variations.

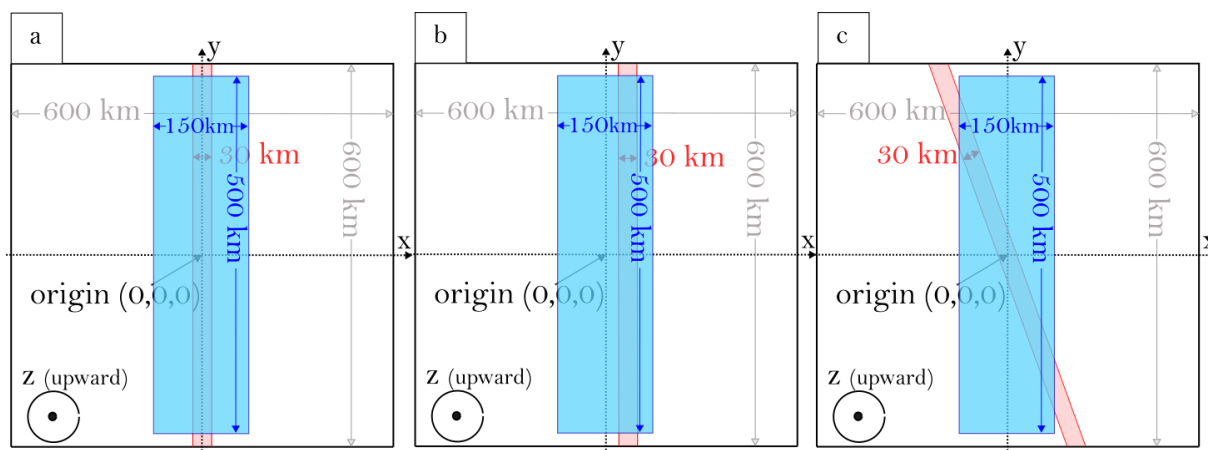


Figure 5.23: Map views of the relative position of the fault and the icecap for the experiments with: (a) centered fault, (b) asymmetric fault and (c) oblique fault.

Depending on the considered zone, the LGM Fuegian ice-sheet has variable orientations relative to the MFF. Indeed, the Fagnano lobe flowed parallel to the MFF system. Whereas in the

Almirantazgo Sound, most of the LGM ice was located on the Cordillera Darwin and in the Magellan Strait lobe. It was an asymmetrical load configuration, overloading the Scotia plate comparatively to South American plate. Along the Magellan Strait western entrance, the MFF is oblique relative to the Grand Campo Nevado ice field. These 3 configurations are processed in different experiments: centered, asymmetric and oblique (Figure 5.23a b c). With ADELI, it is convenient to modify the fault zone position by editing the mesh structure instead of changing spatial pressure conditions. That is the reason why the icecap pressure remains always fixed and centered. During experiment, the velocity and the pressure boundary conditions are applied, as illustrated in Figure 24. The same pressure conditions are applied in model 2-layers and 3-layers (Figure 5.25 a, b).

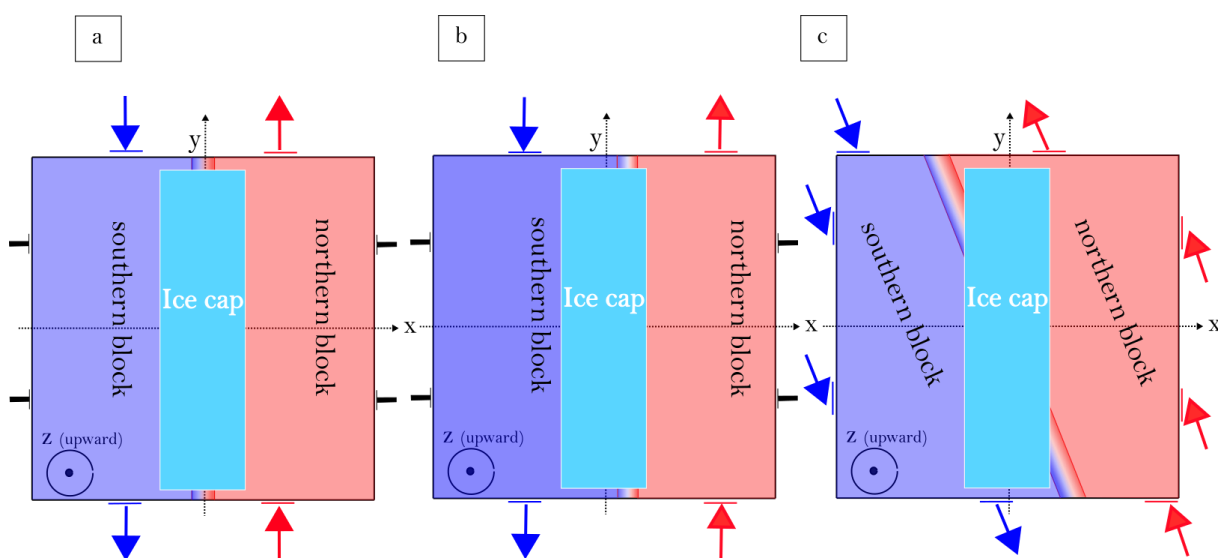


Figure 5.24: Map views of the pressure and the velocity boundary conditions for the experiments with (a) centered fault, (b) asymmetric fault and (c) oblique fault.

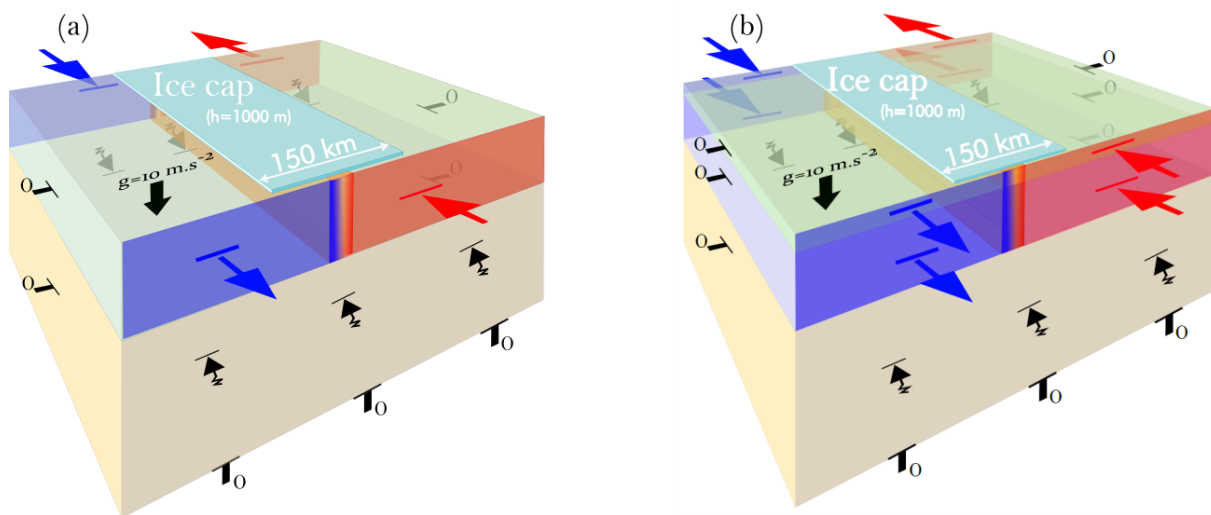


Figure 5.25: (a) 3D sketch of the pressure and the velocity boundary conditions in the 2-layers model; (b) 3D sketch of the pressure and the velocity boundary conditions in the 3-layers model.

V.3.3.1 Experiments without loading

Experiments of reference are set without glaciation. Their respective numbering inside the list of experiments includes a letter 'R'. Each reference experiment has identical rheological parameters as the experiment of which it refers. In the following analysis, experiment and its reference are compared to pinpoint the effects of an icecap.

V.3.3.2 Load history

All scenarios are characterized by 5-time steps (Figure 5.26): initial step without load, rising loading, constant loading, unloading and relaxation. The glacial cycle includes the 3-steps ascending loading, constant loading, unloading. During glaciation, the ice volume grows, and the load magnitude increases linearly to its maximum value, thereby from 0 to 10 MPa (loading). Then, the load remains stable for a couple of thousand years (stable load). During deglaciation, the ice volume collapse, and the load decreases linearly to zero (unloading) in a defined amount of time. Finally, after deglaciation, the load remains null until the end; this is the relaxation phase.

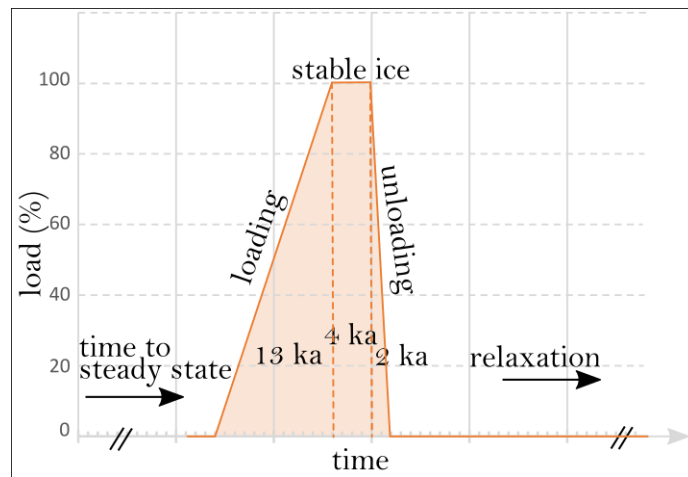


Figure 5.26: Temporal evolution of the load.

Glaciation type	short (a)	short (b) (even nbrs)	Best fit	long
Loading (from 0 to 10 MPa)	13 ka	14 ka	14 ka	40 ka
Stable load (10 MPa)	4 ka	4 ka	6 ka	20 ka
Unloading (from 10 MPa to 0)	2 ka	2 ka	18 ka	10 ka
Total duration (ka)	19	20	38	70

Table 5.3: Type of glaciation cycles.

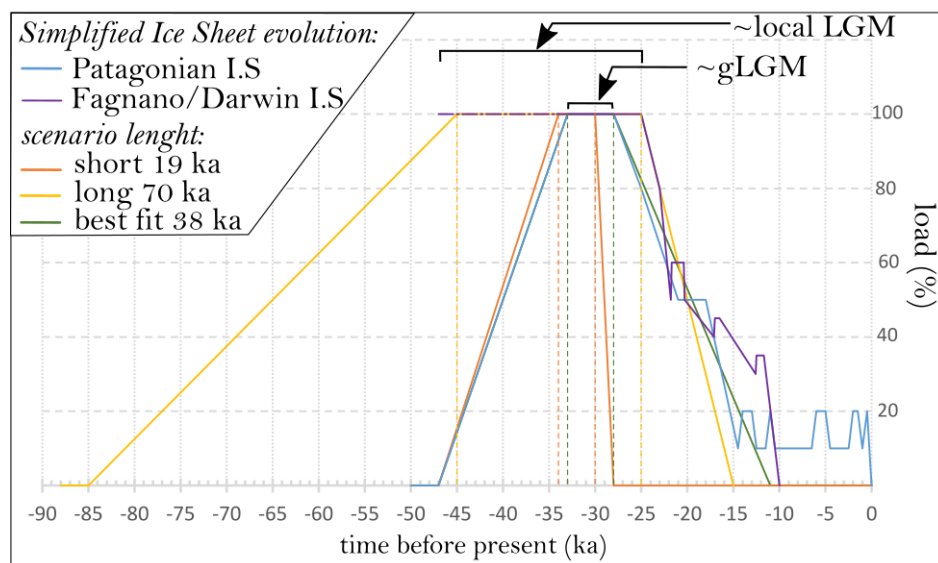


Figure 5.27: Comparison with local LGM, global LGM and the 3 model's load histories.

Our study uses 3 glacial cycle durations 19 ka, 38 ka, and 70 ka (Table 5.3). To investigate the effect of the length of a glacial phase on fault behavior, we set a long glacial cycle (70 ka) and a short glacial cycle (19 ka). The quick process is set to facilitate comparison with substantial work on normal and reverse faults behavior under the Fennoscandia Ice-sheet (Hampel *et al.*, 2010). The Loading, the stand-still, the unloading durations are 13 ka, 4 ka, and 2 ka, respectively (Figure 5.26). However, the Last Glacial phase in the southern hemisphere is characterized by its unique temporal evolution (Figure 5.27). Local LGM (lLGM) of the Magallanes Fault slightly differs from global Patagonian LGM (gLGM) (Figure 5.27). To mimic the advance and retreat of the ice above the Magallanes-Fagnano fault, we set an intermediate glacial cycle of duration 38 ka. This scenario simplifies the temporal evolution of the Patagonian Ice Sheet from Davies *et al.* (2020). Between 47-33 ka before present (BP), the load increases during 14 ka (i.e., the icecap grows), and then remains constant for 4 ka (stable load). At 28 ka BP, ice starts to disintegrate, and deglaciation lasts 18 ka. The ice completely vanishes at 11 ka. The long glaciation scenario (70ka) is divided into 40 ka loading, 20 ka stabilization of the load, and 10 ka progressive unloading (Figure 5.27). Importantly, we acknowledge that the last glacial history of Isla Grande de Tierra del Fuego differs from these simplified scenarios. Our experiments do not account for the Fuegian lobes readvances of the Late-Pleistocene.

V.3.4 Parameters investigated

We can discriminate the glaciation effects thanks to comparing the experiment with and without glaciation. In this way, we can identify the slip-rate evolution due to loading relative to a normal amount of slip without loading.

The fault velocity, either named fault slip-rate, is the ratio between relative displacement between fault sides and this movement's duration. To plot the slip-rate evolution in the following figures, we use a cross-profile. In all the experiments, the cross-profile is perpendicular to the fault and centered in the model (Figure 5.28a, b, c). Two points of reference enable us to compute the relative block motion. These two points are located along the cross-profile and are symmetrical to the fault zone. There are 16 km away from the frame origin and enable us to visualize the two blocks' behavior near the fault.

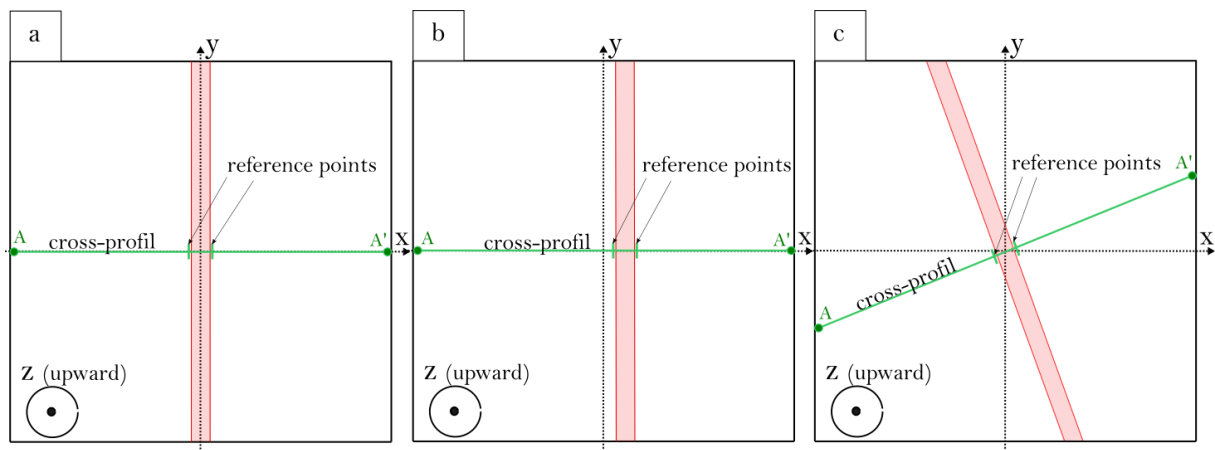


Figure 5.28: Map view of the model surface showing the position of the fault zone relative to the cross-profile and reference points. (a) Model with centered fault zone. (b) Model with asymmetric fault zone. (c) Model with oblique fault zone.

All experiments are summarized in Table 5.4. We investigate the following parameters:

- The thickness of elastic lithosphere (2-layers versus 3-layers model)
- The position of the fault relative to the icecap
- The fault velocity, i.e., tectonic background
- Length of glaciation phase

	Experiment characteristics				Fault geometry				Glaciation				
	duration	nbr of layers	xplotp*	timestep output (yrs)	fault position	strike-slip timestep	slip-rate	rheology &	Start (ky)	scenario [£]			
G0001	100 ka	2	0,05	5 000	Centred	0-10 000 yrs progressive slip-rate then > 10 000 the full slip-rate is imposed until the end of experiment	8 mm.yr ⁻¹	Type 1	10	long			
G0002		2			Assym.								
G0003		2			Oblique								
G0004		3			Centred								
G0005	1 Ma	3	0,01	10 000	Centered		8 mm.yr ⁻¹	Type 2	910	long			
G00R6			1 000	0,001					1 000	Assym.	4 mm.yr ⁻¹	NA	NA
G0006												910	short (a)
GE006												810	short (a)
GOL06												910	long
GS0R6												NA	NA
GS006							910					short (a)	
GSL06			910	long									
GOR23			10 Ma	3		0,001	1 000		Assym.	8 mm.yr ⁻¹	NA	NA	
G0023									centered		8 mm.yr ⁻¹	910	short (a)
GOR33												Oblique	NA
G0033	910	short (a)											
G00R7		NA			NA								
G00R8	2 Ma	3	0,001	2 000	centered	8 mm.yr ⁻¹	NA	NA					
G0008							0 - 1000 yrs progressive, then > 1000 yrs the full slip-rate is imposed until the end of experiment	8 mm.yr ⁻¹	1500	Best fit			
GON08									910	short (a)			
GONb8									910	short (b)			
G00R9									NA	NA			
G0009									1500	Best fit			
GOR10									NA	NA			
G0010									1500	Best fit			
GOR11									NA	NA			
G0011									1500	Best fit			
Gbis6									1 Ma	3	0,001	1 000	Centred
GbiR6	NA	NA											

* Xplotp defines the normalized time interval for creating an output file , ie: timestep output = duration * xplotp.
 & see table 2a, 2b for complete overview of rheology parameters
 £ : see table 3 for description of glaciation scenario

Table 5.4: List of experiments and respective characteristics.

V.3.5 Time to fault steady-state

Despite the velocity conditions are applied in the first thousand years, the relative motion of the two-blocks is not wholly reached instantaneously (Figure 5.29a, b). There is a delay required to achieve a stable strike-slip movement before proceeding to the loading phase. In the beginning, the whole fault zone has an elastic behavior (Figure 5.30a). Gradually, the fault's material reaches the plasticity threshold (Figure 5.30b). In the end, the entire fault zone may have a plastic behavior (Figure 5.30c). This process requires time to achieve a state of steady fault slip-rate.

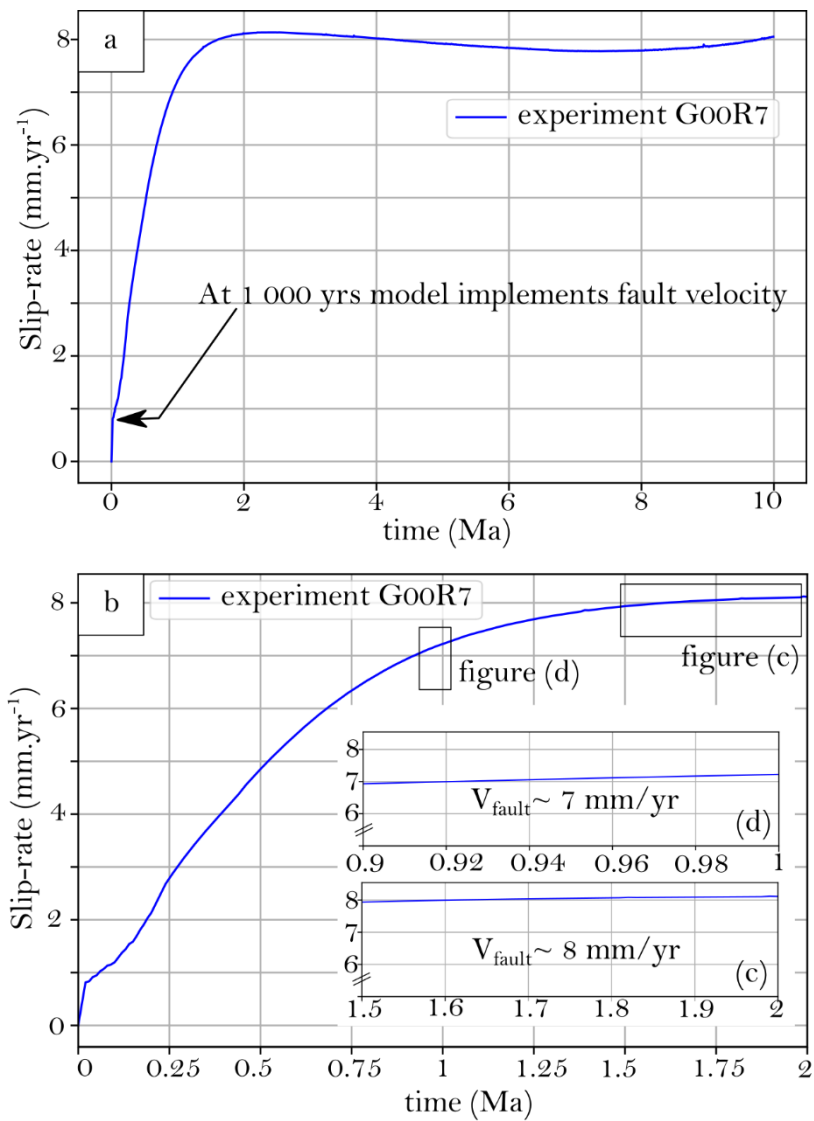


Figure 5.29: (a) Temporal evolution of slip-rate from experiment GooR7 (no loading) over 10 million years. (b) Zoom from 0 to 2 Ma. (c) Zoom from 1.5 Ma to 2Ma. It is the ideal steady-state duration. (d) Zoom from 900 ka to 1 000 ka, this is the alternative steady-state duration.

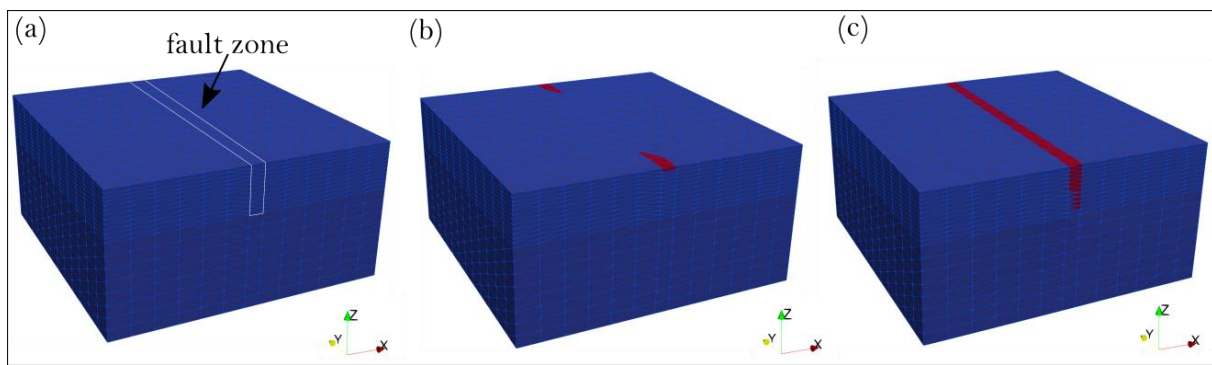


Figure 5.30: Evolution of the strain in the fault zone with 3D view of the model (3-layers experiment) Blue color shows material with elastic behavior. The red color indicates the material that has reached the plastic threshold. (a) Step 1 all the fault zone has elastic behavior. (b) Step 2 shows part of the fault zone has reached plastic threshold. (c) Step 3 shows that all the fault zone has the plastic behavior.

To evaluate the best duration of 'Time to fault steady-state', we experiment a single scenario with an overall length of 10 Ma called GooR7. With a velocity of 4 mm.yr^{-1} imposed on each block, we expected a full strike-slip fault velocity of 8 mm.yr^{-1} (Figure 5.29a). This velocity is reached at $\sim 1.5 \text{ Ma}$ (Figure 5.29b). It is the ideal duration of the initial phase before loading (Figure 5.29c).

However, the 10 Ma experiment required about 24 hours to be achieved. In order to multiply the experiments, we opt for a less-time consuming modeling with a shorter time to steady state at 910 ka and acknowledges our experiments are set with a fault velocity of 7 mm.yr^{-1} . The following comparison between the two experiments shows that this approach yields a reasonable error of $\sim 10\%$.

This alternative scenario allows approaching a steady-state at 910 ka, at which the fault slip-rate is about $\sim 7 \text{ mm.yr}^{-1}$ (Figure 5.29d). Because the velocity is smaller of 12%, we compare the slip-rates changes resulting from loading at 910 ka vs 1.5 Ma (Figure 5.31 & 5.32). The two experiments have the same slip-rate patterns during loading and subsequent unloading (figure 5.31). Figure 5.31b evidences only a difference of amplitude resulting from the difference of slip-rates before loading (Figure 5.31b). Associated cumulated slip is therefore slightly smaller for experiment GoNs8. The loading phases (loading and stable ice) mutes the faults and avoid slip to occur. These cumulated slips delayed are about $\sim 5, 44 \text{ m}$ for loading at 910 ka, and about $\sim 6.03 \text{ m}$ for loading at 1.5 Ma (Figure 5.32b).

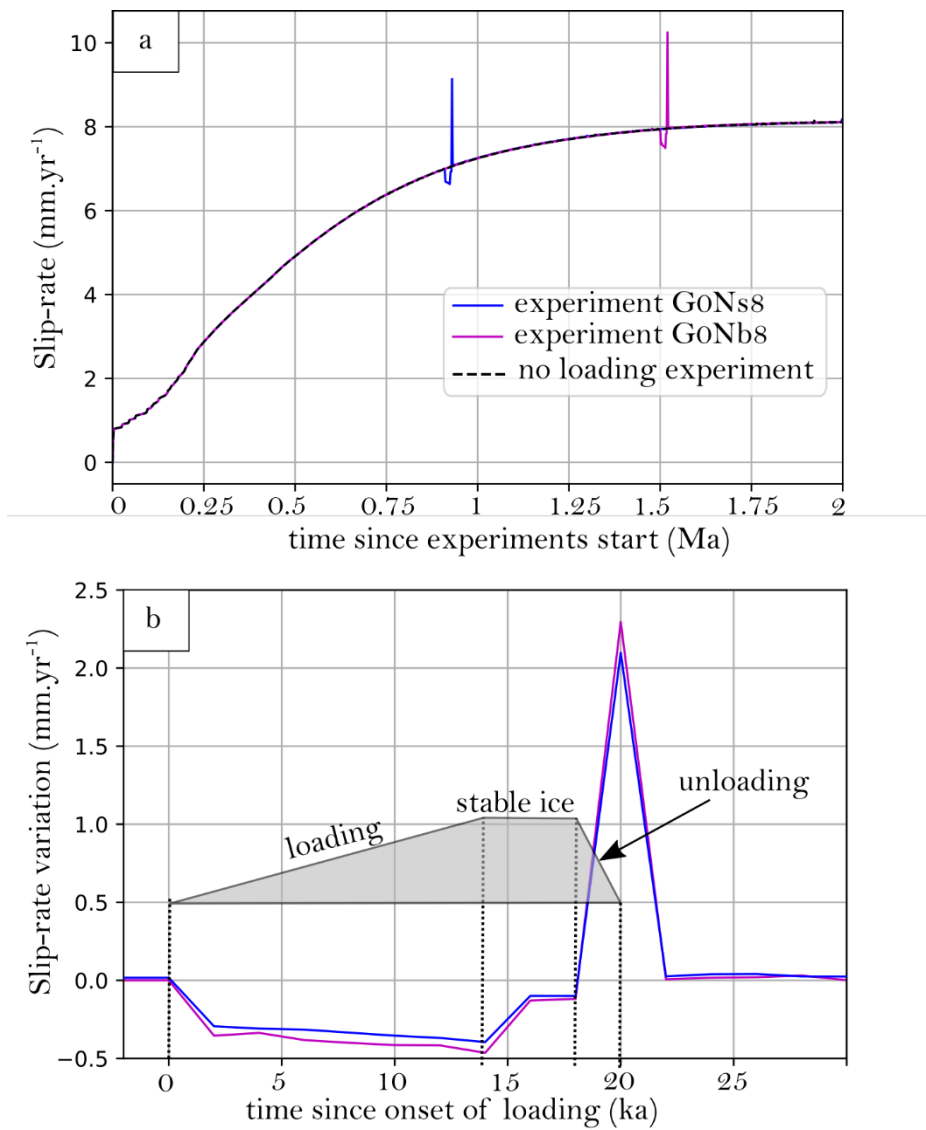


Figure 5.31: Comparison of slip-rates between two experiments which have different initial phase durations. The time to steady-state of GoNs8 is 910 ka (blue curve), whereas for GoNb8 is 1.5Ma (magenta curve). (a) Temporal evolution of cumulated slip over 2 Ma. (b) Decrease (-) or increase (+) of slip-rates relative to experiment without loading. The time is shown since the onset of loading for comparison.

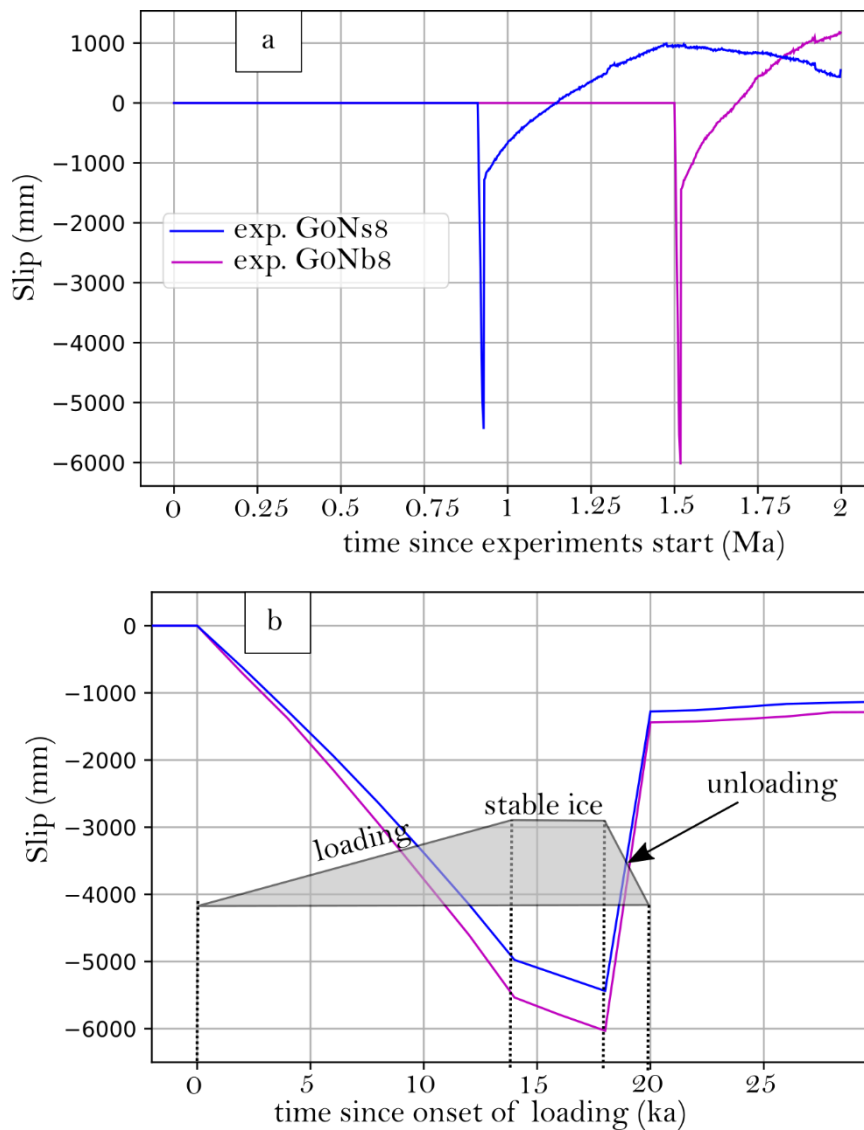


Figure 5.32: (a) Difference of slip cumulated over time between loading experiments (GoNb8, GoNs8) and the experiment without loading. The time to steady-state of GoNs8 is 910 ka (blue curve), whereas GoNb8 is 1.5Ma (magenta curve). The negative difference shows the amount of slip delayed during each phase when the fault decelerates compared to no-load experiment. A positive difference indicates a slip-pulse when the fault accelerates. (b) Zoom-in the same figure with time since the onsets of loading for comparison.

V.4 Model Results

In this section, we consider the experiment with a short initial phase during 910 ka.

V.4.1 Centered Fault Experiments

V.4.1.1 Effect of loading

Here, we focus on experiment G0006 in which the two blocks accommodate the left lateral movement with a rate of $\sim 7 \text{ mm.yr}^{-1}$ (Figure 5.33a) along a centered fault. At 910 ka, the fault is progressively loaded during 13 ka (Figure 5.33b). Under the load, the lithosphere is deflected with rate $V_z = 9 \text{ mm.yr}^{-1}$. During the following 4 ka, the load remains stable. The unload occurs progressively in two thousand years and triggers a rebound dome with maximal vertical velocity $V_z = 60 \text{ mm.yr}^{-1}$ (Figure 5.33b).

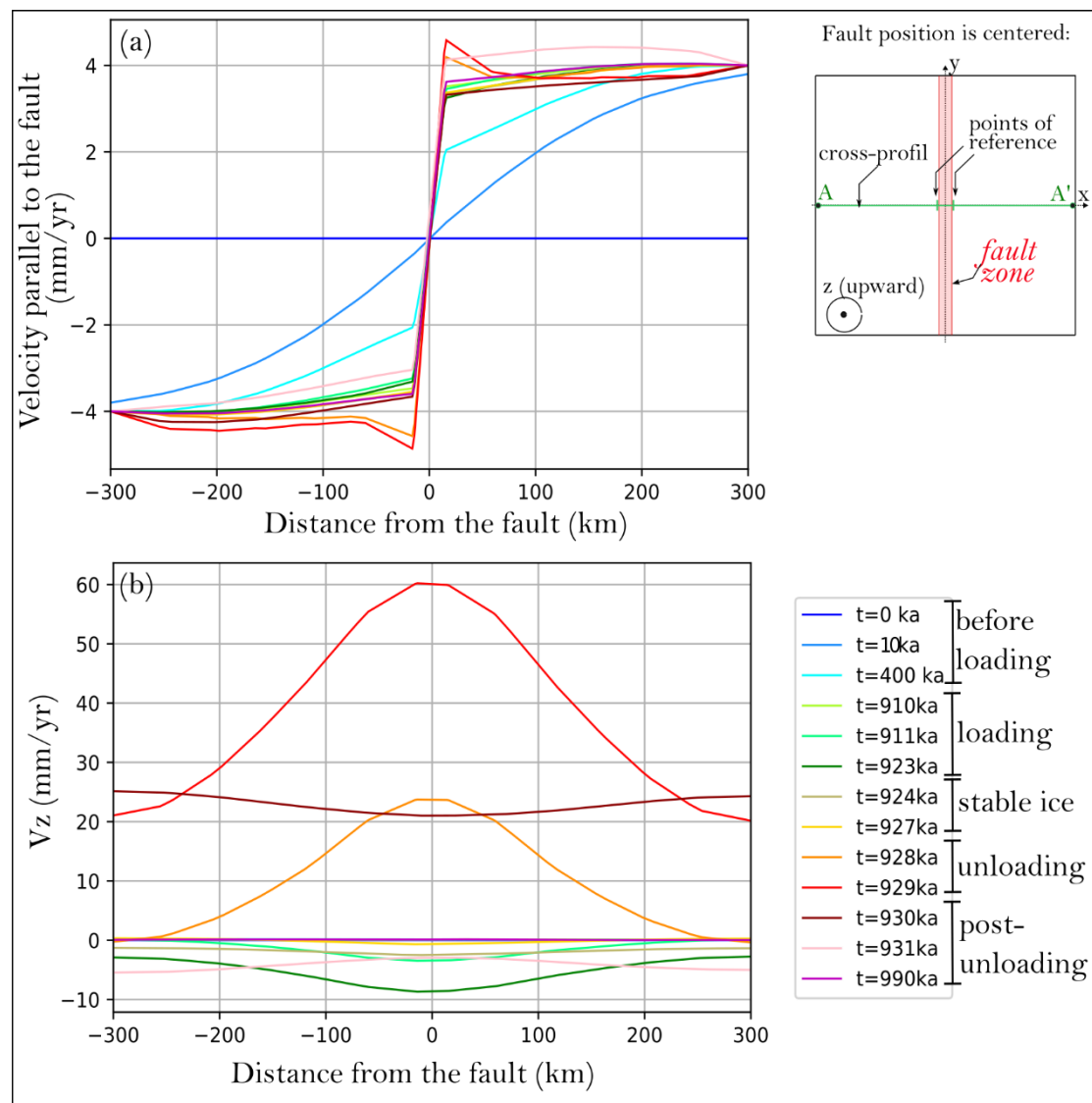


Figure 5.33: Temporal evolution of horizontal (a) and vertical (b) velocities of experiment G0006 (centered fault). Velocities are shown along the cross profile perpendicular to the fault. Distances are shown from the fault center with a fault zone width of 30 km. Colored curves show the time step in ka.

We compare the behavior of experiment G0006 and experiment without load (Figure 5.34b). During loading and subsequent unloading, two different slip patterns can be determined. Loading triggers slip-rate decrease, while unloading leads instantly to a slip-rate pulse (Figure 5.34b). During the primary phase of loading, between 0 ka to 13 ka, the slip-rate decelerates in average of about $-0.38 \text{ mm}\cdot\text{yr}^{-1}$ (Figure 5.34b). Then, when the load is constant between 13 and 17 ka, the slip-rate drops with a slower rate than during the previous phase, the fault velocity slows down about $\sim -0.12 \text{ mm}\cdot\text{yr}^{-1}$. This decreasing velocity results in a slip-delay that increases during the glaciation episode. Because this slip is not released, we consider it is stored and delayed. We

compute the cumulated slip-delay comparing with the experiment without loading, in function of the temporal load evolution (Figure 5.35a). Accordingly, the cumulated slip delays throughout progressive glaciation (0-13 ka) and stable load (13-17 ka) are respectively about ~4.9 meters and ~0.5 m (Figure 5.35b). Thereby, the glaciated period avoids a total slip of ~5.4 meters (Table 5.5).

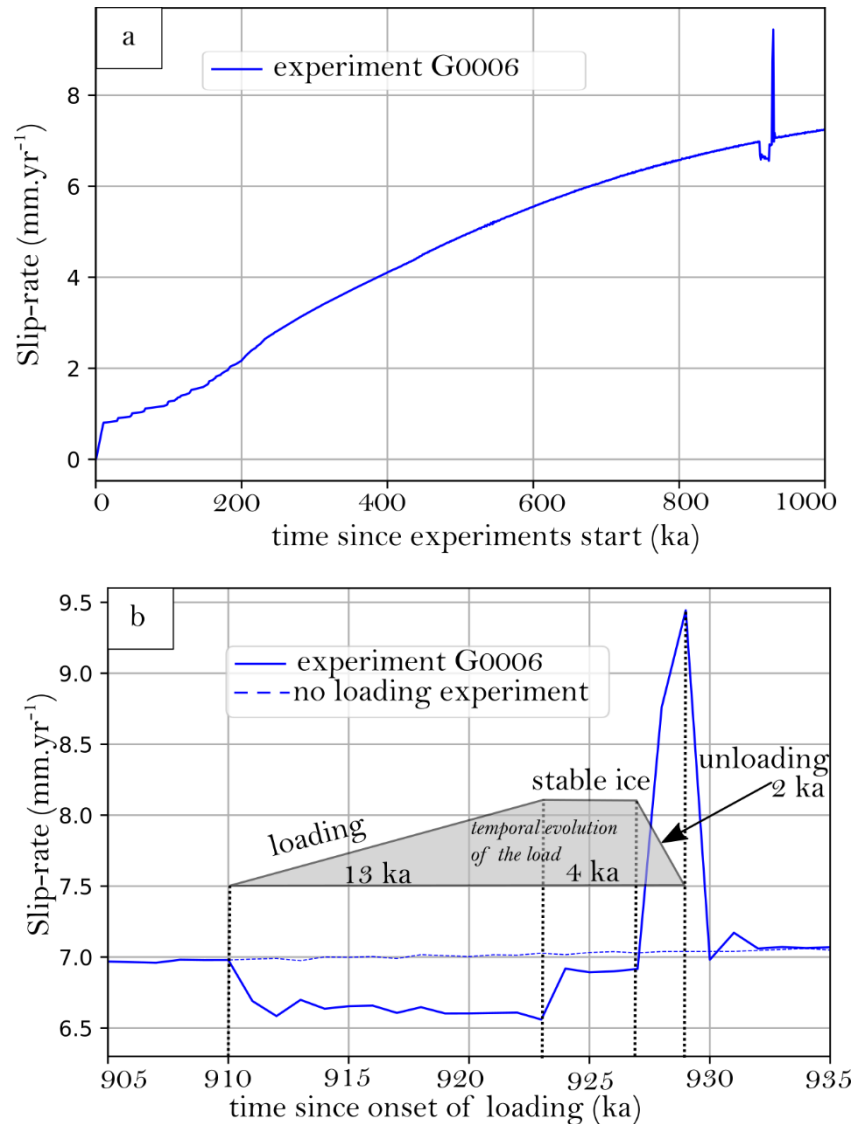


Figure 5.34: Slip-rates of experiment with centered fault (G0006), which after an initiation of 910 ka, underdoes a short glaciation cycle of 19 ka. (a) Temporal evolution of slip-rates over 1 Ma. (b) Zoom in same figure since the onset of glacial loading. Grey triangle shows the temporal evolution of the load.

Interestingly, this cumulated slip-delay is not fully recovered by the subsequent slip-rate pulse. After 17 ka, the fault is unloaded, which triggers a drastic velocity increase reaching about

9.5 mm.yr⁻¹ (Figure 5.34b). This pulse occurs immediately when the unloading starts, even though the unloading should be progressive, reducing from 10 MPa to zero in two thousand years. In average over the deglaciation period (17-19 ka) the slip-rate increases about 2.1 mm.yr⁻¹ which correspond to ~ 4.2 meters of cumulated slip. Consequently, the difference between the delayed slip and the released slip is ~ 1.3 meters (Figure 5.35b) at the end of deglaciation.

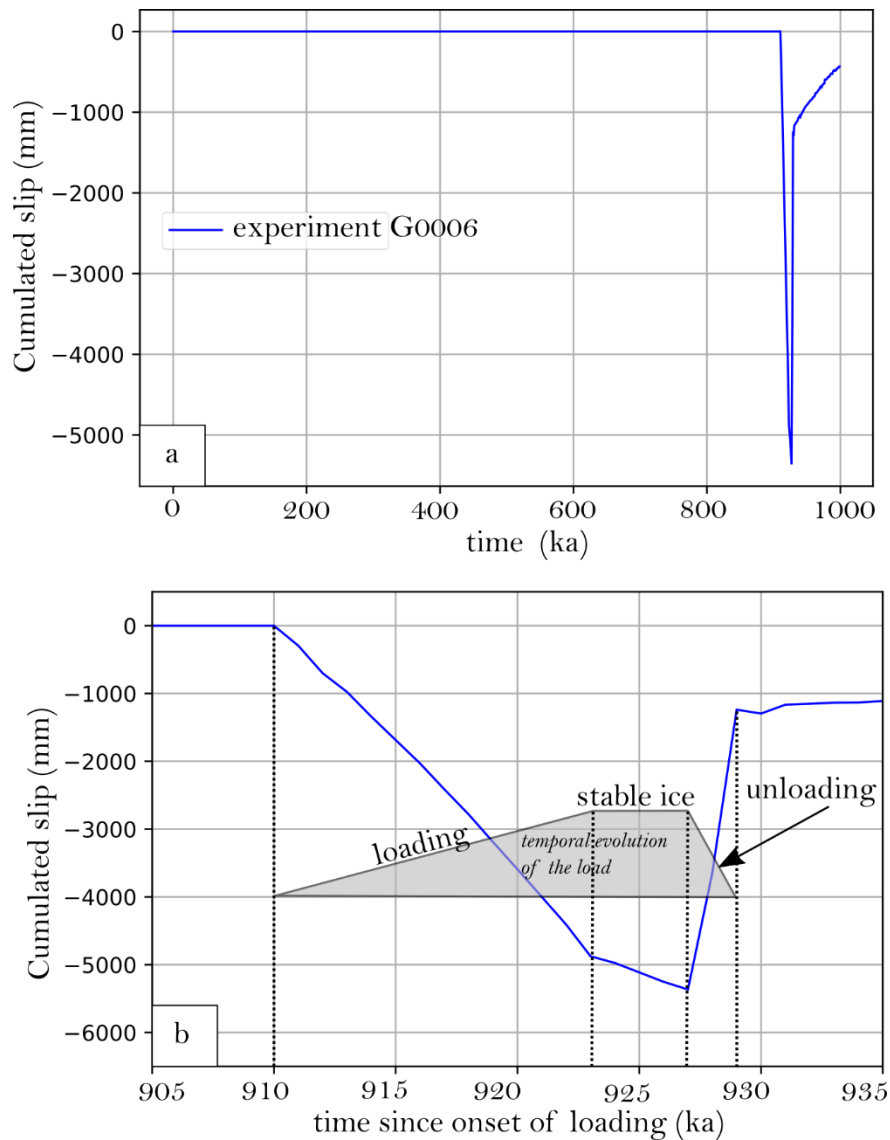


Figure 5.35: (a) Cumulated difference of slip between loading experiment (G0006) and the experiment without loading. Negative difference shows the slip delay in each phase when the fault decelerates compared to the no-load experiment. A positive difference indicates slip pulse when the fault accelerates. (b) Zoom-in the same figure.

After the unloading phase, we see a brief decrease of velocity with value dropping to ~ 7 mm.yr⁻¹, and followed soon after by a second minor increase of up to ~ 7.2 mm.yr⁻¹. The relaxation phase (until the end) lasts 71 ka. In this phase, the slip-rate increases in average about 0.01 mm.yr⁻¹ comparatively with a no-glaciation experiment. It is associated with ~ 0.8 meters of cumulated slip. Even at the end, the slip amount that was 'mute' during glaciation is not fully recovered, and leaves ~ 0.43 meters of unrecovered slip.

	A Initial phase (no load)	B Loading	C Ice-stable	D Unloading	E Post- unloading	B+C Loading + Ice- stable	A+B+C+D+E Time total
duration (ka)	910	13	4	2	71	17	1000
cumulated slip (mm) (-) is delayed, (+) is regained	0	-4876	-490	4127	806	-5366	-433
Mean slip-rate (mm/yr)	0	-0,38	-0,12	2,06	0,01	-0,32	-4,33E-04

Table 5.5: Mean slip rate difference of G0006 with respect to reference experiment G006.

V.4.1.2 Effect of plate velocities

Here, we investigate the effect of the strike-slip rate. We compare experiments G0006 and GS006, in which only the horizontal slip-rate varies, respectively, with 8 mm.yr⁻¹ and 4 mm.yr⁻¹. Both investigations are carried out using the centered fault geometry and same type of glaciation cycle (19 ka). The fastest experiment, G0006, is previously described, and refers to the centered fault with a horizontal velocity of 7 mm.yr⁻¹. In GS006, the velocity accommodated by the fault after 910 ka is ~ 3 mm.yr⁻¹ (Figure 5.36).

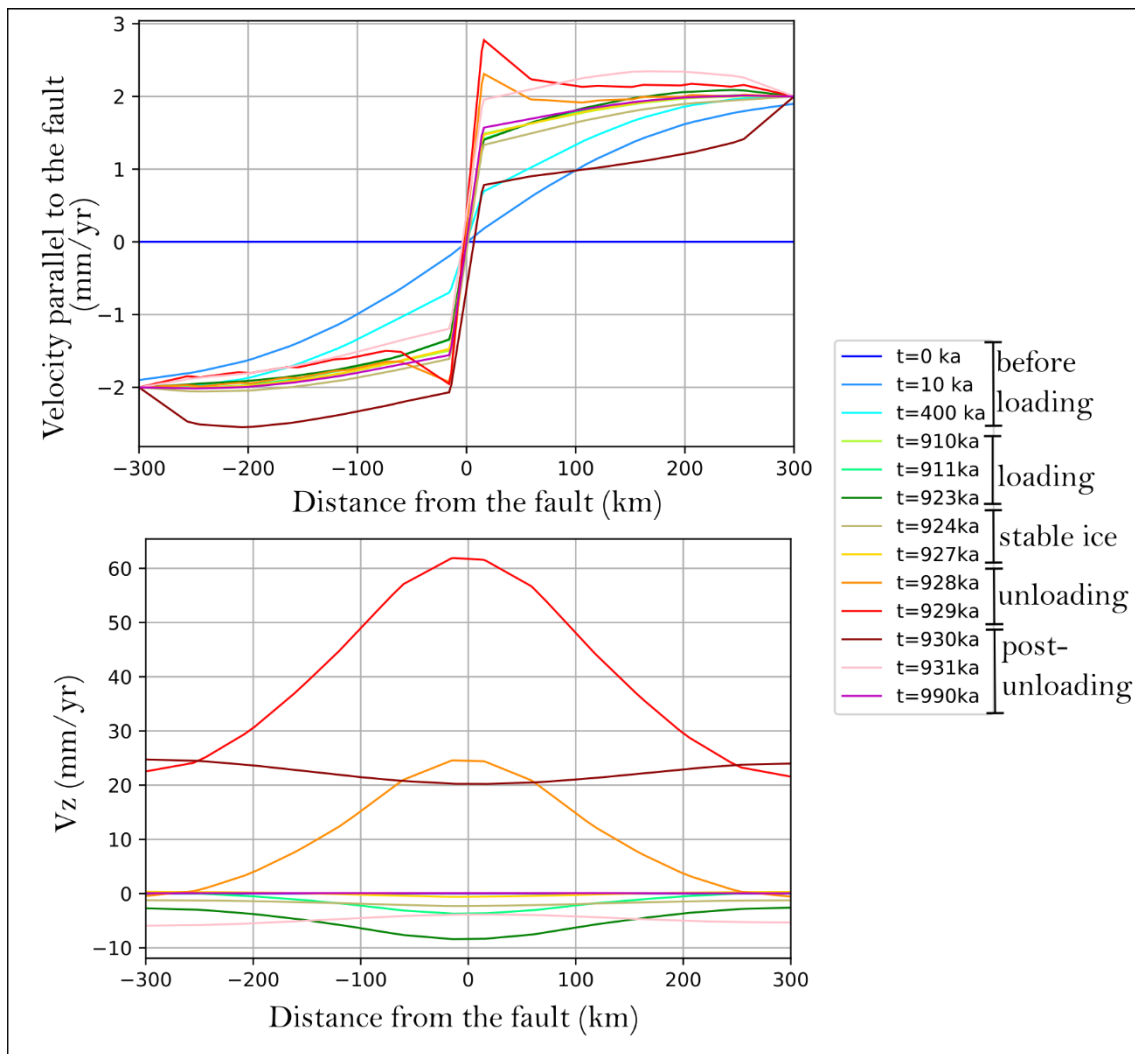


Figure 5.36: Temporal evolution of horizontal (a) and vertical (b) velocities in experiment GSoo6. Velocities are shown along the cross profile perpendicular to the fault. Distances are shown from the fault center with a fault zone width of 30km. Colored curves show the time step in ka.

The slip-rate evolution patterns are the same in both cases and are governed by the load timing (Figure 5.37a). As the slip-rate of GSoo6 is slower than Gooo6, the slip-rate evolution pattern has a lower amplitude (Figure 5.37b). We compare the reference experiment and the GSoo6 experiment in terms of cumulated slip (Figure 5.38). In the GSoo6 model (slow slip-rate), the cumulated slip muted throughout glaciation (0-17 ka) is 3.6 meters. The subsequent slip-rate pulses do not fully recover this cumulated slip (table 5.6). Compared to the reference experiment, the amount of slip regained at unloading is ~2.9 meters. At the end of experiment, 70 ka later, it remains ~0.1 meters of slip muted from the glaciation phase.

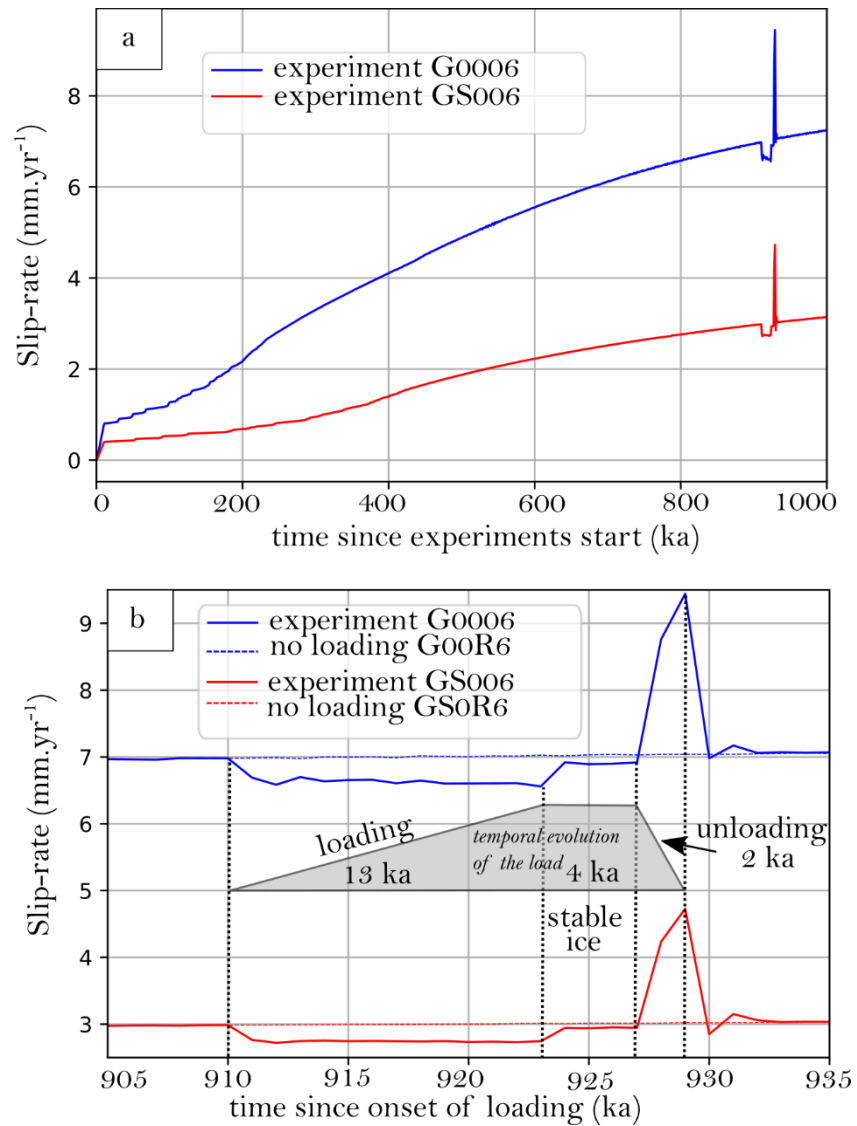


Figure 5.37: (a) Temporal evolution of slip-rates of experiments GS006 (red curve) and G0006 (blue curve). (b) Zoom in same figure since the onset of loading. Grey triangle shows temporal evolution of the load. The dashed curves show slip-rate of experiments without loading GSoR6 (red dashed curve) and GooR6 (blue dashed curve).

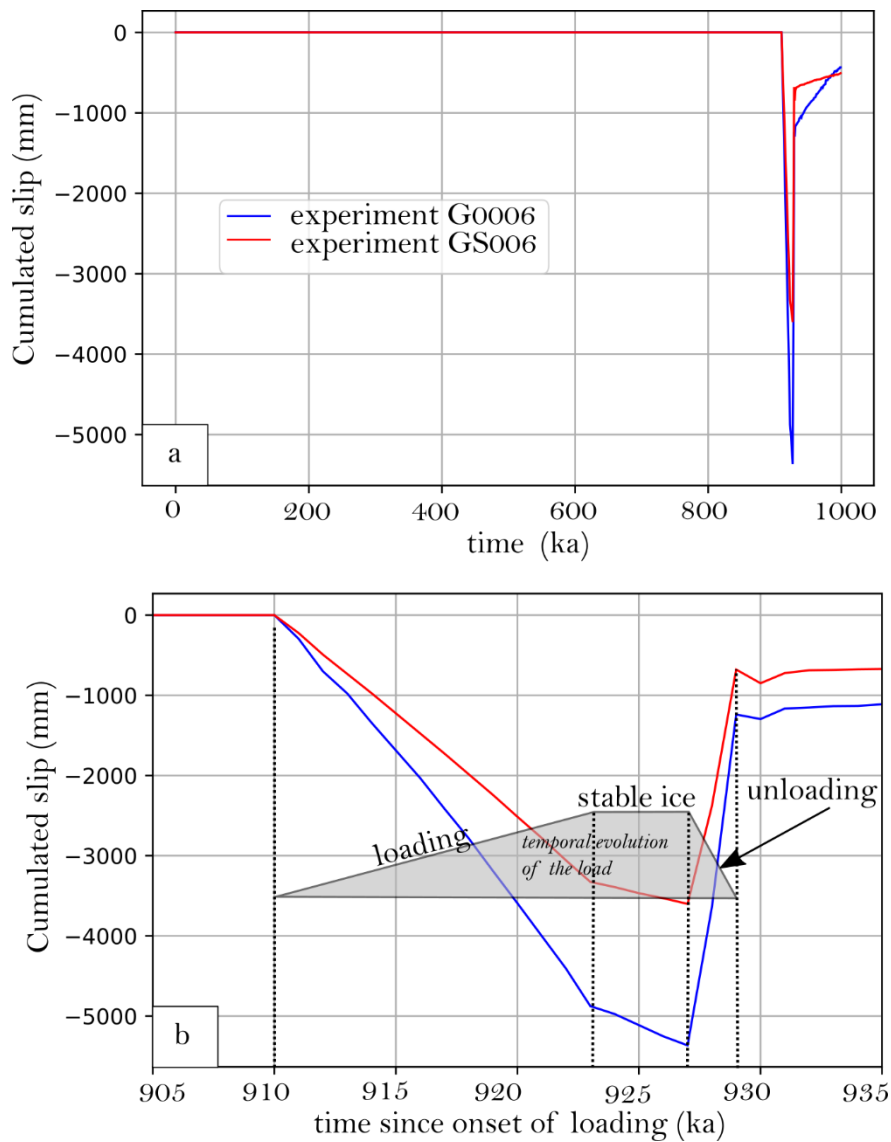


Figure 5.38: (a) Difference of slip between loading experiments GS006 and the experiment without loading GSoR6. (red curves) cumulated over time. Same results are shown for experiment G0006 (fast velocity) in blue curve. The negative difference shows the slip amount delayed during each phase when the fault decelerates compared to no-load experiment. A positive difference indicates slip pulse when the fault accelerates. (b) Zoom-in the same figure.

	A Initial phase (no load)	B Loading	C Ice-stable	D Unloading	E Post- unloading	B+C Loading + Ice-stable	A+B+C+D+E Time total
Phase duration (ka)	910	13	4	2	71	17	1000
cumulated slip (mm) (-) is delayed, (+) is regained	0	-3327	-274	2922	172	-3601	-507
Mean slip-rate (mm/yr)	0	-0,26	-0,07	1,46	0,00	-0,21	-5,07E-04

Table 5.6 Mean slip rate difference of G5006 with respect to reference experiment G0006.

V.4.1.3 4.1.4 Effect of glaciation duration

We compare here experiments G0006 and GL006, in which only the glaciation scenario differs. Both experiments are carried out using the centered fault geometry and identical slip rates of $\sim 7 \text{ mm.yr}^{-1}$. The two glaciations begin simultaneously, but the GL006 glaciation lasts 71 ka whereas the G0006 lasts 19 ka. The GL006 glaciation cycle refers to the type long glaciation (Figure 5.39), with progressive icecap onset from 0-40 ka, followed by a stable load during 20 ka, and by rapid deglaciation in 10 ka. This glaciation refers to a hypothetical longer Fuegian LGM than previously mentioned in literature: a glaciation beginning in MIS₄, ending in MIS₂, without any MIS₃ recession episode.

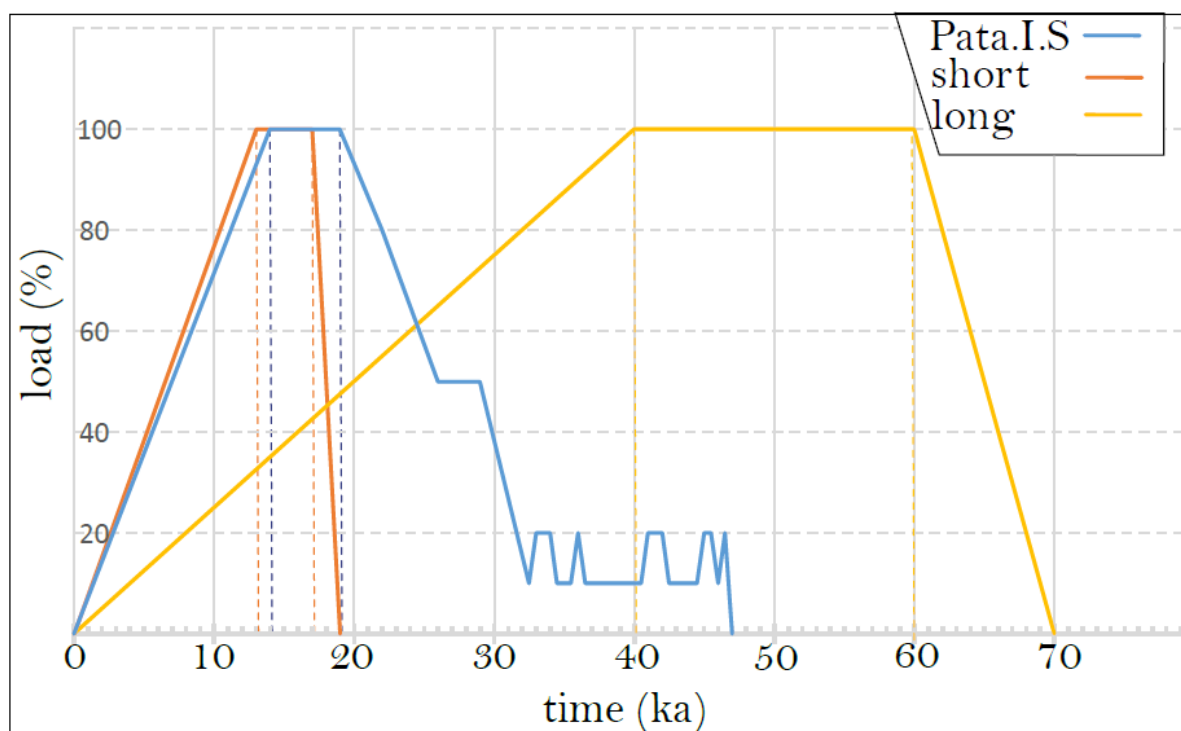


Figure 5.39: Temporal evolution of load for each glaciation type. Pata I.S: glaciation scenario for Patagonian ice sheet has described by (Davies et al., 2020). Short and long glaciation scenarios are with orange and yellow curves.

Because the overall experiments last 1 Ma, and we use the same steady-state duration of 910 ka, the post-loading relaxation of GLo06 only lasts 20 ka while the G0006 relaxation lasts 71 ka. Due to this significant difference, we miss part of the GLo06 fault response, and avoid comparison of post-glacial cumulated slip.

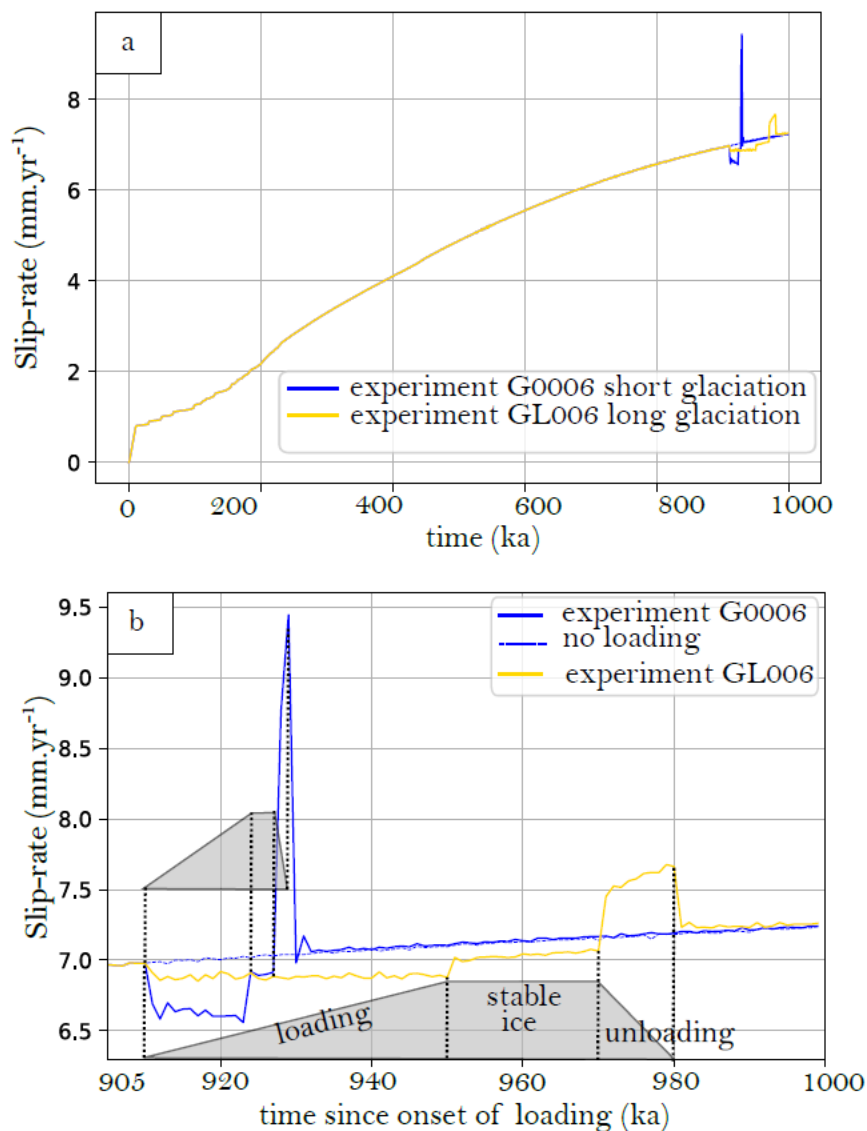


Figure 5.40: (a) Temporal evolution of slip-rates of experiments GLo06 with long glaciation (Yellow curve) and G0006 with short glaciation (blue curve). (b) Zoom in same figure since the onset of loading.

Grey triangle shows temporal evolution of the load. The dashed blue curve show slip-rate of experiments without loading GooR6 (same reference experiment).

We compare the slip-rates evolutions of the two experiments. The general slip-rate patterns are very similar and primarily controlled by the load's temporal evolution (Figure 5.40a). The slip-rate variation of fault in experiment GLoo6 shows a lower amplitude than in experiment Goo06. Despite the identical ice weight imposed in both cases, the loading and subsequent unloading in GLoo6 trigger lesser effects.

The progressive loading during 40 ka induces a decrease in slip-rate of -0.16 mm.yr^{-1} (Figure 5.40b). The velocity reduction avoids a cumulative slip of 6.3 meters, compared to the reference experiment GooR6 (Figure 5.41). These two phases together induce 8.2 meters of cumulated slip delayed over 60 ka of loading. The subsequent deglaciation causes a rapid slip rate increase of slip rate of $+0.41 \text{ mm.yr}^{-1}$. It leads to 4.1 meters of cumulated slip pulse (Table 5.7).

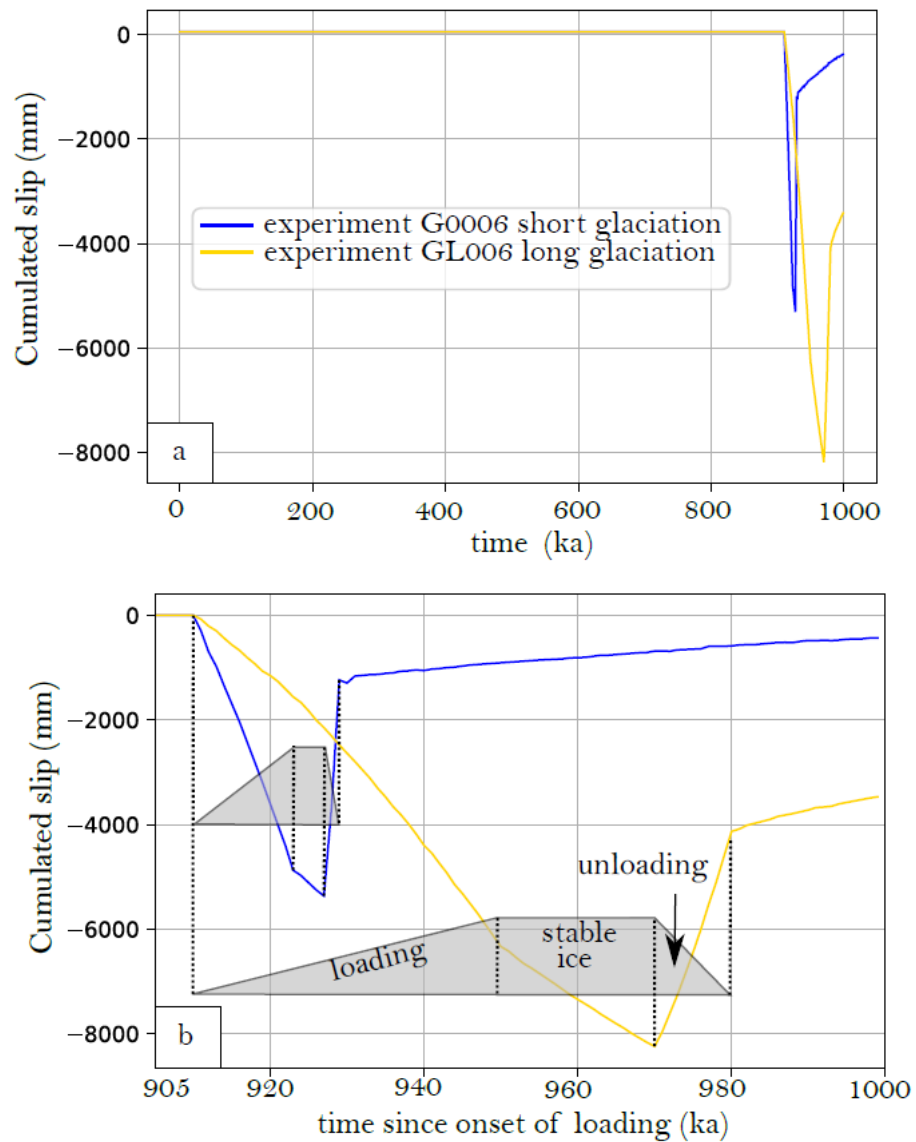


Figure 5.41: (a) Difference of slip cumulated over time between loading experiments GL006 (yellow curve) and its experiment of reference without loading G0006. The same results are shown for experiment G0006 (short glaciation) in blue curve. The negative difference shows the slip delayed during each phase, when the fault decelerates compared to the no-load experiment. The positive difference indicates slip pulse when the fault accelerates. (b) Zoom-in the same figure.

	A	B	C	D	E	B+C	A+B+C+D+E
	Initial phase (no load)	Loading	Ice-stable	Unloading	Post- unloading	Loading + Ice- stable	Time total
Phase duration (ka)	911	40	20	10	19	60	1000
cumulated slip (mm) (-) is delayed, (+) is regained	0	-6335	-1909	4110	662	-8244	-3472
Mean slip-rate (mm/yr)	0	-0,16	-0,10	0,41	0,03	-0,14	-3,47E-03

Table 5.7: Mean slip rate difference of GLoo6 with respect to reference experiment GRoo6.

We note the transition is smoother at the end of the unloading phase than in the short glaciation experiment. Thus, we suspected these oscillations are derived from numerical noises during abrupt transitions.

V.4.2 Asymmetric Fault Experiment

In this asymmetric configuration, the fault is close to one of the ice cap border. Horizontal velocity along the perpendicular cross profile (Figure 5.42a) evidences the fault position is located slightly right-shifted relative to the center of the model.

Like for centered fault, the slip evolution shows the two fundamental patterns of a slip drop at loading and a slip pulse at unloading. During the progressive loading and stable phase, the slip-rate decelerates in average of about -0.34 mm.yr^{-1} and -0.10 mm.yr^{-1} , respectively. Associated cumulated slip delayed over these periods is -4.46 meters (0-13 ka) and -0.39 meters (13-17 ka). The glaciation prevents the fault from slipping of ~ 4.85 meters (Table 5.8).

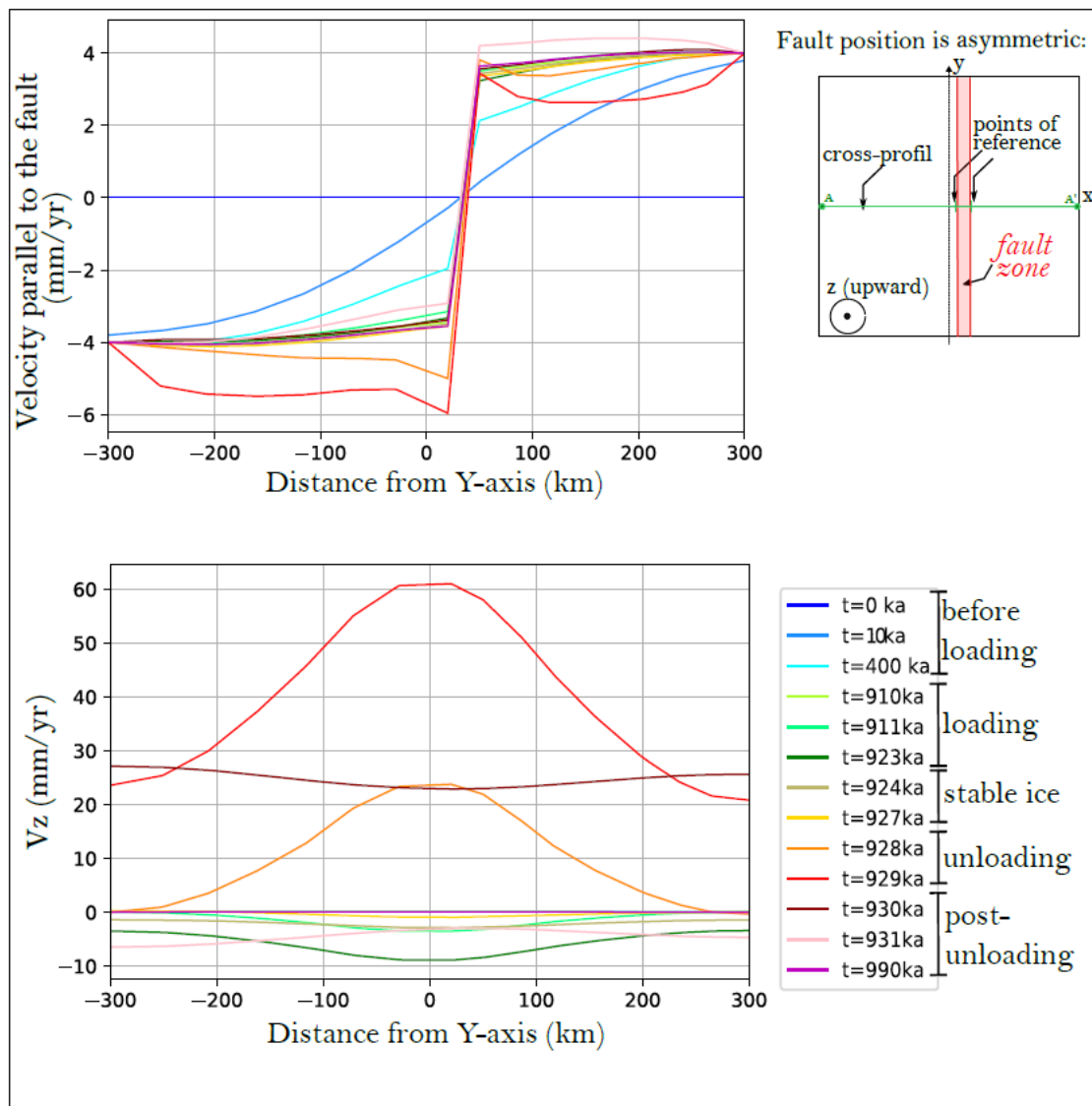


Figure 5.42: Temporal evolution of horizontal (a) and vertical (b) velocities of the asymmetric fault experiment Goo23. Rates are shown along the cross profile orthogonal to the fault. Distances are from the Y-axis. Colored curves show the time step in ka (10³ yrs).

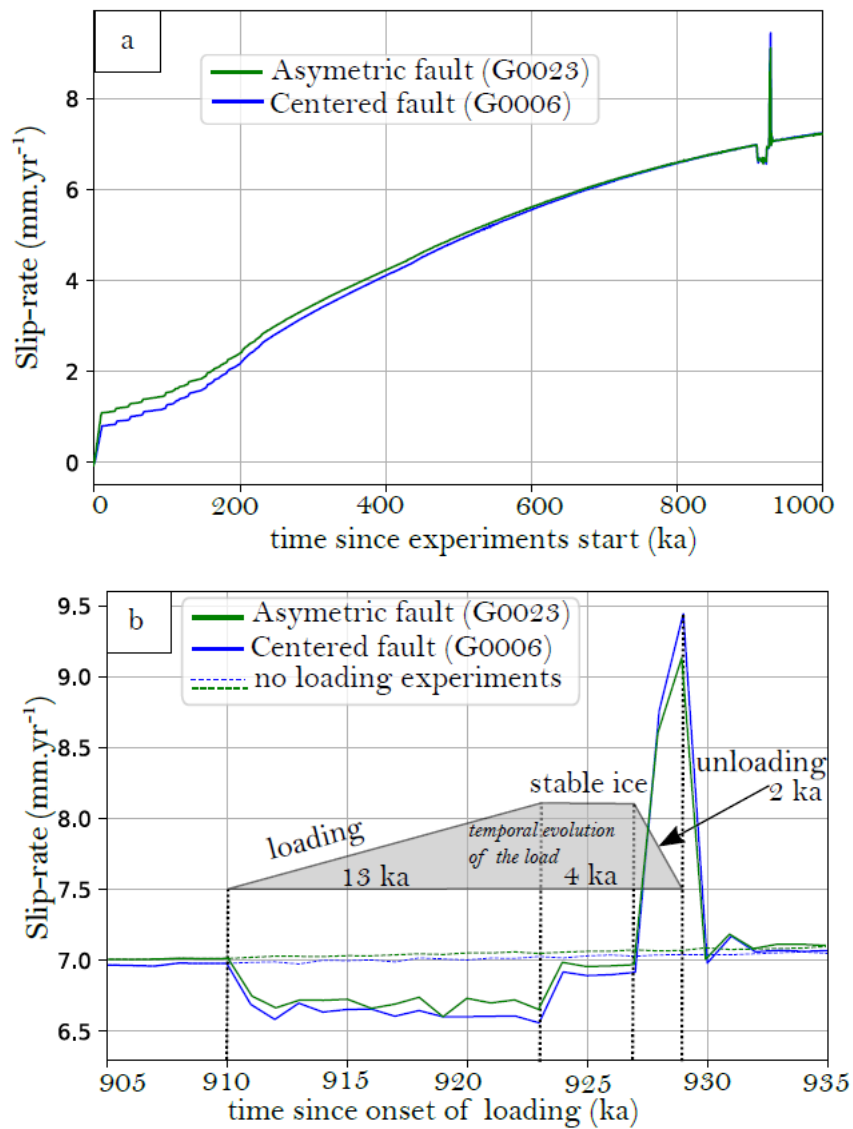


Figure 5.43: Slip-rates of experiments with asymmetric fault G0023 (green curves) and centered fault G0006 (blue curves). Both investigations are conducted simultaneously to steady-state 910 ka and the same short glaciation cycle of 19 ka. (a) Temporal evolution of slip-rates over 1 Ma. (b) Zoom in same figure since the onset of loading.

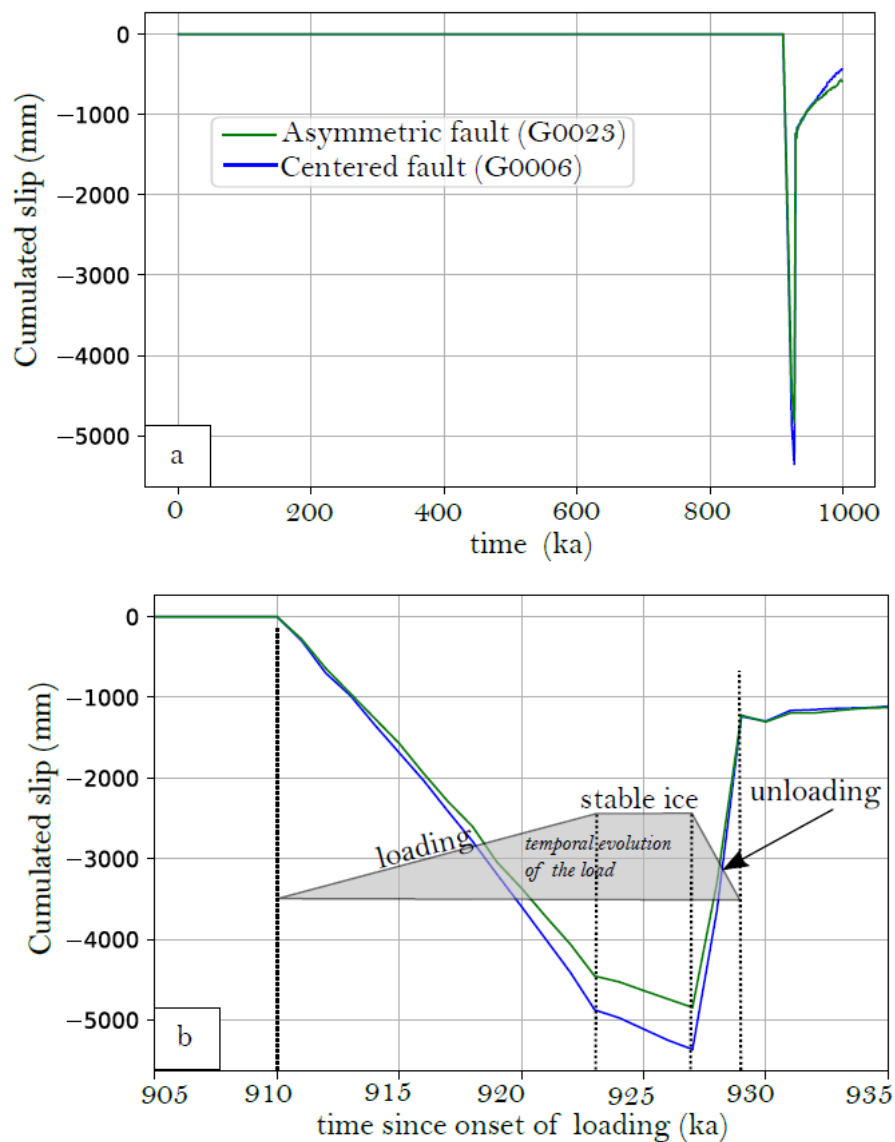


Figure 5.44: (a) Difference of slip between experiments Goo23 and its reference experiment without loading GoR23 (green curves) cumulated over time. Goo23 and GoR23 are set with asymmetric fault. Same results are shown for experiment Goo06 and GooR6 (centered fault) in blue curve. The negative difference shows the slip amount delayed during each phase when the fault decelerates compared to no-load experiment. The positive difference indicates slip pulse when the fault accelerates. (b) Zoom-in the same figure.

During deglaciation (17-19 ka), the slip-rate increases about $+1.81 \text{ mm.yr}^{-1}$, representing an additional slip of $\sim+3.6$ meters. (Figure 5.43). During model relaxation (19 ka – until the end), the slip-rate increases in average about $+0.01 \text{ mm.yr}^{-1}$, resulting in $\sim+0.64$ meters of cumulated slip

(Figure 5.44).

	A	B	C	D	E	B+C	A+B+C+D+E
	Initial phase (no load)	Loading	Ice-stable	Unloading	Post-unloading	Loading + Ice-stable	Time total
Phase duration (ka)	911	13	4	2	70	17	1000
cumulated slip (mm) (-) is delayed, (+) is regained	0	-4457	-389	3623	637	-4846	-586
Mean slip-rate (mm/yr)	0	-0,34	-0,10	1,81	0,01	-0,29	-5,86E-04

Table 5.8: Mean slip rate difference of Goo23 with respect to reference experiment GRo23.

V.4.3 Oblique Fault Experiment

The following experiment is a fault that has an angle θ relative to the icecap. Icecap is always centered on the y-axis (Figure 5.45a). The type of glaciation here is the short glaciation cycle (19 ka). To model a sinistral slip fault on an oblique fault, we apply on the model borders a horizontal velocity divided in two components V_x and V_y . To mime the sinistral motion, we apply a negative V_x on the northern block external border and a positive V_x on the southern block borders (Figure 5.45b). Likewise, the component V_y is applied positively on the northern block and negatively on the southern. The resultant of these components projected onto the fault plane is the velocity parallel to the fault:

$$V_{\text{parallel to the fault}} = V_y \times \cos\theta - V_x \times \sin\theta$$

In this work, we choose a simple geometry to build the model layers with points A, B, C, and D defining the fault zone with respective coordinates of (-125,300), (-95,300), (125, -300), and (95, -300) (Figure 5.45a). In this configuration, the angle θ is $\sim 20,14^\circ$. As shown in section 3, we expected the fault to rupture even under the load. If θ is 60° , we expect the icecap impact to be completely muted. Conversely, with an angle θ of -30° (not tested in this work), we expect the effect to be increased.

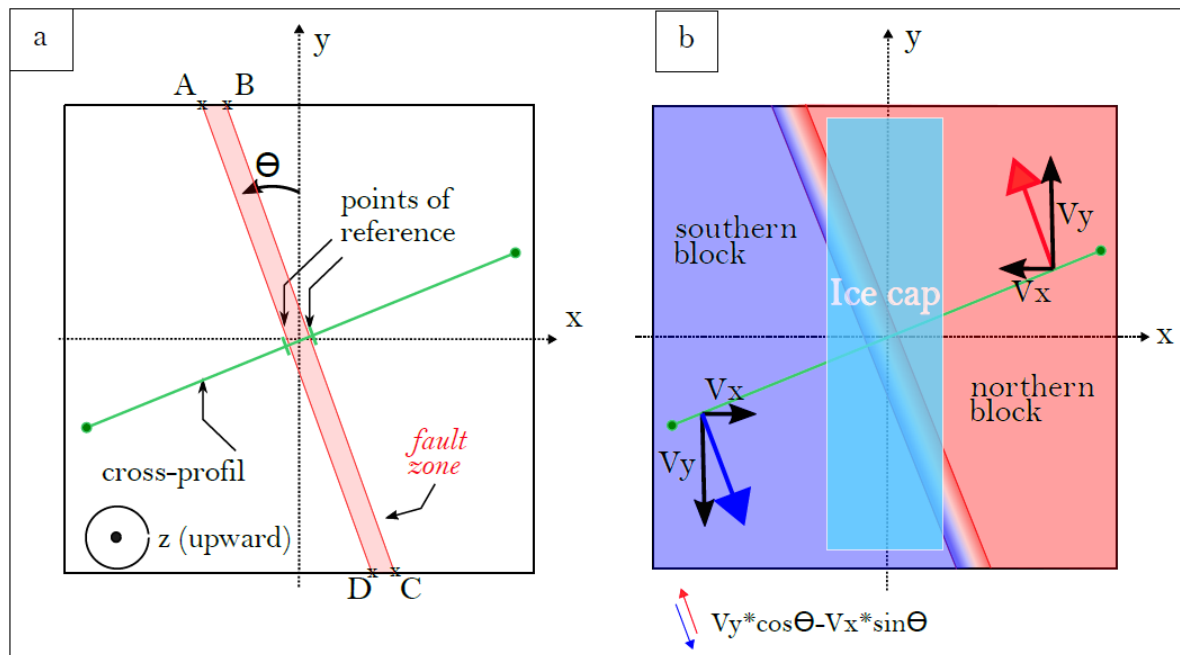


Figure 5.45: (a) Map view of the oblique fault orientations with cross-profile used to illustrate the horizontal velocity evolution. Points of reference are shown on the cross-profile and are used to implement fault slip-rate. (b) Map view of the velocity boundary conditions for the experiments with oblique fault. Red and blue arrows indicate the resultant of the horizontal velocities V_x and V_y for each block.

The model loading leads to subsequent lithosphere bending. Deep under the icecap, the material flows outward of the load. At the surface, where the cross-profile is implemented, the lithosphere is contracted under the ice load. The lithosphere bends and material is shortened in the x -direction. The horizontal velocity V_x indicates a material shortening (Figure 5.46a). We see that the shortening direction is constructive with the V_x direction (strike-slip motion). The V_y component is less affected by the lithosphere bending.

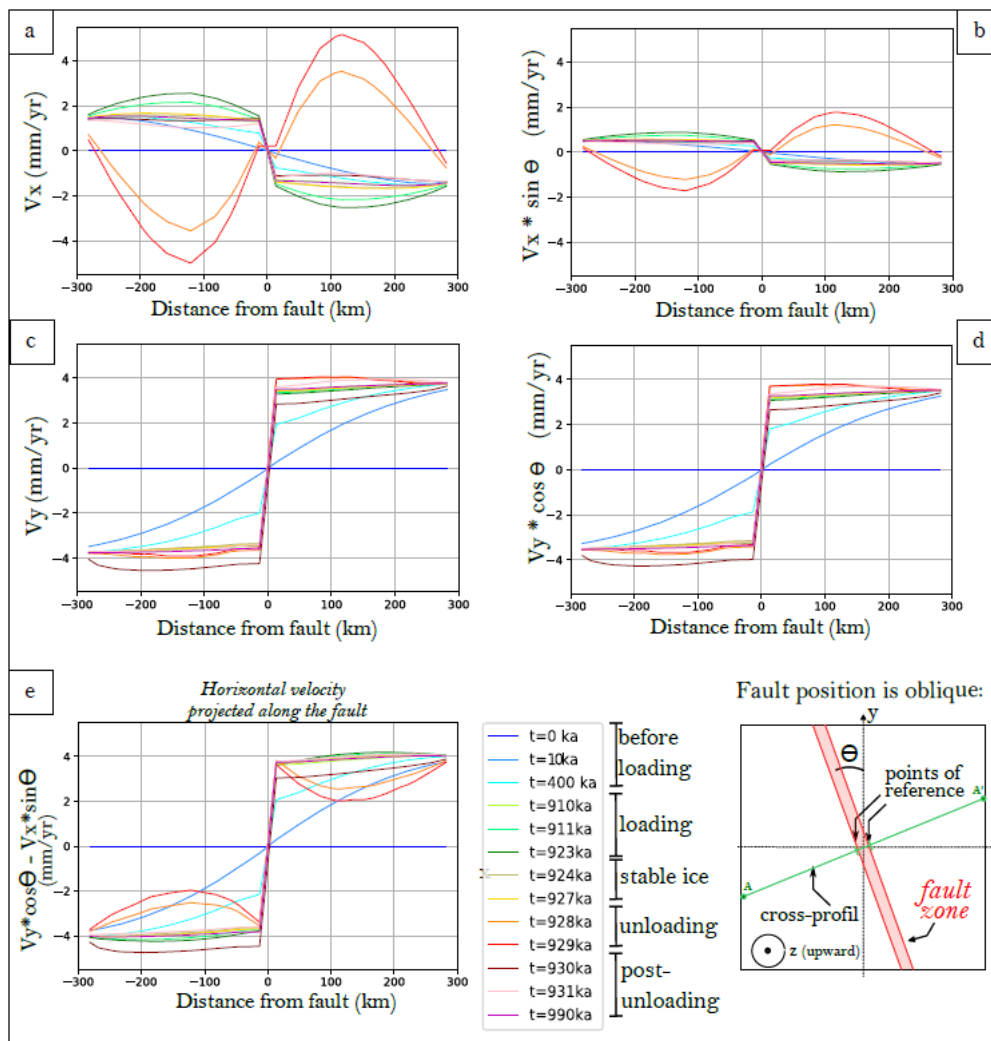


Figure 5.46: Temporal evolution of horizontal velocities of the oblique fault. (a) V_x is the velocity component in the x-axis. (b) $V_x \cdot \sin(\theta)$ is V_x projected onto the fault plane strike (20.14°) of the sinistral-slip fault. (c) V_y is the velocity component in the y-axis. (d) $V_y \cdot \cos(\theta)$ is V_y projected on the fault plane. (e) The resultant horizontal velocity projected onto the fault plane is $V_y \cdot \cos(\theta) - V_x \cdot \sin(\theta)$. Distances are indicated from the fault, and colored curves show the time step in ka.

The horizontal velocities V_x and V_y are projected onto the fault plane $V_x \cdot \sin\theta$, and $V_y \cdot \cos\theta$ (Figure 5.46 c, d). The horizontal velocity parallel to the fault is the resultant of these two components (Figure 5.46e). This resultant is called hereafter the fault velocity (Figure 5.47, magenta curves).

In this configuration with $\theta \sim 20^\circ$, the slip-rate pattern (Figure 5.47) is opposite to the centered fault behavior. The fault slip increases at loading (+0.04 mm/yr) and decreases with stable load (-

0.02 mm/yr) (Table 5.9). This slight acceleration of the fault at loading triggers a cumulated slip of 0.57 meters. It means during glaciation slip occurs and is of ~ 0.57 m.

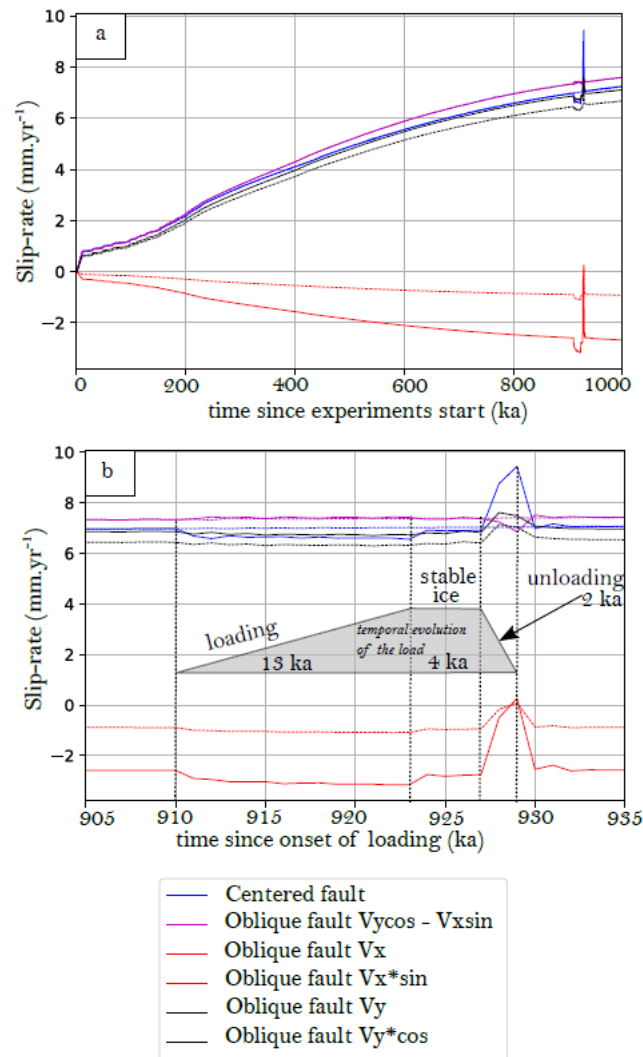


Figure 5.47: Slip-rates of experiment with oblique fault (Goo33) and centered fault (Goo06) (a) Temporal evolution of slip-rates over 1 Ma. (b) Zoom in same figure since the onset of loading.

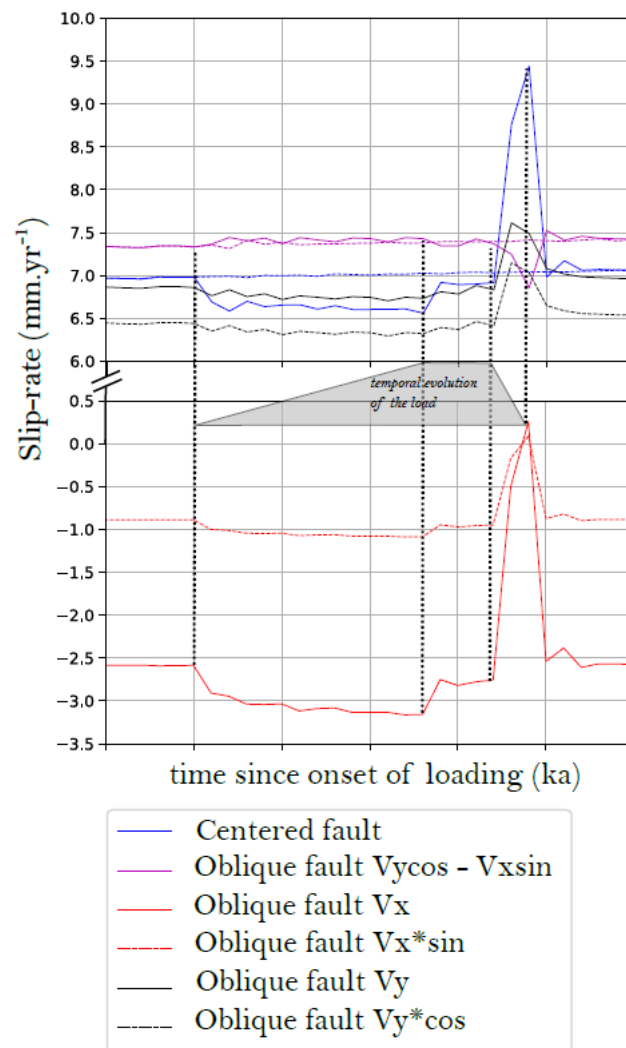


Figure 5.48: (Zoom-in figure 4.15) Slip-rates of fault in experiment with oblique fault compared to experiment with centered fault (blue curve).

At unloading, the fault drops in average of -0.35 mm/yr in two thousand years. Compared to the experiment without loading, there is a cumulated slip delayed of ~ 0.71 meters (figure 5.48, table 5.9).

The centered and the oblique experiments have opposite behavior patterns (Figure 5.49). To simplify, the two fundamental slip patterns during loading and subsequent unloading are (a) slip-drop/slip-pulse for centered experiment, and (b) slip-pulse / slip-drop for oblique experiment. In the oblique experiment the slip drops during deglaciation of ~ -0.7 m. Whereas in the centered experiment, the slip pulses during deglaciation of $\sim +3$ m.

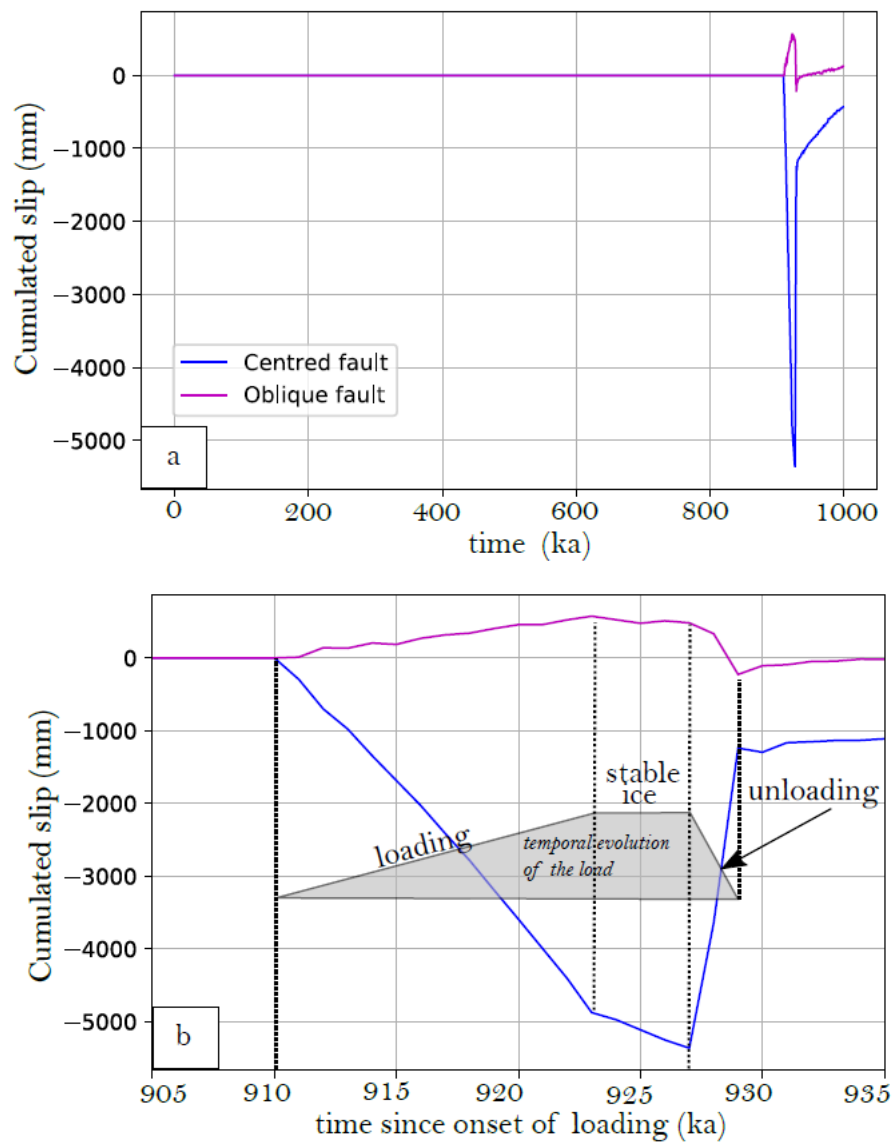


Figure 5.49: (a) Difference of slip between loading experiments (oblique fault Goo33, centered fault Goo06) and their respective experiments without loading (GoR33, GooR6) cumulated over time. The negative difference shows the slip delayed during each phase compared to a no-load experiment. The positive difference indicates slip-pulse. (b) Zoom-in the same figure.

	A	B	C	D	E	B+C	A+B+C+D+E
	Initial phase (no load)	Loading	Ice-stable	Unloading	Post- unloading	Loading + Ice- stable	Time total
Phase duration (ka)	911	13	4	2	70	17	1000
cumulated slip (mm) (-) is delayed, (+) is regained	0	574	-92	-709	354	483	127
Mean slip-rate (mm/yr)	0	0,04	-0,02	-0,35	0,01	0,03	1,27E-04

Table 5.9: Mean slip rate difference of Goo33 with respect to reference experiment GRo33

V.5 Discussions and Conclusion

V.5.1 Interpretation of model Results

This work shows that a strike-slip fault located right beneath the icecap and parallel to it should partially cease to slip during the glaciation phase. Because there is less slip on the fault, it would correspond to a period of relative seismic quiescence in nature. Conversely, when the icecap melts, the fault should experience relative intense faulting that corresponds to a seismic phase. Post-unloading, the fault then returns to its pristine level of steady slip-rates.

Our analytical and finite element modeling results show that the following parameters primarily control the icecap effect:

(1) The icecap orientation relative to the strike-slip fault controls the slip pattern. The fault response is spatially and temporally correlated with the deflexion and the lithosphere's rebound due to glacial loading and unloading. The ice-load stress field is superimposed onto the tectonic background stress field. These interferences can favor or mute the icecap effect, depending on their respective stress orientations. Two fundamentally slip patterns can be identified during loading/unloading phase: (a) drop/pulse or (b) pulse/drop. The pattern (a) is identified when the icecap is parallel, shifted relative to the fault, and oblique to the fault with synthetic orientation (-45° to 0°). When the icecap has antithetic orientation relative to strike-slip, the slip-rate increases during loading and drops at unloading (pattern b).

(2) The load history, which controls the temporal slip-rate evolution. The slip-rate varies in phase with the loading history. The Adeli experiments show the glaciation and deglaciation rates

govern the amount of slip delayed because the material's rheologies depend on the applied stress rate. This effect was not visible in our analytical experiment, as we assumed an elastic lithosphere. For the glaciations of 19 ka and 40 ka, the respective slip pulses are ~+5m and ~+8m.

(3) The initial strike-slip velocity (tectonic stress) governs the duration and the amplitude of the slip-rate variations. The higher is the slip-rate of the fault, the more slip delay is cumulated.

V.5.2 Approach limits

Our Adeli experiment uses a fault zone friction angle of 0.1 to 10° to keep an optimal computational time. It allows the fault to reach earlier a fully plastic behavior. Therefore, in these Adeli experiments, we did not completely study this parameter. It would require further modeling to evaluate the effect of higher friction angle with ADELI.

For the same reason, we set-up a short initiation phase before glacial loading, the steady-state is not fully completed when the glaciation occurs. Therefore, the fault slip-rate continues to increase through time while the glaciation is occurring. Consequently, a small part of the glaciation effect is removed. An experiment with steady-state of 1.5 Ma could solve this issue. Besides, performing experiment of at least 2 Ma would allow better studying the fault's long-term relaxation after the unloading phase.

In our ADELI approach, we focused on the elementary fault orientation relative to the icecap. However, it is essential to model the other directions, especially the orientation that may favor the icecap's effect. As seen in section 2, an orientation of angle $\theta = -60^\circ$ may promote locking the fault at loading.

In this thesis work, we modeled the ultimate glaciation phase effects. However, the Magallanes-Fagnano Fault was successively covered by multiple large ice lobes' advances since the MIS 12. Dating of erratic boulder field in the Strait of Magellan banks have evidence the penultimate glaciation (MIS 4) was more extensive than the LGM. Future work may integrate the entire regional glacial history since the MFF strike-slip onset to improve our understanding on ice-load interaction with the MFF strike-slip.

Finally, at the LGM, the MFF was synchronously ice-free in the east and recovered by a thousand meters-thick ice lobes in the west. We did not take into account this complex configuration. Furthermore, the Atlantic's progressive marine transgression over the eastern MFF may have muted part of the deformation. The western deglaciation may have favor the rupture, while the eastern marine transgression may have muted the MFF. These coeval processes may have contributed to increase the long-term slip rate difference between the two regions. All the above points constitute line of improvement for future investigation with ADELI software.

V.5.3 Conclusion

To conclude, we show that one glacial-interglacial phase can affect the slip-rate of a strike-slip fault. The Adeli experiment with a 3-layers Earth model, with an icecap parallel to the fault, and with friction angle of 10° , shows a post-glacial slip pulse of ~ 5.3 m. In comparison, the analytical approach with icecap parallel to the fault and 10° of friction angle, evidences ~ 7 m of post-glacial slip pulse. The analytical and the finite element approaches suggest very similar slip increase triggered by deglaciation of the strike-slip fault.

However, both approaches evidence that the predicted post-glacial slip pulse is too low to explain the Magallanes-Fagnano slip-rate discrepancy between the Western Magallanes region and the Eastern Tierra del Fuego. Indeed, the cumulated slip difference since the LGM is about ~ 200 m, between the eastern (sinistral offset 115 m) and the western MFF segment (sinistral offset 315 m) MFF segments. The slip amount that could be released by the deglaciation is about ~ 5 to 7 m, which represents no more than 4% of the observed slip discrepancy. Even with the most favourable setup, with oblique icecap relative to the fault (-30°), and with an internal friction angle of 30° , the predicted slip does not exceed 15% of the observed slip difference.



Tanu en los hielos, espíritu Selk nam

Painting generously shared by Elby

Pinturas de propiedad intelectual
Pertenciente a la artista visual Elby
Huerta - Chile Santiago; Uso exclusivo
para tesis, derechos reservados de la
autora.

Copyright © Elby Huerta

CHAPTER VI: Conclusions and Perspectives

This thesis focuses on the Magallanes-Fagnano Fault, which accommodates the relative motion between South-American and Scotia plates. The thesis work carried out in Tierra del Fuego characterizes the Magallanes-Fagnano-Fault behavior over several time-scales: during the Holocene, including the historical period (0-11 700 yrs), and up to the end of the Pleistocene (11 700 – 20 000 yrs). This work was achieved from the 70°W up to 66°W (200 km), from the Almirantazgo Sound to the Atlantic coast representing a third of the entire Magallanes-Fagnano Fault (Figure 6.1).

Part of this thesis work is dedicated to the historical ruptures, and provides unprecedented paleoseismological and dendroseismological data. The new map of the 1879 and 1949 faulting morphologies evidences their respective surface rupture lengths, measuring at least 170 and 200 km, respectively (Figure 6.1). These two major earthquakes disrupted the Ainsworth Peninsula in the Almirantazgo Sound (Chile), continued beneath the Lake Fagnano, and ruptured most of the Argentinian segments. Our dendroseismologic study allows correlating historical ruptures in Argentina and Chile, which considerably increases the estimate of the fault length that broke both in 1879 and in 1949. Besides, our 1949's coseismic displacement measurements demonstrate a maximum sinistral movement of 6.5 ± 0.5 m in the central Tierra del Fuego. These results show that the most significant modern seismicity ($M > 7$) is directly triggered by the South American – Scotia plates relative motion, predominantly accommodated along the Magallanes-Fagnano Fault. Furthermore, recently localised crustal earthquakes (from $1.9 < ML < 5.3$) show a good correlation with the presence of the Magallanes-Fagnano Fault (Ammirati et al., 2020). The authors suggest higher magnitude events are located closer to the fault, whereas moderate magnitude events are rather found in the north, on the Foreland Fold and Thrust Belt (FTB). It leaves little doubt that the MFF is the principal mechanism of modern crustal deformation, which releases the more seismic moment.

Considering the two $M_w > 7$ earthquakes in less than a century, the Magallanes-Fagnano Fault represents a substantial seismic hazard for the region. The associated risk grows as the

population increases rapidly and worsen by extensive urban development on soft glacial and alluvial substrates. For Instance, in 1949, the Tierra del Fuego Province represents ~ 5 000 inhabitants, and today it booms up ~238 000, to whom is added ~ 443 000 tourists each year (INDEC, 2016; INFUETUR, 2019).

In the central Ainsworth Peninsula, the thesis work shows charcoals dated in the trench at 51.1-42.3 cal yr BP and > 44.1 ka BP (apparent age not calibrated). These ages imply the vegetation was present at that period, suggesting the last interglacial MIS 3 was a remarkably pronounced recessional phase in the Almirantazgo Sound. This result reinforces previous chronologies which proposed the MIS 3 as a possible recessional phase (Mercer, 1976; Laugenie, 1984; Rabassa and Clapperton, 1990; Clapperton *et al.*, 1995; Lowell *et al.*, 1995; Denton *et al.*, 1999; Porter, 2020). During stage MIS 3, the paleoclimate would have induced a moderate glacial recession in the Eastern Tierra del Fuego, and a significant retreat in the Western Magellan region, at the foothill of the Cordillera Darwin.

We establish a paleo-seismic calendar with at least seven major paleo-ruptures during the Holocene in Tierra del Fuego (Figure 6.1). Because these paleoearthquakes have ruptured the surface, their respective magnitude is at least Mw 6.5. The last pre-1879 ruptures, in 788 ± 122 and 2165 ± 155 cal yr BP are well correlated with the previous paleoseismic and mass-wasting events studies nearby Tolhuin and in the Lake Fagnano. Two ancient events occurred earlier than 10 776 cal yr BP. West of our trench, authors observed two paleoruptures in dated strata from $4\ 701 \pm 130$ to $5\ 072 \pm 205$, and $5\ 245 \pm 195$ to $8\ 260 \pm 84$. Even though they are not observed in our trench, it perhaps signifies that they primarily ruptured the western territories.

The present-day paleoseismic archives predominantly focus on the Argentinian territory, exhibiting only half of the entire picture. In Chile, our trench is the first attempt to characterize the paleoseismicity on the western part of MFF. We put in evidence at least three events, but insufficient datable material prevents bracketing the age of observed faulted strata. Additional inter-disciplinary works are required to quantify the western fault behavior during Holocene. Future research, combining marine mass-wasting study in Almirantazgo Sound with paleoseismological trench in the Chilean Fjords should yield reliable archives.

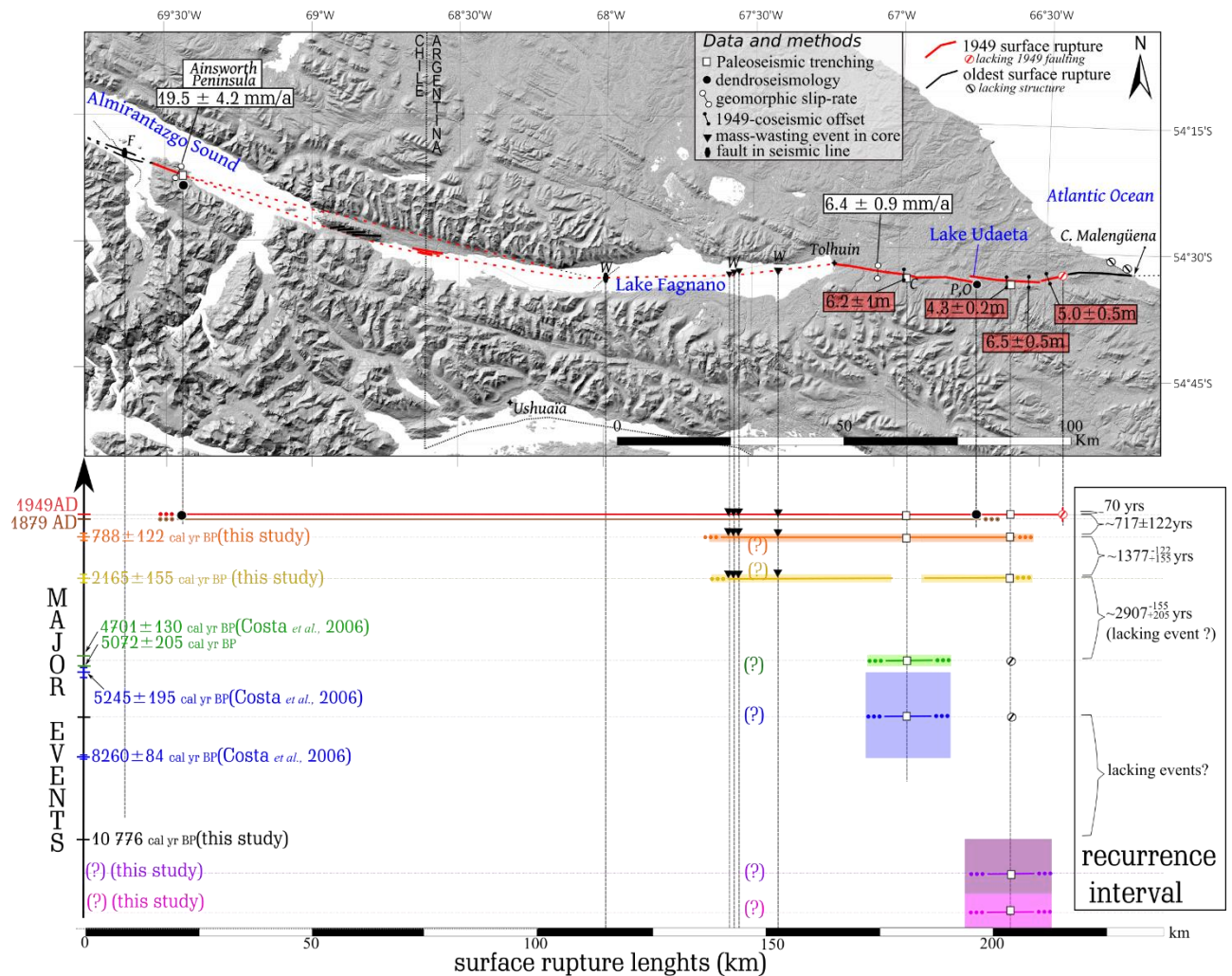


Figure 6.1: Spatial distributions of the Magallanes-Fagnano Fault activity estimated on several time scales: historical activity (last two centuries), Holocene activity (paleo-earthquake records $M_w \geq 7$) and Late-Pleistocene activity (long-term geomorphic offsets). Abbreviations mention the reference to previous works: C: Costa et al., 2006; F: Fernandez et al., 2011; O: Onorato et al. 2016; Pedrera et al., 2014; W: Waldmann 2010.

Our results indicate different time of intervals between major earthquakes over the Holocene in the eastern Magallanes-Fagnano Fault. Indeed, the two pre-1879 ruptures and the 1879 earthquake, shows a recurrence interval from 717 up to 1377 yrs, while the last two earthquakes are associated with a recurrence time < 100 years. Do these results translate a chaotic activity or an exceptional activity over the last two centuries in Tierra del Fuego?

Newly described scarps, ridges, pop-ups, flower structures, and Riedel fractures confirm that the post-glacial strike-slip motion concentrated along the master fault. In Chilean segments, very

little vertical cumulated displacements are observed. In Argentina, from the Lake Fagnano eastern shore to the Atlantic coast, the MFF deformation has a dominant strike-slip displacement associated with alternating northern or southern block uplift.

Back-slip restorations of cumulated sinistral offset combined with ^{10}Be dating allow the first quantification of the Argentinean and Chilean MFF geomorphic slip rates. In Argentina, several landforms with 115 ± 5 m offset in 18 ± 2 ka, yields a left-lateral Late Pleistocene slip rate of 6.4 ± 0.9 mm.yr $^{-1}$. Given that this value is lined-up with ~ 6 mm.yr $^{-1}$ GPS velocity models across the MFFS (Mendoza *et al.*, 2015), the master fault should accommodate almost completely the relative Pleistocene motion between South America and Scotia plates. Besides, the unchanged rates over the different time-scales suggest a stable fault behaviour for the last twenty thousand years in Argentina.

In the Magallanes region, the back-slip restoration of a dozen river channels, that incise glacial deposits, evidences a maximum sinistral offset of 315 ± 15 m. In the area, post-glacial peat bog ages (Boyd *et al.*, 2008; Hall *et al.*, 2019) and new glacial polish ^{10}Be datings (this study), show the ice had already retreated in the Cordillera Darwin by 16.7 ± 2.8 ka BP. Considering that these river channels formed after the glacial retreat implies an exceptionally rapid post-LGM slip-rate of 19.5 ± 4.2 mm/yr.

These results imply a significant long-term E-W fault slip-rate gradient. This gradient coincides geometrically with the unequal distribution of the Pleistocene ice-sheet, voluminous and extensive in the west, and limited in the east. Such ice masses act as a surface load producing a long-lasting viscoelastic deformation of the earth crust, which interfere with the regional tectonic field. We quantify by mechanical models the impact of the glaciation on the MFF to understand if it can explain the totality or part of the slip rate gradient observed. Using an analytical approach and a 3D-finite element numerical modeling, we show preliminary results on glacial isostatic adjustment interaction with strike-slip behavior.

These two approaches show that Earth's material rheologies, load history, and ice sheet orientation primarily control the glaciation effect. With an icecap parallel to the fault, one glacial-interglacial phase can produce a seismic quiescence at loading (slip decrease or stop), and a subsequent seismic burst at unloading (slip pulse). The analytical and the finite element

approaches suggest very similar slip increase. For an icecap parallel to the fault, and with a friction angle of 10° , the predicted post-glacial slip pulse is of ~ 5 m (Adeli model) up to 7 m (analytical approach). The finite-element approach uses a more sophisticated Earth's material setting, and shows that with a 1000 m-thick rectangular icecap centered above a sinistral strike-slip, the glacial load decreases the sinistral slip-rate of ~ -0.4 mm.yr $^{-1}$, and the subsequent deglaciation increases the slip-rate of $+2$ mm.yr $^{-1}$. However, this slip pulse represents no more than 4 % of the observed slip discrepancy between the Western Magallanes region and the Eastern Tierra del Fuego. Indeed, the cumulated slip difference since the LGM is about ~ 200 m, between the eastern (sinistral offset 115 m) and the western MFF segment (sinistral offset 315 m). Even with the most favourable setup, with oblique icecap relative to the fault (-30°), and with an internal friction angle of 30° , the predicted slip does not exceed 15 % of the observed slip difference (analytical approach). Therefore, the climate-driven ice-mass changes only partially explain the slip-rate variation observed in the Magallanes-Fagnano region.

To better constrain postglacial deformation in Chile, new direct and repeatable dating of Pleistocene offsets are crucial. Future investigations on the Almirantazgo Sound paleo-ice-sheet timing and extent during the last glacial/postglacial phase would yield a more precise limit for calculating slip rates. More complex configurations might be tested, and constitute lines of improvement for future investigation with finite element model:

- (1) To extend the experiment duration, which could enable pre-stressing the fault up to near-failure equilibrium with realistic friction angle value;
- (2) To set an unequal spatial ice distribution above the fault, with one-half ice-free and the other half loaded;
- (3) To consider the Magallanes-Fagnano Fault curvature.
- (4) To take into account the progressive marine transgression coeval to the deglaciation, which in the case of the Magallanes-Fagnano Fault may have muted the faulting on the eastern side;

Other hypotheses have to be proposed, and one of them is that we may have underestimated the Chilean offset age. Firstly, it would imply the rivers were carved earlier, during the last interglacial phase, dated in our trench at $> 46.7 \pm 4.4$ cal ka BP. Secondly, these rivers necessarily must have remained active under the LGM ice-sheet. Therefore, it yields several open-questions: how can the drainage system be preserved under a 1-km LGM ice cover flowing orthogonally to

the rivers? Is the LGM Almirantazgo-Fagnano lobe large enough to cover the entire Ainsworth Peninsula?

An alternative explanation may consist that we miss part of the eastern Pleistocene deformation in Tierra del Fuego. [Smalley et al. \(2003\)](#) observed an additional $1\text{--}2\text{ mm.yr}^{-1}$ relative plate motion that may be diffusely distributed across the northern Tierra del Fuego. The GPS stations of northern San Sebastian Bay and southern Santa Cruz Province are moving northward of 1 mm.yr^{-1} with respect to stable South America. The authors proposed that this deformation is localized along a pre-supposed Magellan rift system ([Diraison et al., 2000](#); [Ghiglione et al., 2013](#)). They suggest that this deformation accommodate the Patagonian orocline continuous development or may be associated with the northward continental drift around the south-west corner of South America ([Diraison et al., 2000](#); [Smalley et al., 2003](#); [Ghiglione et al., 2013](#)).

In Chile, we urge the need for GPS station densification to compare the present-day strike-slip behaviour of the Magallanes fault from the Eastern Tierra del Fuego. Furthermore, GPS-measurements in Magallanes region are compulsory to better discriminate the origin of vertical movement between a glacial isostasy adjustment contribution and the neotectonic uplift process along the southernmost Fuegian Andes.

REFERENCES

A

- Aber, J.S. and Ber, A., 2007. *Glaciotectonism*: Elsevier.
- Adams, J., 1989. Postglacial faulting in eastern Canada: nature, origin and seismic hazard implications: *Tectonophysics*, **163**, p. 323–331, doi: [https://doi.org/10.1016/0040-1951\(89\)90267-9](https://doi.org/10.1016/0040-1951(89)90267-9).
- Adaros, R.E., Wiens, D.A., Vera, E.E. and Shore, P.J., 1999. Seismicity and tectonics of southern Patagonia from a local deployment of seismographs: preliminary results. In: *AEO*, 80, Fall Meeting, Suppl, Abstract A52A-05.
- Al Hseinat, M. and Hübscher, C., 2014. Ice-load induced tectonics controlled tunnel valley evolution—instances from the southwestern Baltic Sea: *Quaternary Science Reviews*, **97**, p. 121–135.
- Alvarado, P., Odone, C., Maturana, F. and Fiore, D., 2007. Fueginos: fotografías siglos XIX y XX; imaginarios del fin del mundo, Santiago de Chile, Pehuén, 301 p.: *Santiago de Chile, Pehuén*, p. 301.
- Alvarez-Marron, J., McClay, K.R., Harambour, S., Rojas, L. and Skarmeta, J., 1993. Geometry and Evolution of the Frontal Part of the Magallanes Foreland Thrust and Fold Belt (Vicuna Area), Tierra del Fuego, Southern Chile: *AAPG Bulletin*, **77**, p. 1904–1921, doi: <https://doi.org/10.1306/BDF8F74-1718-11D7-8645000102C1865D>.
- Ammirati, J.-B., Flores, M.C. and Ruiz, S., 2020. Seismicity along the Magallanes-Fagnano fault system: *Journal of South American Earth Sciences*, **103**, p. 102799, doi: 10.1016/j.jsames.2020.102799.
- Arvidsson, R., 1996. Fennoscandian earthquakes: whole crustal rupturing related to postglacial rebound: *Science*, **274**, p. 744–746, doi: <https://doi.org/10.1126/science.274.5288.744>.
- Asenjo Fernandoy, C.S., 2020. Morfotectonica marine y arquitectura del sistema de fallas Magallanes-Fagnano en la region de Magallanes entre los 69°W-71°W, Chile:
- Ashley, G.M., 1975. Rhythmic Sedimentation in Glacial Lake Hitchcock, Massachusetts-Connecticut: , doi: <https://doi.org/10.2110/pec.75.23.0304>.
- Astrade, L., Stoffel, M., Corona, C. and Lopez-Saez, J., 2012. L'utilisation des cernes de croissance des arbres pour l'étude des événements et des changements morphologiques : intérêts, méthodes et apports des recherches alpines à la dendrogéomorphologie: *Géomorphologie: relief, processus, environnement*, **18**, p. 295–316, doi: 10.4000/geomorphologie.9925.

B

- Barker, P.F., 2001. Scotia Sea regional tectonic evolution: implications for mantle flow and palaeocirculation: *Earth-Science Reviews*, **55**, p. 1–39, doi: 10.1016/S0012-8252(01)00055-1.
- Barrientos, S., 2018. The seismic network of Chile: *Seismological Research Letters*,, doi: 10.1785/0220160195.
- Bartov, Y. and Sagy, A., 2004. Late Pleistocene extension and strike-slip in the Dead Sea Basin: *Geological Magazine*, **141**, p. 565–572, doi: <https://doi.org/10.1017/S001675680400963X>.
- Bartov, Y., Stein, M., Enzel, Y., Agnon, A. and Reches, Z., 2002. Lake levels and sequence stratigraphy of Lake Lisan, the late Pleistocene precursor of the Dead Sea: *Quaternary Research*, **57**, p. 9–21, doi: <https://doi.org/10.1006/qres.2001.2284>.
- Bassin, C., 2000. The current limits of resolution for surface wave tomography in North America: *EOS Trans. AGU. 81: Fall Meet. Suppl., Abstract*,.
- Belferman, M., Katsman, R. and Agnon, A., 2018. Effect of large-scale surface water level fluctuations on earthquake recurrence interval under strike-slip faulting: *Tectonophysics*, **744**, p. 390–402, doi: <https://doi.org/10.1016/j.tecto.2018.06.004>.
- Belytschko, T., 1983. An overview of semidiscretization and time integration procedures: *Computational methods for transient analysis(A 84-29160 12-64)*. Amsterdam, North-Holland, 1983,, p. 1–65.
- Benn, D. and Evans, D.J.A., 2014. *Glaciers and Glaciation*, 2nd edition: , p. 916, doi: <https://doi.org/10.4324/9780203785010>.
- Bennett, M.M. and Glasser, N.F., 2011. *Glacial Geology: Ice Sheets and Landforms*: John Wiley & Sons.
- Bentley, M.J., Sugden, D.E., Hulton, N.R.J. and McCULLOCH, R.D., 2005. The Landforms and Pattern of Deglaciation in the Strait of Magellan and Bahía Inútil, Southernmost South America: *Geografiska Annaler: Series A, Physical Geography*, **87**, p. 313–333, doi: 10.1111/j.0435-3676.2005.00261.x.
- Bergsten, F., 1954. The Land Uplift in Sweden from the Evidence of the Old Water Marks: *Geografiska Annaler*, **36**, p. 81–111, doi: 10.1080/20014422.1954.11880859.
- Berthier, E., Vincent, C., Magnússon, E., Gunnlaugsson, Á.P., Pitte, P., Le Meur, E., Masiokas, M., Ruiz, L., Pálsson, F., Belart, J.M.C. and Wagnon, P., 2014. Glacier topography and elevation changes derived from Pléiades sub-meter stereo images: *The Cryosphere*, **8**, p. 2275–2291, doi: 10.5194/tc-8-2275-2014.

- Betka, P., Klepeis, K. and Mosher, S., 2016. Fault kinematics of the Magallanes-Fagnano fault system, southern Chile; an example of diffuse strain and sinistral transtension along a continental transform margin: *Journal of Structural Geology*, **85**, p. 130–153, doi: 10.1016/j.jsg.2016.02.001.
- Bierman, P.R., Gillespie, A.R. and Caffee, M.W., 1995. Cosmogenic Ages for Earthquake Recurrence Intervals and Debris Flow Fan Deposition, Owens Valley, California: *Science*, **270**, p. 447–450, doi: 10.1126/science.270.5235.447.
- Bilham, R. and King, G., 1989. The morphology of strike-slip faults: Examples from the San Andreas Fault, California: *Journal of Geophysical Research: Solid Earth*, **94**, p. 10204–10216, doi: 10.1029/JB094iB08p10204.
- Blair, T.C. and McPherson, J.G., 1999. Grain-Size and Textural Classification of Coarse Sedimentary Particles: *Journal of Sedimentary Research*, **69**, p. 6–19, doi: <https://doi.org/10.2110/jsr.69.6>.
- Blisniuk, P.M., Stern, L.A., Chamberlain, C.P., Idleman, B. and Zeitler, P.K., 2005. Climatic and ecologic changes during Miocene surface uplift in the Southern Patagonian Andes: *Earth and Planetary Science Letters*, **230**, p. 125–142, doi: 10.1016/j.epsl.2004.11.015.
- Bonneuil, C. and Fressoz, J.-B., 2013. *L'événement Anthropocène: la Terre, l'histoire et nous: Seuil*.
- Bonorino, G.G., Rinaldi, V., del Valle Abascal, L., Alvarado, P., Bujalesky, G.G. and Güell, A., 2012. Paleoseismicity and seismic hazard in southern Patagonia (Argentina-Chile; 50°–55°S) and the role of the Magallanes-Fagnano transform fault: *Natural Hazards*, **61**, p. 337–349, doi: <https://doi.org/10.1007/s11069-011-9917-2>.
- Borrello, Á.V., 1962. Sobre los diques clásticos de Tierra del Fuego: *Revista del museo de la Plata*, **5**, p. 155–191.
- Boyd, B.L., Anderson, J.B., Wellner, J.S. and Fernandez, R.A., 2008. The sedimentary record of glacial retreat, Marinelli Fjord, Patagonia: regional correlations and climate ties: *Marine Geology*, **255**, p. 165–178.
- Brandes, C., Steffen, H., Sandersen, P.B., Wu, P. and Winsemann, J., 2018. Glacially induced faulting along the NW segment of the Sorgenfrei-Tornquist Zone, northern Denmark: Implications for neotectonics and Lateglacial fault-bound basin formation: *Quaternary Science Reviews*, **189**, p. 149–168, doi: <https://doi.org/10.1016/j.quascirev.2018.03.036>.
- Braucher, R., Brown, E.T., Bourlès, D.L. and Colin, F., 2003. In situ produced ¹⁰Be measurements at great depths: implications for production rates by fast muons: *Earth and Planetary Science Letters*, **211**, p. 251–258, doi: 10.1016/S0012-821X(03)00205-X.
- Breitsprecher, K. and Thorkelson, D.J., 2009. Neogene kinematic history of Nazca–Antarctic–Phoenix slab windows beneath Patagonia and the Antarctic Peninsula: *Tectonophysics*, **464**, p. 10–20, doi: 10.1016/j.tecto.2008.02.013.

- Brides, T., 1879. Southern Mission. Tierra del Fuego: *The South American Missionary Magazine*, p. 151- 156.
- Bridges, Esteban.L., 1952. *El Último Confín De La Tierra - Uttermost Part Of The Earth*: Emecé Editores, S.A - Buenos Aires.
- Bridges, T. and Canclini, A., 2001. *Los indios del último confín: sus escritos para la South American Missionary Society*: Zagier & Urruty Publ.
- Briner, J.P., Miller, G.H., Davis, P.T. and Finkel, R.C., 2006. Cosmogenic radionuclides from fiord landscapes support differential erosion by overriding ice sheets: *Geological Society of America Bulletin*, **118**, p. 406–420, doi: <https://doi.org/10.1130/B25716.1>.
- Brodzikowski, K. and Loon, A.J. van, 1990. *Glacigenic Sediments*: Elsevier.
- Broster, B.E., Allen, P. and Burke, K.B.S., 1994. A multidisciplinary assesment of postglacial seismic disturbance: Miramichi area, New Brunswick, Canada: *Quaternary International*, 20, 1993, pp 151–161. In: *International Journal of Rock Mechanics and Mining Sciences & Geomechanics Abstracts* Pergamon, p. 268.
- Broster, B.E. and Burke, K.B.S., 1990. Glacigenic postglacial faulting at Saint John, New Brunswick: , doi: <https://doi.org/10.4138/1697>.
- Brown, E.T., Edmond, J.M., Raisbeck, G.M., Yiou, F., Kurz, M.D. and Brook, E.J., 1991. Examination of surface exposure ages of Antarctic moraines using in situ produced ¹⁰Be and ²⁶Al: *Geochimica et Cosmochimica Acta*, **55**, p. 2269–2283, doi: [https://doi.org/10.1016/0016-7037\(91\)90103-C](https://doi.org/10.1016/0016-7037(91)90103-C).
- Brüggen, J., 1943. Contribución a la geología sísmica de Chile.: *Revista Chilena de Historia y Geografía*, **103**, p. 108–174.
- Bruhn, R.L. and Dalziel, I.W.D., 1977. Destruction of the Early Cretaceous Marginal Basin in the Andes of Tierra Del Fuego: *Island Arcs, Deep Sea Trenches and Back-Arc Basins*, p. 395–405, doi: <https://doi.org/10.1029/ME001p0395>.
- Buffoni, C., Sabbione, N.C., Connon, G. and Ormaechea, J.L., 2009. Localización de hipocentros y determinación de su magnitud en Tierra del Fuego y zonas aledañas: *Geoacta*, **34**, p. 75–86.
- Bujalesky, G.G., Heusser, C.J., Coronato, A.M., Roig, C.E. and Rabassa, J.O., 1997. Pleistocene glaciolacustrine sedimentation at Lago Fagnano, Andes of Tierra Del Fuego, Southernmost South America: *Quaternary Science Reviews*, **16**, p. 767–778, doi: 10.1016/S0277-3791(97)00018-8.
- Burbank, D.W. and Anderson, R.S., 2009. *Tectonic geomorphology*: John Wiley & Sons.
- Burns, K.L., Rickard, M.J., Belbin, L. and Chamalaun, F., 1980. Further palaeomagnetic confirmation of the magellanes orocline: *Tectonophysics*, **63**, p. 75–90, doi: 10.1016/0040-1951(80)90108-0.

Bustos, J., 1931. Estudio sismológico de Chile con los temblores y terremotos producidos en los últimos cuatro siglos.: *Anales de la Universidad de Chile*, **1**, p. 59–91.

Byerlee, J., 1978. Friction of rocks: *Rock friction and earthquake prediction*., p. 615–626, doi: https://doi.org/10.1007/978-3-0348-7182-2_4.

C

Caldenius, C.C., 1932. Las Glaciaciones Cuaternarias en la Patagonia y Tierra del Fuego: *Geografiska Annaler*, **95**, doi: <https://doi.org/10.2307/519583>.

Cande, S.C. and Leslie, R.B., 1986. Late Cenozoic tectonics of the Southern Chile Trench: *Journal of Geophysical Research: Solid Earth*, **91**, p. 471–496, doi: 10.1029/JB091iB01p00471.

Carey, S.W., 1958. The tectonic approach to continental drift, in *Continental Drift: A Symposium: Hobart, Tasmania, Geology Department, University of Tasmania*., p. 177–355.

Casali, R. and Manzi, L.M., 2017. Etnicidades capitalistas: el rol de la Estancia San Pablo en el entramado de resistencia selk'nam. Tierra del Fuego, 1904-1930: *Magallania (Punta Arenas)*, **45**, p. 109–133, doi: 10.4067/S0718-22442017000200109.

Castano, J.C., 1977. Zonificación sísmica de la República Argentina: *Publicación Técnica N° 5*., p. 40.

Chapman, A., 1989. *El fin de un mundo: Los Selk'nam de Tierra del Fuego (End of a World: The Selknam of Tierra Del Fuego)*: Vázquez Mazzini Editores, Buenos Aires.

Chapman, A., 2010. *European encounters with the Yamana people of Cape Horn, before and after Darwin*: Cambridge University Press.

Chéry, J., Zoback, M. and Hassani, R., 2001. Rheology, strain and stress of the San Andreas Fault in central and northern California: A 3-D thermomechanical modeling study: *J. Geophys. Res.*, **106**, p. 051–071, doi: <https://doi.org/10.1029/2001JB000382>.

Chevalier, M.-L., Leloup, P.H., Replumaz, A., Pan, J., Liu, D., Li, H., Gourbet, L. and Métois, M., 2016. Tectonic-geomorphology of the Litang fault system, SE Tibetan Plateau, and implication for regional seismic hazard: *Tectonophysics*, **682**, p. 278–292, doi: <https://doi.org/10.1016/j.tecto.2016.05.039>.

Chinnery, M.A., 1965. The vertical displacements associated with transcurrent faulting: *Journal of Geophysical Research (1896-1977)*, **70**, p. 4627–4632, doi: <https://doi.org/10.1029/JZ070i018p04627>.

Chmeleff, J., von Blanckenburg, F., Kossert, K. and Jakob, D., 2010. Determination of the ¹⁰Be half-life by multicollector ICP-MS and liquid scintillation counting: *Nuclear*

- Christie-Blick, N. and Biddle, K.T., 1985. Deformation and Basin Formation Along Strike-Slip Faults: , doi: <https://doi.org/10.2110/pec.85.37.0001>.
- Cisternas, Armando and Vera, E., 2008. Sismos históricos y recientes en Magallanes: *Magallania (Punta Arenas)*, **36**, p. 43–51, doi: 10.4067/S0718-22442008000100004.
- Clapperton, C.M., 1993. Quaternary geology and geomorphology of South America: *Elsevier*,, p. 779 p.: ill., map.
- Clapperton, C.M., Sugden, D.E., Kaufman, D.S. and McCulloch, R.D., 1995. The Last Glaciation in Central Magellan Strait, Southernmost Chile: *Quaternary Research*, **44**, p. 133–148, doi: 10.1006/qres.1995.1058.
- Clark, P.U., Dyke, A.S., Shakun, J.D., Carlson, A.E., Clark, J., Wohlfarth, B., Mitrovica, J.X., Hostetler, S.W. and McCabe, A.M., 2009. The last glacial maximum: *science*, **325**, p. 710–714, doi: <https://doi.org/10.1126/science.1172873>.
- Cook, J., 1777. *A Voyage Towards the South Pole, and Round the World: Performed in His Majesty's Ships the Resolution and Adventure, in the Years 1772, 1773, 1774, and 1775*: W. Strahan & T. Cadell.
- Coronato, A., Meglioli, A. and Rabassa, J., 2004b. Glaciations in the Magellan Straits and Tierra del Fuego, southernmost South America (J. Ehlers and P. L. Gibbard, Eds.): *Developments in Quaternary Sciences*, **2**, p. 45–48, doi: [https://doi.org/10.1016/S1571-0866\(04\)80110-6](https://doi.org/10.1016/S1571-0866(04)80110-6).
- Coronato, A., Ponce, F., Rabassa, J. and Sepälä, M., 2008. Evidencias morfológicas del englazamiento del valle del río Ewan, Tierra del Fuego.: , p. 1196- 1197.
- Coronato, A., Ponce, F., Seppälä, M. and Rabassa, J., 2008b. Englazamiento del valle del río Fuego durante el Pleistoceno tardío, Tierra del Fuego, Argentina: *Congreso Geológico Argentino*,, p. 1194–1195.
- Coronato, A., Roig, C. and Mir, X., 2002a. Geoformas glaciarias de la región oriental del Lago Fagnano, Tierra del Fuego, Argentina. In: *Actas XV Congreso Geológico Argentino. El Calafate, Argentina (23-26 de abril, 2002). CD-Rom. Artículo*.
- Coronato, A., Roig, C. and Mir, X., 2002b. Geoformas glaciarias de la región oriental del Lago Fagnano, Tierra del Fuego, Argentina. In: *Actas XV Congreso Geológico Argentino. El Calafate, Argentina (23-26 de abril, 2002). CD-Rom. Artículo*.
- Coronato, A., Seppälä, M., Ponce, J.F. and Rabassa, J., 2009. Glacial geomorphology of the Pleistocene lake Fagnano ice lobe, Tierra del Fuego, southern South America: *Geomorphology*, **112**, p. 67–81, doi: <https://doi.org/10.1016/j.geomorph.2009.05.005>.
- Costa, C.H., Smalley, R., Velasco, M.S., Schwart, D.P., Ellis, M. and Ahumada, E.A., 2006. Paleoseismic observations of an onshore transform boundary: the Magallanes-Fagnano

fault, Tierra del Fuego, Argentina: *Revista de la Asociación Geológica Argentina*, **61** (4), p. 647–657.

Craig, T.J., Calais, E., Fleitout, L., Bollinger, L. and Scotti, O., 2016. Evidence for the release of long-term tectonic strain stored in continental interiors through intraplate earthquakes: *Geophysical Research Letters*, **43**, p. 6826–6836, doi: <https://doi.org/10.1002/2016GL069359>.

Crowell, J.C., 1974. Origin of Late Cenozoic Basins in Southern California: ABSTRACT: *AAPG Bulletin*, **57**, p. 774–774, doi: <https://doi.org/10.1306/819A436C-16C5-11D7-8645000102C1865D>.

Cundall, P. and Board, M., 1988. A microcomputer program for modelling large-strain plasticity problems International Conference on Numerical Methods in Geomechanics Abstracts: *Innsbruck (Austria)*.

Cunningham, W.D., 1993. Strike-slip faults in the southernmost Andes and the development of the Patagonian orocline: *Tectonics*, **12**, p. 169–186, doi: <https://doi.org/10.1029/92TC01790>.

Cunningham, W.D., Klepeis, K.A., Gose, W.A. and Dalziel, I.W.D., 1991. The Patagonian Orocline: New paleomagnetic data from the Andean magmatic arc in Tierra del Fuego, Chile: *Journal of Geophysical Research: Solid Earth*, **96**, p. 16061–16067, doi: 10.1029/91JB01498.

D

Da Mosto, A. and Allegrì, M., 1894. *Il primo viaggio intorno al globo di Antonio Pigafetta: e le sue Regole sull'arte del navigare*: Auspice il Ministero della pubblica istruzione.

Dalziel, I.W.D., 1981. Back-Arc Extension in the Southern Andes: A Review and Critical Reappraisal: *Philosophical Transactions of the Royal Society of London Series A*, **300**, p. 319–335, doi: 10.1098/rsta.1981.0067.

Dalziel, I.W.D., 1986. Collision and Cordilleran orogenesis: an Andean perspective: *Geological Society, London, Special Publications*, **19**, p. 389–404, doi: 10.1144/GSL.SP.1986.019.01.22.

Dalziel, I. and Cortés, R., 1972. Tectonic style of the southernmost Andes and the Antarctandes: *XXIV International Geological Congress Proceedings, Montreal, Canada*, p. 316–327.

Dalziel, I.W.D., Kligfield, R., Lowrie, W. and Opdyke, N.D., 1973. *Paleomagnetic data from the southernmost Andes and the Antarctandes, Implications of Continental Drift to the Earth Sciences, 1 DH Tarling, SK Runcorn, 87–101*: Academic, San Diego, Calif.

Dalziel, I.W., Lawver, L.A., Norton, I.O. and Gahagan, L.M., 2013. The Scotia Arc: genesis, evolution, global significance: *Annual Review of Earth and Planetary Sciences*, **41**, p. 767–793, doi: 10.1146/annurev-earth-050212-124155.

- Darvill, C.M., Bentley, M.J., Stokes, C.R., Hein, A.S. and Rodés, Á., 2015b. Extensive MIS 3 glaciation in southernmost Patagonia revealed by cosmogenic nuclide dating of outwash sediments: *Earth and Planetary Science Letters*, **429**, p. 157–169, doi: <https://doi.org/10.1016/j.epsl.2015.07.030>.
- Darwin, C., 1840. *Journal of Researches Into the Geology and Natural History of the Varoius Countries Visited by HMS Beagle, Under the Command of Captain Fitzroy from 1832 to 1836 by Charles Darwin*: Colburn.
- Darwin, C., 1875. Voyage d'un naturaliste autour du monde fait à bord du navire Le Beagle de 1831 à 1836 par Charles Darwin: , doi: <https://doi.org/10.5962/bhl.title.10600>.
- Davies, B.J., Darvill, C.M., Lovell, H., Bendle, J.M., Dowdeswell, J.A., Fabel, D., García, J.-L., Geiger, A., Glasser, N.F., Gheorghiu, D.M., Harrison, S., Hein, A.S., Kaplan, M.R., Martin, J.R.V., Mendelova, M., Palmer, A., Pelto, M., Rodés, Á., Sagredo, E.A., Smedley, R.K., Smellie, J.L. and Thorndycraft, V.R., 2020. The evolution of the Patagonian Ice Sheet from 35 ka to the present day (PATICE): *Earth-Science Reviews*, **204**, p. 103152, doi: 10.1016/j.earscirev.2020.103152.
- De Geer, G., 1940. Geochronologia suecica principes: *Kungl. sv. vetenskapsakademiens handlingar*, **3**, p. 367p.
- De Geer, G., 1890. Om Skandinaviens nir\aaförändringar under kvartär-perioden: *Geologiska Föreningen i Stockholm Förhandlingar*, **12**, p. 61–110, doi: <https://doi.org/10.1080/11035899009442248>.
- Dehls, J.F., Olesen, O., Olsen, L. and Blikra, L.H., 2000. Neotectonic faulting in northern Norway; the Stuuragurra and Nordmannvikdalen postglacial faults: *Quaternary science reviews*, **19**, p. 1447–1460, doi: [https://doi.org/10.1016/S0277-3791\(00\)00073-1](https://doi.org/10.1016/S0277-3791(00)00073-1).
- DeMets, C., Gordon, R.G. and Argus, D.F., 2010. Geologically current plate motions: *Geophysical Journal International*, **181**, p. 1–80, doi: 10.1111/j.1365-246X.2009.04491.x.
- DeMets, C., Gordon, R.G., Argus, D.F. and Stein, S., 1990. Current plate motions: *Geophysical Journal International*, **101**, p. 425–478, doi: 10.1111/j.1365-246X.1990.tb06579.x.
- DeMets, C., Gordon, R.G., Argus, D.F. and Stein, S., 1994. Effect of recent revisions to the geomagnetic reversal time scale on estimates of current plate motions: *Geophysical Research Letters*, **21**, p. 2191–2194, doi: <https://doi.org/10.1029/94GL02118>.
- Dennell, R., 2015. Human Origin Sites and the World Heritage Convention in the Americas: The Applicability of World Heritage Criteria for the First Populations in the Americas: *World Heritage Papers 42 UNESCO 2015*, **1**.
- Denton, G.H., Heusser, C.J., Lowel, T.V., Moreno, P.I., Andersen, B.G., Heusser, L.E., Schlüchter, C. and Marchant, D.R., 1999. Interhemispheric Linkage of Paleoclimate During the Last Glaciation: *Geografiska Annaler: Series A, Physical Geography*, **81**, p. 107–153, doi: 10.1111/1468-0459.00055.

- Desai, C.S. and Siriwardane, H.J., 1984. *Constitutive laws for engineering materials with emphasis on geologic materials*: Prentice-Hall.
- Dietrich, R., Ivins, E.R., Casassa, G., Lange, H., Wendt, J. and Fritsche, M., 2010. Rapid crustal uplift in Patagonia due to enhanced ice loss: *Earth and Planetary Science Letters*, **289**, p. 22–29, doi: 10.1016/j.epsl.2009.10.021.
- Dillehay, T.D., 2003. Las culturas del Pleistoceno tardío en Suramérica: *Maguaré*,.
- Dillehay, T.D., 1999. The late pleistocene cultures of South America: *Evolutionary Anthropology: Issues, News, and Reviews: Issues, News, and Reviews*, **7**, p. 206–216, doi: [https://doi.org/10.1002/\(SICI\)1520-6505\(1999\)7:6<206::AID-EVAN5>3.0.CO;2-G](https://doi.org/10.1002/(SICI)1520-6505(1999)7:6<206::AID-EVAN5>3.0.CO;2-G).
- Dillehay, T.D., 2000. The settlement of the Americas: a new prehistory:
- Diraison, M., Cobbold, P.R., Gapais, D., Rossello, E.A. and Le Corre, C., 2000. Cenozoic crustal thickening, wrenching and rifting in the foothills of the southernmost Andes: *Tectonophysics*, **316**, p. 91–119, doi: 10.1016/S0040-1951(99)00255-3.
- Domack, E.W. and Powell, R., 2018. Chapter 7 - Modern Glaciomarine Environments and Sediments: An Antarctic Perspective (J. Menzies and J. J. M. van der Meer, Eds.): *Past Glacial Environments (Second Edition)*,, p. 181–272, doi: <https://doi.org/10.1016/B978-0-08-100524-8.00030-0>.
- Dublé Almeida, D., 1938. Diario de viaje al río Santa Cruz, Patagonia: *Revista Chilena de Historia y Geografía*, **93**, p. 254–279.
- Dunai, T.J., 2010. Cosmogenic Nuclides: Principles, concepts and applications in the Earth surface sciences: *Cambridge University Press*,, doi: 10.1017/CBO9780511804519.
- Duvall, A.R., Clark, M.K., Kirby, E., Farley, K.A., Craddock, W.H., Li, C. and Yuan, D.-Y., 2013. Low-temperature thermochronometry along the Kunlun and Haiyuan Faults, NE Tibetan Plateau: Evidence for kinematic change during late-stage orogenesis: *Tectonics*, **32**, p. 1190–1211, doi: 10.1002/tect.20072.
- Dyke, A.S., 2004. An outline of North American deglaciation with emphasis on central and northern Canada: *Developments in Quaternary Sciences*, **2**, p. 373–424, doi: [https://doi.org/10.1016/S1571-0866\(04\)80209-4](https://doi.org/10.1016/S1571-0866(04)80209-4).
- Dziewonski, A.M. and Anderson, D.L., 1981. Preliminary reference Earth model: *Physics of the Earth and Planetary Interiors*, **25**, p. 297–356, doi: 10.1016/0031-9201(81)90046-7.

E

- Eagles, G., 2004. Tectonic evolution of the Antarctic–Phoenix plate system since 15 Ma: *Earth and Planetary Science Letters*, **217**, p. 97–109, doi: 10.1016/S0012-821X(03)00584-3.

-
- Ekman, M., 1991. A concise history of postglacial land uplift research (from its beginning to 1950): *Terra Nova*, **3**, p. 358–365, doi: <https://doi.org/10.1111/j.1365-3121.1991.tb00163.x>.
- Ekman, M., 2013. *An Investigation of Celsius' Pioneering Determination of the Fennoscandian Land Uplift Rate, and of His Mean Sea Level Mark*: Summer Institute for Historical Geophysics.
- Esteban, F.D., Tassone, A., Isola, J.I., Lodolo, E. and Menichetti, M., 2018. Geometry and structure of the pull-apart basins developed along the western South American-Scotia plate boundary (SW Atlantic Ocean): *Journal of South American Earth Sciences*, **83**, p. 96–116, doi: 10.1016/j.jsames.2018.02.005.
- Esteban, F.D., Tassone, A., Lodolo, E., Menichetti, M., Lippai, H., Waldmann, N., Darbo, A., Baradello, L. and Vilas, J.F., 2014. Basement geometry and sediment thickness of Lago Fagnano (Tierra del Fuego): *Andean geology*, **41**, p. 293–313, doi: <https://doi.org/10.5027/andgeoV41n2-a02>.

F

- Fabel, D., Stroeven, A.P., Harbor, J., Kleman, J., Elmore, D. and Fink, D., 2002. Landscape preservation under Fennoscandian ice sheets determined from in situ produced ¹⁰Be and ²⁶Al: *Earth and Planetary Science Letters*, **201**, p. 397–406, doi: 10.1016/S0012-821X(02)00714-8.
- Febrer, J.M., Plasencia, M.P. and Sabbione, N.C., 2000. Local and regional seismicity from Ushuaia broadband station observations (Tierra del Fuego): *Terra Antartica*, **8**, p. 35–40.
- Ferdinand, M., 2019. Une écologie décoloniale-Penser l'écologie depuis le monde caribéen: , doi: <https://doi.org/10.3917/pro.375.0052>.
- Fernández, R.A., Anderson, J.B., Wellner, J.S. and Hallet, B., 2011. Timescale dependence of glacial erosion rates: A case study of Marinelli Glacier, Cordillera Darwin, southern Patagonia: *Journal of Geophysical Research: Earth Surface*, **116**, doi: 10.1029/2010JF001685.
- Fernández, R., Gulick, S., Rodrigo, C., Domack, E. and Leventer, A., 2017. Seismic stratigraphy and glacial cycles in the inland passages of the Magallanes región of Chile, southernmost South America: *Marine Geology*, **386**, p. 19–31, doi: <https://doi.org/10.1016/j.margeo.2017.02.006>.
- Fernández, R., Gulick, S., Rodrigo, C., Domack, E., Leventer, A. and Saustруп, S., 2013. The seismic record of late glacial variations in the Strait of Magellan: New clues for the interpretation of the glacial history of Magallanes. In: *GeoSur2013* p. 4.
- Feyling-Hanssen, R.W., 1966. Geologiske observasjoner i Sandnesområdet: *Norges geologiske undersøkelse*, **242**, p. 26–43.

- Fildani, A. and Hessler, A.M., 2005. Stratigraphic record across a retroarc basin inversion: Rocas Verdes-Magallanes Basin, Patagonian Andes, Chile: *Geological Society of America Bulletin*, **117**, p. 1596, doi: 10.1130/B25708.1.
- Fitzroy, R. and King, P., 2018. *Narrative of the surveying voyages of His Majesty's Ships Adventure and Beagle, between the years 1826 and 1836*: Litres.
- Fjeldskaar, W., Lindholm, C., Dehls, J.F. and Fjeldskaar, I., 2000. Postglacial uplift, neotectonics and seismicity in Fennoscandia: *Quaternary Science Reviews*, **19**, p. 1413–1422, doi: 10.1016/S0277-3791(00)00070-6.
- Flores Véliz, M.C., 2017. Estudio de la sismicidad en la región de Magallanes: Facultad de Ciencias Físicas y Matemáticas, Universidad de Chile; Centro Sismológico National Universidad de Chile Informe de Práctica FCFM y CSN, 30 p.
- Forsyth, D.W., 1975. Fault plane solutions and tectonics of the South Atlantic and Scotia Sea: *Journal of Geophysical Research*, **80**, p. 1429–1443, doi: 10.1029/JB080i011p01429.
- Fosdick, J.C., Romans, B.W., Fildani, A., Bernhardt, A., Calderon, M. and Graham, S.A., 2011. Kinematic evolution of the Patagonian retroarc fold-and-thrust belt and Magallanes foreland basin, Chile and Argentina, 51°30'S: *Geological Society of America Bulletin*, **123**, p. 1679–1698, doi: 10.1130/B30242.1.
- Fritts, H.C., 1976. *Tree Rings and Climate*: Harcourt Brace Jovanovich Publishers, London, New York, San Francisco.

G

- García, S., 2013. Vestigios Patrimoniales del aserradero Caleta María, Tierra del Fuego (Chile): *Magallania (Punta Arenas)*, **41**, p. 53–82, doi: <https://doi.org/10.4067/S0718-22442013000100003>.
- García O, S., 2015. Los orígenes de las comunicaciones terrestres en el sur de Tierra del Fuego (Chile): *Magallania (Punta Arenas)*, **43**, p. 5–45, doi: 10.4067/S0718-22442015000200001.
- Ghiglione, M.C., 2002. Diques clásticos asociados a deformación transcurrente en depósitos sinorogénicos del Mioceno inferior de la Cuenca Austral: *Revista de la Asociación Geológica Argentina*, **57**, p. 103–118.
- Ghiglione, M.C., 2003. Estructura y evolución tectónica del Cretácico-Terciario de la costa Atlántica de Tierra del Fuego: *Estructura y Evolución Tectónica del Cretácico-Terciario de la costa atlántica de Tierra del Fuego (PhD thesis) Ciudad de Buenos Aires (150 pp.)*.
- Ghiglione, M.C., 2016. Geodynamic Evolution of the Southernmost Andes: Connections with the Scotia Arc: *Springer*., doi: <https://doi.org/10.1007/978-3-319-39727-6>.

- Ghiglione, M.C. and Cristallini, E.O., 2007. Have the southernmost Andes been curved since Late Cretaceous time? An analog test for the Patagonian Orocline: *Geology*, **35**, p. 13, doi: 10.1130/G22770A.1.
- Ghiglione, M.C., Likerman, J., Barberón, V., Giambiagi, L.B., Aguirre-Urreta, B. and Suarez, F., 2014. Geodynamic context for the deposition of coarse-grained deep-water axial channel systems in the Patagonian Andes: *Basin Research*, **26**, p. 726–745, doi: 10.1111/bre.12061.
- Ghiglione, M.C., Navarrete-Rodríguez, A.T., González-Guillot, M. and Bujalesky, G., 2013. The opening of the Magellan Strait and its geodynamic implications: *Terra Nova*, **25**, p. 13–20, doi: 10.1111/j.1365-3121.2012.01090.x.
- Ghiglione, M.C., Quinteros, J., Yagupsky, D., Bonillo-Martínez, P., Hlebszevitch, J., Ramos, V.A., Vergani, G., Figueroa, D. and Quesada, S., 2010. Structure and tectonic history of the foreland basins of southernmost South America: *Journal of South American Earth Sciences*, **29**, p. 262–277, doi: 10.1016/j.jsames.2009.07.006.
- Ghiglione, M.C. and Ramos, V.A., 2005. Progression of deformation and sedimentation in the southernmost Andes: *Tectonophysics*, **405**, p. 25–46, doi: 10.1016/j.tecto.2005.05.004.
- Glasser, N.F. and Ghiglione, M.C., 2009. Structural, tectonic and glaciological controls on the evolution of fjord landscapes: *Geomorphology*, **105**, p. 291–302, doi: 10.1016/j.geomorph.2008.10.007.
- Gordillo, S., Bujalesky, G.G., Pirazzoli, P.A., Rabassa, J.O. and Saliège, J.-F., 1992. Holocene raised beaches along the northern coast of the Beagle Channel, Tierra del Fuego, Argentina: *Palaeogeography, Palaeoclimatology, Palaeoecology*, **99**, p. 41–54, doi: [https://doi.org/10.1016/0031-0182\(92\)90006-Q](https://doi.org/10.1016/0031-0182(92)90006-Q).
- Gosse, J.C. and Phillips, F.M., 2001. Terrestrial in situ cosmogenic nuclides: theory and application: *Quaternary Science Reviews*, **20**, p. 1475–1560, doi: 10.1016/S0277-3791(00)00171-2.
- Gregersen, S., 2002. Earthquakes and change of stress since the ice age in Scandinavia: *Bulletin of the Geological Society of Denmark*, **49**, p. 73–78.
- Gregersen, S. and Voss, P., 2010. Irregularities in Scandinavian postglacial uplift/subsidence in time scales tens, hundreds, thousands of years: *Journal of Geodynamics*, **50**, p. 27–31, doi: <https://doi.org/10.1016/j.jog.2009.11.004>.
- Grosset, J., Mazzotti, S., Vernant, P., Chéry, J. and Manchuel, K., 2019. Strike-slip fault reactivation in the Western Alps due to Glacial Isostatic Adjustment: , p. 31, doi: <https://doi.org/10.5194/egusphere-egu2020-8505>.
- Guilderson, T.P., Burckle, L., Hemming, S. and Peltier, W.R., 2000. Late Pleistocene sea level variations derived from the Argentine Shelf: *Geochemistry, Geophysics, Geosystems*, **1**, doi: 10.1029/2000GC000098.

- Guillaume, B., 2008. Évolution cénozoïque des Andes méridionales: approche morphotectonique, géochronologique et apports de la modélisation analogique: *Université Toulouse III - Paul Sabatier*, p. 330.
- Guillaume, B., Martinod, J., Husson, L., Roddaz, M. and Riquelme, R., 2009. Neogene uplift of central eastern Patagonia: Dynamic response to active spreading ridge subduction? *Tectonics*, **28**, doi: 10.1029/2008TC002324.
- Gusinde, M., 1951. *Los fueguinos, Hombres Primitivos en la Tierra del Fuego (Urmenschen im Feuerland): De investigador a compañero de tribu' (Version directa del Aleman por Diego Bermudez Camacho): Alfonso XII, 12- Sevilla, Escuela de Estudios Hispánicos-Americanos de Sevilla.*

H

- Hall, B.L., Denton, G., Lowell, T., Bromley, G.R.M. and Putnam, A.E., 2017. Retreat of the Cordillera Darwin icefield during Termination I: *Cuadernos de Investigación Geográfica*, **43**, p. 751–766, doi: 10.18172/cig.3158.
- Hall, B.L., Lowell, T.V., Bromley, G.R.M., Denton, G.H. and Putnam, A.E., 2019. Holocene glacier fluctuations on the northern flank of Cordillera Darwin, southernmost South America: *Quaternary Science Reviews*, **222**, p. 105904, doi: 10.1016/j.quascirev.2019.105904.
- Hall, B.L., Porter, C.T., Denton, G.H., Lowell, T.V. and Bromley, G.R., 2013. Extensive recession of Cordillera Darwin glaciers in southernmost South America during Heinrich stadial 1: *Quaternary Science Reviews*, **62**, p. 49–55, doi: <https://doi.org/10.1016/j.quascirev.2012.11.026>.
- Hallet, B., 2016. Raw ship-based Multibeam Sonar Data acquired during R/V Nathaniel B. Palmer expedition NBP0505 (2005): , doi: 10.1594/IEDA/306282.
- Hampel, A. and Hetzel, R., 2006. Response of normal faults to glacial-interglacial fluctuations of ice and water masses on Earth's surface: *Journal of Geophysical Research: Solid Earth*, **111**, doi: <https://doi.org/10.1029/2005JB004124>.
- Hampel, A., Hetzel, R. and Densmore, A.L., 2007. Postglacial slip-rate increase on the Teton normal fault, northern Basin and Range Province, caused by melting of the Yellowstone ice cap and deglaciation of the Teton Range? *Geology*, **35**, p. 1107–1110, doi: <https://doi.org/10.1130/G24093A.1>.
- Hampel, A., Hetzel, R., Maniatis, G. and Karow, T., 2009. Three-dimensional numerical modeling of slip rate variations on normal and thrust fault arrays during ice cap growth and melting: *Journal of Geophysical Research: Solid Earth*, **114**, doi: <https://doi.org/10.1029/2008JB006113>.
- Hampel, A., Karow, T., Maniatis, G. and Hetzel, R., 2010. Slip rate variations on faults during glacial loading and post-glacial unloading: implications for the viscosity structure of the

-
- lithosphere: *Journal of the Geological Society*, **167**, p. 385–399, doi: <https://doi.org/10.1144/0016-76492008-137>.
- Hanks, T.C. and Kanamori, H., 1979. A moment magnitude scale: *Journal of Geophysical Research: Solid Earth*, **84**, p. 2348–2350, doi: <https://doi.org/10.1029/JB084iB05p02348>.
- Haraway, D., Ishikawa, N., Gilbert, S.F., Olwig, K., Tsing, A.L. and Bubandt, N., 2016. Anthropologists are talking—about the Anthropocene: *Ethnos*, **81**, p. 535–564, doi: <https://doi.org/10.1080/00141844.2015.1105838>.
- Harding, T.P., 1985. Seismic Characteristics and Identification of Negative Flower Structures, Positive Flower Structures, and Positive Structural Inversion: *AAPG Bulletin*, **69**, p. 582–600, doi: <https://doi.org/10.1306/AD462538-16F7-11D7-8645000102C1865D>.
- Hassani, R., Jongmans, D. and Chéry, J., 1997. Study of plate deformation and stress in subduction processes using two-dimensional numerical models: *Journal of Geophysical Research: Solid Earth*, **102**, p. 17951–17965, doi: <https://doi.org/10.1029/97JB01354>.
- Henton, J.A., Craymer, M.R., Ferland, R., Dragert, H., Mazzotti, S. and Forbes, D.L., 2006. Crustal motion and deformation monitoring of the Canadian landmass: *Geomatica*, **60**, p. 173–191.
- Hervé, F., Fanning, C.M., Pankhurst, R.J., Mpodozis, C., Klepeis, K., Calderón, M. and Thomson, S.N., 2010. Detrital zircon SHRIMP U–Pb age study of the Cordillera Darwin Metamorphic Complex of Tierra del Fuego: sedimentary sources and implications for the evolution of the Pacific margin of Gondwana: *Journal of the Geological Society*, **167**, p. 555–568, doi: 10.1144/0016-76492009-124.
- Hervé, F., Pankhurst, R.J., Fanning, C.M., Calderón, M. and Yaxley, G.M., 2007. The South Patagonian batholith: 150 my of granite magmatism on a plate margin: *Lithos*, **97**, p. 373–394, doi: 10.1016/j.lithos.2007.01.007.
- Hervé, M., Suárez, M. and Puig, A., 1984. The Patagonian Batholith S of Tierra del Fuego, Chile: timing and tectonic implications: *Journal of the Geological Society*, **141**, p. 909–917, doi: 10.1144/gsjgs.141.5.0909.
- Hetzl, R. and Hampel, A., 2005. Slip rate variations on normal faults during glacial–interglacial changes in surface loads: *Nature*, **435**, p. 81–84, doi: <https://doi.org/10.1038/nature03562>.
- Heusser, C.J., 1994a. Paleoindians and fire during the late Quaternary in southern South America: *Revista Chilena de Historia Natural*, **67**, p. 435–443.
- Heusser, C.J., 1994b. Quaternary paleoecology of Fuego-Patagonia: *Revista do Instituto Geológico*, **15**, p. 7–26, doi: <https://doi.org/10.5935/0100-929X.19940002>.
- Hogg, A.G., Heaton, T.J., Hua, Q., Palmer, J.G., Turney, C.S., Southon, J., Bayliss, A., Blackwell, P.G., Boswijk, G. and Ramsey, C.B., 2020. SHCal20 Southern Hemisphere calibration, 0–55,000 years cal BP: *Radiocarbon*, p. 1–20, doi: <https://doi.org/10.1017/RDC.2020.59>.
-

Hogg, A.G., Hua, Q., Blackwell, P.G., Niu, M., Buck, C.E., Guilderson, T.P., Heaton, T.J., Palmer, J.G., Reimer, P.J. and Reimer, R.W., 2013. SHCal13 Southern Hemisphere calibration, 0–50,000 years cal BP: *Radiocarbon*, **55**, p. 1889–1903, doi: https://doi.org/10.2458/azu_js_rc.55.16783.

Hulton, N.R.J., Purves, R.S., McCulloch, R.D., Sugden, D.E. and Bentley, M.J., 2002. The Last Glacial Maximum and deglaciation in southern South America: *Quaternary Science Reviews*, **21**, p. 233–241, doi: 10.1016/S0277-3791(01)00103-2.

Hunt, A.G. and Malin, P.E., 1998. Possible triggering of Heinrich events by ice-load-induced earthquakes: *Nature*, **393**, p. 155–158, doi: <https://doi.org/10.1038/30218>.

I

INDEC, 2016. Población estimada por sexos para total del país y provincias. Años 2010-2040: *Instituto Nacional de Estadística y Censos (Argentina)*,.

INFUETUR, 2019. Anuario Estadístico de Turismo, Tierra del Fuego, Año 2017 y primer semestre 2018: *División de Procesamiento y Análisis Estadístico, Instituto Fueguino de Turismo (INFUETUR)*.,, p. 78.

INPRES, 2004. Terremotos históricos ocurridos en la República Argentina:

Isla, F.I. and Bujalesky, G., 2004. El maremoto de los Yaganes: *Nexos, UNMDP, Mar del Plata*, **19**, p. 29–33.

Ivins, E.R. and James, T.S., 2004. Bedrock response to Llanquihue Holocene and present-day glaciation in southernmost South America: *Geophysical Research Letters*, **31**, doi: 10.1029/2004GL021500.

Ivins, E.R., James, T.S. and Klemann, V., 2003. Glacial isostatic stress shadowing by the Antarctic ice sheet: *Journal of Geophysical Research: Solid Earth*, **108**, doi: <https://doi.org/10.1029/2002JB002182>.

Izagirre, E., Darvill, C.M., Rada, C. and Aravena, J.C., 2018. Glacial geomorphology of the Marinelli and Pigafetta glaciers, Cordillera Darwin Icefield, southernmost Chile: *Journal of Maps*, **14**, p. 269–281, doi: <https://doi.org/10.1080/17445647.2018.1462264>.

J

Jacoby, G.C., Sheppard, P.R. and Sieh, K.E., 1988. Irregular Recurrence of Large Earthquakes Along the San Andreas Fault: Evidence from Trees: *Science*, **241**, p. 196–199, doi: 10.1126/science.241.4862.196.

-
- Jacoby, G.C. and Ulan, L.D., 1983. Tree ring indications of uplift at Icy Cape, Alaska, related to 1899 earthquakes: *Journal of Geophysical Research: Solid Earth*, **88**, p. 9305–9313, doi: 10.1029/JB088iB11p09305.
- Jakobsson, M., Björck, S., O’Regan, M., Flodén, T., Greenwood, S.L., Swärd, H., Lif, A., Ampel, L., Koyi, H. and Skelton, A., 2014. Major earthquake at the Pleistocene-Holocene transition in Lake Vättern, southern Sweden: *Geology*, **42**, p. 379–382, doi: <https://doi.org/10.1130/G35499.1>.
- Jamieson, T.F., 1882. *On the Cause of the Depression and Re-elevation of the Land During the Glacial Period*: Stephen Austin and Sons, Printers, Hertford.
- Jamieson, T.F., 1865. On the history of the last geological changes in Scotland: *Quarterly Journal of the Geological Society*, **21**, p. 161–204, doi: <https://doi.org/10.1144/GSL.JGS.1865.021.01-02.24>.
- Jaschek, E.U., Sabbione, N.C. and Sierra, P.J., 1982. *Reubicación de sismos localizados en territorio Argentino, 1920-1963*: Observatorio Astronomico de la Universidad nacional de la Plata.
- Johnsen, S.J., Clausen, H.B., Dansgaard, W., Fuhrer, K., Gundestrup, N., Hammer, C.U., Iversen, P., Jouzel, J. and Stauffer, B., 1992. Irregular glacial interstadials recorded in a new Greenland ice core: *Nature*, **359**, p. 311–313, doi: <https://doi.org/10.1038/359311a0>.
- Johnston, A.C., 1987. Suppression of earthquakes by large continental ice sheets: *Nature*, **330**, p. 467–469, doi: <https://doi.org/10.1038/330467a0>.
- Johnston, A.C., 1989. The effect of large ice sheets on earthquake genesis: *Earthquakes at North-Atlantic passive margins: Neotectonics and postglacial rebound*, p. 581–599, doi: https://doi.org/10.1007/978-94-009-2311-9_34.
- Jopling, A.V. and Walker, R.G., 1968. Morphology and origin of ripple-drift cross-lamination, with examples from the Pleistocene of Massachusetts: *Journal of Sedimentary Research*, **38**, p. 971–984, doi: 10.1306/74D71ADC-2B21-11D7-8648000102C1865D.

K

- Kaennel, M. and Schweingruber, F., 1995. *Multilingual glossary of dendrochronology. Terms and definitions in english, german, french, spanish, italian, portuguese, and russian.*: Paul Hapt Publishers Berne, Stuttgart Vienna.
- Kagan, E., Stein, M., Agnon, A. and Neumann, F., 2011. Intrabasin paleoearthquake and quiescence correlation of the late Holocene Dead Sea: *Journal of Geophysical Research: Solid Earth*, **116**, doi: <https://doi.org/10.1029/2010JB007452>.
- Kaplan, M.R., Fogwill, C.J., Sugden, D.E., Hulton, N.R.J., Kubik, P.W. and Freeman, S., 2008. Southern Patagonian glacial chronology for the Last Glacial period and implications for

- Southern Ocean climate: *Quaternary Science Reviews*, **27**, p. 284–294, doi: <https://doi.org/10.1016/j.quascirev.2007.09.013>.
- Kearey, P., Klepeis, K.A. and Vine, F.J., 2009. *Global tectonics*: John Wiley & Sons.
- Kierulf, H.P., Steffen, H., Simpson, M.J.R., Lidberg, M., Wu, P. and Wang, H., 2014. A GPS velocity field for Fennoscandia and a consistent comparison to glacial isostatic adjustment models: *Journal of geophysical research: solid earth*, **119**, p. 6613–6629, doi: <https://doi.org/10.1002/2013JB010889>.
- Kinck, J.J., Husebye, E.S. and Larsson, F.R., 1993. The Moho depth distribution in Fennoscandia and the regional tectonic evolution from Archean to Permian times: *Precambrian Research*, **64**, p. 23–51, doi: 10.1016/0301-9268(93)90067-C.
- Klepeis, K.A., 2010. Relationship between uplift of the metamorphic core of the southernmost Andes and shortening in the Magallanes foreland fold and thrust belt, Tierra del Fuego, Chile: *Tectonics*, **13**, p. 882–904, doi: 10.1029/94TC00628.
- Klepeis, K.A., 1993. Structural studies of deformation along convergent and transform plate boundaries in the western Scotia Arc.:
- Klepeis, K.A., 1994. The Magallanes and Deseado fault zones: Major segments of the South American-Scotia transform plate boundary in southernmost South America, Tierra del Fuego: *Journal of Geophysical Research: Solid Earth*, **99**, p. 22001–22014, doi: <https://doi.org/10.1029/94JB01749>.
- Klepeis, K.A. and Austin, J.A., 1997. Contrasting styles of superposed deformation in the southernmost Andes: *Tectonics*, **16**, p. 755–776, doi: <https://doi.org/10.1029/97TC01611>.
- Klinger, Y., Xu, X., Tapponnier, P., Van der Woerd, J., Lasserre, C. and King, G., 2005. High-resolution satellite imagery mapping of the surface rupture and slip distribution of the $M_w \sim 7.8$, 14 November 2001 Kokoxili earthquake, Kunlun fault, northern Tibet, China: *Bulletin of the Seismological Society of America*, **95**, p. 1970–1987, doi: 10.1785/0120040233.
- Koch, A., Brierley, C., Maslin, M.M. and Lewis, S.L., 2019. Earth system impacts of the European arrival and Great Dying in the Americas after 1492: *Quaternary Science Reviews*, **207**, p. 13–36, doi: <https://doi.org/10.1016/j.quascirev.2018.12.004>.
- Koppes, M., Hallet, B. and Anderson, J., 2009. Synchronous acceleration of ice loss and glacial erosion, Glaciar Marinelli, Chilean Tierra del Fuego: *Journal of Glaciology*, **55**, p. 207–220, doi: 10.3189/002214309788608796.
- Korschinek, G., Bergmaier, A., Faestermann, T., Gerstmann, U.C., Knie, K., Rugel, G., Wallner, A., Dillmann, I., Dollinger, G., von Gostomski, Ch.L., Kossert, K., Maiti, M., Poutivtsev, M. and Remmert, A., 2010. A new value for the half-life of ^{10}Be by Heavy-Ion Elastic Recoil Detection and liquid scintillation counting: *Nuclear Instruments and Methods in Physics Research Section B: Beam Interactions with Materials and Atoms*, **268**, p. 187–191, doi: 10.1016/j.nimb.2009.09.020.

-
- Koto, B., 1893. On the cause of the great earthquake in central Japan: *J. Coll. of Sci. Imp. Univ. Tokyo*, **5**, p. 295–353.
- Kreemer, C., Hammond, W.C. and Blewitt, G., 2018. A robust estimation of the 3-D intraplate deformation of the North American plate from GPS: *Journal of Geophysical Research: Solid Earth*, **123**, p. 4388–4412, doi: <https://doi.org/10.1029/2017JB015257>.
- Kujansuur, R., 1964. Nuorista siirroksista Lapissa. Summary: Recent faults in Lapland.: , p. 3,36.
- Kukkonen, I., T., Olesen, O., Ask, M.V.S. and PFDP working group, 2010. Postglacial faults in Fennoscandia: targets for scientific drilling: *GFF*, **Vol. 132 (Pt. 1, March)**, p. pp 71-81, doi: <https://doi.org/10.1080/11035891003692934>.

L

- La Prensa Austral, 1949. Violentísimo movimiento sísmico puso en alarma a la población faltando cinco minutos para las tres de la madrugada de hoy.:
- Lacroix, P., Berthier, E. and Taipei, E., 2020. Seismic reactivation of landslides in the Colca valley, Peru, detected using Pleiades images, *Remote Sensing of Environment*, In review.:
- Lagabrielle, Y., Goddérís, Y., Donnadiou, Y., Malavieille, J. and Suarez, M., 2009. The tectonic history of Drake Passage and its possible impacts on global climate: *Earth and Planetary Science Letters*, **279**, p. 197–211, doi: 10.1016/j.epsl.2008.12.037.
- Lagerbäck, R. and Sundh, M., 2008. *Early Holocene faulting and paleoseismicity in northern Sweden*: Geological Survey of Sweden, Sveriges geologiska undersökning, Print: Alfa Print AB, Solna.
- Lagerlund, E., 1977. Till studies and neotectonics in northwest Skiine, south Sweden: *Boreas*, **6**, p. 159–166, doi: <https://doi.org/10.1111/j.1502-3885.1977.tb00344.x>.
- Lal, D., 1991. Cosmic ray labeling of erosion surfaces: in situ nuclide production rates and erosion models: *Earth and Planetary Science Letters*, **104**, p. 424–439, doi: 10.1016/0012-821X(91)90220-C.
- Lal, D., 1988. In situ-produced cosmogenic isotopes in terrestrial rocks: *Annual Review of Earth and Planetary Sciences*, **16**, p. 355–388, doi: 10.1146/annurev.ea.16.050188.002035.
- Lambeck, K., Smither, C. and Johnston, P., 1998. Sea-level change, glacial rebound and mantle viscosity for northern Europe: *Geophysical Journal International*, **134**, p. 102–144, doi: <https://doi.org/10.1046/j.1365-246x.1998.00541.x>.
- Lange, H., Casassa, G., Ivins, E.R., Schröder, L., Fritsche, M., Richter, A., Groh, A. and Dietrich, R., 2014. Observed crustal uplift near the Southern Patagonian Icefield

- constrains improved viscoelastic Earth models: *Geophysical Research Letters*, **41**, p. 805–812, doi: 10.1002/2013GL058419.
- Laugenie, C., 1984. Le dernier cycle glaciaire quaternaire et la construction des nappes fluviales d'avant-pays dans les Andes chiliennes: *Bulletin de l'Association française pour l'étude du quaternaire*, **21**, p. 139–145, doi: <https://doi.org/10.3406/quate.1984.1502>.
- Le Dortz, K., Meyer, B., Sébrier, M., Braucher, R., Bourlès, D., Benedetti, L., Nazari, H. and Foroutan, M., 2012. Interpreting scattered in-situ produced cosmogenic nuclide depth-profile data: *Quaternary Geochronology*, **11**, p. 98–115, doi: 10.1016/j.quageo.2012.02.020.
- Legoupil, D., 2011. Guanaco hunting among the Selk'nam of Tierra del Fuego: poor traceability of temporary halt and versatility of the kill site: *P@ lethnology*, **3**, p. 21–40.
- Legoupil, D., 2009. GUANACO HUNTING AMONG THE SELK'NAM OF TIERRA DEL FUEGO: Current Archaeological Approaches: *LABORATOIRE TRAVAUX ET RECHERCHES ARCHÉOLOGIQUES SUR LES CULTURES, LES ESPACES ET LES SOCIÉTÉS*, p. 22.
- Libby, W.F., 1955. Radiocarbon dating: *University of Chicago Press*, p. 175p.
- Lindblom, E., Lund, B., Tryggvason, A., Uski, M., Böldvarsson, R., Juhlin, C. and Roberts, R., 2015. Microearthquakes illuminate the deep structure of the endglacial Pärvie fault, northern Sweden: *Geophysical Journal International*, **201**, p. 1704–1716, doi: <https://doi.org/10.1093/gji/ggv112>.
- Livermore, R., Hillenbrand, C.-D., Meredith, M. and Eagles, G., 2007. Drake Passage and Cenozoic climate: An open and shut case? *Geochemistry, Geophysics, Geosystems*, **8**, doi: 10.1029/2005GC001224.
- Livermore, R., Nankivell, A., Eagles, G. and Morris, P., 2005. Paleogene opening of Drake Passage: *Earth and Planetary Science Letters*, **236**, p. 459–470, doi: 10.1016/j.epsl.2005.03.027.
- Lodolo, E., Menichetti, M., Bartole, R., Ben-Avraham, Z., Tassone, A. and Lippai, H., 2003. Magallanes-Fagnano continental transform fault (Tierra del Fuego, southernmost South America): *Tectonics*, **22**, p. 15–26, doi: <https://doi.org/10.1029/2003TC001500>.
- Lomnitz, C., 1970. Major earthquakes and tsunamis in Chile during the period 1535 to 1955: *Geologische Rundschau*, **59**, p. 938–960, doi: <https://doi.org/10.1007/BF02042278>.
- Lopez Saez, J. and Corona, C., 2015. La dendrogéomorphologie : Principes, Méthodes, Applications: , p. 53, doi: DOI: 10.13140/RG.2.1.2923.0560.
- Lothrop, S.K., 1928. The Indians of Tierra del Fuego. An Account of the Ona, Yahgan, Alacaluf and Haush Natives of the Fuegian Archipelago: *New York*,, doi: <https://doi.org/10.5479/sil.472342.39088016090599>.

Lowell, T.V., Heusser, C.J., Andersen, B.G., Moreno, P.I., Hauser, A., Heusser, L.E., Schlüchter, C., Marchant, D.R. and Denton, G.H., 1995. Interhemispheric Correlation of Late Pleistocene Glacial Events: *Science*, **269**, p. 1541–1549, doi: 10.1126/science.269.5230.1541.

Lozano, J.G., Tassone, A., Bran, D.M., Lodolo, E., Menichetti, M., Cerredo, M.E., Esteban, F., Ormazabal, J.P., Ísola, J. and Baradello, L., 2018. Glacial-related morphology and sedimentary setting of a high-latitude lacustrine basin: The Lago Chepelmut (Tierra del Fuego, Argentina): *Journal of South American Earth Sciences*, **86**, p. 259–270, doi: <https://doi.org/10.1016/j.jsames.2018.06.020>.

Lundqvist, J. and Lagerbäck, R., 1976. The Pärve Fault: a late-glacial fault in the Precambrian of Swedish Lapland: *Geologiska Föreningen i Stockholm Förhandlingar*, **98**, p. 45–51, doi: <https://doi.org/10.1080/11035897609454337>.

M

Madden, C., Haddad, D.E., Salisbury, J.B., Zielke, O., Arrowsmith, J.R., Weldon, R.J. and Colunga, J., 2013. Appendix R: Compilation of slip in the last event data and analysis of last event, repeated slip, and average displacement for recent and prehistoric ruptures: *US Geological Survey Open-File Report*, **1165**, p. 65.

Malehmir, A., Andersson, M., Mehta, S., Brodic, B., Munier, R., Place, J., Maries, G., Smith, C., Kamm, J. and Bastani, M., 2016. Post-glacial reactivation of the Bollnas fault, central Sweden: a multidisciplinary geophysical investigation: *Solid Earth*, **7**, p. 509–527, doi: <https://doi.org/10.5194/se-7-509-2016>.

Malumián, N., 1999. La sedimentación en la Patagonia extraandina. In ‘La sedimentación y el volcanismo terciarios en la Patagonia extraandina’. Instituto de Geología y Recursos Minerales: *Geol Argent An SEGEMAR*, **29**, p. 557–612.

Malumián, N. and Caramés, 1997. Upper Campanian-Paleogene from the Río Turbio coal measures in southern Argentina: micropaleontology and the Paleocene/Eocene boundary: *Journal of South American Earth Sciences*, **10**, p. 189–201, doi: 10.1016/S0895-9811(97)00015-1.

Malumián, N., Panza, J.L.A. and Parisi, C., 2000. Hoja Geológica 5172-III Yacimiento Río Turbio:

Mann, P., Hempton, M.R., Bradley, D.C. and Burke, K., 1983. Development of Pull-Apart Basins: *The Journal of Geology*, **91**, p. 529–554, doi: <https://doi.org/10.1086/628803>.

Margold, M., Stokes, C.R. and Clark, C.D., 2018. Reconciling records of ice streaming and ice margin retreat to produce a palaeogeographic reconstruction of the deglaciation of the Laurentide Ice Sheet: *Quaternary Science Reviews*, **189**, p. 1–30, doi: 10.1016/j.quascirev.2018.03.013.

- Martinic, Mateo.B., 1988. El gran temblor de tierra de 1879 en la Patagonia Austral.: *Revista Patagónica*, p. 30–31.
- Martinic, Mateo.B., 2008. Registro Historico de Antecedentes Volcanicos y Sismicos en la Patagonia Austral y la Tierra del Fuego: *Magallania, Punta Arenas*, vol.36, n.2, p. pp.5-18, doi: <https://doi.org/10.4067/S0718-22442008000200001>.
- Massone, M., 1988. Artefactos óseos del yacimiento arqueológico Tres Arroyos (Tierra del Fuego). In: *Anales del Instituto de la Patagonia*.
- Massone, M.M., 2004. *Los cazadores después del hielo*: Museo de Historia Natural.
- Massone, M., 1987. Los cazadores paleoindios de Tres Arroyos (Tierra del Fuego). In: *Anales del Instituto de la Patagonia*.
- Matsuda, T., Ota, Y., Ando, M. and Yonekura, N., 1978. Fault mechanism and recurrence time of major earthquakes in southern Kanto district, Japan, as deduced from coastal terrace data: *GSA Bulletin*, **89**, p. 1610–1618, doi: 10.1130/0016-7606(1978)89<1610:FMARTO>2.0.CO;2.
- Matthew, G.F., 1894. *Movements of the Earth's Crust at St. John, NB: In Post-glacial Times*:
- McCalpin, J.P., 1996. Chapter 1 Introduction to paleoseismology: *International Geophysics*, **62**, p. 1–32, doi: [https://doi.org/10.1016/S0074-6142\(96\)80068-4](https://doi.org/10.1016/S0074-6142(96)80068-4).
- McCalpin, J.P., 2009. *Paleoseismology*: International Geophysics SERIES.
- McCalpin, J., 2002. *Post-Bonneville paleoearthquake chronology of the Salt Lake City segment, Wasatch fault zone, from the 1999" Megatrench" site*: Utah Geological Survey.
- McCalpin, J. and Forman, S.L., 2002. *Post-Provo paleoearthquake chronology of the Brigham City segment, Wasatch fault zone, Utah*: Utah Geological Survey.
- McCalpin, J.P. and Nishenko, S.P., 1996. Holocene paleoseismicity, temporal clustering, and probabilities of future large ($M > 7$) earthquakes on the Wasatch fault zone, Utah: *Journal of Geophysical Research: Solid Earth*, **101**, p. 6233–6253, doi: [https://doi.org/10.1016/S0074-6142\(96\)80068-4](https://doi.org/10.1016/S0074-6142(96)80068-4).
- McClay, K. and Bonora, M., 2001. Analog models of restraining stepovers in strike-slip fault systems: *AAPG bulletin*, **85**, p. 233–260, doi: <https://doi.org/10.1306/8626C7AD-173B-11D7-8645000102C1865D>.
- Mcculloch, R.D. and Bentley, M.J., 1998. Late glacial ice advances in the Strait of Magellan, southern Chile: *Quaternary Science Reviews*, **17**, p. 775–787, doi: 10.1016/S0277-3791(97)00074-7.
- McCulloch, R.D., Fogwill, C.J., Sugden, D.E., Bentley, M.J. and Kubik, P.W., 2005. Chronology of the last glaciation in central Strait of Magellan and Bahía Inútil, southernmost South America: *Geografiska Annaler: Series A, Physical Geography*, **87**, p. 289–312, doi: <https://doi.org/10.1111/j.0435-3676.2005.00260.x>.

-
- McGill, S.F. and Sieh, K., 1991. Surficial offsets on the central and eastern Garlock fault associated with prehistoric earthquakes: *Journal of Geophysical Research: Solid Earth*, **96**, p. 21597–21621, doi: 0148-0227/91/91JB-02030505.00.
- Meglioli, A., 1993. Glacial geology and chronology of southernmost Patagonia and Tierra del Fuego, Argentina and Chile.: , p. 1.
- Meigs, A. and Sauber, J., 2000. Southern Alaska as an example of the long-term consequences of mountain building under the influence of glaciers: *Quaternary Science Reviews*, **19**, p. 1543–1562, doi: doi:10.1016/s0277-3791(00)00077-9.
- Meisling, K.E. and Sieh, K.E., 1980. Disturbance of trees by the 1857 Fort Tejon earthquake, California: *Journal of Geophysical Research: Solid Earth*, **85**, p. 3225–3238, doi: <https://doi.org/10.1029/JB085iB06p03225>.
- Mendoza, L., Perdomo, R., Hormaechea, J.L., Cogliano, D.D., Fritsche, M., Richter, A. and Dietrich, R., 2011. Present-day crustal deformation along the Magallanes–Fagnano Fault System in Tierra del Fuego from repeated GPS observations: *Geophysical Journal International*, **184**, p. 1009–1022, doi: 10.1111/j.1365-246X.2010.04912.x.
- Mendoza, L., Richter, A., Fritsche, M., Hormaechea, J.L., Perdomo, R. and Dietrich, R., 2015. Block modeling of crustal deformation in Tierra del Fuego from GNSS velocities: *Tectonophysics*, **651–652**, p. 58–65, doi: 10.1016/j.tecto.2015.03.013.
- Mendoza, L., Richter, A., Hormaechea, J.L., Perdomo, R., Cogliano, D.D., Dietrich, R. and Fritsche, M., 2010. Do crustal deformations observed by GPS in Tierra del Fuego (Argentina) reflect glacial-isostatic adjustment? *The Cryosphere Discuss*, **4**, doi: 10.5194/tcd-4-1635-2010.
- Menichetti, M., Lodolo, E. and Tassone, A., 2008. Structural geology of the Fuegian Andes and Magallanes fold-and-thrust belt - Tierra del Fuego Island: *Geologica Acta*, **6**, p. 19–42, doi: 10.1344/104.000000239.
- Menounos, B., Clague, J.J., Osborn, G., Davis, P.T., Ponce, F., Goehring, B., Maurer, M., Rabassa, J., Coronato, A. and Marr, R., 2013. Latest Pleistocene and Holocene glacier fluctuations in southernmost Tierra del Fuego, Argentina: *Quaternary Science Reviews*, **77**, p. 70–79, doi: 10.1016/j.quascirev.2013.07.008.
- Menzies, J., 1996. Past Glacial Environments: Sediments, Forms, And Techniques: *John Menzies*, **2**, p. 595.
- Mercer, J.P., 1983. Cenozoic glaciation in the Southern Hemisphere: *annual Review of Earth and Planetary Sciences*,, p. 99–132, doi: <https://doi.org/10.1146/annurev.earth.11.050183.000531>.
- Mercer, J., 1976. Glacial history of southernmost South America: *Quarter. Res.*, **6**, p. 125–166, doi: [https://doi.org/10.1016/0033-5894\(76\)90047-8](https://doi.org/10.1016/0033-5894(76)90047-8).
- Miotti, L. and Salemme, M., 2004. Poblamiento, movilidad y territorios entre las sociedades cazadoras-recolectoras de Patagonia: *Complutum*, **15**, p. 177–206, doi: [https://doi.org/10.1016/S1571-0866\(07\)10022-1](https://doi.org/10.1016/S1571-0866(07)10022-1).

-
- Montessus de Ballore, F., 1912. Geografía sísmica de Chile.: *Revista Chilena de Historia y Geografía*, **7**, p. 178–195.
- Mörner, N.-A., 1978. Faulting, fracturing, and seismicity as functions of glacio-isostasy in Fennoscandia: *Geology*, **6**, p. 41–45, doi: 10.1130/0091-7613(1978)6<41:FFASAF>2.0.CO;2).
- Mörner, N.-A., 1972. Isostasy, eustasy and crustal sensitivity: *Tellus*, **24**, p. 586–592, doi: <https://doi.org/10.3402/tellusa.v24i6.10687>.
- Mörner, N.-A., 1979. The Fennoscandian Uplift and Late Cenozoic Geodynamics: Geological Evidence: *GeoJournal*, **3**, p. 287–318.
- Mörner, N.-A., 1969. The Late Quaternary history of the Kattegatt Sea and the Swedish West Coast: deglaciation, shorelevel displacement, chronology, isostasy and eustasy [PhD Thesis].
- Mörner, N.-A., 2014. Varve chronology: *Geochronology: Methods and Case Studies*, p. 73–87, doi: <https://doi.org/10.5772/58630>.
- Mpodozis, C., Mella, P. and Pavda, D., 2011. Estratigrafía y megasecuencias sedimentarias en la cuenca Austral-Magallanes, Argentina y Chile. In: *VIII Congreso de Exploración y Desarrollo de Hidrocarburos*.
- Muir-Wood, R., 2000. Deglaciation seismotectonics: a principal influence on intraplate seismogenesis at high latitudes: *Quaternary Science Reviews*, **19**, p. 1399–1411, doi: [https://doi.org/10.1016/S0277-3791\(00\)00069-X](https://doi.org/10.1016/S0277-3791(00)00069-X).
- Muir-Wood, R., 1989. Extraordinary deglaciation reverse faulting in northern Fennoscandia: *Earthquakes at North-Atlantic passive margins: neotectonics and postglacial rebound*, p. 141–173, doi: https://doi.org/10.1007/978-94-009-2311-9_10.

N

- Nishiizumi, K., Imamura, M., Caffee, M.W., Southon, J.R., Finkel, R.C. and McAninch, J., 2007. Absolute calibration of ¹⁰Be AMS standards: *Nuclear Instruments and Methods in Physics Research Section B: Beam Interactions with Materials and Atoms*, **258**, p. 403–413, doi: 10.1016/j.nimb.2007.01.297.
- Nishiizumi, K., Winterer, E.L., Kohl, C.P., Klein, J., Middleton, R., Lal, D. and Arnold, J.R., 1989. Cosmic Ray Production Rate of ¹⁰Be and ²⁶Ar in quartz from glacially polished rocks: *Journal of Geophysical Research*, **94**, p. 17, 907–17,915, doi: <https://doi.org/10.1029/JB094iB12p17907>.
- Nissen, E., Walker, R.T., Bayasgalan, A., Carter, A., Fattahi, M., Molor, E., Schnabel, C., West, A.J. and Xu, S., 2009. The late Quaternary slip-rate of the Har-Us-Nuur fault (Mongolian Altai) from cosmogenic ¹⁰Be and luminescence dating: *Earth and Planetary Science Letters*, **286**, p. 467–478, doi: 10.1016/j.epsl.2009.06.048.

O

- Obermeier, S.F., 1996. Use of liquefaction-induced features for paleoseismic analysis—an overview of how seismic liquefaction features can be distinguished from other features and how their regional distribution and properties of source sediment can be used to infer the location and strength of Holocene paleo-earthquakes: *Engineering Geology*, **44**, p. 1–76, doi: [https://doi.org/10.1016/S0013-7952\(96\)00040-3](https://doi.org/10.1016/S0013-7952(96)00040-3).
- Ojala, A.E., Mattila, J., Ruskeeniemi, T., Markovaara-Koivisto, M., Palmu, J.-P., Nordbäck, N., Lindberg, A., Aaltonen, I., Savunen, J. and Sutinen, R., 2019. *Postglacial Faults in Finland—a Review of PGSDyn–project Results*: Posiva Oy, Eurajoki, Finland.
- Olivero, E. and Malumián, N., 2008. Mesozoic-Cenozoic stratigraphy of the Fuegian Andes, Argentina: *Geologica Acta*, **6**, p. 5–18.
- Onorato, M.R., 2018. Influencia de la neotectónica y la glaciectónica en geoformas y depósitos sedimentarios glaciogénicos: Herramientas para el estudio y análisis de los procesos glaciectónicos y la paleosismicidad en la Isla Grande de Tierra del Fuego:
- Onorato, M.R., Coronato, A., Perucca, L., Rabassa, J. and López, R., 2017. Morpho-bathymetry and surficial morphology of Udaeta Lake, along the Magallanes-Fagnano fault system, Tierra del Fuego, Argentina: *Journal of South American Earth Sciences*, **76**, doi: <https://doi.org/10.1016/j.jsames.2017.02.001>.
- Onorato, M.R., Perucca, L., Coronato, A., Rabassa, J. and López, R., 2016. Seismically-induced soft-sediment deformation structures associated with the Magallanes–Fagnano Fault System (Isla Grande de Tierra del Fuego, Argentina): *Sedimentary Geology*, **344**, p. 135–144, doi: <https://doi.org/10.1016/j.sedgeo.2016.04.010>.
- Onorato, M.R., Perucca, L.P., López, R. and Blanc, P., 2020. EVIDENCIAS MORFOTECTÓNICAS EN EL SISTEMA DE FALLAS MAGALLANES-FAGNANO, BORDE TRANSFORMANTE ENTRE LAS PLACAS SUDAMERICANA Y SCOTIA, ISLA GRANDE DE TIERRA DEL FUEGO, ARGENTINA: *Revista de la Asociación Geológica Argentina*, **77**.
- O’Sullivan, P.E., 1983. Annually-laminated lake sediments and the study of Quaternary environmental changes — a review: *Quaternary Science Reviews*, **1**, p. 245–313, doi: 10.1016/0277-3791(83)90008-2.

P

- Page, R., 1970. Dating episodes of faulting from tree rings: effects of the 1958 rupture of the Fair-weather fault on tree growth.: *Dating episodes of faulting from tree rings: effects of the 1958 rupture of the Fair-weather fault on tree growth.*, **81**, p. 3085–94, doi: [https://doi.org/10.1130/0016-7606\(1970\)81\[3085:DEOFFT\]2.0.CO;2](https://doi.org/10.1130/0016-7606(1970)81[3085:DEOFFT]2.0.CO;2).

-
- Palacios R, A., 2013. NOTAS HISTÓRICAS DEL PRIMER SISMO REGISTRADO EN LA CIUDAD DE PUNTA ARENAS Y EN LA REGIÓN DE MAGALLANES EN FEBRERO DE 1879: *Magallania (Punta Arenas)*, **41**, p. 215–220, doi: <https://doi.org/10.4067/S0718-22442013000200012>.
- Palmu, J.-P., Ojala, A.E., Ruskeeniemi, T., Sutinen, R. and Mattila, J., 2015. LiDAR DEM detection and classification of postglacial faults and seismically-induced landforms in Finland: a paleoseismic database: *GFF*, **137**, p. 344–352, doi: <https://doi.org/10.1080/11035897.2015.1068370>.
- Pankhurst, R.J., 2000. Episodic Silicic Volcanism in Patagonia and the Antarctic Peninsula: Chronology of Magmatism Associated with the Break-up of Gondwana: *Journal of Petrology*, **41**, p. 605–625, doi: 10.1093/petrology/41.5.605.
- Patton, H., Hubbard, A., Andreassen, K., Auriac, A., Whitehouse, P.L., Stroeven, A.P., Shackleton, C., Winsborrow, M., Heyman, J. and Hall, A.M., 2017. Deglaciation of the Eurasian ice sheet complex: *Quaternary Science Reviews*, **169**, p. 148–172, doi: 10.1016/j.quascirev.2017.05.019.
- Patton, H., Hubbard, A., Andreassen, K., Winsborrow, M. and Stroeven, A.P., 2016. The build-up, configuration, and dynamical sensitivity of the Eurasian ice-sheet complex to Late Weichselian climatic and oceanic forcing: *Quaternary Science Reviews*, **153**, p. 97–121, doi: <https://doi.org/10.1016/j.quascirev.2016.10.009>.
- Pedreira, A., Galindo-Zaldívar, J., Ruiz-Constán, A., Bohoyo, F., Torres-Carbonell, P., Ruano, P., Maestro, A. and González-Castillo, L., 2014. The last major earthquakes along the Magallanes–Fagnano fault system recorded by disturbed trees (Tierra del Fuego, South America): *Terra Nova*, **26**, p. 448–453, doi: <https://doi.org/10.1111/ter.12119>.
- Pelayo, A.M. and Wiens, D.A., 1989. Seismotectonics and relative plate motions in the Scotia Sea region: *Journal of Geophysical Research: Solid Earth*, **94**, p. 7293–7320, doi: 0148-0227/89 / 88JB-04217505.00.
- Peltier, W.R., 2004. Global Glacial Isostasy and the Surface of the Ice-Age Earth: The ICE-5G (VM2) Model and GRACE: *Annual Review of Earth and Planetary Sciences*, **32**, p. 111–149, doi: 10.1146/annurev.earth.32.082503.144359.
- Peltier, C., Kaplan, M.R., Schaefer, J.M., Soteres, R., Sagredo, E.A. and Aravena, J.C., 2016. A glacial chronology of the strait of magellan. In: *Proceedings AGU Fall Meeting Abstracts*.
- Peñaloza, F., 2015. Transpacific Discourses of Primitivism and Extinction on “Fuegians” and “Tasmanians” in the Nineteenth and Twentieth Centuries. In: *Transpacific Americas : Encounters and Engagements Between the Americas and the South Pacific* Routledge studies in anthropology, Taylor & Francis Group, p. 115–135.
- Perucca, L., Alvarado, P. and Saez, M., 2016. Neotectonics and seismicity in southern Patagonia: *Geological Journal*, **51**, p. 545–559, doi: [https://doi.org/10.1016/S1571-0866\(07\)10005-1](https://doi.org/10.1016/S1571-0866(07)10005-1).

-
- Perucca, L. and Bastias, H., 2008. Neotectonics, seismology and paleoseismology: *Developments in Quaternary Sciences*, **11**, p. 73–94, doi: [https://doi.org/10.1016/S1571-0866\(07\)10005-1](https://doi.org/10.1016/S1571-0866(07)10005-1).
- Perucca, L., Pérez, A. and Navarro, C., 2006. Fenómenos de licuefacción asociados a terremotos históricos. Su análisis en la evaluación del peligro sísmico en la Argentina: *Revista de la Asociación Geológica Argentina*, **61**, p. 567–578.
- Philip, H. and Meghraoui, M., 1983. Structural analysis and interpretation of the surface deformations of the El Asnam Earthquake of October 10, 1980: *Tectonics*, **2**, p. 17–49, doi: 10.1029/TC002i001p00017.
- Poblete, F., Roperch, P., Arriagada, C., Ruffet, G., Ramírez de Arellano, C., Hervé, F. and Poujol, M., 2016. Late Cretaceous–early Eocene counterclockwise rotation of the Fuegian Andes and evolution of the Patagonia–Antarctic Peninsula system: *Tectonophysics*, **668–669**, p. 15–34, doi: 10.1016/j.tecto.2015.11.025.
- Poblete, F., Roperch, P., Hervé, F., Diraison, M., Espinoza, M. and Arriagada, C., 2014. The curved Magallanes fold and thrust belt: Tectonic insights from a paleomagnetic and anisotropy of magnetic susceptibility study: *Tectonics*, **33**, p. 2526–2551, doi: 10.1002/2014TC003555.
- Poli, D., Remondino, F., Angiuli, E. and Agugiaro, G., 2015. Radiometric and geometric evaluation of GeoEye-1, WorldView-2 and Pléiades-1A stereo images for 3D information extraction: *ISPRS Journal of Photogrammetry and Remote Sensing*, **100**, p. 35–47, doi: 10.1016/j.isprsjprs.2014.04.007.
- Poliakov, A.N.B., Cundall, P.A., Podladchikov, Y.Y. and Lyakhovsky, V.A., 1993. An explicit inertial method for the simulation of viscoelastic flow: an evaluation of elastic effects on diapiric flow in two-and three-layers models: *Flow and Creep in the Solar System: observations, modeling and Theory*, p. 175–195, doi: https://doi.org/10.1007/978-94-015-8206-3_12.
- Porter, S.C., 2020. Character and ages of Pleistocene drifts in a transect across the Strait of Magellan: *Quaternary of South America and Antarctic Peninsula*, p. 35–49, doi: <https://doi.org/10.1201/9781003079361-2>.
- Puntieri, J., Raffaele, E., Martinez, P., Barthélémy, D. and Brion, C., 1999. Morphological and architectural features of young *Nothofagus pumilio* (Poepp. & Endl.) Krasser (Fagaceae): *Botanical Journal of the Linnean Society*, **130**, p. 395–410, doi: 10.1111/j.1095-8339.1999.tb00529.x.
- Puntieri, J.G., Souza, M.S., Brion, C., Mazzini, C. and Barthélémy, D., 2003. Axis Differentiation in Two South American *Nothofagus* Species (Nothofagaceae): *Annals of Botany*, **92**, p. 589–599, doi: 10.1093/aob/mcg175.

R

- Rabassa, J., 2011. The Late Cenozoic of Patagonia and Tierra del Fuego: , p. 523, doi: <https://doi.org/10.1111/j.1095-8312.2011.01681.x>.
- Rabassa, J. and Clapperton, C.M., 1990. Quaternary glaciations of the southern Andes: *Quaternary Science Reviews*, **9**, p. 153–174, doi: 10.1016/0277-3791(90)90016-4.
- Rabassa, J., Coronato, A., Bujalesky, G., Salemme, M., Roig, C., Meglioli, A., Heusser, C., Gordillo, S., Roig, F., Borrromei, A. and Quattrocchio, M., 2000. Quaternary of Tierra del Fuego, Southernmost South America: an updated review: *Quaternary International*, **68–71**, p. 217–240, doi: 10.1016/S1040-6182(00)00046-X.
- Rabassa, J., Coronato, A. and Martínez, O., 2011. Late Cenozoic glaciations in Patagonia and Tierra del Fuego: an updated review: *Biological Journal of the Linnean Society*, **103**, p. 316–335, doi: 10.1111/j.1095-8312.2011.01681.x.
- Rabinowitz, P.D. and LaBrecque, J., 1979. The Mesozoic South Atlantic Ocean and evolution of its continental margins: *Journal of Geophysical Research: Solid Earth*, **84**, p. 5973–6002, doi: 10.1029/JB084iB11p05973.
- Raff, J.A. and Bolnick, D.A., 2014. Palaeogenomics: genetic roots of the first Americans: *Nature*, **506**, p. 162–163, doi: <https://doi.org/10.1038/506162a>.
- Ramos, V.A., 1989. Andean Foothills Structures in Northern Magallanes Basin, Argentina: *AAPG Bulletin*, **73**, p. 887–903, doi: 10.1306/44B4A28A-170A-11D7-8645000102C1865D.
- Ramsey, C.B., 2009. Bayesian analysis of radiocarbon dates: *Radiocarbon*, **51**, p. 337–360, doi: <https://doi.org/10.1017/S0033822200033865>.
- Ramsey, C.B., 2017. Methods for Summarizing Radiocarbon Datasets: *Radiocarbon*, **59**, p. 1809–1833, doi: <https://doi.org/10.1017/RDC.2017.108>.
- Reguzzoni, M., Sampietro, D. and Sansò, F., 2013. Global Moho from the combination of the CRUST2.0 model and GOCE data: *Geophysical Journal International*, **195**, p. 222–237, doi: 10.1093/gji/ggt247.
- Richter, A., Groh, A., Horwath, M., Ivins, E., Marderwald, E., Hormaechea, J.L., Perdomo, R. and Dietrich, R., 2019. The Rapid and Steady Mass Loss of the Patagonian Icefields throughout the GRACE Era: 2002–2017: *Remote Sensing*, **11**, p. 909, doi: 10.3390/rs11080909.
- Richter, A., Ivins, E., Lange, H., Mendoza, L., Schröder, L., Hormaechea, J.L., Casassa, G., Marderwald, E., Fritsche, M. and Perdomo, R., 2016. Crustal deformation across the Southern Patagonian Icefield observed by GNSS: *Earth and Planetary Science Letters*, **452**, p. 206–215, doi: <https://doi.org/10.1016/j.epsl.2016.07.042>.

- Ritz, J.F., Brown, E.T., Bourlès, D.L., Philip, H., Schlupp, A., Raisbeck, G.M., Yiou, F. and Enkhtuvshin, B., 1995. Slip rates along active faults estimated with cosmic-ray-exposure dates: Application to the Bogd fault, Gobi-Altai, Mongolia: *Geology*, **23**, p. 1019–1022, doi: 10.1130/0091-7613(1995)023<1019:SRAAFE>2.3.CO;2.
- Ritz, J.-F., Vassallo, R., Braucher, R., Brown, E.T., Carretier, S. and Bourlès, D.L., 2006. Using in situ-produced ^{10}Be to quantify active tectonics in the Gurvan Bogd mountain range (Gobi-Altay, Mongolia): *SPECIAL PAPERS-GEOLOGICAL SOCIETY OF AMERICA*, **415**, p. 87–110, doi: 10.1130/2006.2415(06).
- Rojas, L. and Mpodozis, C., 2006. Geología estructural de la Faja Plegada y Corrida del sector chileno de Tierra del Fuego, Andes patagónicos australes. In: *Congreso Geológico Chileno, No. 11: Actas* p. 325–358.
- Roy, S., Vassallo, R., Martinod, J., Ghiglione, M.C., Sue, C. and Allemand, P., 2020. Co-seismic deformation and post-glacial slip rate along the Magallanes-Fagnano fault, Tierra Del Fuego, Argentina: *Terra Nova*, **32**, p. 1–10, doi: <https://doi.org/10.1111/ter.12430>.

S

- Salemme, M.C. and Miotti, L.L., 2008. Archeological hunter-gatherer landscapes since the latest Pleistocene in Fuego-Patagonia: *Developments in Quaternary Sciences*, **11**, p. 437–483, doi: [https://doi.org/10.1016/S1571-0866\(07\)10022-1](https://doi.org/10.1016/S1571-0866(07)10022-1).
- Salisbury, J., Rockwell, T.K., Middleton, T.J. and Kenneth, H., 2012. LiDAR and field observations of slip distribution for the most recent surface ruptures along the central San Jacinto fault: *Bulletin of the Seismological Society of America*, **102**, p. 598619, doi: 10.1785/0120110068.
- Sandoval, F.B. and De Pascale, G.P., 2020. Slip rates along the narrow Magallanes fault System, tierra Del fuego Region, patagonia: *Scientific reports*, **10**, p. 1–13, doi: <https://doi.org/10.1038/s41598-020-64750-6>.
- Sandwell, D.T. and Smith, W.H., 1997. Marine gravity anomaly from Geosat and ERS 1 satellite altimetry: *Journal of Geophysical Research: Solid Earth*, **102**, p. 10039–10054, doi: 0148-0227/97/96JB-03223\$09.00.
- Sauber, J.M. and Molnia, B.F., 2004. Glacier ice mass fluctuations and fault instability in tectonically active Southern Alaska: *Global and Planetary Change*, **42**, p. 279–293, doi: 10.1016/j.gloplacha.2003.11.012.
- Sauber, J., Plafker, G., Molnia, B.F. and Bryant, M.A., 2000. Crustal deformation associated with glacial fluctuations in the eastern Chugach Mountains, Alaska: *Journal of Geophysical Research: Solid Earth*, **105**, p. 8055–8077, doi: <https://doi.org/10.1029/1999JB900433>.

- Scher, H.D. and Martin, E.E., 2006. Timing and Climatic Consequences of the Opening of Drake Passage: *Science*, **312**, p. 428–430, doi: 10.1126/science.1120044.
- Schmitt, K., 1991. Schmitt, K. (1991). Sandstone Intrusions in the Andina Fold-Thrust Belt (51–54 S): Implications for the paleohydrogeologic Evolution of the Southernmost Andes.: Graduate School of Arts and Science, Columbia University, 263 p.
- Scholz, C.H., 2002. The Mechanics of Earthquakes and Faulting: *The Mechanics of Earthquakes and Faulting*, by Christopher H. Scholz, pp. 496. ISBN 0521652235. Cambridge, UK: Cambridge University Press, June 2002., doi: <https://doi.org/10.1017/CBO9780511818516>.
- Schwartz, D.P. and Coppersmith, K.J., 1984. Fault behavior and characteristic earthquakes: Examples from the Wasatch and San Andreas Fault Zones: *Journal of Geophysical Research: Solid Earth*, **89**, p. 5681–5698, doi: 10.1029/JB089iB07p05681.
- SERNAGEOMIN, 2003. Mapa Geológico de Chile: versión digital. 1:1000000, Servicio Nacional de Geología y Minería, CHILE, Publicación Geológica Digital, No. 4 (CD-ROM, versión 1.0, 2003):
- Serrano, R., 1880. Diario de la excursión a la isla grande de la Tierra del Fuego durante los meses de enero y febrero de 1879: *Anuario Hidrográfico de la Marina de Chile*, **VI**, p. 151–204.
- Shean, D.E., Alexandrov, O., Moratto, Z.M., Smith, B.E., Joughin, I.R., Porter, C. and Morin, P., 2016. An automated, open-source pipeline for mass production of digital elevation models (DEMs) from very-high-resolution commercial stereo satellite imagery: *ISPRS Journal of Photogrammetry and Remote Sensing*, **116**, p. 101–117, doi: 10.1016/j.isprsjprs.2016.03.012.
- Shilts, W.W., Rappol, M. and Blais, A., 1992. Evidence of late and postglacial seismic activity in the Témiscouata–Madawaska Valley, Quebec–New Brunswick, Canada: *Canadian Journal of Earth Sciences*, **29**, p. 1043–1069, doi: <https://doi.org/10.1139/e92-085>.
- SHOA Chilean Navy, 1998. CARTA NÁUTICA BAHÍA INÚTIL A SENO ALMIRANTAZGO Y ACCESO NORTE AL CANAL MAGDALENA N°12500.:
- Shroder, J.F., 1978. Dendrogeomorphological Analysis of Mass Movement on Table Cliffs Plateau, Utah: *Quaternary Research*, **9**, p. 168–185, doi: 10.1016/0033-5894(78)90065-0.
- Shroder, J.F. and Butler, D.R., 1986. Tree-Ring Analysis in the Earth Sciences: *International Symposium on Ecological Aspect of tree-Ring Analysis*,.
- Sieh, K.E., 1981. *A review of geological evidence for recurrence times of large earthquakes*: American Geophysical Union Washington, DC.
- Simon, K.M., James, T.S., Henton, J.A. and Dyke, A.S., 2016. A glacial isostatic adjustment model for the central and northern Laurentide Ice Sheet based on relative sea level and GPS measurements: *Geophysical Journal International*, **205**, p. 1618–1636, doi: 10.1093/gji/ggw103.

-
- Simpson, J. and Chaigneau, F., 1880. Diario llevado por los tenientes Simpson y Chaigneau : En Latorre, Exploracion de las aguas de Skyring o del Despejo.: *Anuario Hidrográfico de la Marina de Chile*, **VI**, p. 73–96.
- Smalley, R., Kendrick, E., Bevis, M.G., Dalziel, I.W.D., Taylor, F., Lauría, E., Barriga, R., Casassa, G., Olivero, E. and Piana, E., 2003. Geodetic determination of relative plate motion and crustal deformation across the Scotia-South America plate boundary in eastern Tierra del Fuego: *Geochemistry, Geophysics, Geosystems*, **4**, p. 1070, doi: <https://doi.org/10.1029/2002GC000446>.
- Smith, C.A., Sundh, M. and Mikko, H., 2014. Surficial geology indicates early Holocene faulting and seismicity, central Sweden: *International Journal of Earth Sciences*, **103**, p. 1711–1724, doi: <https://doi.org/10.1007/s00531-014-1025-6>.
- Solonenko, V.P., 1973. Paleoseismogeology: *Izv. Acad. Sci. USSR, Phys. Solid Earth*, **9**, p. 3–16.
- Somoza, R. and Ghidella de Hurtis, M.E., 2005. Convergencia en el margen occidental de América del Sur durante el Cenozoico: Subducción de Nazca, Farallon y Aluk:
- Soteres, R.L., Peltier, C., Kaplan, M.R. and Sagredo, E.A., 2020. Glacial geomorphology of the Strait of Magellan ice lobe, southernmost Patagonia, South America: *Journal of Maps*, **16**, p. 299–312, doi: 10.1080/17445647.2020.1736197.
- Stanfors, R. and Ericsson, L.O., 1993. Post-glacial faulting in the Lansjärv area, Northern Sweden. Comments from the expert group on a field visit at the Molberget post-glacial fault area, 1991: Swedish Nuclear Fuel and Waste Management Co.
- Steer, P., Simoes, M., Cattin, R. and Shyu, J.B.H., 2014. Erosion influences the seismicity of active thrust faults: *Nature Communications*, **5**, p. 5564, doi: <https://doi.org/10.1038/ncomms6564>.
- Steffen, R., Eaton, D.W. and Wu, P., 2012. Moment tensors, state of stress and their relation to post-glacial rebound in northeastern Canada: *Geophysical Journal International*, **189**, p. 1741–1752, doi: 10.1111/j.1365-246X.2012.05452.x.
- Stein, S., Sleep, N.H., Geller, R.J., Wang, S.-C. and Kroeger, G.C., 1979. Earthquakes along the passive margin of eastern Canada: *Geophysical Research Letters*, **6**, p. 537–540, doi: <https://doi.org/10.1029/GL006i007p00537>.
- Stern, C.R., 2008. Holocene tephrochronology record of large explosive eruptions in the southernmost Patagonian Andes: *Bulletin of Volcanology*, **70**, p. 435–454, doi: 10.1007/s00445-007-0148-z.
- Stewart, I.S., Sauber, J. and Rose, J., 2000. Glacio-seismotectonics: ice sheets, crustal deformation and seismicity: *Quaternary Science Reviews*, **19**, p. 1367–1389, doi: [https://doi.org/10.1016/S0277-3791\(00\)00094-9](https://doi.org/10.1016/S0277-3791(00)00094-9).
- Stoffel, M., Bollschweiler, M., Butler, D.R. and Luckman, B.H., 2010. Tree Rings and Natural Hazards: A State-of-Art: , p. 486, doi: <https://doi.org/10.1007/978-90-481-8736-2>.

-
- Stokes, C.R., 2017. Deglaciation of the Laurentide Ice Sheet from the Last Glacial Maximum.: *Cuadernos de investigación geográfica.*, **43**, p. 377–428, doi: <https://doi.org/10.18172/cig.3237>.
- Stone, J.O., 2000. Air pressure and cosmogenic isotope production: *Journal of Geophysical Research: Solid Earth*, **105**, p. 23753–23759, doi: 10.1029/2000JB900181.
- Stuiver, M., 1970. Tree Ring, Varve and Carbon-14 Chronologies: *Nature*, **228**, p. 454–455, doi: 10.1038/228454a0.
- Stumpf, A., Malet, J.-P., Allemand, P. and Ulrich, P., 2014. Surface reconstruction and landslide displacement measurements with Pléiades satellite images: *ISPRS Journal of Photogrammetry and Remote Sensing*, **95**, p. 1–12, doi: 10.1016/j.isprsjprs.2014.05.008.
- Suárez, M., 1979. A Late Mesozoic island arc in the southern Andes, Chile: *Geological Magazine*, **116**, p. 181–190, doi: 10.1017/S0016756800043594.
- Suárez, M., Hervé, M. and Puig, A., 1985. Hoja Isla Hoste e islas adyacentes: 1:250000 Servicio Nacional de Geología y Minería: *Carta Geológica de Chile.*, p. 133.
- Sugden, D.E., Bentley, M.J., Fogwill, C.J., Hulton, N.R. j, Mcculloch, R.D. and Purves, R.S., 2005. Late-glacial glacier events in southernmost south america: a blend of ‘northern’ and ‘southern’ hemispheric climatic signals? *Geografiska Annaler: Series A, Physical Geography*, **87**, p. 273–288, doi: 10.1111/j.0435-3676.2005.00259.x.
- Sugden, D.E. and John, B.S., 1976. *Glaciers and landscape: a geomorphological approach*: Edward Arnold London.
- Swan, F.H., Schwartz, D.P. and Cluff, L.S., 1980. Recurrence of moderate to large magnitude earthquakes produced by surface faulting on the Wasatch fault zone, Utah: *Bulletin of the Seismological Society of America*, **70**, p. 1431–1462.

T

- Tassone, A., Lippai, H., Lodolo, E., Menichetti, M., Comba, A., Hormaechea, J.L. and Vilas, J.F., 2005. A geological and geophysical crustal section across the Magallanes–Fagnano fault in Tierra del Fuego: *Journal of South American Earth Sciences*, **19**, p. 99–109, doi: <https://doi.org/10.1016/j.jsames.2004.12.003>.
- Tassone, A., Lodolo, E., Menichetti, M., Yagupsky, D.L., Caffau, M. and Vilas, J.F.A., 2008. Seismostratigraphic and structural setting of the Malvinas Basin and its southern margin (Tierra del Fuego Atlantic offshore): *Geologica Acta*, **6**, p. 55–67.
- Thomas, C.R., 1949. Geology and Petroleum Exploration in Magallanes Province, Chile: *AAPG Bulletin*, **33**, p. 1553–1578, doi: <https://doi.org/10.1306/3D933DEE-16B1-11D7-8645000102C1865D>.

- Thomas, C., Livermore, R. and Pollitz, F., 2003. Motion of the Scotia Sea plates: *Geophysical Journal International*, **155**, p. 789–804, doi: 10.1111/j.1365-246X.2003.02069.x.
- Thomson, S.N., 2002. Late Cenozoic geomorphic and tectonic evolution of the Patagonian Andes between latitudes 42° S and 46° S: An appraisal based on fission-track results from the transpressional intra-arc Liquiñe-Ofqui fault zone: *Geological Society of America bulletin*, **114**, p. 1159–1173, doi: [https://doi.org/10.1130/0016-7606\(2002\)114<1159:LCGATE>2.0.CO;2](https://doi.org/10.1130/0016-7606(2002)114<1159:LCGATE>2.0.CO;2).
- Ton-That, T., 1997. *40Ar/39Ar dating of basaltic lava flows and the geology of the Lago Buenos Aires region, Santa Cruz Province: Argentina*: Université of Genève.
- Ton-That, T., Singer, B., Mörner, N.A. and Rabassa, J., 1999. Datación por el método 40Ar/39Ar de lavas basálticas y geología del Cenozoico Superior en la región del Lago Buenos Aires, provincia de Santa Cruz, Argentina: *Revista de la Asociación Geológica Argentina*, **54**, p. 333–352.
- Torres Carbonell, P.J., Dimieri, L.V., Olivero, E.B., Bohoyo, F. and Galindo-Zaldívar, J., 2014. Structure and tectonic evolution of the Fuegian Andes (southernmost South America) in the framework of the Scotia Arc development: *Global and Planetary Change*, **123**, p. 174–188, doi: 10.1016/j.gloplacha.2014.07.019.
- Torres-Carbonell, P.J., Olivero, E.B. and Dimieri, L.V., 2008. Control en la magnitud de desplazamiento de rumbo del Sistema Transformante Fagnano, Tierra del Fuego, Argentina: *Revista geológica de Chile*, **35**, p. 63–77, doi: <https://doi.org/10.5027/andgeoV35n1-a03>.
- Townend, J. and Zoback, M.D., 2000. How faulting keeps the crust strong: *Geology*, **28**, p. 399–402, doi: [https://doi.org/10.1130/0091-7613\(2000\)028<0399:HFKTCS>2.3.CO;2](https://doi.org/10.1130/0091-7613(2000)028<0399:HFKTCS>2.3.CO;2).
- Turcotte, D. and Schubert, G., 2014. *Geodynamics*: Cambridge university press.
- Turpeinen, H., Hampel, A., Karow, T. and Maniatis, G., 2008. Effect of ice sheet growth and melting on the slip evolution of thrust faults: *Earth and Planetary Science Letters*, **269**, p. 230–241, doi: <https://doi.org/10.1016/j.epsl.2008.02.017>.

U

- Umhoefer, P.J., Whitney, D.L., Teyssier, C., Fayon, A.K., Casale, G.C. and Heizler, M.T., 2007. Yo-yo tectonics in a wrench zone, Central Anatolian fault zone, Turkey: *Exhumation Associated with Continental Strike-Slip Fault Systems: Geological Society of America Special Paper.*, p. 35- 57, doi: [https://doi.org/10.1130/2007.2434\(03\)](https://doi.org/10.1130/2007.2434(03)).
- UNAVCO Plate Motion Calculator: 2020, software@unavco.org.
- Underwood, P., 1983. *Dynamic Relaxtion*, in " *ComputationalMethods for TransientAnalysis*", Belytschko, T., Hyghes, TJR, editors: Elsevier SciencePublishers.

V

Vassallo, R., Ritz, J.-F., Braucher, R. and Carretier, S., 2005. Dating faulted alluvial fans with cosmogenic ^{10}Be in the Gurvan Bogd mountain range (Gobi-Altay, Mongolia): climatic and tectonic implications: *Terra Nova*, **17**, p. 278–285, doi: 10.1111/j.1365-3121.2005.00612.x.

W

Walcott, R.I., 1970. Isostatic response to loading of the crust in Canada: *Canadian Journal of Earth Sciences*, **7**, p. 716–727, doi: <https://doi-org.insu.bib.cnrs.fr/10.1139/e70-070>.

Walder, J. and Hallet, B., 1979. Geometry of Former Subglacial Water Channels and Cavities: *Journal of Glaciology*, **23**, p. 335–346, doi: 10.3189/S0022143000029944.

Waldmann, N., 2008. Late Quaternary environmental changes in Lago Fagnano, Tierra del Fuego (54 S): reconstructing sedimentary processes, natural hazards and paleoclimate [Sc 4040]: University of Geneva, FACULTE DES SCIENCES, Département de géologie et de paléontologie, 154 p.

Waldmann, N., Anselmetti, F.S., Ariztegui, D., James A. Austin, J., Pirouz, M., Moy, C.M. and Dunbar, R., 2011. Holocene mass-wasting events in Lago Fagnano, Tierra del Fuego (54°S): implications for paleoseismicity of the Magallanes-Fagnano transform fault: *Basin Research*, **23**, p. 171–190, doi: <https://doi.org/10.1111/j.1365-2117.2010.00489.x>.

Waldmann, N., Ariztegui, D., Anselmetti, F.S., Coronato, A. and Austin Jr, J.A., 2010. Geophysical evidence of multiple glacier advances in Lago Fagnano (54 S), southernmost Patagonia: *Quaternary Science Reviews*, **29**, p. 1188–1200, doi: <https://doi.org/10.1016/j.quascirev.2010.01.016>.

Wallace, R.E., 1981. Active faults, paleoseismology, and earthquake hazards in the western United States: *Earthquake prediction: an international review*, **4**, p. 209–216, doi: <https://doi.org/10.1029/ME004p0209>.

Wallace, R.E., 1977. Profiles and ages of young fault scarps, northcentral Nevada: *Geol. Soc. Am. Bull.*, p. 1267–1281, doi: [https://doi.org/10.1130/0016-7606\(1977\)88<1267:PAAOYF>2.0.CO;2](https://doi.org/10.1130/0016-7606(1977)88<1267:PAAOYF>2.0.CO;2).

Wells, D.L. and Coppersmith, K.J., 1994. New empirical relationships among magnitude, rupture length, rupture width, rupture area, and surface displacement: *Bulletin of the Seismological Society of America*, **84**, p. 974–1002.

-
- Whitehouse, P., 2009. Glacial isostatic adjustment and sea-level change: state of the art report.:
- Whitney, D.L., Umhoefer, P.J., Teyssier, C. and Fayon, A.K., 2008. Yo-yo Tectonics of the Niğde Massif During Wrenching in Central Anatolia: *TURKISH JOURNAL OF EARTH SCIENCES*, **17**, p. 209–217.
- Winslow, M.A., 1982. The structural evolution of the Magallanes Basin and neotectonics in the southernmost Andes: *Antarctic Geoscience*, **4**, p. 143–154.
- Woodcock, N.H. and Fischer, M., 1986. Strike-slip duplexes: *Journal of Structural Geology*, **8**, p. 725–735, doi: [https://doi.org/10.1016/0191-8141\(86\)90021-0](https://doi.org/10.1016/0191-8141(86)90021-0).
- Wu, P., 1998. Intraplate earthquakes and post-glacial rebound in eastern Canada and Northern Europe: *Dynamics of the Ice Age Earth: A Modern Perspective*, p. 603–628, doi: <https://doi.org/10.4028/www.scientific.net/RC.38>.
- Wu, P. and Hasegawa, H.S., 1996. Induced stresses and fault potential in eastern Canada due to a realistic load: a preliminary analysis: *Geophysical Journal International*, **127**, p. 215–229, doi: <https://doi.org/10.1111/j.1365-246X.1996.tb01546.x>.
- Wu, P. and Johnston, P., 2000. Can deglaciation trigger earthquakes in N. America? *Geophysical Research Letters*, **27**, p. 1323-1326., doi: <https://doi.org/10.1029/1999GL011070>.
- Wu, P., Johnston, P. and Lambeck, K., 1999. Postglacial rebound and fault instability in Fennoscandia: *Geophysical Journal International*, **139**, p. 657–670, doi: <https://doi.org/10.1046/j.1365-246x.1999.00963.x>.
- Wu, P. and Mazzotti, S., 2007. Effects of a lithospheric weak zone on postglacial seismotectonics in eastern Canada and the northeastern United States: *SPECIAL PAPERS-GEOLOGICAL SOCIETY OF AMERICA*, **425**, p. 113, doi: [https://doi.org/10.1130/2007.2425\(09\)](https://doi.org/10.1130/2007.2425(09)).

Y

- Yamaguchi, D.K., Atwater, B.F., Bunker, D.E., Benson, B.E. and Reid, M.S., 1997. Tree-ring dating the 1700 Cascadia earthquake: *Nature*, **389**, p. 922–923, doi: 10.1038/40048.
- Yamaguchi, D.K. and Hoblitt, R.P., 1995. Tree-ring dating of pre-1980 volcanic flowage deposits at Mount St. Helens, Washington: *GSA Bulletin*, **107**, p. 1077–1093, doi: 10.1130/0016-7606(1995)107<1077:TRDOPV>2.3.CO;2.

Z

Zielke, O., Klinger, Y. and Arrowsmith, J.R., 2015. Fault slip and earthquake recurrence along strike-slip faults—Contributions of high-resolution geomorphic data: *Tectonophysics*, **638**, p. 43–62, doi: <https://doi.org/10.1016/j.tecto.2014.11.004>.

ANNEXES

Co-seismic deformation and post-glacial slip rate along the Magallanes-Fagnano fault, Tierra Del Fuego, Argentina

Sandrine Roy¹  | Riccardo Vassallo¹  | Joseph Martinod¹ | Matías C. Ghiglione²  |
Christian Sue^{1,3}  | Pascal Allemand⁴ 

¹ISTerre, Univ. Grenoble Alpes, Université Savoie Mont Blanc, CNRS, IRD, IFSTTAR, Grenoble, France

²IDEAN-CONICET - Universidad de Buenos Aires, Buenos Aires, Argentina

³CNRS UMR6249, Université Bourgogne Franche-Comté, Besançon, France

⁴Laboratoire de Géologie, Université Claude Bernard Lyon 1, Villeurbanne, France

Correspondence

Sandrine Roy, Institute of Earth Sciences ISTerre, Université Savoie Mont Blanc, 73376 Le Bourget-du-Lac, Grenoble, France. Email: s.roy.unistra@gmail.com

Funding information

Direction Générale de la Recherche Scientifique et du Développement Technologique, Grant/Award Number: PhD Scholarship Sandrine ROY; Argentinian-French ECOS-SUD, Grant/Award Number: A15U02

Abstract

Across the extreme south of Patagonia, the Magallanes-Fagnano Fault (MFF) accommodates the left-lateral relative motion between South America and Scotia plates. In this paper, we present an updated view of the geometry of the eastern portion of the MFF outcropping in Tierra del Fuego. We subdivide the MFF in eight segments on the basis of their deformation styles, using field mapping and interpretation of high-resolution imagery. We quantify coseismic ruptures of the strongest recorded 1949, M_w 7.5 earthquake, and determine its eastern termination. We recognize several co-seismic offsets in man-made features showing a sinistral shift up to 6.5 m, greater than previously estimated. Using ^{10}Be cosmogenic nuclides depth profiles, we date a cumulated offset in post-glacial morphologies and estimate the long-term slip rate of the eastern MFF. We quantify a 6.4 ± 0.9 mm/a left-lateral fault slip rate, which overlaps geodetic velocity and suggests stable fault behaviour since Pleistocene.

1 | INTRODUCTION

The Magallanes-Fagnano Fault (MFF) accommodates the sinistral motion between the Scotia and South America plates along a 600 km fault system that crosses the Isla Grande de Tierra del Fuego from the western channel of the Magellan Strait to the Atlantic coast (Figure 1a). This active transform boundary continues eastward along the North Scotia Ridge towards South Georgia (Betka, Klepeis, & Mosher, 2016; Dalziel, Lawver, Norton, & Gahagan, 2013; Esteban, Tassone, Isola, Lodolo, & Menichetti, 2018; Klepeis, 1994). In Tierra del Fuego, GNSS data indicate that active deformations are localized on the MFF, and that present-day fault velocity ranges between -5.9 ± 0.2 mm/a (Mendoza et al., 2015) and -6.6 ± 1.3 mm/a (Smalley et al., 2003). The locking depth of the eastern MFF is estimated at about 11 ± 5 km (Mendoza et al., 2015).

In this work, we focus on the Eastern MFF between the Fagnano Lake and the Atlantic coast in Tierra del Fuego (Figure 1b). Two major seismic events occurred in 1879 and 1949. On the 1 February 1879,

several European settlements reported an earthquake of intensity VII Modified Mercalli Scale (MMS) near Punta Arenas and VIII MMS in Tierra del Fuego (Cisternas & Vera, 2008), that was later estimated having magnitude 7–7.5 (Lomnitz, 1970). In 1949, two main earthquakes occurred on December 17 at 6:53 (GMT) (M_w 7.75), and at 15:07 (GMT) (M_w 7.5), followed by several aftershocks of unknown magnitude (Febrer, Plasencia, & Sabbione, 2000; Jäschke, Sabbione, & Sierra, 1982). We report in Figure 1b the position of 1949 epicentres according to different authors. Co-seismic surface ruptures (Figure 2a) were described at Fagnano and Udaeta Lakes shoreline and in the Estancia La Correntina (Costa et al., 2006; Lodolo et al., 2003; Pedrera et al., 2014). The maximum horizontal component associated with the 1949 ruptures was estimated up to 4 m (Costa et al., 2006).

Intertwined with the tectonic activity, the landscape of Tierra del Fuego has been shaped by the alternating advance and retreat of the Fuegian Patagonian ice-sheet (Coronato, Seppälä, Ponce, & Rabassa, 2009; Glasser & Ghiglione, 2009; Waldmann, 2008; Waldmann, Ariztegui, Anselmetti, Coronato, & Austin, 2010). A major glacial lobe

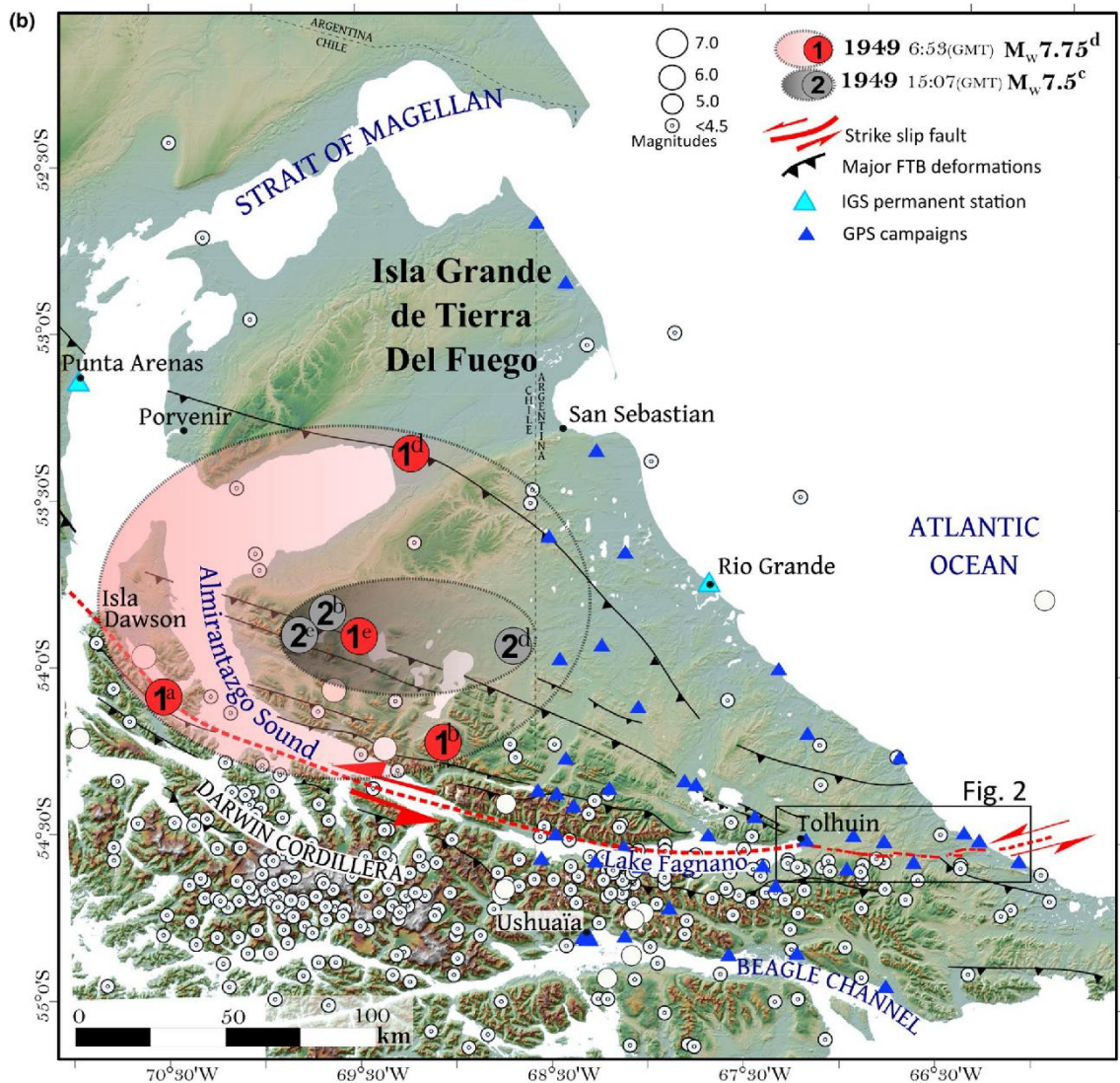
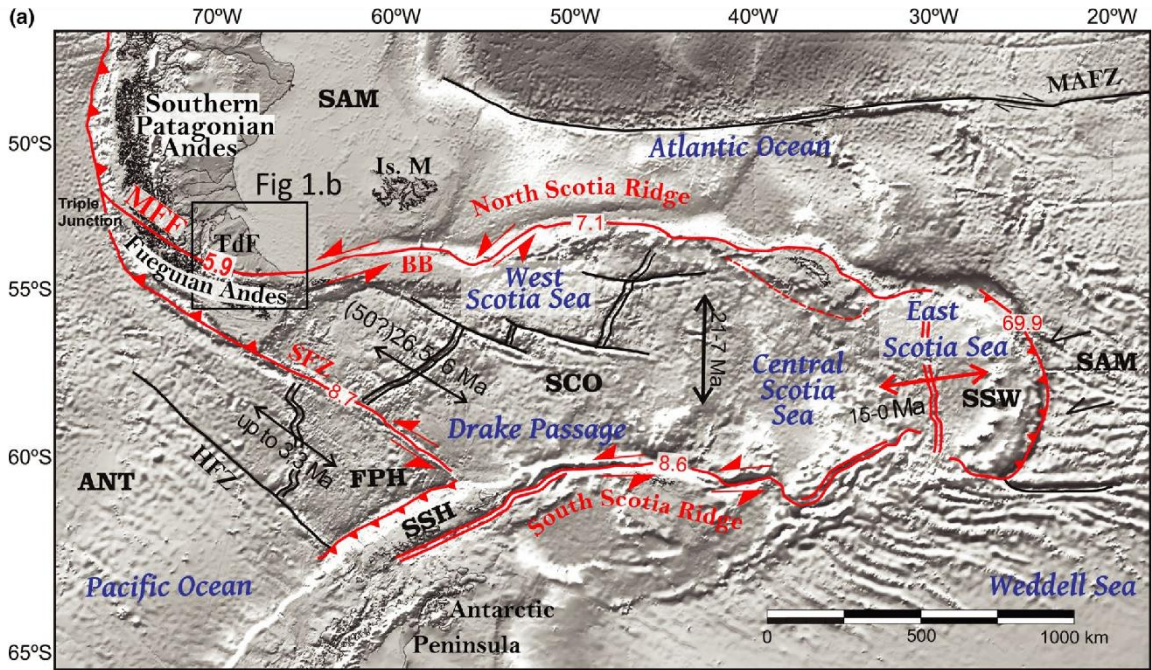


FIGURE 1 (a) Tectonic setting of southernmost Andes with plate boundary velocities (mm/a) (from: Barker, 2001; Dalziel et al., 2013; Ghiglione et al., 2010; Thomas, Livermore, & Pollitz, 2003), superimposed on greyscale topography and bathymetry (Sandwell & Smith, 1997). Relative strike-slip motion of MFF from (Mendoza et al., 2015). Red lines are active structures; black lines are extinct tectonic features. ANT, Antarctic plate; BB, Burdwood Bank; FPH, Former Phoenix plate; HFZ, Hero Fracture Zone; Is. M, Islas Malvinas; MFF, Magallanes-Fagnano Fault; MAFZ, Malvinas-Agulhas Fracture Zone; SAM, South America plate; SCO, Scotia plate; SFZ, Shackleton Fracture Zone; SSH, South Shetland plate; SSW, South Sandwich plate, TdF, Isla Grande de Tierra del Fuego. (b) Faults and seismicity of Tierra del Fuego. The trace of the MFF is shown with a red dotted line, and the major fold-thrust belt (from Glasser & Ghiglione, 2009) are shown with black lines. We reported historical 1949 earthquakes epicentre locations proposed by (a) Castano (1977); (b) Jaschek et al. (1982); (c) Lomnitz (1970); (d) Pelayo and Wiens (1989); (e) U.S. Geological Survey (2017); Red and grey shaded ellipses refer to the most consistent region for epicentre location of the two main 1949 shocks. Catalogue of earthquakes are from (Buffoni, Sabbione, Connon, & Ormaechea, 2009; Febrer et al., 2000; Flores Véliz, 2017; Pelayo & Wiens, 1989). Locations of GPS sites measured in Mendoza et al. (2015) [Colour figure can be viewed at wileyonlinelibrary.com]

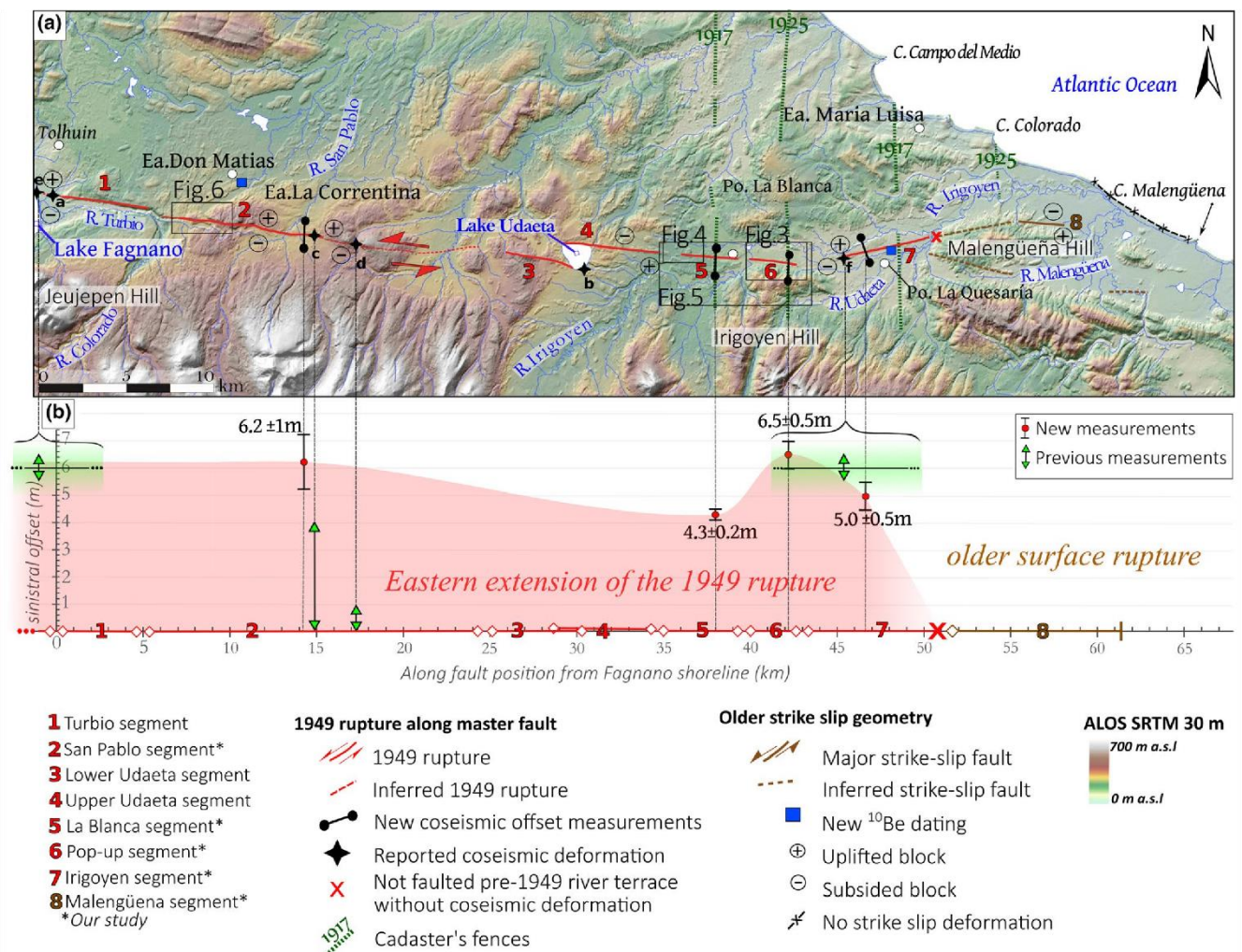


FIGURE 2 (a) Structural map of the eastern MFF. The 1949 surface ruptures are shown as red lines, and the segments with evidences of long-term slip are shown as brown lines. The red cross symbolizes the eastern termination of the 1949 surface rupture. Reported coseismic surface deformations: (a) sag pond and vertical scarp (~0.5 to 1 m) in Fagnano gravel bar (Lodolo et al., 2003); (b) liquefaction and truncated-tree line features (Onorato et al., 2016; Pedrera et al., 2014); (c) and (d), respectively, 'San Pablo' and 'Oliva' disrupted fences mentioned by (Costa et al., 2006). (e) and (f) show two previous reported offsets by eyewitnesses without exact locations (Costa et al., 2006). The relative uplifted blocks are shown with a circled plus sign. The base map is DEM SRTM ALOS Word 3D-30m (© JAXA). (b) 1949 sinistral horizontal offsets along the eastern MFF. Red dots and their associated error bars correspond to measurements from this study. Previous reported offset using green triangles and green shaded rectangles showing the range of possible locations. The 1949 surface rupture continues westward through the Fagnano lake [Colour figure can be viewed at wileyonlinelibrary.com]

flowed eastward from the Darwin Cordillera (Figure 1b) and carved a deep valley now partly occupied by the Fagnano Lake, while east of the lake, smaller tributary glaciers flowed northward above the fault,

and eroded part of the pre-glacial strike-slip morphologies (Coronato, Meglioli, & Rabassa, 2004). Consequently, the reconstruction of the last deglaciation timing and the related deposit locations are crucial

to understand when and where post-glacial strike-slip faulting were recorded. In our work, we built high resolution digital elevation model from Pléiades images combined with extensive field work to study the remarkable imprint of the tectonic activity left in the glaciofluvial deposits and analyse the geometry and kinematics of the fault ruptures.

The Holocene activity of the MFF has been studied at some specific sites by Costa et al. (2006), Waldmann et al. (2011), Esteban et al. (2014), Onorato, Perucca, Coronato, Rabassa, and López (2016), Perucca, Alvarado, and Saez (2016). In this paper, we present a detailed description of the 65-km long onshore part of the fault located east of Fagnano Lake, including the previously unstudied 30 km-long segments located east of Udaeta lake. We describe the 1949 rupture, and reassess the horizontal offset and the coseismic rupture length with new observations of unprecedented described features. Finally, we describe the geomorphic cumulated offset to constrain the average MFF long-term slip rate since the Late-Pleistocene.

2 | EASTERN MFF GEOMETRY

East of Fagnano Lake, the MFF strike is $N90^{\circ}$ – 95° , i.e. sub-parallel to the Palaeogene structures that conform the Fuegian thin-skinned

fold and thrust belt (Ghiglione & Ramos, 2005; Klepeis & Austin, 1997). We subdivide the fault into eight segments with their singular geomorphic expressions. All segments are characterized by a main strike-slip kinematics, however, a moderate dip-slip component results in the relative uplift of either the southern or northern block (Figure 2). The deformation style varies along the 65 km length of the fault and exposes both localized and more distributed patterns. We observe on most of the segments Riedel faults (Figure 3a) with a minor vertical component. Orientations indicate R-shear synthetic fractures ranging $N70^{\circ}$ – 75° (Figure 3).

In other segments, the tectonic deformation is distributed over fault in a sheared zone. At the northern foothill of Sierra Irigoyen along segment 6, we identify a 3-km-long alignment of hectometric pop-up structures (Figure 4a). They consist in asymmetric 2–6 m-high rhomboidal hills, elongated in their ENE, WSW axis. The inner part exposes $N80^{\circ}$ -striking Riedel faults (Figure 4b,d). On pop-ups, trees trunks of 100 years old are progressively tilted towards the external border, evidencing that the elevation of these structures amplified during the last earthquake (Figure 4c,e). This particular expression of surface deformation, distributed on transpressive structures, is located in an active flood plain. The presence of unconsolidated sand material and water may favour this deformation style.

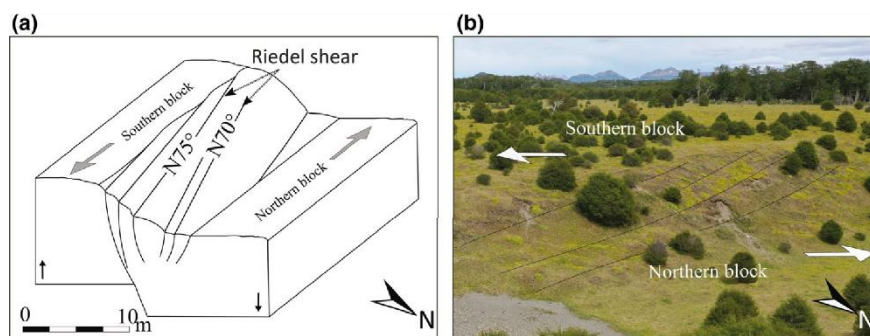


FIGURE 3 Deformation style of the segment 5 (a) Block diagram of Riedel faults with a long-term dip-slip component; (b) Field photography of the Riedel faults [Colour figure can be viewed at wileyonlinelibrary.com]

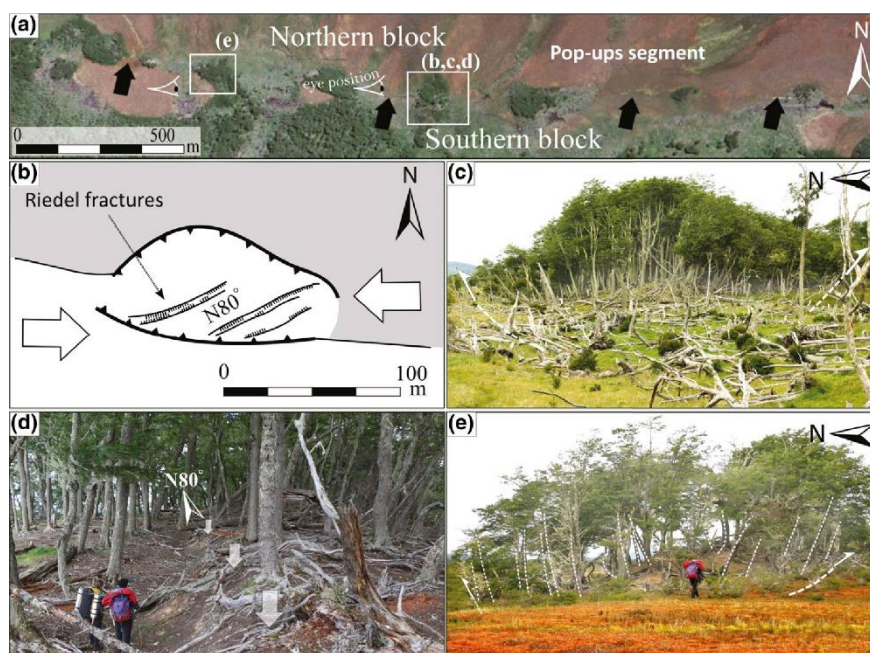


FIGURE 4 Geometry and style of the pop-up structures along segment 6 (a) General view of the pop-ups alignment (green forested patches); (b) detailed structural sketch of one pop-up showing Riedel faults; (c) pop-up structure with fan shaped tilted trees; (d) Riedel fault within a pop-up; (e) pop-up structure with tilted tree [Colour figure can be viewed at wileyonlinelibrary.com]

3 | THE 1949 CO-SEISMIC RUPTURE

Costa et al. (2006) interviewed several eyewitnesses of the 1949 earthquakes and concluded that the horizontal offset did not exceed 4 m. Some witnesses however reported lateral offsets as large as 6 m. Unfortunately, these observations are not supported by field measurements and their precise location is missing. A more exhaustive and accurate offsets estimation is therefore fundamental to improve earthquake scaling behaviour for this fault.

We observe many preserved markers of the co-seismic ruptures from the last earthquake sequence, some of them giving information on the 1949 sinistral offset. Two offsets have been measured (Figure 5) in sheep fences corresponding to the Argentinean land registers of the early 20th century (Casali & Manzi, 2017). These limits correspond to several tens of kilometres N-S straight wired connected fences which can easily be mapped from satellite images (Figure 5a). In segments 5 and 6, fence offsets evidence a 4 ± 0.2 m and a 6.5 ± 0.5 m sinistral shift, respectively (Figure 5b,c). However, it is not possible discriminating whether the offset originated from one or from the sum of the two successive shocks. Also, no evidence of creeping has been noticed since the new fences replaced the pre-1949 ones (Figure 5d).

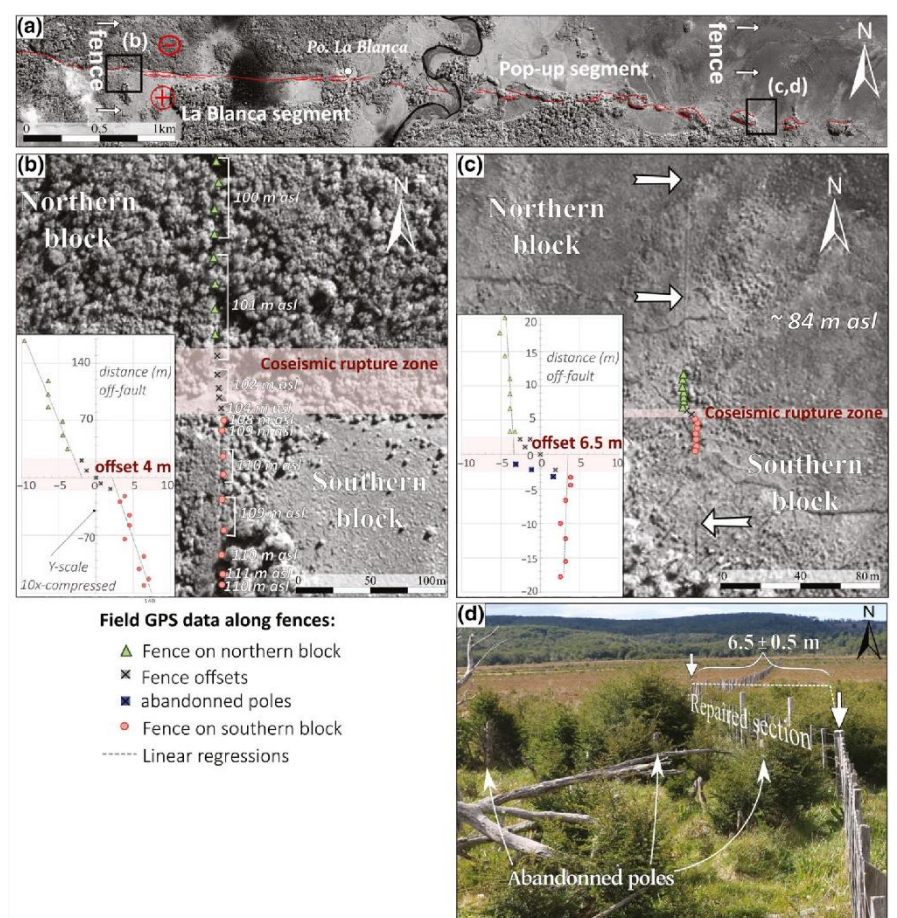
Another offset is measured at the segment 7 (Figure 2), where $N75^\circ$ lineament have been previously noticed (Ghiglione, 2003).

The fault is crossed by a stream flowing southward which undergoes a sharp sinistral offset of $5 \text{ m} \pm 0.5 \text{ m}$. Besides, in the segment 2 a $6.2 \pm 1 \text{ m}$ sinistral offset is also visible in the foundations of an abandoned broken bridge that spanned over the fault line. These field measurements evidence the horizontal component of the rupture on different segments and show that largest offsets are up to 6–6.5 m. This value is higher than previously measured (4 m) and is consistent with observations noticed by eyewitnesses of the 1949 event.

The easternmost offset measured is localized within the segment 7. Eastward, no geomorphic evidence of the rupture could be observed in pre-1949 river terraces, suggesting that the surface rupture did not propagate farther east (Figure 2b). Along the segment 8, the fault trace is visible in a continuous 5 m-high scarp. However, this scarp is much more degraded than in the western segments. These characteristics are consistent with the occurrence of older ruptures along this segment. We did not observe any strike-slip evidence between the Colorado and Malengüena Capes.

Our observations show that 1949 co-seismic rupture zone ended at 50 km east of the Lake Fagnano shoreline. Westward of our study zone, the rupture continues across the Fagnano lake parallel to its EW elongate geometry. It could die out somewhere along the 100 km of the lake or continue further west in

FIGURE 5 (a) Pléiade image above the fault segments 5 and 6 showing the location of offset fences. (b) and (c) GPS points along fences superimposed on Pléiade images, respectively, at segments 5 and 6. Note: on the figure (b) the NS scale of the lower graph has been compressed 10 times. White arrow in (c) highlight the trace of the fences away from the coseismic rupture zone. (d) Photography of measured sinistral offset along the segment 6, showing some of the disrupted fence abandoned poles [Colour figure can be viewed at wileyonlinelibrary.com]



the Magellan Strait. Nevertheless, the lack of observation on the western part of the MFF prevent to identify the 1949 surface ruptures termination.

4 | POST-GLACIAL SLIP RATE

Here, we use the changes in the hydrological network following the Fuegian glaciers retreat to assess the post-glacial long-term slip rate.

The segment 2 crosscuts four well-defined geomorphic markers within a 2 km-long zone (Figure 2a): a dead valley, its associated meander, one topographic depression and one ridge (Figure 6a). We use the respective edges of the geomorphic markers (Figure 6b) to assess the left-lateral offset using the back-slip restoration technique (e.g. Klinger et al., 2005; McGill & Sieh, 1991). The piercing points all match with the best correlation at 115 ± 5 m displacement (Figure 6c).

This restoration shows that these various markers are synchronous and probably related to a main landscape formation phase

corresponding to the ice retreat. After restoration, the dead-valley recovers its characteristic shape before the abandonment. This valley was carved by meltwater streams following the retreat of tributary glaciers. Such glaciers have also been described further to the west in Jeujepen hill (Figure 2a; Coronato, Roig, & Mir, 2002). Glacial and Glaciofluvial erosion erased previous strike-slip offset. Such markers fix the beginning of the tectonic surface deformation record in this segment, providing a relative slip chronometer.

By dating the exposure of the youngest sediments of the fossil drainage system, we date the abandonment of the valley and the onset of the subsequent tectonic deformation record. Sampling took place respectively near the Estancia Don Matias and the Puesto La Quesaria (Figure 2a) with established procedures (Braucher, Brown, Bourlès, & Colin, 2003; Ritz et al., 2006). We sampled quartz cobbles for cosmic ray exposure dating using ^{10}Be along two vertical profiles. Surfaces are flat and underwent negligible erosion, thus we assume a zero denudation rate for age calculations. We use the least-square

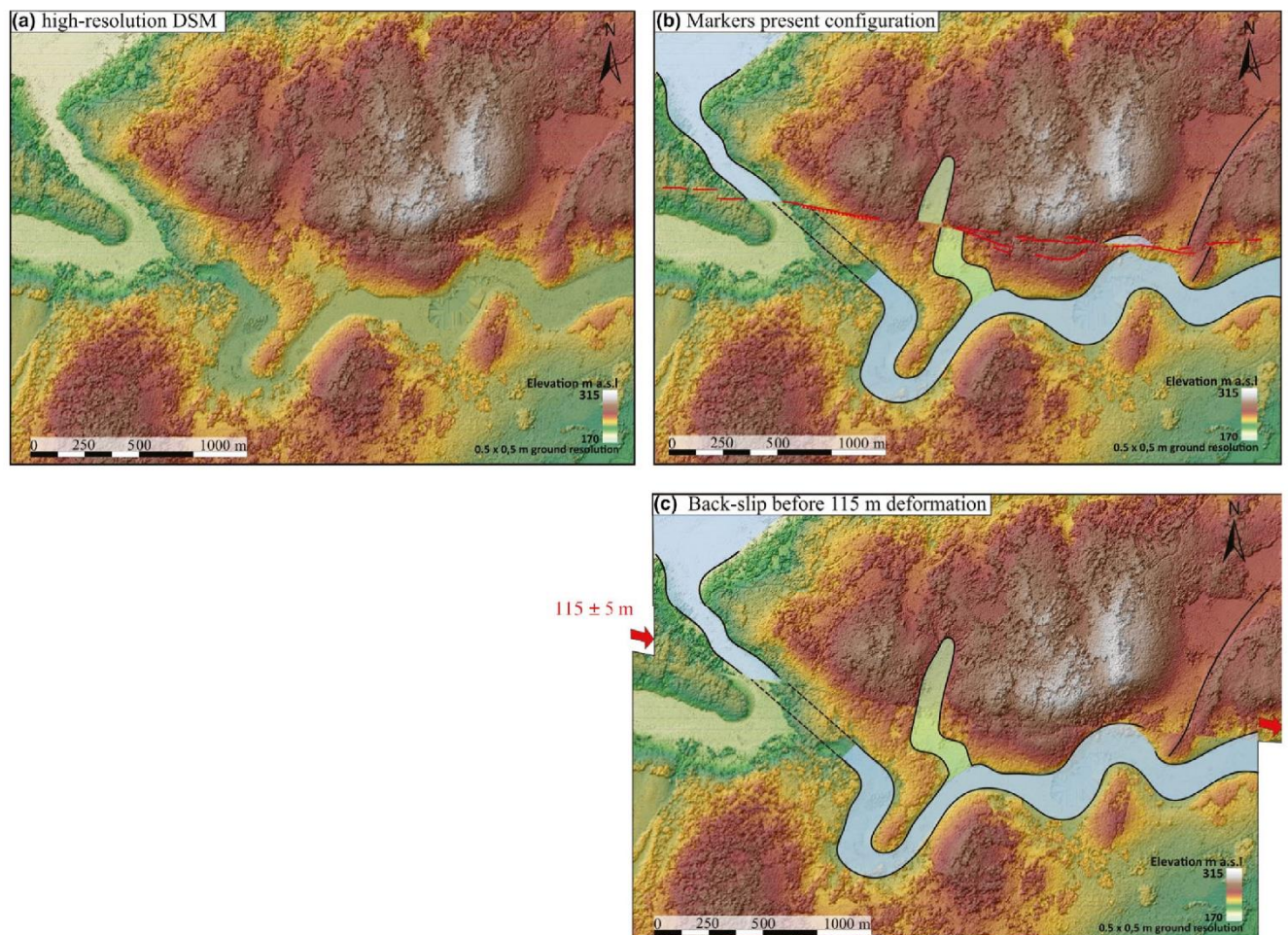


FIGURE 6 Back-slip deformation of post-glacial morphologies along segment 2. (a) High resolution DSM showing the dead valley drainage system, (b) markers superimposed on DSM with strike-slip (red lines), and offsets in geomorphic markers (black lines): abandoned valley with associated truncated meander (blue cover), hanging valley (green cover) and a hill's ridge (single black line). Lines are used as piercing point crossing the fault trace. We projected each flank of the abandoned valley on the fault plane to identify piercing points. (c) Back slip deformation of markers, the piercing points match for 115 ± 5 m cumulated offset [Colour figure can be viewed at wileyonlinelibrary.com]

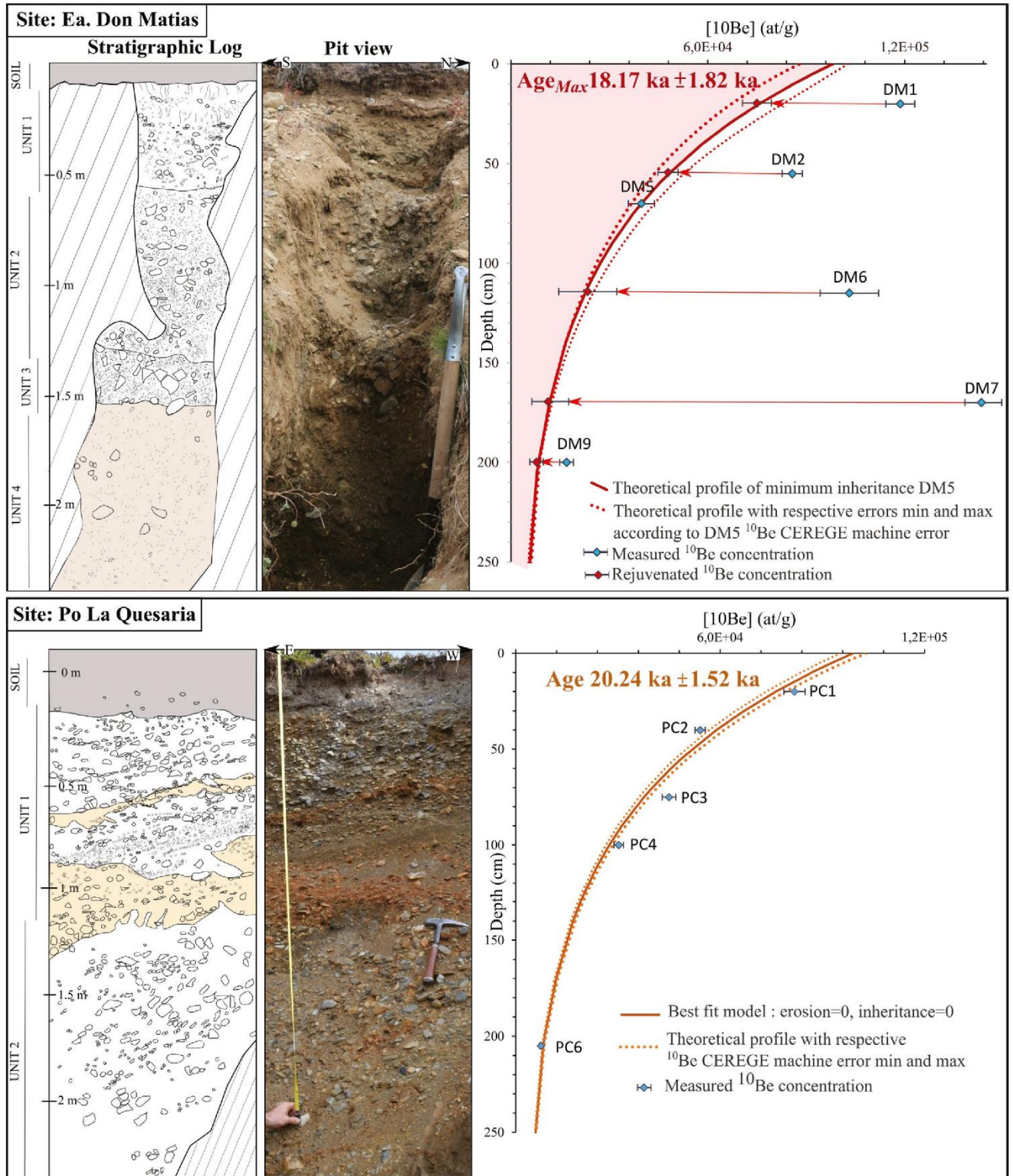


FIGURE 7 ¹⁰Be depth profiles with respective stratigraphic log and pit view of site Estancia Don Matias and Puesto La Quesaria (see Figure 2 for location). ¹⁰Be production rate has been calibrated for local latitudes and elevations (Stone, 2000), using the modified functions of (Lal, 1991), which stands in quartz production of 4.92 ± 0.43 at $\text{g}^{-1} \text{a}^{-1}$ at sea level and high latitude. Calculations were performed using attenuation lengths of 150, 1,500 and 5,300 g/cm^2 with associated relative contributions of 97.85%, 1.50% and 0.65% (Braucher et al., 2003). We employ the currently accepted ¹⁰Be half-life value of 1.387 ± 0.012 10^6 years (Chmeleff, Blanckenburg, Kossert, & Jakob, 2010; Korschinek et al., 2010; Nishiizumi et al., 2007). Measurements were completed at the accelerator mass spectrometry facility ASTER (Aix-en-Provence, France) after preparation at the ISTERre GeoThermoChronology platform (Grenoble, France) [Colour figure can be viewed at wileyonlinelibrary.com]

inversion to model theoretical curves on both profiles for ^{10}Be concentration measurements.

Estancia Don Matias' terrace stratigraphic log presents four facies of well-sorted sandy gravel matrix with gradational contacts resulting from glaciofluvial depositions (Figure 7). The predominance of subangular and subrounded clasts in the two lower levels (unit 3 and 4) indicates a short glaciofluvial transport. The concentrations distribution does not decrease exponentially with depth, evidencing that sample may have two exposure sources: the common post-depositional cosmogenic nuclide production and their own pre-depositional production, which is responsible for an intrinsic ^{10}Be inheritance value. Based on these hypotheses, we apply the profile rejuvenation methodology (Le Dortz et al., 2012). We select the sample (DM5) with the minimum ^{10}Be concentration normalized by depth. It has the lowest inherited concentration among all the profile samples. Its apparent exposure age is, therefore, the closest to the true post-depositional age of the valley. The ^{10}Be concentration of sample DM5 yields a maximum age of valley abandonment at -18 ± 2 ka. This age fixes the beginning of the tectonic deformation record. In the same area, age based on ^{14}C of basal peat bog grown on top of moraine deposits confirm that ice retreat in this region started before -14 ka (Coronato et al., 2009).

At Puesto La Quesaria, we sampled the highest preserved alluvial terrace, whose formation is supposed to be synchronous of regional glacial retreat. The profile exposes pebble to gravel clasts in a sandy matrix characteristic of meltwater channel environment (Figure 7). Here, the distribution of ^{10}Be concentrations decreases exponentially with depth following the theoretical curve of ^{10}Be production (Brown et al., 1991; Dunai, 2010), suggesting that inherited cosmogenic concentrations are negligible compared to post-depositional concentrations. These concentrations yield a terrace exposure age of 20.2 ± 1.5 ka, overlapping the maximum age obtained near the Estancia Don Matias.

These ages characterize the main recession phase during which the tributaries glaciers retreated above the Southern Hills (Coronato et al., 2009; Rabassa, Coronato, & Martínez, 2011; Waldmann et al., 2010). The abandonment of the glaciofluvial valleys resulting from ice retreat fossilized the associated drainage system allowing the preservation of fault activity in the landscape since 18–20 ka. The cumulated offset observed in the valley near by the Estancia Don Matias since this period yields a geomorphic slip-rate of 6.4 ± 0.9 mm/a.

5 | DISCUSSION AND CONCLUSIONS

We explore the main post-glacial deformations recorded along the eastern sector of the MFF from Lake Fagnano to the Atlantic coast and integrated previously documented geometries. Newly described strike-slip structures, pop-ups, and Riedel fractures are mapped with the relative vertical motion of blocks. The analysis of high-resolution topographic models and satellite images does not show any significant deformation on secondary structures, confirming that strike-slip motion concentrates along the master fault as already suggested by GPS data inversion (Mendoza et al., 2011).

We chart the 1949 surface primary ruptures and measured related sinistral slips. We document horizontal offsets up to 6.5 ± 0.5 m. Surface rupture can be followed along 50 km from the Fagnano Lake shoreline to the tip of the segment 7. According to the main shocks magnitudes the 1949 surface rupture probably continued beneath Fagnano Lake, but the lack of direct access to the western part of the MFF prevent to identify the 1949 western surface ruptures termination.

Back-slip restoration of offset glaciofluvial markers combined with ^{10}Be dating allow the first quantification of the geomorphic slip rate for this fault. The offset started to accumulate when the local glacial catchment source vanished and associated drainage system was abandoned -18 ± 2 ka ago. Our results yield a left-lateral Late Pleistocene slip rate of 6.4 ± 0.9 mm/a over this period. This value overlaps the present-day velocity estimated using geodetic data. The unchanged fault slip rate over the different time-scale suggests a stable fault behaviour since glaciers retreat.

Previous indirect attempts of major MFF earthquake recurrence estimations are divergent and possibly biased by the method used. The shorter proposed recurrence interval is about 350–850 years (Waldmann et al., 2011) while the longer is 3,000–4,500 years (Costa et al., 2006). The former study uses as a proxy the mass-wasting events in Fagnano Lake, which may integrate events triggered on other structures, while the latter is based on a single palaeoseismological trench, in which sedimentary and tectonic record are not complete and some events may not be registered. Considering the 1949 co-seismic offsets in the area around the long-term slip-rate measurement, we obtained an average offset of 6 ± 0.5 m. With a geomorphic slip rate of 6.4 ± 0.9 mm/a, and based on the average co-seismic offset of 1949, we propose a frequency of large earthquakes event about $1,000 \pm 215$ years.

ACKNOWLEDGEMENTS

This research is part of a bilateral scientific cooperation project between Argentinian Mincyt–Universidad de Buenos Aires, and the University Savoie Mont-Blanc (ISTerre) and the Besancon University, funded by the Argentinian-French ECOS-SUD under grant project A15U02. We acknowledge the French CNRS-INSU (project PICS and SYSTER). We address special thanks to J. Carcaillet (ISTerre GeoThermoChronology platform) for his guidance in cosmogenic dating and warmly thank F. Massot and O. Romeyer for their technical support. We are also deeply grateful to M. P. Escayola (UNTDF Universidad Tierra Del Fuego), M. Bauducco and C. Maure for their direct and efficient support in Tierra del Fuego. The authors thank J.L. Paños, E.S. Ampuero, K.A. Vargas Saldivia, and P.J. López, for kindly authorizing us to work on their lands. The manuscript was greatly improved due to careful reviews by F. Visini, P. Burrato and Associate Editor C. Chiarabba.

DATA AVAILABILITY STATEMENT

The data that support the findings of this study are available on request from the corresponding author.

ORCID

Sandrine Roy  <https://orcid.org/0000-0003-3541-7765>

Riccardo Vassallo  <https://orcid.org/0000-0003-2785-8835>

Matías C. Ghiglione  <https://orcid.org/0000-0002-0243-3251>

Christian Sue  <https://orcid.org/0000-0002-2472-5001>

Pascal Allemand  <https://orcid.org/0000-0003-1269-6298>

REFERENCES

- Barker, P. F. (2001). Scotia sea regional tectonic evolution: Implications for mantle flow and palaeocirculation. *Earth-Science Reviews*, 55, 1–39. [https://doi.org/10.1016/S0012-8252\(01\)00055-1](https://doi.org/10.1016/S0012-8252(01)00055-1)
- Betka, P., Klepeis, K., & Mosher, S. (2016). Fault kinematics of the Magallanes-Fagnano fault system, southern Chile: An example of diffuse strain and sinistral transtension along a continental transform margin. *Journal of Structural Geology*, 85, 130–153. <https://doi.org/10.1016/j.jsg.2016.02.001>
- Braucher, R., Brown, E. T., Bourlès, D. L., & Colin, F. (2003). In situ produced ^{10}Be measurements at great depths: Implications for production rates by fast muons. *Earth and Planetary Science Letters*, 211, 251–258. [https://doi.org/10.1016/S0012-821X\(03\)00205-X](https://doi.org/10.1016/S0012-821X(03)00205-X)
- Brown, E. T., Edmond, J. M., Raisbeck, G. M., Yiou, F., Kurz, M. D., & Brook, E. J. (1991). Examination of surface exposure ages of Antarctic moraines using in situ produced ^{10}Be and ^{26}Al . *Geochimica et Cosmochimica Acta*, 55, 2269–2283. [https://doi.org/10.1016/0016-7037\(91\)90103-C](https://doi.org/10.1016/0016-7037(91)90103-C)
- Buffoni, C., Sabbione, N. C., Connon, G., & Ormaechea, J. L. (2009). Localización De Hipocentros Y Determinación De Su Magnitud En Tierra Del Fuego Y Zonas Aledañas. *GeoActa*, 34, 75–86.
- Casali, R., & Manzi, L. M. (2017). Etnicidades capitalistas: El rol de la Estancia San Pablo en el entramado de resistencia selk'nam. *Tierra del Fuego, 1904–1930. Magallania (Punta Arenas)*, 45, 109–133. <https://doi.org/10.4067/S0718-22442017000200109>
- Castano, J. C. (1977). Zonificación sísmica de la República Argentina. *Publicación Técnica*, 5, 40.
- Chmeleff, J., von Blanckenburg, F., Kossert, K., & Jakob, D. (2010). Determination of the ^{10}Be half-life by multicollector ICP-MS and liquid scintillation counting. *Nuclear Instruments and Methods in Physics Research Section B: Beam Interactions with Materials and Atoms*, 268, 192–199. <https://doi.org/10.1016/j.nimb.2009.09.012>
- Cisternas, A., & Vera, E. (2008). Sismos históricos y recientes en Magallanes. *Magallania (Punta Arenas)*, 36, 43–51. <https://doi.org/10.4067/S0718-22442008000100004>
- Coronato, A., Meglioli, A., & Rabassa, J. (2004). Glaciations in the Magellan Straits and Tierra del Fuego, southernmost South America. In J. Ehlers, & P. L. Gibbard (Eds.), *Developments in quaternary sciences, Quaternary glaciations extent and chronology. PART III: South America, Asia, Africa, Australia and Antarctica*. vol. 2. (pp. 45–48). Amsterdam, the Netherlands: Elsevier.
- Coronato, A., Roig, C., & Mir, X. (2002). Geoformas glaciares de la región oriental del Lago Fagnano, Tierra del Fuego, Argentina. In Actas XV Congreso Geológico Argentino. El Calafate, Argentina (23–26 de abril, 2002). CD-Rom. Artículo.
- Coronato, A., Seppälä, M., Ponce, J. F., & Rabassa, J. (2009). Glacial geomorphology of the Pleistocene lake Fagnano ice lobe, Tierra del Fuego, Southern South America. *Geomorphology*, 112, 67–81. <https://doi.org/10.1016/j.geomorph.2009.05.005>
- Costa, C. H., Smalley, R., Velasco, M. S., Schwart, D. P., Ellis, M., & Ahumada, E. A. (2006). Paleoseismic observations of an onshore transform boundary: The Magallanes-Fagnano fault, Tierra Del Fuego, Argentina. *Revista de la Asociación Geológica Argentina*, 61(4), 647–657.
- Dalziel, I. W., Lawver, L. A., Norton, I. O., & Gahagan, L. M. (2013). The Scotia arc: Genesis, evolution, global significance. *Annual Review of Earth and Planetary Sciences*, 41, 767–793. <https://doi.org/10.1146/annurev-earth-050212-124155>
- Dunai, T. J. (2010). *Cosmogenic Nuclides: Principles, concepts and applications in the Earth surface sciences*. Cambridge, UK: Cambridge University Press. <https://doi.org/10.1017/CBO9780511804519>
- Esteban, F. D., Tassone, A., Isola, J. I., Lodolo, E., & Menichetti, M. (2018). Geometry and structure of the pull-apart basins developed along the western South American-Scotia plate boundary (SW Atlantic Ocean). *Journal of South American Earth Sciences*, 83, 96–116. <https://doi.org/10.1016/j.jsames.2018.02.005>
- Esteban, F. D., Tassone, A., Lodolo, E., Menichetti, M., Lippai, H., Waldmann, N., ... Vilas, J. F. (2014). Basement Geometry and Sediment Thickness of Lago Fagnano (Tierra Del Fuego). *Andean Geology*, 41, 293–313.
- Febrer, J. M., Plasencia, M. P., & Sabbione, N. C. (2000). Local and regional seismicity from Ushuaia broadband station observations (Tierra del Fuego). *Terra Antarctica*, 8, 35–40.
- Flores Véliz, M. C. (2017). Estudio de la sismicidad en la región de Magallanes. Facultad de Ciencias Físicas y Matemáticas, Universidad de Chile; Centro Sismológico Nacional Universidad de Chile Informe de Práctica FCFM y CSN, 30 p.
- Ghiglione, M. C. (2003). Estructura y evolución tectónica del Cretácico-Terciario de la costa Atlántica de Tierra del Fuego: *Estructura y Evolución Tectónica del Cretácico-Terciario de la costa atlántica de Tierra del Fuego* (PhD thesis) Ciudad De Buenos Aires (150 pp.).
- Ghiglione, M. C., Quinteros, J., Yagupsky, D., Bonillo-Martínez, P., Hlebszevitch, J., Ramos, V. A., ... Zapata, Y. T. (2010). Structure and tectonic history of the foreland basins of southernmost South America. *Journal of South American Earth Sciences*, 29, 262–277. <https://doi.org/10.1016/j.jsames.2009.07.006>
- Ghiglione, M. C., & Ramos, V. A. (2005). Progression of deformation and sedimentation in the southernmost Andes. *Tectonophysics*, 405, 25–46. <https://doi.org/10.1016/j.tecto.2005.05.004>
- Glasser, N. F., & Ghiglione, M. C. (2009). Structural, tectonic and glaciological controls on the evolution of fjord landscapes. *Geomorphology*, 105, 291–302. <https://doi.org/10.1016/j.geomorph.2008.10.007>
- Jaschek, E. U., Sabbione, N. C., & Sierra, P. J. (1982). Reubicación de sismos localizados en territorio Argentino, 1920–1963. Observatorio Astronomico de la Universidad nacional de la Plata.
- Klepeis, K. A. (1994). The Magallanes and Deseado fault zones: Major segments of the South American-Scotia transform plate boundary in southernmost South America, Tierra Del Fuego. *Journal of Geophysical Research: Solid Earth*, 99, 22001–22014. <https://doi.org/10.1029/94JB01749>
- Klepeis, K. A., & Austin, J. A. (1997). Contrasting styles of superposed deformation in the southernmost Andes. *Tectonics*, 16, 755–776. <https://doi.org/10.1029/97TC01611>
- Klinger, Y., Xu, X., Tapponnier, P., Van der Woerd, J., Lasserre, C., & King, G. (2005). High-resolution satellite imagery mapping of the surface rupture and slip distribution of the M_w 7.8, 14 November 2001 Kokoxili earthquake, Kunlun Fault, Northern Tibet, China. *Bulletin of the Seismological Society of America*, 95, 1970–1987. <https://doi.org/10.1785/0120040233>
- Korschinek, G., Bergmaier, A., Faestermann, T., Gerstmann, U. C., Knie, K., Rugel, G., ... Remmert, A. (2010). A new value for the half-life of ^{10}Be by heavy-ion elastic recoil detection and liquid scintillation counting. *Nuclear Instruments and Methods in Physics Research Section B: Beam Interactions with Materials and Atoms*, 268, 187–191. <https://doi.org/10.1016/j.nimb.2009.09.020>
- Lal, D. (1991). Cosmic ray labeling of erosion surfaces: In situ nuclide production rates and erosion models. *Earth and Planetary Science Letters*, 104, 424–439. [https://doi.org/10.1016/0012-821X\(91\)90220-C](https://doi.org/10.1016/0012-821X(91)90220-C)
- Le Dortz, K., Meyer, B., Sébrier, M., Braucher, R., Bourlès, D., Benedetti, L., ... Foroutan, M. (2012). Interpreting scattered in-situ produced

- cosmogenic nuclide depth-profile data. *Quaternary Geochronology*, 11, 98–115. <https://doi.org/10.1016/j.quageo.2012.02.020>
- Lodolo, E., Menichetti, M., Bartole, R., Ben-Avraham, Z., Tassone, A., & Lippai, H. (2003). Magallanes-Fagnano continental transform fault (Tierra del Fuego, southernmost South America). *Tectonics*, 22, 15–26. <https://doi.org/10.1029/2003TC001500>
- Lomnitz, C. (1970). Major earthquakes and tsunamis in Chile during the period 1535 to 1955. *Geologische Rundschau*, 59, 938–960. doi:<https://doi.org/10.1007/BF02042278>.
- McGill, S. F., & Sieh, K. (1991). Surficial offsets on the central and eastern Garlock fault associated with prehistoric earthquakes. *Journal of Geophysical Research: Solid Earth*, 96, 21597–21621. 0148-0227/91/j1365-246X.2010.04912.x
- Mendoza, L., Perdomo, R., Hormaechea, J. L., Cogliano, D. D., Fritsche, M., Richter, A., & Dietrich, R. (2011). Present-day crustal deformation along the Magallanes-Fagnano Fault System in Tierra del Fuego from repeated GPS observations. *Geophysical Journal International*, 184, 1009–1022. <https://doi.org/10.1111/j.1365-246X.2010.04912.x>
- Mendoza, L., Richter, A., Fritsche, M., Hormaechea, J. L., Perdomo, R., & Dietrich, R. (2015). Block modeling of crustal deformation in Tierra del Fuego from GNSS velocities. *Tectonophysics*, 651–652, 58–65. <https://doi.org/10.1016/j.tecto.2015.03.013>
- Nishiizumi, K., Imamura, M., Caffee, M. W., Southon, J. R., Finkel, R. C., & McAninch, J. (2007). Absolute calibration of ^{10}Be AMS standards. *Nuclear Instruments and Methods in Physics Research Section B: Beam Interactions with Materials and Atoms*, 258, 403–413. <https://doi.org/10.1016/j.nimb.2007.01.297>
- Onorato, M. R., Perucca, L., Coronato, A., Rabassa, J., & López, R. (2016). Seismically-induced soft-sediment deformation structures associated with the Magallanes-Fagnano Fault System (Isla Grande de Tierra del Fuego, Argentina). *Sedimentary Geology*, 344, 135–144. <https://doi.org/10.1016/j.sedgeo.2016.04.010>
- Pedraza, A., Galindo-Zaldívar, J., Ruiz-Constán, A., Bohoyo, F., Torres-Carbonell, P., Ruano, P., ...González-Castillo, L. (2014). The last major earthquakes along the Magallanes-Fagnano fault system recorded by disturbed trees (Tierra del Fuego, South America). *Terra Nova*, 26, 448–453. <https://doi.org/10.1111/ter.12119>
- Pelayo, A. M., & Wiens, D. A. (1989). Seismotectonics and relative plate motions in the Scotia Sea region. *Journal of Geophysical Research: Solid Earth*, 94, 7293–7320. 0148-0227/89/88jB-04217505.00
- Perucca, L., Alvarado, P., & Saez, M. (2016). Neotectonics and seismicity in southern Patagonia. *Geological Journal*, 51, 545–559. <https://doi.org/10.1002/gj.2649>
- Rabassa, J., Coronato, A., & Martínez, O. (2011). Late Cenozoic glaciations in Patagonia and Tierra del Fuego: An updated review. *Biological Journal of the Linnean Society*, 103, 316–335. <https://doi.org/10.1111/j.1095-8312.2011.01681.x>
- Ritz, J.-F., Vassallo, R., Braucher, R., Brown, E. T., Carretier, S., & Bourlès, D. L. (2006). Using in situ-produced ^{10}Be to quantify active tectonics in the Gurvan Bogd mountain range (Gobi-Altay, Mongolia). *Special Papers-Geological Society of America*, 415, 87–110. [https://doi.org/10.1130/2006.2415\(06\)](https://doi.org/10.1130/2006.2415(06))
- Sandwell, D. T., & Smith, W. H. (1997). Marine gravity anomaly from Geosat and ERS 1 satellite altimetry. *Journal of Geophysical Research: Solid Earth*, 102, 10039–10054. 0148-0227/97/96jB-03223\$09.00
- Smalley, R., Kendrick, E., Bevis, M. G., Dalziel, I. W. D., Taylor, F., Lauria, E., ...Piana, E. (2003). Geodetic determination of relative plate motion and crustal deformation across the Scotia-South America plate boundary in eastern Tierra del Fuego. *Geochemistry, Geophysics, Geosystems*, 4, 1070. doi:<https://doi.org/10.1029/2002GC000446>.
- Stone, J. O. (2000). Air pressure and cosmogenic isotope production. *Journal of Geophysical Research: Solid Earth*, 105, 23753–23759. <https://doi.org/10.1029/2000jB900181>
- Thomas, C., Livermore, R., & Pollitz, F. (2003). Motion of the Scotia Sea plates. *Geophysical Journal International*, 155, 789–804. <https://doi.org/10.1111/j.1365-246X.2003.02069.x>
- U.S. Geological Survey (2017). Earthquake facts and statistics. National Earthquake Information Center, PDE.
- Waldmann, N. (2008). Late Quaternary environmental changes in Lago Fagnano, Tierra del Fuego (54 S): reconstructing sedimentary processes, natural hazards and paleoclimate [Sc 4040]. Faculte Des Sciences, Département de géologie et de paléontologie, University of Geneve, 154 p.
- Waldmann, N., Anselmetti, F. S., Ariztegui, D., Austin, J. A., Pirouz, M., Moy, C. M. and Dunbar, R. (2011). Holocene mass-wasting events in Lago Fagnano, Tierra del Fuego (54°S): implications for paleoseismicity of the Magallanes-Fagnano transform fault. *Basin Research*, 23, 171–190. doi:<https://doi.org/10.1111/j.1365-2117.2010.00489.x>
- Waldmann, N., Ariztegui, D., Anselmetti, F. S., Coronato, A., & Austin, J. A. Jr (2010). Geophysical evidence of multiple glacier advances in Lago Fagnano (54 S), southernmost Patagonia. *Quaternary Science Reviews*, 29, 1188–1200. <https://doi.org/10.1016/j.quascirev.2010.01.016>

How to cite this article: Roy S, Vassallo R, Martinod J, Ghiglione MC, Sue C, Allemand P. Co-seismic deformation and post-glacial slip rate along the Magallanes-Fagnano fault, Tierra Del Fuego, Argentina. *Terra Nova*. 2020;32:1–10. <https://doi.org/10.1111/ter.12430>

ANNEXE B - Chapter II - Coordinates and photographs
of the two trenches ; Photographs of trenches
samples.

Trench near Estancia Don Matias : -54.55021° -66.47161°



Photo 1 : Trench near Estancia Don Matias -54.55021 -66.47161



Photo 2 : Trench near Estancia Don Matias -54.55021 -66.47161



Photo 3: Samples from the trench near Estancia Don Matias -54.55021 -66.47161

Trench near Puesto La Quesaria -54.52300 -67.04391



Photo 4 Trench near Puesto La Quesaria -54.52300 -67.04391



Photo 5 Trench near Puesto La Quesaria -54.52300 -67.04391



Photo 6: Samples from the trench Puesto La Quesaria -54.52300 -67.04391

ANNEXE C - CHAPTER III - Morphotectonics: La Blanca segment

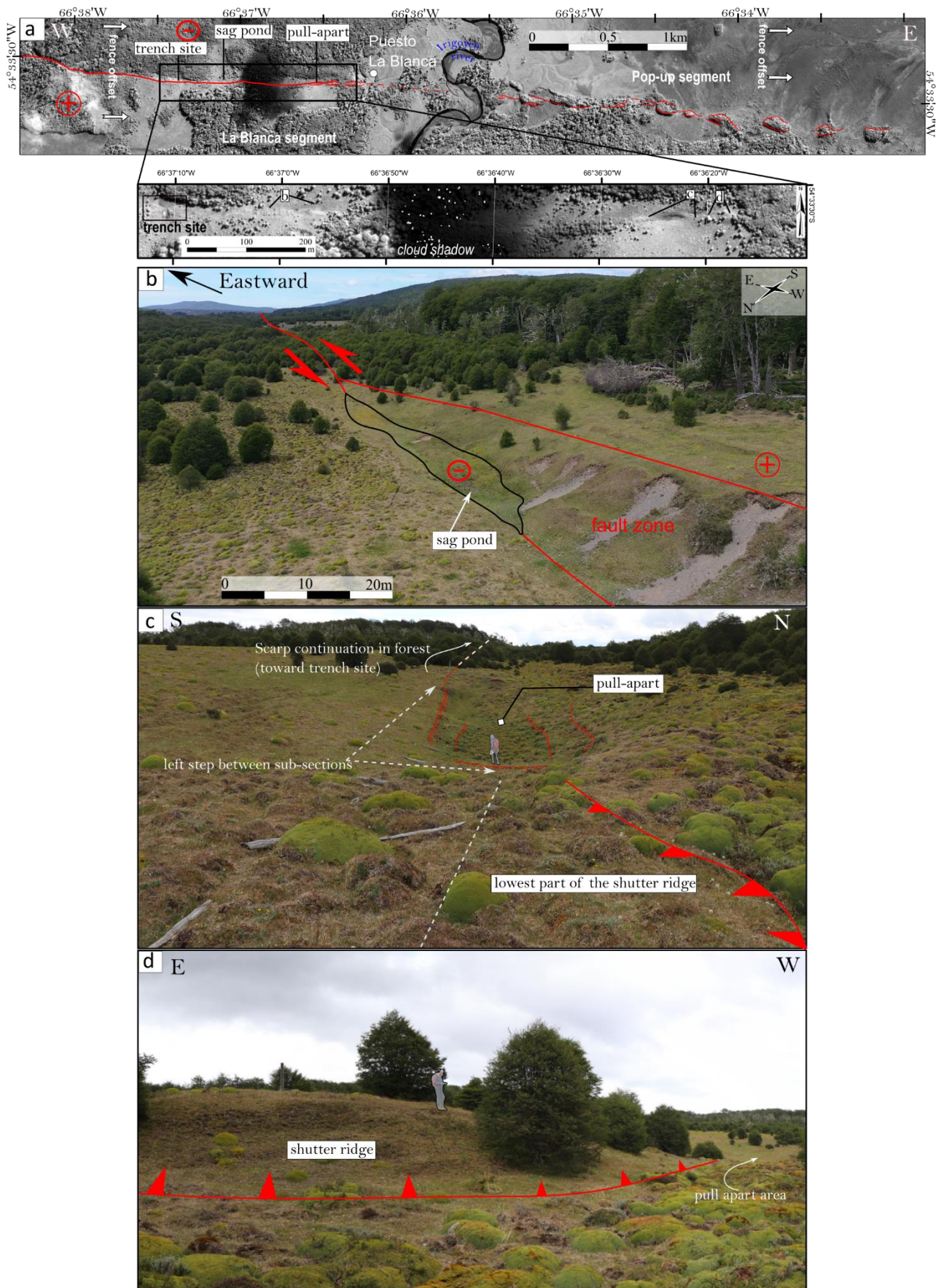
New remarkable tectonic geomorphologies are documented in the La Blanca segment, including sag ponds, pull-apart, and shutter ridges. Exceptionally preserved Riedels arranged in positive flower structure between the Scotia Plate and the South American plates indicate a local reverse strike-slip movement during Late-Holocene. Our study area is located 40 km east of the Lake Fagnano. The La Blanca segment is the eastern prolongation of the Northern Udaeta Fault, which bonds the active pull-apart basin Udaeta (Onorato *et al.*, 2017).

However, the connexion between these segments is not recognizable in satellite images (Figure 1b). The La Blanca's geometry exposes a remarkably distinct and continuous elongated shutter ridges with several sag-ponds and one small pull-apart (Figure 2a). The ridge is 10-20 meters wide, and the height varies along several kilometers from 1 up to 11 meters high. The average ridge's trend is N90°. The eastern end of these morphologies is identified within the actual Irigoyen river, which crosses the fault scarp and the western tip at 54°33'29,55" S, 66.39'0.66" W. Pronounced faulting geomorphic features are identified such as several topographic depressions (Figure 2b). They may not directly result from tectonic activity, but they are the hydrological response to the ridge uplift, and most probably act as a water gap. These sag ponds are typically 10 to 60 m long for 5-10 meters wide and very shallow. The dried surfaces with desiccation cracks indicate that rainfall may seasonally fill these landforms.

Toward the segment eastern end, the leading ridge vanished in a left step-over of 30 m toward the north and of 80 m-long (Figure 2c). A decametre-scale shutter ridge about 4 m high follows this step-over (Figure 2d). The geometry controls extensional deformation according to the sinistral slip and left-stepping direction of the two sub-sections. We identified several imbricated vertical faults, each of them exposed significant vertical displacement ~0.5-1 m (Figure 2c). They are arranged in a rhomboidal asymmetric shape and enclose a small graben

about ~ 5 m deep. These features' structural style is almost identical to that observed in the pull-apart development elastic dislocation theory model (Mann *et al.*, 1983) and analog model in sandbox (Woodcock and Fischer, 1986; McClay and Bonora, 2001). They indicate a hard-linkage between the two sub-sections that accommodate local volume change along a discrete pull-apart.

(Next page) Figure annexe B: (a) location map with Pleiades image; (b) sag-pond; (c) pull-apart resulting from the left-stepping arrangement between the shutter ridge (foreground) and the continuation of the fault scarp in the forest (background); (d) shutter ridge; (standing person for scale).



ANNEXE D – CHAPTER III - 3D analysis of Riedel in trench site La Blanca

The trench site shows four main Riedel fractures A, B, C and D with orientation N75° to N70° (Figure 2). In trenches, the geometries of the faults are consistent with what is observed in the surface morphology. These Riedels crosscut the trench n°1 and n°2, and correspond respectively to the main fault FT2 in trench n°2, and to the pair of faults F9/F10 (not apparent on western wall) and F1/F19 in trench n°1 (Figure 10). As previously shown, these reverse dip-slip faults disrupt the soil horizon and reached the surface with a vertical displacement about 10-20 cm. They are associated with the last ruptures either 1879 and/or 1949. They are well-preserved on the topography which implied necessarily that they are relatively young morphologies. Even though the left-lateral movement is predominant along the MFF, these microfaults show a shortening component. The principal shortening components is NS oriented, almost orthogonally with respect to the tectonic boundary. These reverse dip slip faults are responsible for a local uplift of paleosoil and arranged in a positive flower structure (Figure 10). The inward-dipping fault splays have profiles ranging from steep upthrust (FT2, F9/F10) to shallow-dipping thrust (F1/F19). However, it is not possible to verify if the faults merge at depth, as suggested by worldwide example of strike-slip contractional block (Harding, 1985).

Regionally, it seems the deformation style alternate along a single yet complex strike-slip zone, including the Udaeta pull apart (Onorato *et al.*, 2017), La Blanca positive flower ridge, La Blanca small pull-apart and aligned pop-up structures (Roy *et al.*, 2020). As suggested by theoretical studies of strike-slip, these regions may indicate the motion of adjacent crustal blocks, which induced localized crustal extension and shortening (Chinnery, 1965; Christie-Blick and Biddle, 1985; Bilham and King, 1989).

This architectural complexity is widely recognized in worldwide transcurrent intracontinental fault, like the Kunlun Tibetan fault, the Central Anatolian fault and the San Andrea fault (Umhoefer *et al.*, 2007; Whitney *et al.*, 2008; Duvall *et al.*, 2013) and is known as 'porpoising structure' (Crowell, 1974) or 'yoyo structure' (Umhoefer *et al.*, 2007).

Since the youngest deposits are affected by multiple reverse faults with vertical uplift, it can be interpreted that since the Late Holocene, this segment is experiencing significant shortening.

The cumulated vertical displacement is $\sim +11$ m (La Blanca ridge). On the other hand, the same deposit seems to be affected by a local graben with ~ -5 m of subsidence (La Blanca pull-apart). Further investigation is required to determine if these secondary contractional and extensional bends are coeval.

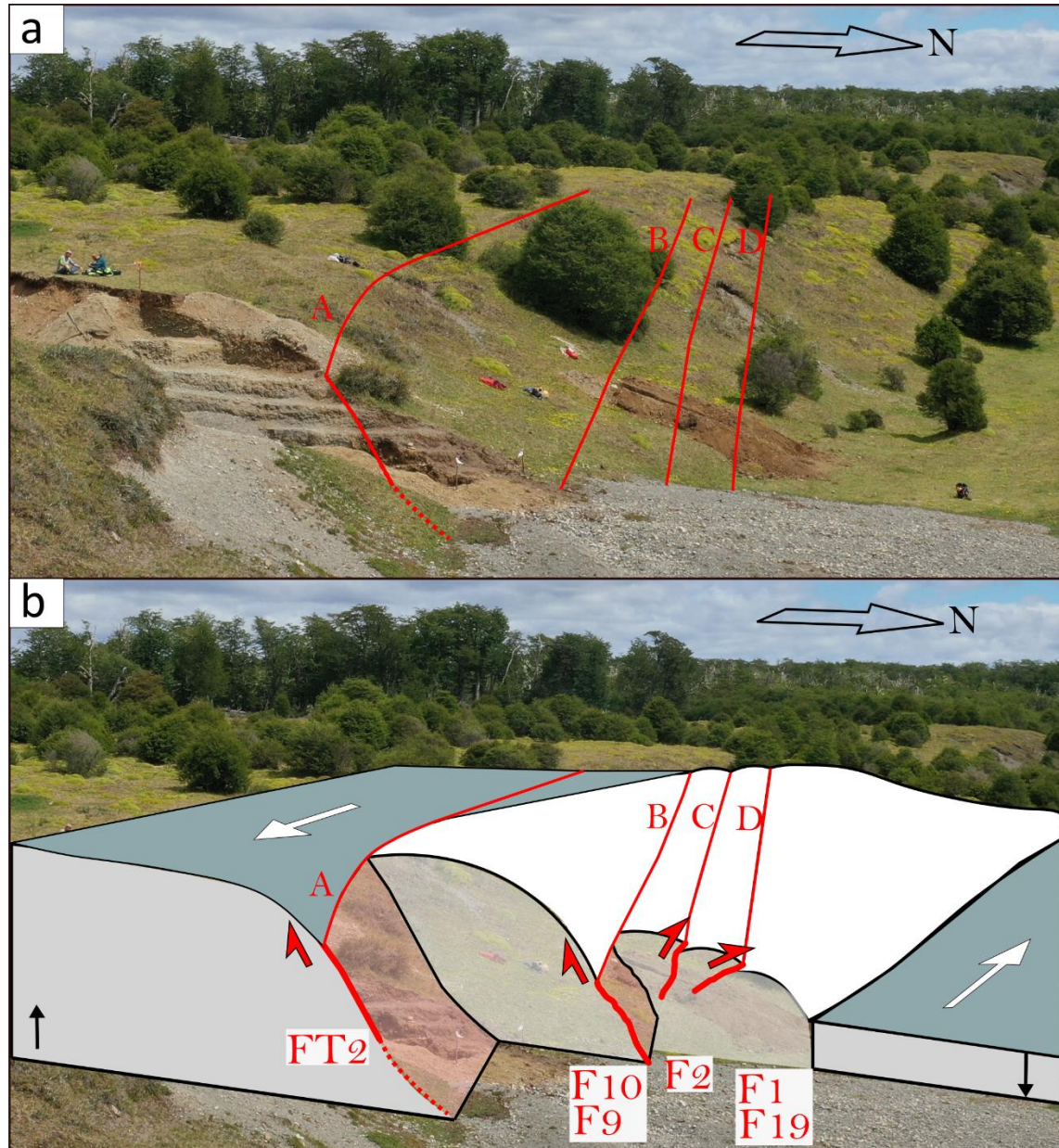
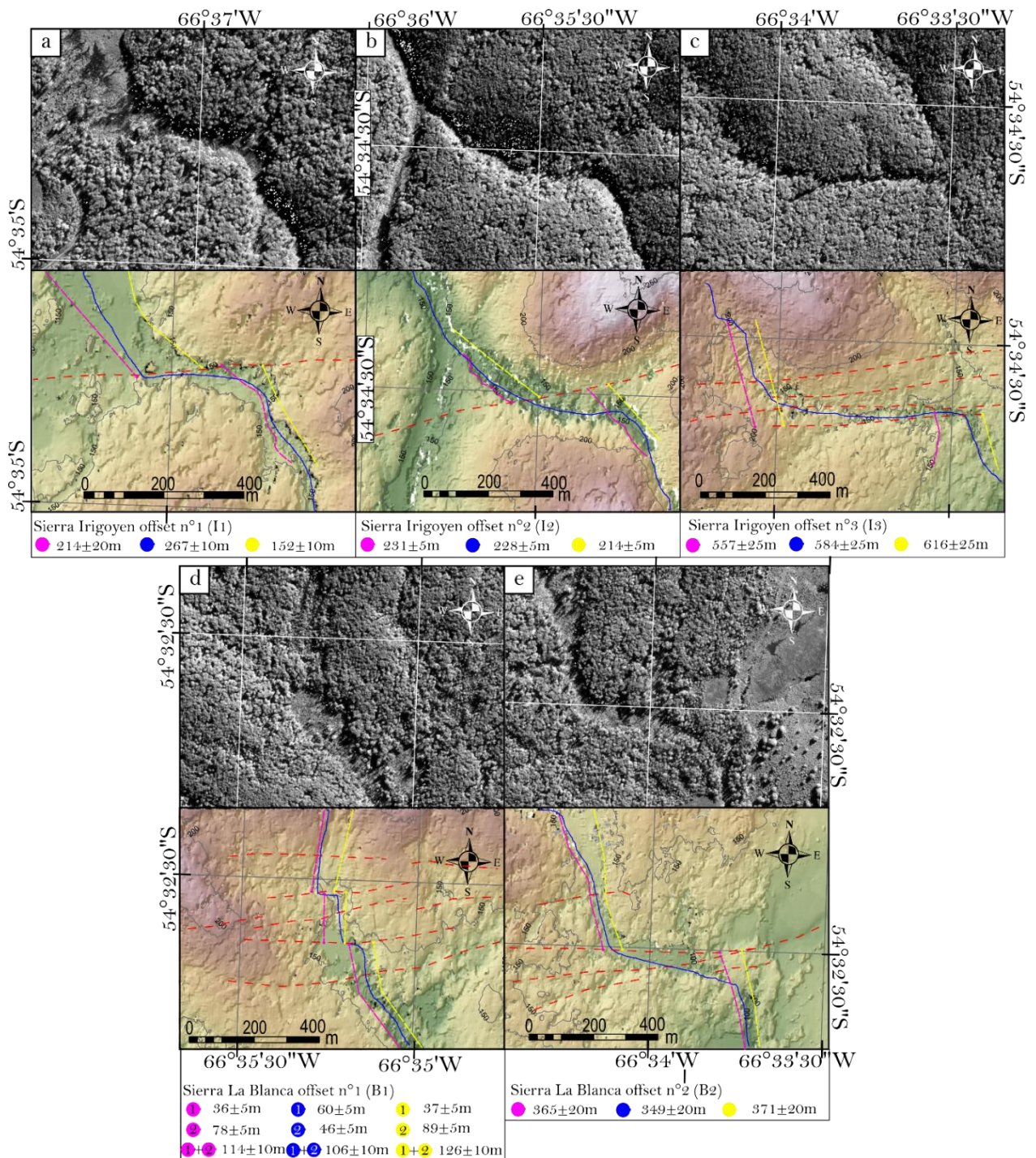


Figure Annexe C: (a) Photograph and (b) block diagram showing the relationship between topographic Riedels and reverse faults from the trench analysis. They form a positive flower structure. The sinistral movement is shown with exaggerated offset between the uplifted blocks of the structure. The Riedels are listed A, B, C, and D. Note that in figure g(a) the trench n°1 is not fully excavated and it does not show the final extend of the trench.

ANNEXE E - CHAPTER III - Multiple deviated rivers in the Sierra Irigoyen

Figure Annexe D: Measurements of long-term offsets following methods of chapter 4 (Zielke *et al.*, 2015).



ANNEXE F – CHAPTER IV, Trench Chile Eastern Wall

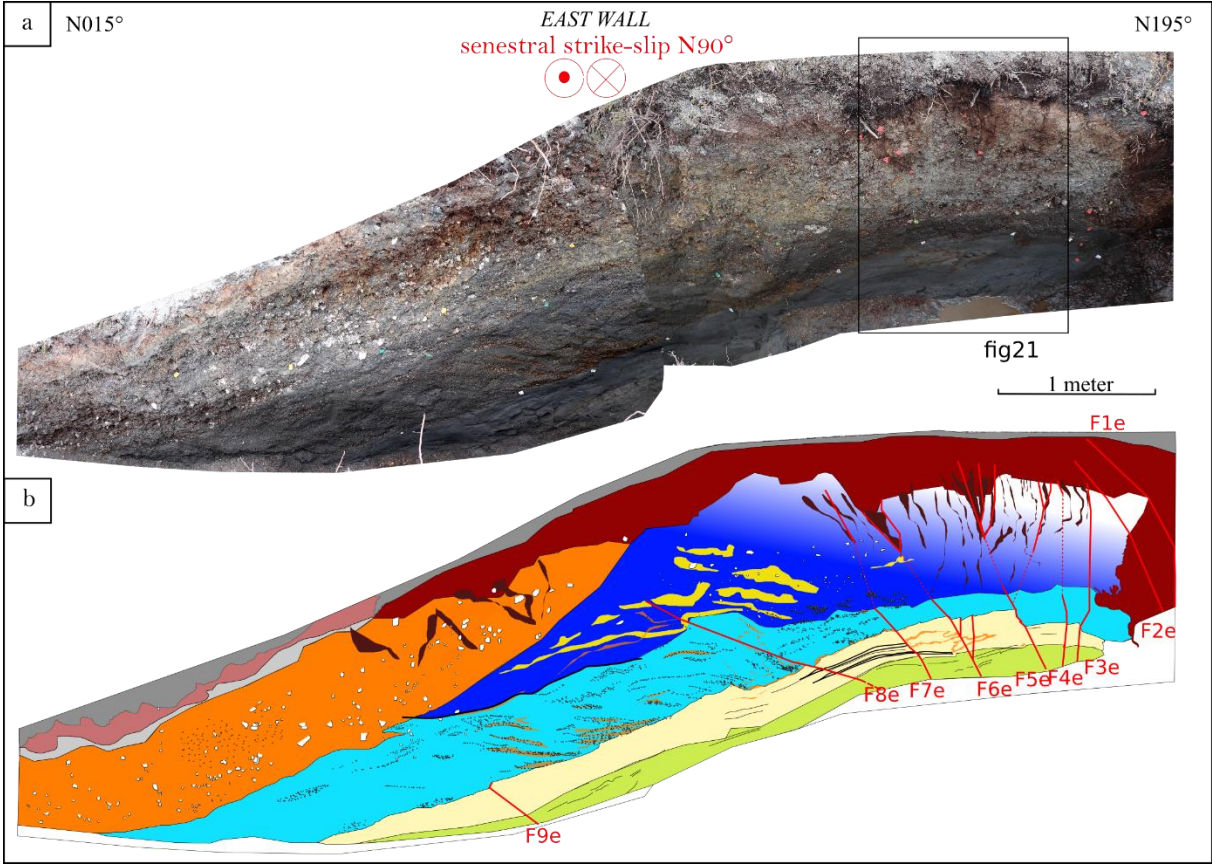


Figure Annexe E: Mosaic views of the trench's eastern wall across the Ainsworth fault section (a) photographic mosaic; (b) with interpretative logs.

ANNEXE G – CHAPTER IV, Be10 sample sites Cordillera Paciencia and Puerto Toto.





ANNEXE H – CHAPTER IV – Modern landslides in
Almirantazgo Sound

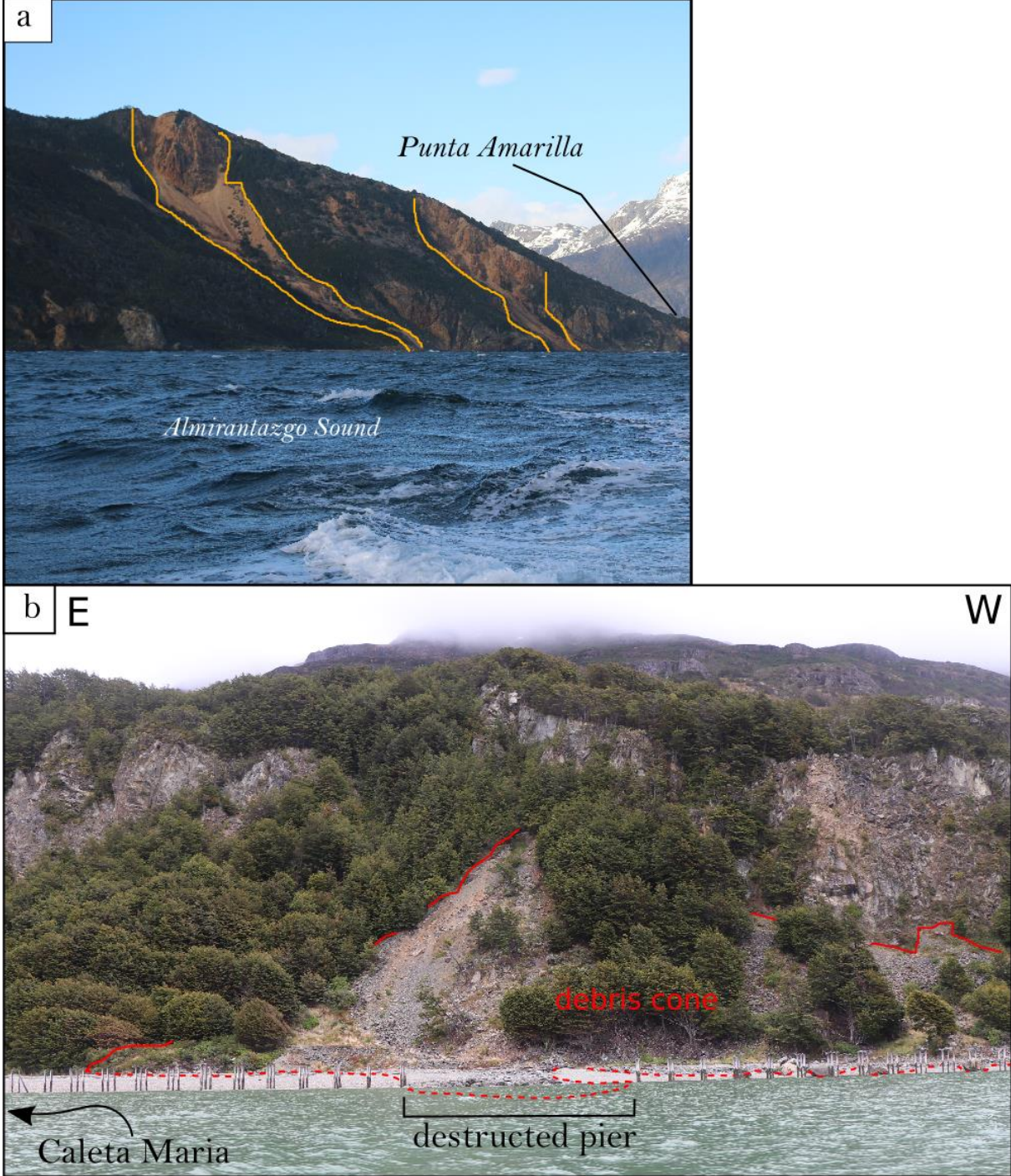
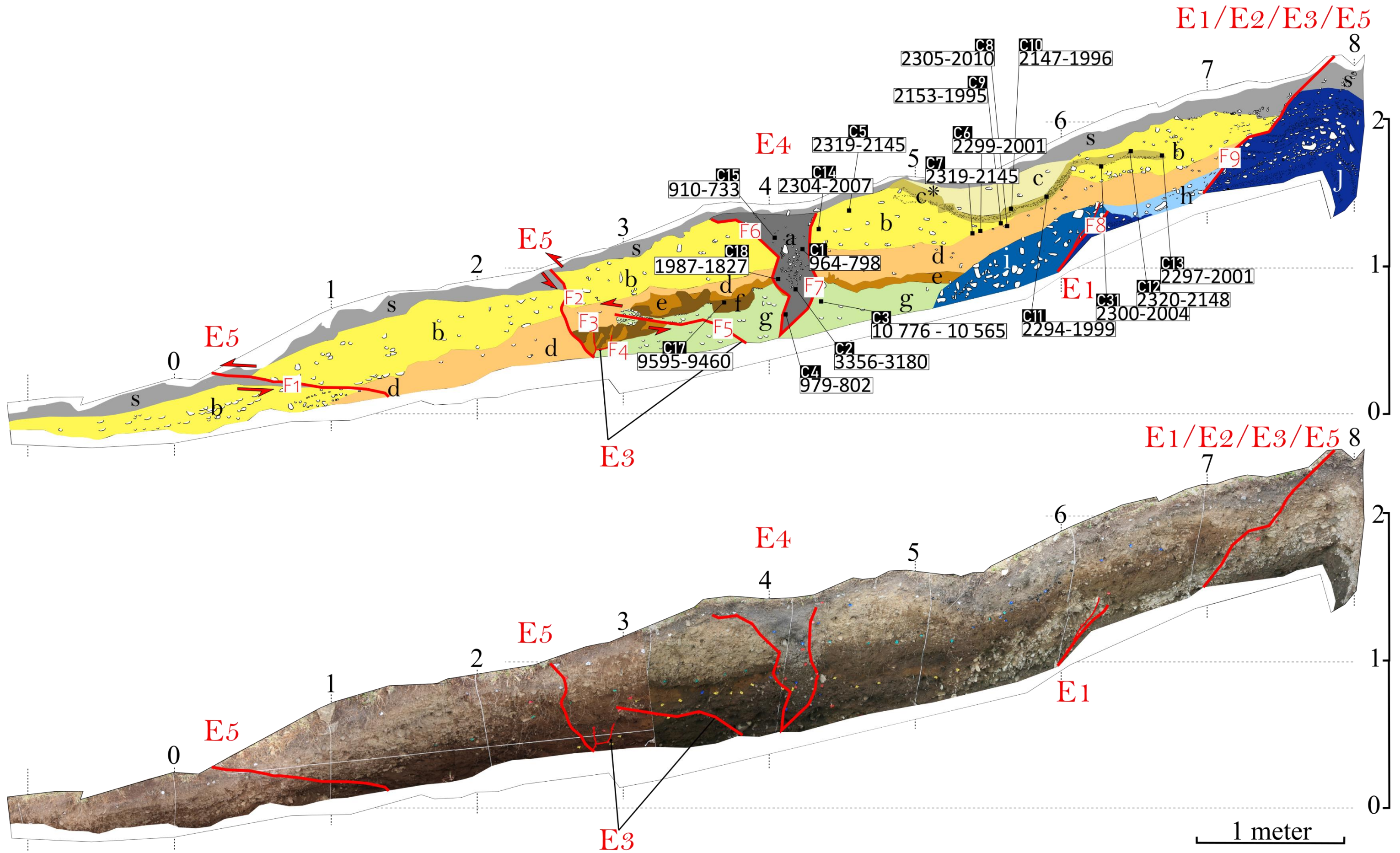


Figure Annexe F: (a) Multiples landslides on the Punta Amarilla. (b) Landslides along the Caleta Maria Southern banks.

NORTH

Eastern wall of La Blanca trench

SOUTH



NORTH

Western wall of La Blanca trench

SOUTH

